Laser Directed Energy Deposition Additive Manufacturing of Oxide Dispersion Strengthened (ODS) FeCrAl Under a Reactive Atmosphere

A Dissertation Presented for the
Doctor of Philosophy
Degree
The University of Tennessee, Knoxville

Ty C. Austin
August 2024

ACKNOWLEDGEMENTS

My graduate career path has been anything but smooth. From a global pandemic slamming the brakes on any appreciable research progress to learning how to balance being a father, husband, and researcher to moving halfway across the country and starting a full-time job prior to completing my research and dissertation, I can confidently say that I took the path less traveled. Without the unyielding support of countless individuals, completing this chapter of my academic career would not have been possible.

First, I would like to thank Dr. Steven Zinkle for his mentorship and guidance. Dr. Zinkle time and time again went out of his way to ensure that any impediments to my progress within his control were taken care of so I could focus on the task at hand. I was routinely amazed at his ability to always have an answer to any problem and his dedication to ensuring that his students had every tool possible to be successful. I will forever be grateful for his unwavering patience, endless wisdom, and willingness to let me make my own way. I would also like to thank Dr. Niyanth Sridharan for continuously pushing me to be a better researcher. While we may not have seen eye-to-eye often, I believe hearing a dissenting opinion is crucial for growth and staying openminded.

I want to thank Dr. Caleb Massey for his immense willingness to go out of his way to ensure that I had the materials and know-how to “get good data”. I will forever be grateful for his mentorship, friendship, and the constant compassion he showed helping those around him be successful. I want to thank Dr. Eric Lass for his determination in making sure that I had the proper tools to better understand the why behind my research. I am also thankful to Dr. Stephen Taller for his mentorship, kindness, and willingness to adapt to the unique situation created by the pandemic. To the many personnel at Oak

Ridge National Laboratory and the University of Tennessee that helped me along the way, you have my sincerest appreciation. I would like to specifically acknowledge and thank Brian Jordan for his patience, open-mindedness, and flexibility while assisting me in modifying equipment and performing the experiments that this work covers. I want to thank Thomas Siggillino for his persistent willingness to learn and help wherever possible as the demands on my time grew.

Finally, I would like to thank my friends and family. I am beyond grateful for Dr. Yao Li's willingness to answer all of the ridiculous microscopy questions that I had regardless of the hour of day. His kindness, humor, and empathy always managed to make the best of any situation. I also want to thank Logan Scott, Remington Reed, and Spencer Butler for their unconditional friendship and support.

Finally and most importantly, I would like to thank my wife, Cecelia Austin, for her steadfast love, support, and faith in me. Words cannot do justice to the describe how important your belief in me was even when mine faltered. I cannot thank you enough for the sacrifices you have made to allow me to pursue my interests and goals while balancing becoming a mother and starting your career. Your devotion is inspiring.

ABSTRACT

Oxide dispersion strengthened (ODS) FeCrAl alloys combine the improved high-temperature corrosion resistance provided by Al additions with the improved mechanical properties and irradiation resistance provided by fine nanoscale precipitate dispersions. Directed energy deposition (DED) additive manufacturing (AM) providing oxygen during powder consolidation allows for potential increased geometric complexity, local microstructure control, and part throughput while avoiding the pitfalls often plaguing conventional mechanical alloying (MA) based ODS manufacturing of batch-to-batch variability, long lead times, low throughput, and anisotropic mechanical properties. In this work laser-based DED AM of ODS FeCrAl was capable of significant oxygen retention (up to 0.11 wt%) and moderate precipitate number densities (~10^{20} m^{-3}) [approximately 10 to the 20th power per cubic meter) while maintaining acceptable part quality (part density > 99%). Unfortunately, significant amounts of oxide forming elements were wasted by precipitate agglomeration. The influence of Si, Ti, and O additions on oxide wettability, metal-oxide interfacial energy, and oxide incorporation into an Fe matrix was tested in an attempt to mitigate deleterious oxide agglomeration and maximize nanoscale precipitate production.

TABLE OF CONTENTS

CHAPTER ONE: INTRODUCTION AND GENERAL INFORMATION 1

1.1. Importance of Advanced Materials for Current Nuclear Reactors 1

1.2. Importance of Advanced Materials for Advanced Nuclear Fission and Fusion Reactors 2

1.3. Radiation Damage Fundamentals 4

1.4. Microstructural Engineering for Corrosion and Irradiation Resistance 7

1.5. Conventional Methods for ODS Manufacturing 9

1.5.1. Powder Metallurgy 9

1.5.2. Casting 11

1.5.3. Welding/Joining 13

1.6. Additive Manufacturing 14

CHAPTER TWO: LITERATURE REVIEW 18

2.1. Sinks and the Benefits of High Sink Strength 18

2.1.1. Influence of Sinks on Mechanical Properties 18

2.1.2. Influence of Sinks on Irradiation Resistance 31

2.2. Oxide Chemistry 37

2.3. Conventional Manufacturing 41

2.4. Gas Atomization Reaction Synthesis (GARS) 45

2.5. Additive Manufacturing of ODS Alloys Using Oxygen Containing Powder 47

2.6. Additive Manufacturing of ODS Alloys Using Reactive Atmospheres for *In Situ* Oxidation 49
2.7. Oxygen Absorption and Retention Under Additive Manufacturing 53
2.8. Oxide Agglomeration 56
2.9. Reducing Oxide Agglomeration 58
2.10. Research Objective Summary 60
CHAPTER THREE: MATERIALS AND METHODS 64
3.1. Characterization Methods 64
3.1.1. Inductively Coupled Plasma-Optical Emission Spectrometry (ICP-OES) and Inert Gas Fusion (IGF) 64
3.1.2. Optical Microscopy 65
3.1.3. Microhardness 66
3.1.4. Electron Microscopy 67
3.1.4.1. Scanning Electron Microscopy 67
3.1.4.2. Focused Ion Beam 67
3.1.4.3. Scanning Transmission Electron Microscopy 68
3.1.5. Atom Probe Tomography 69
3.2. Experimental Design 69
3.2.1. Influence of Operating Parameters on *In Situ* Oxidation 69
3.2.2. Influence of Alloying on Agglomeration and Precipitation 74
CHAPTER FOUR: INFLUENCE OF OPERATING PARAMETERS ON *IN SITU* OXIDATION 88
4.1. Build Quality 88

4.1.1. Build Composition 88
4.1.2. Defect Density and Cracking 90
4.2. Agglomeration 100
4.2.1. Inclusion Formation 100
4.2.2. Wasted Y and O 103
4.3. Precipitation 104
4.3.1. Characterization by Scanning Transmission Electron Microscopy 104
4.3.2. Characterization by Atom Probe Tomography 113
4.4. Mechanical Property Testing 121
4.4.1. Vickers Microhardness 121
4.4.2. Precipitate Strengthening 124
4.5. Build Property – Operating Parameter Relationships 127
4.5.1. Influence of Operating Parameters on Build Quality 127
4.5.2. Influence of Operating Parameters on O Content 131
4.6. Summary 150
CHAPTER FIVE: INFLUENCE OF ALLOYING ON AGGLOMERATION AND PRECIPITATION 151
5.1. Build Quality 151
5.1.1. Build Composition 151
5.1.2. Defect Density and Solidification Cracking 156
5.2. Agglomeration 174
5.3. Nanoscale Precipitation and Grain Boundary Segregation 180

5.3.1. Scanning Electron Microscopy 180
5.3.2. Atom Probe Tomography 187
5.4. Mechanical Property Testing 198
5.4.1. Vickers Microhardness 198
5.4.2. Precipitate Strengthening 198
5.5. Summary 202
CHAPTER SIX: CONCLUSIONS AND FUTURE WORK 203
6.1. Summary of Experimental Results 203
6.2. Future Work 211
LIST OF REFERENCES 214
VITA 242

LIST OF TABLES

Table 2.1: Comparison of ODS-Steel Fabrication Methods (PBF-LB = powder bed fusion – laser beam, MA = mechanical alloying, HE = hot extrusion, SPS = spark plasma sintering, HIP = hot isostatic pressing, GARS = gas atomization reaction synthesis, CR = cold rolling, FC = friction consolidation, N.R. = not reported) [9, 29, 38, 42-45, 47, 62, 80, 86-89, 136, 138, 139]. 51

Table 3.1: Sample processing parameters (atm = atmosphere, wg = welding gas, C = continuous raster pattern, P = pulsed raster pattern, * = HT'd specimen).* indicates specimen underwent a post-build heat treatment of 1 hr at 600 °C 72

Table 3.2: Densities of common related oxides compared with liquid iron. 75

Table 3.3: Varied alloying expected specimen composition (ignoring changes in oxygen content). 83

Table 3.4: Varied alloying operating parameters. 85

Table 4.1: ICP-OES/IGF Compositional Analysis (MA = mechanical alloying, GARS = gas atomization reaction synthesis) 89

Table 4.2: Estimation of Y and O consumed by agglomerates and remaining in solution (assuming YAM oxide phase). 105

Table 4.3: STEM precipitate analysis of specimens with the largest amount of O left in solution and their heat-treated counterparts. 105

Table 4.4: Expected changes in microhardness and YS based on precipitate strengthening. Two model alloys are provided for comparison. Expected microhardness and YS values are calculated using the results of a hardening

model and the microhardness value reported for Fe-12Cr-6Al as provided by Wang et al. [154]. 125

Table 4.5: Rosenthal's equation simulation results of thermally unique build conditions (excluding pulsed rastering). 148

Table 5.1: ICP-OES/IGF Compositional analysis of as-built specimens for varied alloying experiment. 152

Table 5.2: DICTRA simulation input parameters for TiC and SiC dissolution. 169

Table 5.3: STEM precipitate analysis of unique alloyed specimens. 181

Table 5.4: Expected changes in UTS based on precipitate strengthening. 201

Table 5.5: Summarized relevant results on the influence of TiC additions to FeCrAl weld strength from Gussev, Field, and Yamamoto. C35M067TC is an approximated strength of an alloy with a TiC addition as in this experiment using a linear regression of the literature data [11]. 201

Table 6.1: Oxygen content required (wt%) required for various precipitate sizes, number densities, and phases relevant to ODS FeCrAl. Red cells are O concentrations near or above those achieved using PM techniques. 207

LIST OF FIGURES

Figure 1.1: Examination of varied Cr and Al compositions of FeCrAl alloys on corrosion performance under 1200°C steam [10]. 3

Figure 1.2: Overview of expected operating conditions for current and future reactor concepts. Very High Temperature Reactor (VHTR), Super Critical Water Reactor (SCWR), Gas Fast Reactor (GFR), Lead Fast Reactor (LFR), Sodium Fast Reactor (SFR), Molten Salt Reactor (MSR) [3]. 5

Figure 1.3: Schematic of the powder metallurgy process of making ODS alloy cladding [14]. 10

Figure 1.4: Unpredictable degradation rate of steam generator tubes produced by batch processing [21]. 12

Figure 2.1: Sink recombination and annihilation mechanisms: a) Self-interstitial atoms (SIAs, green dumbbell) recombining with a diffusing and trapped vacancy (red circles), b) SIAs and vacancies diffuse to a SIA loop and a dislocation acting as sinks resulting in loop growth and dislocation climb [13]. 19

Figure 2.2: Dislocation pileup at a grain boundary in 304 stainless steel [90]. 21

Figure 2.3: a) Coherent precipitate with minimal lattice strain, b) coherent precipitate with some lattice strain, c) semi-coherent precipitate with some lattice strain relieved by dislocation formation (denoted by D), d) incoherent precipitate [1]. 23

Figure 2.4: a) Small, semi-coherent $Y_4Al_2O_9$ precipitate found in a 16Cr-ODS steel. b) Larger, primarily incoherent $Y_4Al_2O_9$ precipitate [2]. 24

Figure 2.5: Cutting of a precipitate with a dislocation moving from left to right [3]. 26

Figure 2.6: Orowan looping mechanism with dislocation line moving from left to right [3]. 26

Figure 2.7: Strength comparison of ODS and non-ODS alloys up to 800°C [6]. 29

Figure 2.8: Creep rupture property comparison of ODS and non-ODS ferritic-martensitic steels [27]. 30

Figure 2.9: a) Presence of ODS precipitates in 14YWT and MA957 reduce the embrittlement experienced after irradiation [101]. b) Increases in sink strength and utilization of high sink strengths are responsible for the mitigation of hardening and embrittlement [27]. 33

Figure 2.10: Presence of ODS precipitates reduces the amount of void swelling caused by irradiation [27]. 35

Figure 2.11: Cartoons (top) and TEM micrographs (bottom) showing the progressive states of accumulating He within oxides: a) helium residing inside the oxide interstitials, b) small helium bubble attached to a small oxide, c) a large helium bubble spread over the surface of a small oxide, d) a large helium bubble trapped at the surface of a larger oxide [101]. 36

Figure 2.12: Schematic of the evolution of oxide particles dispersed in a steel alloy during irradiation [105] 38

Figure 2.13: Ellingham diagram for common oxides showing free energy of formation (driving force or attraction of metals to O) for Y_2O_3 is significantly lower than FeO at the melting temperature [43]. 38

Figure 2.14: Oxide size distribution dependency on Y:Ti ratio for ODS steel produced using powder metallurgy [112]. 40

Figure 2.15: Effect of extensive aging on microhardness of ODS MA597 [113]. 42

Figure 2.16: Effect of thermal aging at various temperatures on coarsening of precipitates in MA957 [115]. 43

Figure 2.17: Schematic demonstrating the GARS process of introducing oxygen to metal powder [43]. 46

Figure 2.18: Chromia chemical reservoir at prior particle boundaries acts as an oxygen source for Y-oxide formation during consolidation and subsequent heat treatments [43]. 48

Figure 2.19: a) Equilibrium concentration of H, N, and O in Fe using a) diatomic and b) monatomic pure gas environments (p_i = 1 atm/5x10^{-2} atm, 1 atm/ 10^{-6} atm, 10^{-9} atm/10^{-8} atm, respectively) as a function of temperature [141]. 55

Figure 2.20: Schematic of melt pool turbulence [146]. 57

Figure 2.21: Sessile drop experiment to measure liquid metal-solid oxide contact angle [149]. 61

Figure 3.1: Schematic of DED AM process using in situ oxidation: a) consolidation under air, b) under Ar with Ar-O2 blended gas stream. 71

Figure 3.2: Effect of Si additions on the contact angle (wettability) of Fe- 9wt%Cr on a Y2O3 substrate [61]. 76

Figure 3.3: Effects of Ti additions (a. 0 wt% Ti to 0.7 wt% Ti; b. 1.5 wt% Ti) and temperature on the contact angle (wettability) of 25wt%Cr white cast iron on a Al_2O_3 substrate [60]. 78

Figure 3.4: Effect of O content and temperature on the interfacial energy of liquid Fe on Al_2O_3. a) comparison of influence of O, S, Se, and Te content on contact angle. b) Changes in O content and temperature affect contact angle. Filled shapes are tested on Al_2O_3. Empty shapes are tested on ZrO_2 [160, 162]. 79

Figure 3.5: Gas incidence fraction heatmap used to determine the laser power and tool speed for the varied alloying experiments. 86

Figure 4.1: Optical mosaic micrographs of the as-built specimens (1 to 10; top to bottom) created in the preliminary work using a reactive atmosphere or a reactive welding gas. Z direction is up on each micrograph. 91

Figure 4.2: Comparison of the measured specimen as-built defect density. 96

Figure 4.3: EBSD inverse pole figures of Specimen 8 showing a) intergranular (two left arrows) and b) transgranular (two right arrows) cracking mechanisms. Z direction is into the page. 97

Figure 4.4: Scheil solidification simulation from ThermoCalc of the alloy used (M2O3C is Y2O3). 99

Figure 4.5: a. Optical micrograph of specimen 8, b. Backscatter electron image of an oxide inclusion in specimen 8 (indicated by the outline in a. and arrow in b.). Z direction is up in these specimens. 101

Figure 4.6: EELS spectra of the oxide inclusion from Specimen 8 with the a. Al K-, b. O K-, c. Y L-, and d. Cr L-edges shown in comparison to YAG and YAM reference spectra [172]. 102

Figure 4.7: EDS maps of a large Y-rich precipitate found in Specimen 6. 107

Figure 4.8: EDS maps of a large core- and-shell precipitate with oxides bound in a Y-rich shell. The linescan path is denoted by a green line. 108

Figure 4.9: EDS linescan of core-and-shell precipitate in **Figure 4.8**. 109

Figure 4.10: EDS maps of co-precipitation occurring in Specimen 12. 110

Figure 4.11: EDS maps of co-precipitation occurring in Specimen 13. 111

Figure 4.12: Temperature vs. O concentration phase diagram for our alloy. Region color = specimen before/after HT; Red = 6/11, blue = 7/12, green = 8/13. Bulk O concentrations and O left in solution are noted. TCFE9 was the database used for simulation. 112

Figure 4.13: EDS maps showing precipitation and Y segregation along a grain boundary. 114

Figure 4.14: EDS maps of a Y-oxide and Y-rich intermetallic phase in Specimen 11. 115

Figure 4.15: APT reconstructions of Needle 1 from Specimen 11 with a dispersoid. Isosurfaces outlined in purple with species of importance shown. 116

Figure 4.16: APT reconstructions of Needle 2 from Specimen 11 with a dispersoid. Isosurfaces outlined in purple with species of importance shown. 117

Figure 4.17: Proximity histograms of Specimen 11 Needle 1 (a) and Needle 2 (b). 119

Figure 4.18: Vickers hardness measurements of all specimens including as- received powder (0) and HT'd samples of specimen 6, 7, and 8 (11, 12, and 13, respectively) compared with hardness values of non-ODS model FeCrAl alloys from literature (shown by the dashed line) [154]. 123

Figure 4.19: Energy Density v. Part Density of all as-built specimens. 128

Figure 4.20: Power deposited for pulsed raster bead pass (Specimen 3; a) and continuous raster bead pass (Specimen 4; b). 130

Figure 4.21: Equilibrium O concentration in liquid steel as a function of liquid temperature. Partial pressure of O was $3.85x10^{-3}$ atm for dissolution of diatomic O and $7.66x10^{-3}$ atm for dissolution of monatomic O. 134

Figure 4.22: Thermal heatmaps for specimens 2, 5, 6, 7, 8, 10 with x-y plane on the left (a, c, e, g, i, k) and x-z plane on the right (b, d, f, h, j, l). The laser path of travel is to the right of each heatmap. Laser is traveling to the left of the page. 137

Figure 4.23: Diagram of contours being used for determining thermal gradient. Laser is traveling to the left of the page. 139

Figure 4.24: Comparison of laser power to average solidification velocity of listed specimens. 141

Figure 4.25: Comparison of average (blue) and maximum (red) solidification velocities to specimen O content. Note: the data point for Max. Solidification Velocity of Specimen 2 is shifted to the left 0.04 mm/s to prevent its overlap with Specimen 5. 142

Figure 4.26: a. Comparison of melt pool lifetime (blue), b. gas incidence time (red), and c. gas incidence fraction (green) to specimen O content. 145

Figure 5.1: Comparison of minor alloying element concentrations of TiC (a) and SiC (b) added specimens to as-received powder and expected concentrations. 154

Figure 5.2: Comparison of as-built specimen O concentration. Specimens labeled in red used FeCrAl powder after a 350 °C, 1 h pre-build heat treatment. 155

Figure 5.3: Phase diagram for as-received powder, B1, and B2 as predicted by Thermo-Calc. 157

Figure 5.4: Phase diagram for B3, B3F, and B4 as predicted by Thermo-Calc. 158

Figure 5.5: Phase diagram for B5 and B6 as predicted by Thermo-Calc. 159

Figure 5.6: Mosaics of optical micrographs of the as-built specimens (B1 to B6; top to bottom) created from varied alloying additions. Z direction is up. 160

Figure 5.7: Optical micrograph from B4 showing what types of defects are present. The lack of fusion defect is attached to an oxide agglomerate. Z direction is up. 163

Figure 5.8: Comparison of as-built specimen defect density across different alloying conditions. 164

Figure 5.9: DICTRA simulations to predict the potential for complete dissolution of a) TiC and b) Si @; T = 1500 °C, right: T = 2345 °C) powder particles. 166

Figure 5.10: Inverse pole figures of longitudinal and transverse cross- sections from the top 10 mm of each specimen. Insets, when provided, show increased magnification of finer grained areas outlined in black on the main

micrograph. White arrows mark examples of solidification cracking. 170

Figure 5.11: Solidification cracking criterion analysis: a) Scheil simulation approaching $f_s = 1$, b) derivative of Scheil simulation as $f_s^{0.5}$ approaches 1. 172

Figure 5.12: Solidification cracking criterion analysis showing the influence of a) increased oxygen content and b) increased alloying. 173

Figure 5.13: Comparison of specimen agglomeration with respect to changing alloying, total area (blue bars, left) and number of agglomerates (black squares, right). 175

Figure 5.14: Comparison of average agglomerate area (a) and average agglomerate equivalent diameter (b). Error bars represent the Standard Error of the mean of each dataset. 176

Figure 5.15: Agglomerate area (left) and equivalent diameter (right) distributions for each specimen. 178

Figure 5.16: STEM EDS maps of Y-rich intermetallic precipitation in as-built B1. White arrows are pointing to other precipitates present in the matrix. 183

Figure 5.17: STEM EDS maps of co-precipitation of Y-oxides and Y-rich intermetallic precipitation in B2HT. White arrows are pointing to other similar precipitates present in the matrix. 184

Figure 5.18: STEM EDS maps of co-precipitation of Y-oxides and TiC in B4HT. White arrows are pointing to other similar precipitates present in the matrix. 185

Figure 5.19: STEM EDS maps of co-precipitation of Y-oxides and Cr- carboxides in B6. White arrows are pointing to other similar precipitates present in the matrix. 186

Figure 5.20: STEM EDS maps of TiC enriched in Cr from B4. 188

Figure 5.21: STEM EDS maps of a grain boundary from B4 showing Y, Ti, and C enrichment. 189

Figure 5.22: APT reconstruction of Needle 43794 from Specimen B4 with parts of a grain boundary and multiple precipitates captured. Proximity histograms of the large TiC precipitate marked with a black arrow are included. 190

Figure 5.23: APT reconstruction of Needle 43792 from Specimen B4HT with parts of a grain boundary and multiple precipitates captured. Proximity histograms of the large TiC precipitate marked with a black arrow are included. 191

Figure 5.24: APT reconstruction of Needle 43814 from Specimen B4HT. Proximity histograms of a large Y-rich intermetallic phase (top) and a TiC precipitate without Cr infiltration (bottom) are included with the referenced precipitates marked by a black arrow. 192

Figure 5.25: APT reconstruction of Needle 43772 from Specimen B6. Proximity histograms of a CrC precipitate enriched in Ti (top) and a YC precipitate enriched in Ti (bottom) are included with the referenced precipitates marked by a black arrow. 193

Figure 5.26: 1-dimensional concentration profile through an edge of a grain boundary (marked with black arrow; Cr-rich angled region) captured in B4. 195

Figure 5.27: 1-dimensional concentration profile through an edge of a grain boundary (marked with black arrow; Y-rich region across needle tip) captured in B4HT. 196

Figure 5.28: 1-dimensional concentration profile through a grain boundary (marked with black arrow; bounded Y-rich region) captured in B6. 197

Figure 5.29: Vickers microhardness measurements of all specimens. 199

Figure 6.1: Comparison of this work's precipitate characteristics to literature values of other methods for producing ODS alloys. DED = directed energy deposition, PBF = powder bed fusion, GARS = experiments using gas atomization reactions synthesis powder and powder metallurgy techniques, and MA = experiments using mechanical alloyed powder and powder metallurgy techniques. This work's experiments are shown by the starred results. 205

Figure 6.2: Scheil simulation of Specimen B4. TCFE9 was used for this simulation. .. 209

CHAPTER ONE

INTRODUCTION AND GENERAL INFORMATION

1.1. IMPORTANCE OF ADVANCED MATERIALS FOR CURRENT NUCLEAR REACTORS

The events at Fukushima Daiichi drew significant attention to possible shortcomings of current structural materials used in conventional light water reactors (LWRs). After a tsunami knocked out power and flooded backup generators for the reactor cooling pumps, loss of coolant circulation and nuclear decay heat led to an increasing reactor core temperature. Rising temperatures caused reactor coolant to boil off and eventual failure of the Zr-based cladding. Exposure of Zr-based cladding interior and exterior to high temperature steam led to rapid oxidation, heat generation, and hydrogen gas formation in the reactor core; an unfortunate combination causing an explosion [4].

Failure of Zr-based fuel cladding during this beyond design basis (BDB) event renewed research interest in accident tolerant fuel (ATF) cladding materials that would increase available response time and reduce the probability of catastrophic outcomes. Researchers turned to materials capable of forming stable chromia (Cr-coated Zr-based cladding), alumina (FeCrA cladding), and silica (SiC/SiC cladding) passivation layers as potential alternatives to Zr-based alloys [5]. Due to use in other areas of a reactor core, Fe-based alloy performance in LWRs has been well studied [6, 7]. Unfortunately, the usual Fe-Cr alloy system is not sufficient for cladding operating conditions. The oxide film created by Cr begins to degrade at temperatures above 700°C. Developing alloys that combine solute Cr and Al (FeCrAl alloys) reinforces that oxide film to withstand that high

temperature oxidizing environment as shown in **Figure 1.1.** where FeCrAl alloys with varied Cr and Al content are compared for their corrosion performance in 1200°C steam [8-15]. Additionally, the added corrosion resistance from added Al solute provides FeCrAl alloys with acceptable chemical compatibility with super critical water, Pb-Bi eutectic, and Pb-Li working fluids commonly used in advanced nuclear fission and fusion designs [12, 16-18].

1.2. Importance of Advanced Materials for Advanced Nuclear Fission and Fusion Reactors

Concerns over climate change and the environmental effects of extensive fossil fuel consumption have driven the pursuit and development of alternative, emissions-free sources of electricity [19, 20]. Great advances have been made in the fields of solar and wind power technologies, but non-intermittent base load energy production is critical to ensure the stability of the power grid. Nuclear power provides a reliable, continuous, emissions-free source of power to meet those needs with a 92.7% annual average capacity factor (in contrast to coal: 49.1%, geothermal: 69.8%, hydroelectric: 36.0%, solar-photovoltaic: 24.4%, solar-thermal: 20.5%, or wind: 34.4%) [21]. However, the current nuclear power fleet is surviving on technology developed in the late 1960s with a design lifetime of 40 years [22]. Many existing plants are seeking a second operating license extension to 80 years from their already extended 60 year licenses [23]. Meanwhile, few Generation III or Generation IV reactor designs have been built regardless of the advances in reactor efficiency, safety, and reliability that they may provide [22].

A significant hurdle to the implementation of Generation IV reactor designs is a lack of structural materials capable of withstanding the extreme environments inside

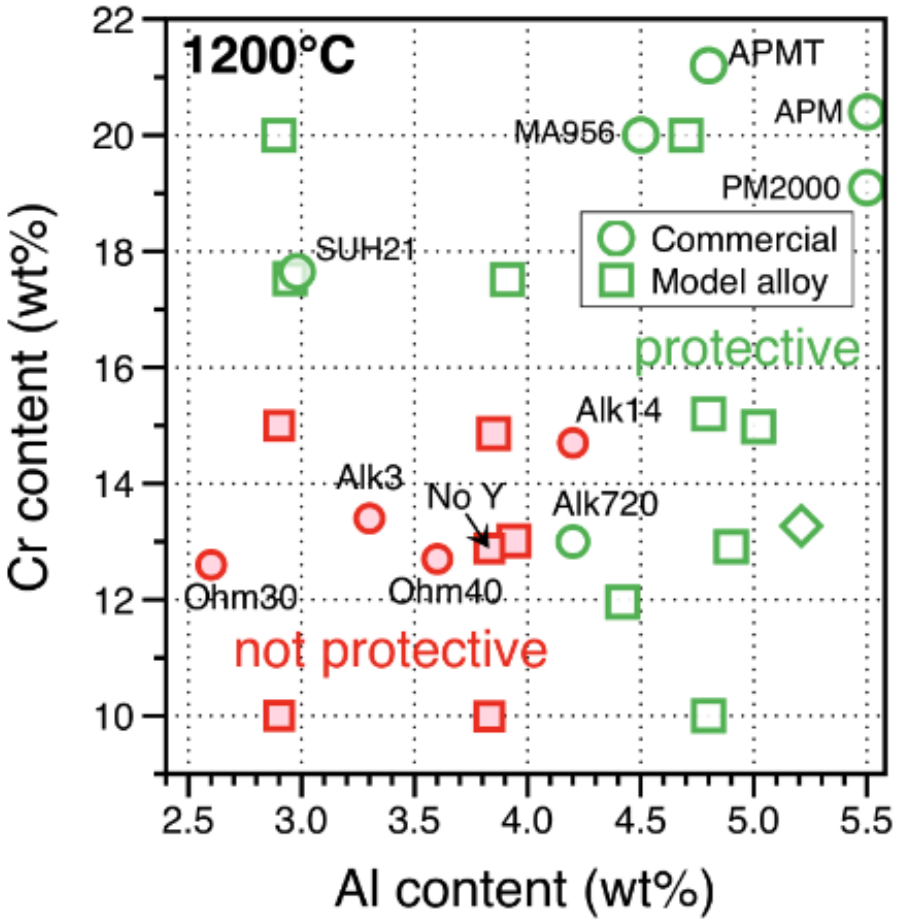

Figure 1.1: Examination of varied Cr and Al compositions of FeCrAl alloys on corrosion performance under 1200°C steam [13].

[6, 7, 20, 24]. A similar materials hurdle exists for fusion reactors [6, 19, 20, 24-26]. As noted by Bloom et al. [20], the conditions present in advanced fission and fusion nuclear reactor systems have collided and share many of the same issues. Both system concepts require ultra-high-performance materials capable of surviving in environments with higher operating temperatures, higher energy neutron economies, higher lifetime radiation damage levels, increased corrosion complexity, and increased helium production while also needing to maintain high strength and thermal creep resistance [7, 16, 20, 25-30]. Compared to current LWRs, increases in expected operating temperatures from 300°C to 600°C+, maximum irradiation doses from 1 dpa (displacements per atom; a measure of irradiation damage representing the average number of displacements of each atom in a material's crystal lattice) to 30-150 dpa, and transmutation helium production from 0.1 appm to 3 appm and as high as 1550 appm for fusion systems [20]. This disparity in expected operating conditions for current LWRs and advanced fission and fusion reactor designs is further demonstrated in the plot borrowed from Zinkle and Busby in 2009 in **Figure 1.2**. To engineer materials to survive in such extreme environments, Zinkle and Snead in 2014 proposed 3 methods to create materials with high irradiation resistance: 1. engineer high sink strength materials, 2. operate in temperature regimes that prevents vacancy mobility, and 3. choose radiation resistant matrix phases [26].

1.3. Radiation Damage Fundamentals

As a material is irradiated, neutrons and other energetic atoms can strike and scatter off atoms sitting on the lattice sites that make up the crystalline structure of a material. These displaced atoms can become defects in a material called Frenkel pairs.

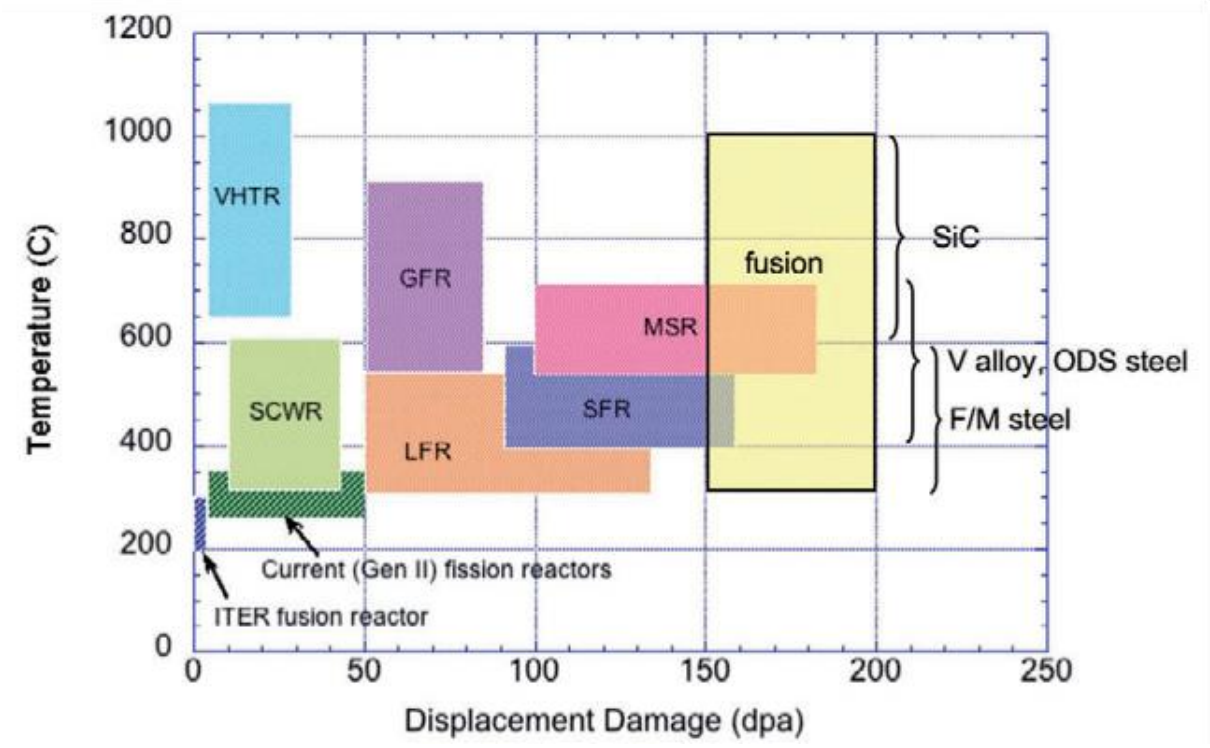

Figure 1.2: Overview of expected operating conditions for current and future reactor concepts. Very High Temperature Reactor (VHTR), Super Critical Water Reactor (SCWR), Gas Fast Reactor (GFR), Lead Fast Reactor (LFR), Sodium Fast Reactor (SFR), Molten Salt Reactor (MSR) [6]

Frenkel pairs consist of interstitials (atoms sitting outside lattice sites) and vacancies (empty lattice sites). These interstitials and vacancies can either remain as individual entities, cluster into larger groups of like defects, recombine with one another, or diffuse to an interface (dislocations, incoherent precipitates, grain boundaries, voids, and He bubbles) within the material often referred to as a sink. At these sinks, these Frenkel pair defects can then recombine reducing the effective irradiation damage to the material [16].

The mobility of Frenkel pairs and the various defects they can coalesce into is a function of the operating temperature (T) and the melting point (T_m) of the material-also known as the homologous temperature (T/T_m). Starting at low operating temperatures, > 0.05 T_m (Stage I), interstitial atoms gain long-range mobility and can start to form various kinds of defect clusters. As operating temperatures rise above 0.2 T_m (Stage III), individual vacancies begin to migrate and cavities (gas-filled bubbles or underpressurized voids) can begin to form. The movement of these types of defects can encourage the formation of undesirable precipitate phases or deleterious solute segregation to grain boundaries. Above 0.3 T_m (Stage V) the thermal dissolution of small vacancy clusters becomes possible and void swelling of metal alloys becomes prominent [26].

The presence, movement, and clustering of these defects can often have large deleterious effects on the material properties and structural performance of a given part under irradiation. The five main effects of radiation damage in structural materials are [6, 19, 26, 31]:

1. Radiation hardening and embrittlement: occurs < 0.4 T_m, > 0.1 dpa; accumulation of defects impedes the movement of dislocations while stress is applied to a

material often leading to an increase in strength, a decrease in ductility, and a transition from ductile to brittle fracture mechanisms at a given temperature

2. Radiation-induced precipitation and phase formation: occurs 0.3 – 0.6 T_m, > 10 dpa; the movement of vacancies in a crystal lattice necessitates the movement of atoms and potentially more of one type of atom than others which can lead to a heterogeneous arrangement that favors the formation of deleterious phases or unwanted precipitates
3. Irradiation creep: occurs < 0.45 T_m, > 10 dpa; preferential formation and movement of defects due to stress resulting in a dimensional change of a material without a change in volume
4. Cavity induced volumetric swelling: occurs 0.3 – 0.6 T_m, > 10 dpa; agglomeration of vacancies beyond the thermal equilibrium concentration leads to dimensional change including a change in volume
5. High temperature He embrittlement: occurs > 0.5 T_m, > 10 – 100 appm He; neutron induced (n,α) transmutation reactions produce He that can migrate to grain boundaries and produce large cavities

1.4. Microstructural Engineering for Corrosion and Irradiation Resistance

FeCrAl alloys are a promising option for ATF cladding due to their comparable corrosion resistance to zirconium alloys in LWR conditions in addition to their excellent chemical compatibility with high temperature steam [32-34]. Unfortunately, the thermal neutron absorption cross section of FeCrAl alloys is noticeably higher than Zr alloys. To offset this difference, either an increase in fuel enrichment in the core or a decrease in cladding thickness must occur [4, 35]. This can be achieved by engineering the alloy

microstructure to maximize strength, minimize radiation damage, and allow for a reduction in thickness. By adding significant amounts of nanoscale oxide dispersoids all three microstructural engineering goals can be achieved and the current low enrichment regulatory limits (< 5% ^{235}U) for commercial LWR fuels can be maintained without affecting the reactor neutronics [9, 15, 16, 26, 36-38].

Adding a significant number of nanoscale oxide precipitates inhibits the motion of dislocations under stress improving the overall alloy strength. Further, adding a significant number of nanoscale oxide precipitate into the alloy dramatically increases the number of interfaces therein. As described in Section 1.3, the addition of many interfaces or sinks to allow for defect recombination/annihilation in a material is one of the three key methods of creating materials to survive in extreme environments and reduce the deleterious effects of radiation damage. By encouraging defect recombination, the effects of radiation hardening/embrittlement, irradiation creep, cavity induced volumetric swelling, and high temperature He embrittlement can potentially be dramatically reduced [16, 26]. The literature suggests that precipitate number densities on the order of 10^{23} m^{-3} are needed to achieve minimal negative effects from irradiation damage [39]. The addition of these nanoscale oxide dispersoids creates what is commonly referred to as an oxide dispersion strengthened (ODS) alloy, and it is this combination of the strong corrosion resistance of FeCrAl alloys and nanoscale ODS dispersions that provides so much promise for uses in both current nuclear fission reactors and advanced nuclear fission and fusion reactor designs.

1.5. Conventional Methods for ODS Manufacturing

Unfortunately, there is currently no perfect process for manufacturing ODS alloys. Both powder metallurgy and casting processes have thus far shown positive and negative attributes.

1.5.1. Powder Metallurgy

Powder metallurgy is generally considered the standard for ODS alloy production [40]. An example method for creating ODS alloy cladding materials such as those used in nuclear reactors is shown in **Figure 1.3**. The powder metallurgy process begins with mechanically alloying (MA) base alloy and yttria powders for upwards of 40+ hours [17, 38]. MA smashes blended powder particles together eventually breaking them down and leading to Y and O dissolution into a base alloy. Milled powders are then canned and degassed before consolidation using hot isostatic pressing (HIPing) or hot extrustion (HE) where fine oxide precipitates form [41]. This process can achieve number densities between 10^{23} m^{-3} and 10^{24} m^{-3} [9, 29, 38, 42-45]. As an alternative to mechanical alloying, Rieken developed the gas atomization reaction synthesis (GARS) process in 2011. This process uses an impinging reactive gas on the molten metal droplets as they are gas atomized creating a chromia shell on the surface. These powders are then consolidated like the mechanically alloyed powders where the chromia shell breaks down and the more stable yttria-based oxide phases form at number densities reaching 10^{22} m^{-3} [46-49]. After consolidation the ingot often undergoes extensive thermomechanical treatments to refine the microstructure, precipitate out the oxides, and shape the part. The main benefit of powder metallurgy techniques are the relatively small particle sizes (~ 1 to 5 nm) and high number densities of precipitates (10^{22} to 10^{24} m^{-3}) **[9, 29, 38, 42-45]**. This process

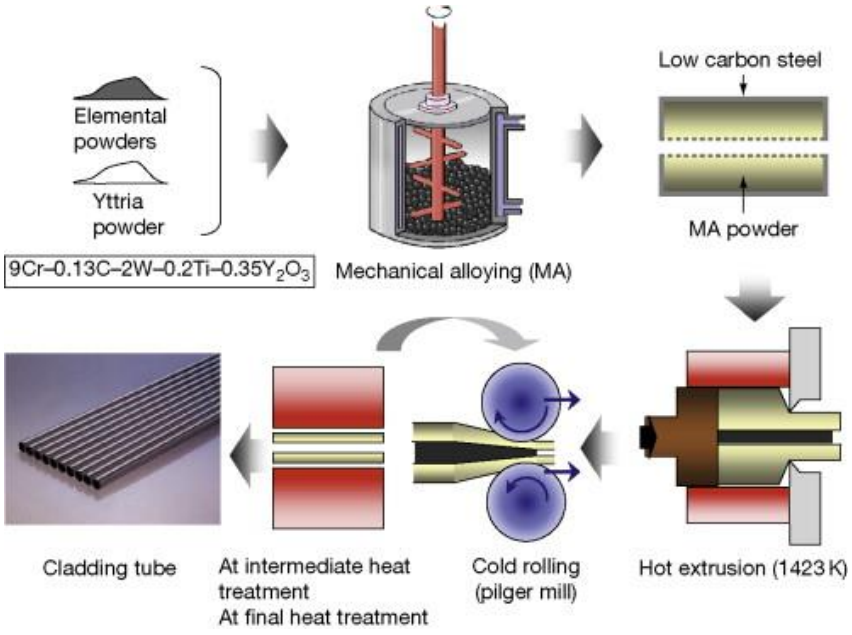

Figure 1.3: Schematic of the powder metallurgy process of making ODS alloy cladding [17].

results in long lead times, material contamination, batch-to-batch variation, and anisotropic material properties **[9, 16, 17, 29, 38, 50, 51]**. As an example of how some of these issues can negatively affect the nuclear industry, Was in 2007 noted how batch processing of steam generator tubes led to unpredictable degradation rates with no obvious cause (shown in **Figure 1.4**) **[24]**.

1.5.2. Casting

More traditional casting processes have been examined for producing ODS alloys with aims of decreasing process complexity. Applications of casting processes for ODS alloys have ranged from simply adding Y_2O_3 powder directly to the liquid alloy to oxygen dissolution from the atmosphere to oxygen sequestration of what already exists in the raw materials to internal oxidation **[52-58]**. For internal oxidation, an oxygen carrier material such as Fe_2O_3 or TiO_2 is used to introduce oxygen into the melt **[52, 53]**. These carrier powders dissolve in the melt and oxides are precipitated out during cooling or subsequent thermomechanical treatments. Experiments have even been done with electromagnetic mixing during the casting process [59]. The main drawbacks to casting for ODS alloy production are the general formation of larger than desired (> 5 – 10 nm) oxide inclusions and, as a result, lower number densities than those from powder metallurgy techniques (10^{16} to 10^{20} m^{-3} vs. 10^{23} to 10^{24} m^{-3}) [9, 29, 38, 42-45, 52-58]. It is widely believed a combination of the poor metallic-ceramic wettability between the Y-O phase and the Fe matrix and the relatively lower oxide density leads to increased particle size, lower number density, and overall poorer nanoscale distributions of dispersoids [60, 61].

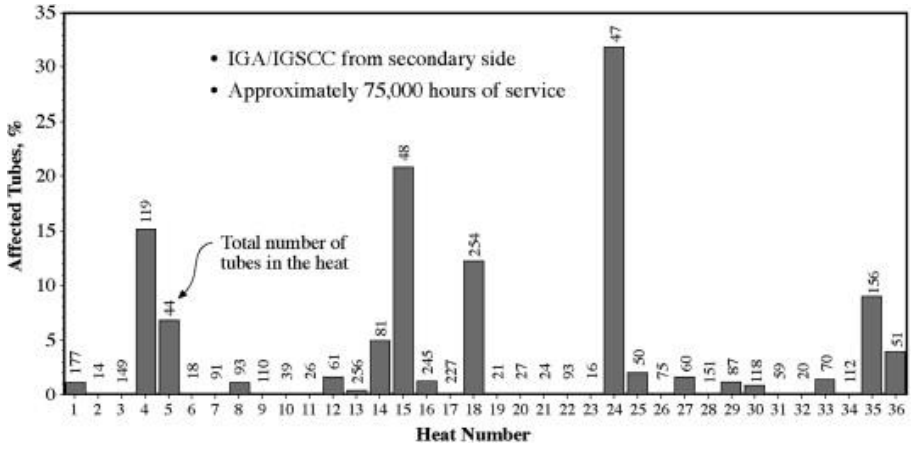

Figure 1.4: Unpredictable degradation rate of steam generator tubes produced by batch processing [24].

1.5.3. Welding/Joining

In addition to any difficulties producing ODS alloy parts, welding or joining them together is also a non-trivial task. Significant work has been done to examine the potential of typical fusion-based and solid-state based welding techniques to join ODS parts. In general, joining processes for ODS alloys usually result in degraded properties in and around the joint **[30, 62]**.

Conventional arc-based welding and laser beam welding techniques often result in deleterious agglomeration of oxides disturbing the important nanoscale precipitate dispersion **[63, 64]**. Some recent work with laser beam welding shows promise to minimize these issues by better modulating the laser and encouraging weldment grain refinement, but further work still needs to be done **[63, 65, 66]**. Friction welding (FW) and friction stir welding (FSW) offer a solid-state alternative joining process. They utilize large forces and rotation parts to heat up the joint between two pieces and encourage physical mixing between them. Temperatures are intended to be kept below the melting point to avoid oxide agglomeration. Unfortunately, precipitate agglomeration (10 nm to 40+ nm), undesirable grain growth from dynamic recrystallization (890 nm to 12.5 um), and limited part geometries often plague FW and FSW joined parts **[67-69]**.

Much work has also been done examining the potential for resistance welding techniques as solid-state joining alternatives. Utilizing large pressures to hold parts together and resistance heating via large continuous currents or instantaneous capacitor discharges, these methods soften the contact area of the joint such that the force provided can encourage a metallurgical bond. These methods have been shown to have little effect on the valuable nanoscale oxide dispersions with appropriate operating parameters.

However, hairline crack formation, partial melting, incomplete bonding, grain coarsening from dynamic recrystallization, and minor part deformation have occurred during recent joining experiments **[64, 70-72]**.

Similar solid-state joining work has been done using hot compression and diffusion bonding. This technique has shown capable to bond ODS alloys to themselves as well as other non-ODS steels. The nanoscale dispersions were generally unaffected although slight decreases in ultimate tensile strength (UTS) up to 20% and total elongation (TE) up to 4% compared to the base materials did occur. When joining dissimilar materials, it was paramount that special consideration be given to any potential fast diffusing species that could cause phase changes as they diffuse to and/or across the joint. Using a sacrificial interlayer between the ODS and non-ODS alloy was able to stifle this diffusion and protect the integrity of the joint **[73, 74]**. Another drawback of this method is the extensive amount of time required as a single weld would take over three hours not including preparation work and post-weld heat treatments **[72]**.

1.6. Additive Manufacturing

As demonstrated above, the manufacturing and joining processes for ODS alloys are non-trivial. Each has their merits and detractions. The advent of additive manufacturing (AM) technologies provides a few additional alternative manufacturing methods with potential benefits of increased geometric complexity, localized microstructure control, and part throughput compared to conventional manufacturing processes [75-77]. The high solidification rates of AM processes (DED ~ $7x10^{-3}$ m/s, PBF-LB ~ 0.5 m/s) could potentially prevent the agglomeration and low number densities plaguing casting ($5.5x10^{-5}$ m/s) and fusion joining experiments ($2x10^{-4}$ m/s) [75, 77-79].

Several studies have examined the potential of using mechanically alloyed or mixed matrix/oxide powders primarily with powder bed fusion – laser beam (PBF-LB) AM system with varied levels of success. Researchers achieved nanoscale precipitation, but parts were plagued with crack/porosity defects (as low as 97% density), low dispersoid number densities (10^{21} m^{-3}), and slag or large oxide formation (> 50 nm) [62, 80-82]. Additionally, due to the use of mechanically alloyed powder, many of these experiments would still be subject to long lead times, milling contamination, and batch-to-batch variation.

Alternatively, an oxygen-rich environment could be used during the AM process to avoid issues associated with mechanical alloying. The high solidification velocity during AM would allow for O to be absorbed *in situ* via two mechanisms: 1. O reacts with deoxidizers (Cr, Al, Y, etc.) in the molten alloy to form oxides in the liquid melt pool that are captured by the solid-liquid interface as dispersoids or inclusions, or 2. Diatomic or monatomic O dissolves into a liquid melt pool that solidifies more quickly than the O can diffuse away from the solid-liquid interface (i.e. solute trapping) forming an oxygen rich solid solution. These increased solidification rates during AM processes could potentially lead to enhanced solute trapping and ultimately supersaturated solid solutions [75, 77, 83, 84]. Post-build heat treatments (HTs) or the subsequent thermal cycling as a part is built layer-by-layer would then encourage Y-O precipitation.

Preliminary work has been done examining the potential to use *in situ* oxidation with AM consolidation under an O-rich reactive gas atmosphere. Thus far experiments with 316L and other austenitic steel compositions using Si, Ti, or Y as their primary deoxidizers have had varied levels of success (PBF-LB with reactive gas: precipitate

diameter 50 to 100 nm and number densities approaching 10^{21} m^{-3}; DED with reactive gas: precipitate diameter 75 to 165 nm with number densities approaching 10^{18} m^{-3}) [85-89]. The main struggle is reducing dispersoid size and maximizing dispersion number densities. Major inconsistencies also mar the comparison of mechanical properties between *in situ* oxidation AM ODS steels, conventionally manufactured ODS steels, and non-ODS AM steel analogues. Authors reported improvements in strength and ductility, increased ductility with decreased strength, or no appreciable difference in mechanical properties. More work needs to be done to thoroughly evaluate the effects of AM, in particular AM with *in situ* oxidation, on the mechanical properties of ODS steels and the stability of these dispersoids under thermal aging or irradiation.

This work seeks to better understand the influence of laser-based directed energy deposition (L-DED) AM using *in situ* oxidation on the potential to produce ODS FeCrAl alloys with nanoscale dispersions. The main objectives are to:

- Examine how changes in the different operating parameters affect oxygen dissolution and retention
- Develop a basic understanding of the mechanisms driving oxygen dissolution and retention during L-DED AM
- Improve achievable dispersoid number densities to approach powder metallurgy methods
- Examine how the oxide-metal interfacial energy relationship contributes to agglomeration and inclusion formation

This understanding will be used to demonstrate the potential for AM processes as viable alternatives to conventional powder metallurgy techniques for producing ODS alloys designed for service in nuclear environments.

CHAPTER TWO
LITERATURE REVIEW

2.1. Sinks and the Benefits of High Sink Strength

As alluded to in Chapter 1, use of large numbers of sinks (dislocations, incoherent precipitates, grain boundaries, voids, and He bubbles) creating a material with a high sink strength can be quite beneficial at minimizing irradiation effects due to the inherent attraction of Frenkel pair defects to sink interfaces as shown in **Figure 2.1** [16, 90]. In addition to reducing the effects of irradiation, large numbers of sinks also tend to improve overall material strength. Unfortunately, not all sinks are created equal. While potentially acting as recombination centers for Frenkel pair defects, voids and bubbles can also lead to undesirable amounts of void swelling in a material. This leaves grain boundaries, dislocations, and precipitates as the preferred candidates for producing high sink strength materials.

2.1.1. Influence of Sinks on Mechanical Properties

Large numbers of grain boundaries has a significant influence on a material's strength. Assuming constant material volume, increased numbers of grain boundaries result in decreased grain size and an increase in overall material strength. This relationship is described using a mechanism called Hall-Petch strengthening and modeled by the relationship in Equation 2.1.

$$\sigma_o = \sigma_i + kD^{-\frac{1}{2}} \tag{2.1}$$

where σ_o is the yield strength, σ_i is a defect free material's resistance to dislocation movement, k represents the relative hardening from grain boundaries, and D is the average diameter of the grains.

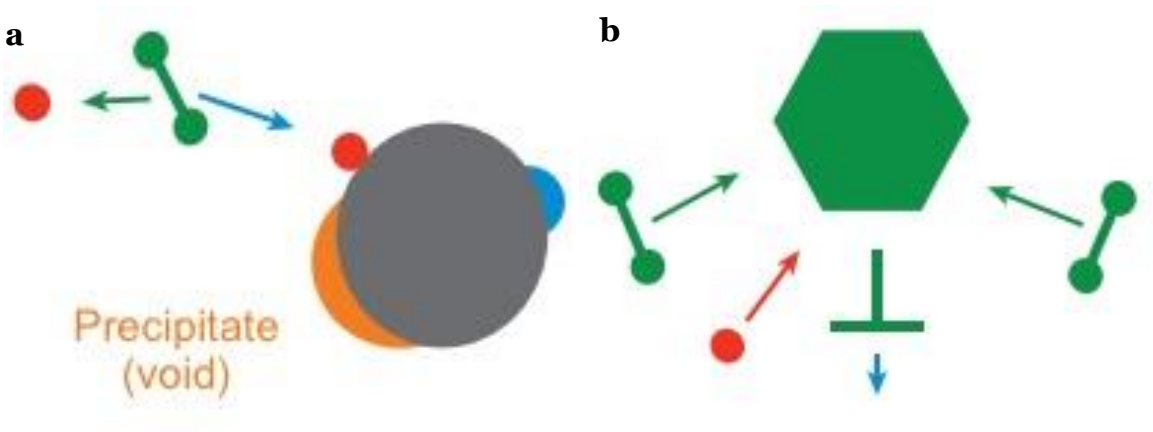

Figure 2.1: Sink recombination and annihilation mechanisms: a) Self-interstitial atoms (SIAs, green dumbbell) recombining with a diffusing and trapped vacancy (red circles), b) SIAs and vacancies diffuse to a SIA loop and a dislocation acting as sinks resulting in loop growth and dislocation climb [16].

The relative increase in strength provided by grain boundaries can be determined by

$$k = \frac{G\sqrt{b}}{5M} \tag{2.2}$$

where G is the shear modulus (100 GPa), b is the magnitude of the Burgers vector (0.25 nm), and M is a measure of misorientation in a crystal (assumed to be 3 for BCC Fe). M is also known as the Taylor factor and equal to the inverse of the Schmid factor [3, 91]. The inverse square root dependence of Equation 2.1 on average grain size (D) demonstrates how quickly decreasing grain size can increase a material's strength while also providing locations for Frenkel defect recombination. Physical a grain boundary acts as an inhibitor to dislocation movement in a material as stress is applied. This causes dislocations to begin to pileup along grain boundaries until enough stress builds up to overcome the strength of a grain boundary and propagate through it. An example of dislocation pileup is shown in **Figure 2.2**.

Large numbers of dislocations can also significantly increase the strength of a material while acting as irradiation defect sinks. Using a similar relationship to the Hall-Petch equation above, Equation 2.3 represents the relative increase in strength provided by large number of dislocations.

$$\sigma_0 = \sigma_i + \alpha G b \rho^{\frac{1}{2}} \tag{2.3}$$

where α is the hardening efficiency of an obstacle and ρ is the dislocation density measured in the number of dislocations per unit area [3]. The strength that dislocations provide stems from their physical interaction with one another and other objects in a material. Dislocations induce two different types of strain, tensile and compressive. Like magnetic poles, similar types of strain repel one another which inhibits movement of one dislocation past another and increases material strength [3].

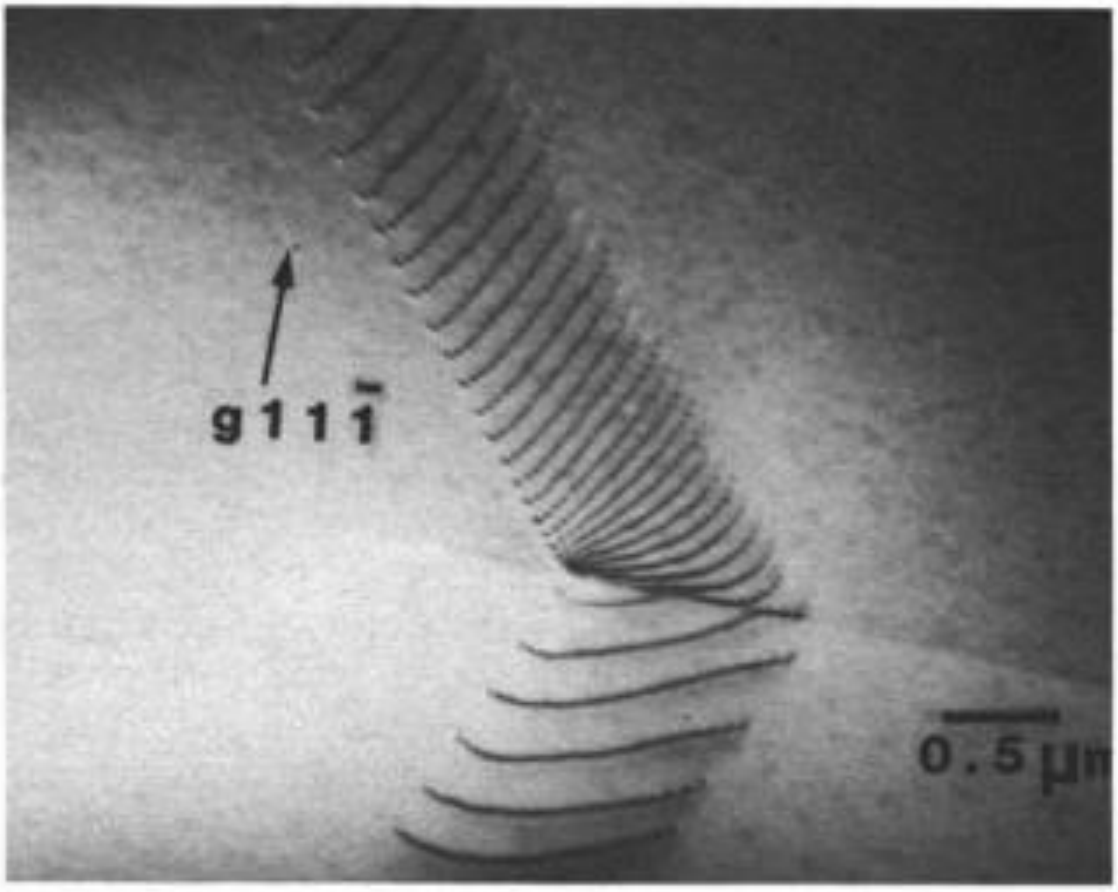

Figure 2.2: Dislocation pileup at a grain boundary in 304 stainless steel [92].

Precipitates can also act as sources of strengthening while doubling as irradiation defect sinks. Precipitates, due to crystal lattice mismatch across a precipitate-matrix interface, induce surrounding strain fields. How a precipitate provides strength to a material is dependent on how moving dislocations interact with it and its strain field, which is often described by a precipitate's coherency with a bulk matrix. Precipitates can either be coherent, semi-coherent, or incoherent. A precipitate is fully coherent when the mismatch between the different crystal structures of a precipitate and bulk matrix are minimal. As a precipitate increases in size, so does its mismatch with the bulk matrix resulting in an increased strain field. As the lattice strain becomes sufficiently high, dislocations begin to form along a precipitate surface to accommodate increased mismatch. This represents a transition of a precipitate from coherent to semi-coherent. This persists as a precipitate continues to grow until complete mismatch exists between a precipitate and a bulk matrix. A precipitate is now considered to be incoherent [1, 3, 91]. This is demonstrated in **Figure 2.3**. Further, as precipitate size increases, its shape tends to change. Small, coherent precipitates are primarily faceted and square or rectangular in shape [2, 93, 94]. As they increase in size, precipitates become more spherical in shape as shown in **Figure 2.4**.

The mechanism by which dislocations interact with precipitates-dislocation shearing or Orowan looping-is determined by which mechanism requires the least amount of energy to occur. For small, coherent precipitates dislocation shearing is generally favored. As a dislocation approaches these small, coherent precipitates, it begins to interact with a precipitate's strain field. As stress builds, a moving dislocation

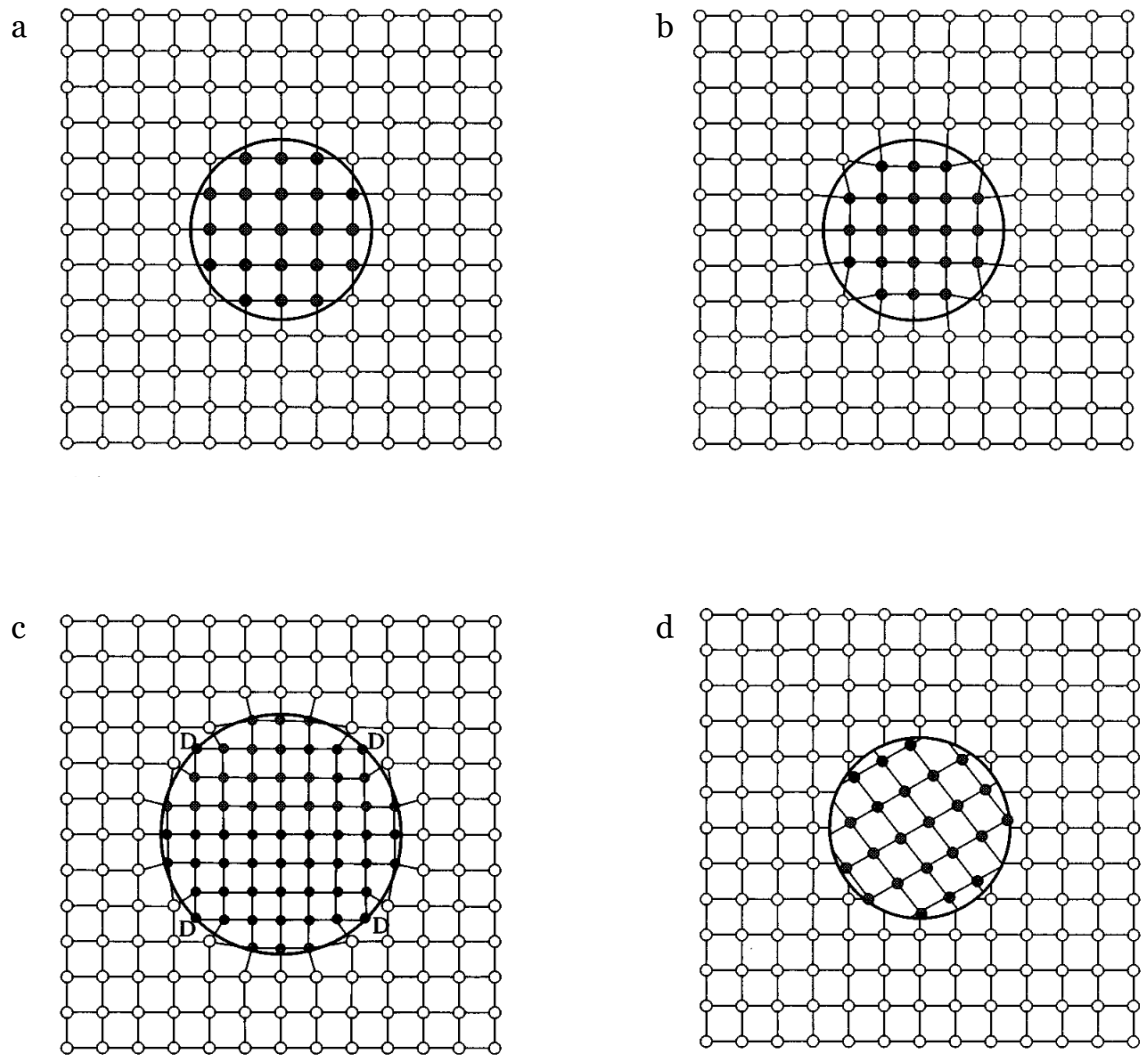

Figure 2.3: a) Coherent precipitate with minimal lattice strain, b) coherent precipitate with some lattice strain, c) semi-coherent precipitate with some lattice strain relieved by dislocation formation (denoted by D), d) incoherent precipitate [1].

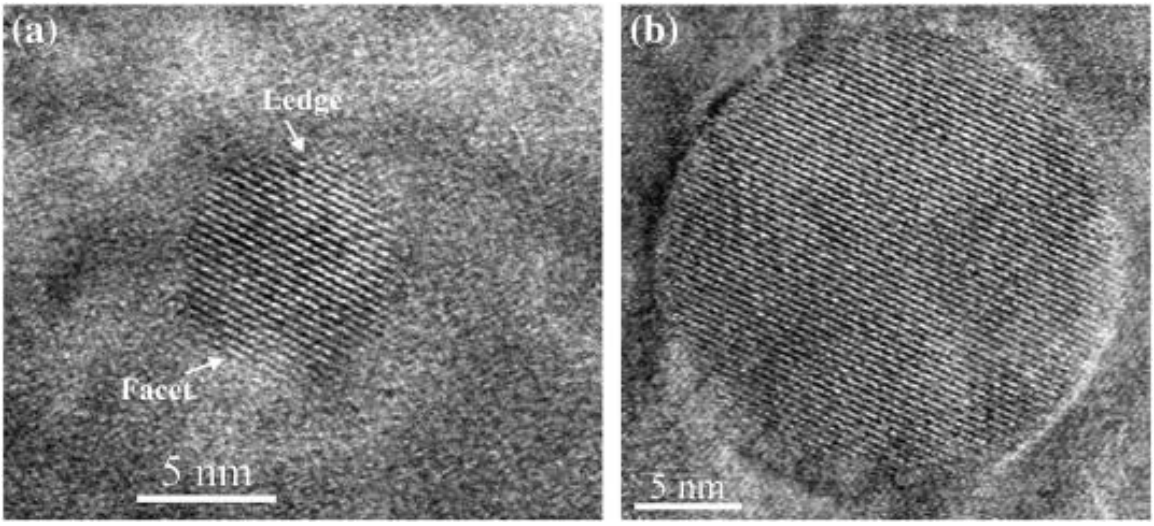

Figure 2.4: a) Small, semi-coherent $Y_4Al_2O_9$ precipitate found in a 16Cr-ODS steel. b) Larger, primarily incoherent $Y_4Al_2O_9$ precipitate [2].

will begin to overcome a precipitate's strain field and attach to a precipitate surface. This attachment is temporary until sufficient stress is applied by a dislocation to begin deforming or shearing a precipitate as shown in **Figure 2.5**. A coherent precipitate's resistance to shear is determined by the differences in physical properties of the precipitate compared to the bulk alloy. Mismatches in lattice parameter, stacking-fault energies, atomic ordering, moduli, and surface energies all determine the relative resistance of a coherent precipitate to shear.

As precipitates increase in size and become incoherent, the Orowan looping mechanism becomes more common. As a dislocation line approaches an incoherent precipitate, instead of adhering to its surface, it begins to bow around the precipitate as the stress fields of the dislocation line and incoherent precipitate begin to interact (shown in **Figure 2.6)**. As stress builds, this trapped dislocation line continues to bend around a precipitate until it reaches some critical curvature value. As this happens, parts of a dislocation line meet on the other side of a precipitate. These parts have opposing strain fields that annihilate and form a dislocation loop around a precipitate. As subsequent dislocation lines approach these precipitates, they interact with an enlarged strain field caused by the new dislocation loop. This leads to continuously increased amounts of strain hardening from this additional dislocation-dislocation interaction [91]. The strength added to a matrix by this inhibition of dislocation movement by incoherent precipitates is described by the Orowan-Ashby equation.

$$\Delta\sigma_y = \frac{0.13Gb}{\lambda}\ln\left(\frac{r}{b}\right) \tag{2.4}$$

where λ is equal to the precipitate spacing and r is the radius of the precipitate [3].

An alternative model proposed by Seeger in 1958 for the increase in yield strength

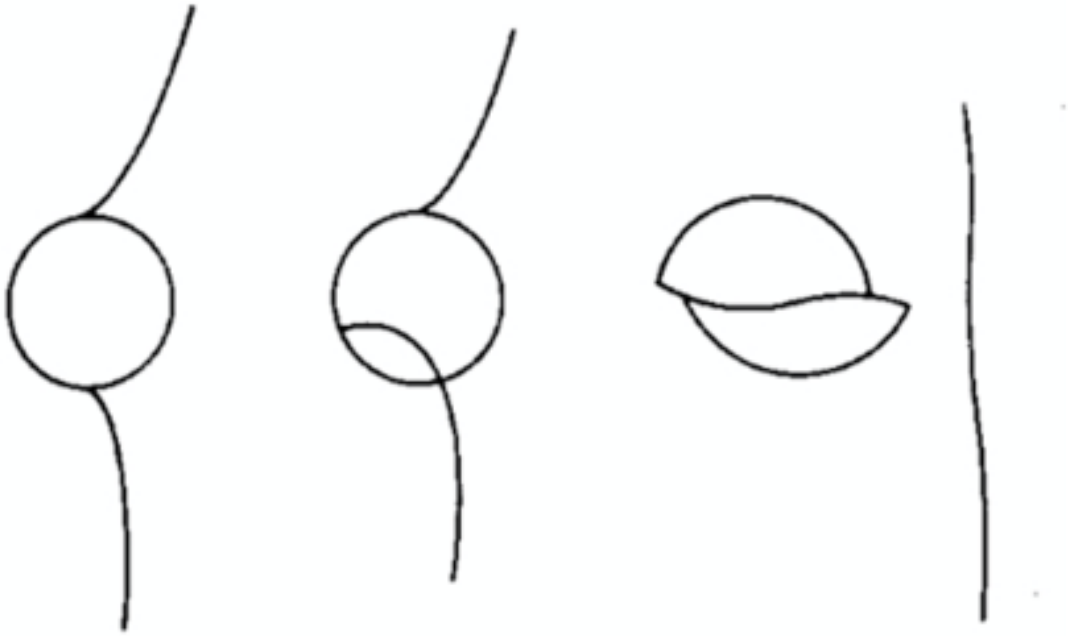

Figure 2.5: Cutting of a precipitate with a dislocation moving from left to right [3].

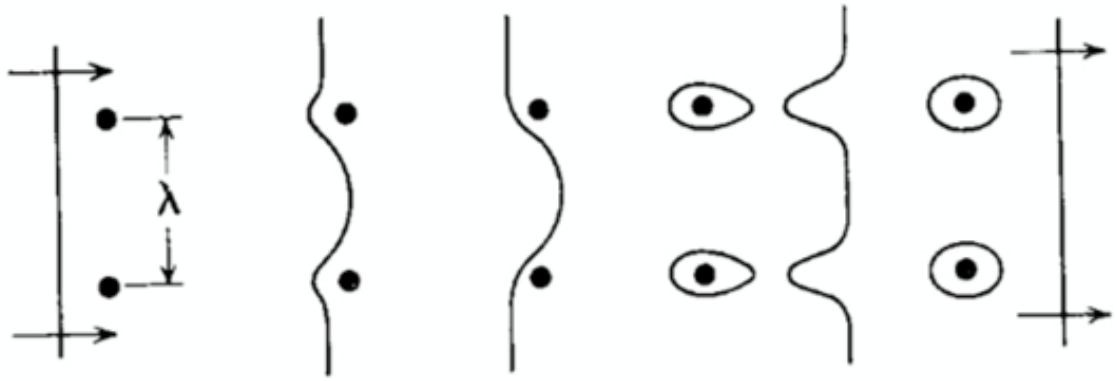

Figure 2.6: Orowan looping mechanism with dislocation line moving from left to right [3].

from a dispersion of spherical precipitates is

$$\Delta\sigma_y = \frac{M\alpha\mu b}{\lambda} \approx M\alpha\mu b\sqrt{Nd} \tag{2.5}$$

where α is the obstacle strength factor, μ is the shear modulus, N is the obstacle number density (m^{-3}), and d is the obstacle average diameter (nm) [10, 95-98]. For weaker obstacles (e.g. coherent precipitates), an alternative model by Friedel [99] accounted for dislocation shear through obstacles by increasing the inter-obstacle distance.

$$\Delta\sigma_y = \alpha M\mu b d N^{\frac{2}{3}} \tag{2.6}$$

where α is assumed to be ~ 1/8. Other values of α are acceptable; 1/8 was found to fit well in the above work by Friedel.

Focusing on the influence of the variety of defects produced in 304 and 316 steels under irradiation, Tan and Busby developed semi-empirical dispersed barrier hardening relationships. To better calculate the strengthening factor (α) of precipitates, dislocation loops, and cavities up to 12nm in size they used Equation 2.7.

$$\alpha = k_1 \ln(k_2 d) \tag{2.7}$$

where k_1 = 0.1757 and k_2 = 2.7013 are fit parameters for spherical precipitates, and d is the diameter of the obstacle in nanometers [96]. Alternatively, Tan and Busby proposed a second equation (Equation 2.8) for calculating the amount of hardening specifically for spherical precipitates based on the Orowan mechanism with the least simplification.

$$\Delta\sigma_y = \frac{0.135M\mu b\sqrt{Nd}}{(1-\nu)^{\frac{1}{2}}(1-0.816d\sqrt{Nd})} \ln\left(\frac{0.816d}{r_0}\right) \tag{2.8}$$

where ν is Poisson's Ratio and r_0 is the dislocation core radius in nm. They note that r_0 is generally a multiple of the Burgers vector ranging from $1*b$ to $4*b$ [96]. The overall increase in hardening decreases as the dislocation core radius increases. This is expected

as this simulates an increase in the interaction distance between dislocations and precipitates. To account for the contributions of Hall-Petch grain boundary strengthening, strain hardening from dislocation-dislocation interaction, and dispersion of precipitates to the base strength of a material, an appropriate root sum square and linear superposition relationship is required [100].

As mentioned in Chapter 1, ODS materials capitalize on the incorporation of large numbers of nanoscale oxide precipitates to increase the alloy's overall sink strength. The presence of these precipitates pins grain boundaries (i.e. Zener pinning), pins dislocations, and inhibits slip under stress. Combined, this reduces the potential for recrystallization and grain growth at higher operating temperatures improving high temperature strength and high temperature creep resistance compared to their non-ODS counterparts [16, 101, 102]. **Figure 2.7** shows a comparison of strength of ODS FeCrAl alloys vs a non-ODS FeCrAl alloy across increasing temperatures. As shown, there is a 200-250 MPa improvement in strength even at high temperatures [9]. **Figure 2.8** demonstrates how the presence of ODS precipitates improves the high temperature creep resistance of these alloys by dramatically increasing the time to rupture and allowing for increased amount of stress simultaneously. For example, at a creep rupture time of 100 hours, the addition of ODS precipitates allowed for an increased creep rupture stress from roughly 140 MPa to 320 MPa. Further, at a creep rupture stress of 200 MPa, the creep rupture time increased from around 1 hour to 1000s of hours. The variation across ODS steel properties is likely due to varied alloy compositions and fabrication conditions across multiple studies) [30].

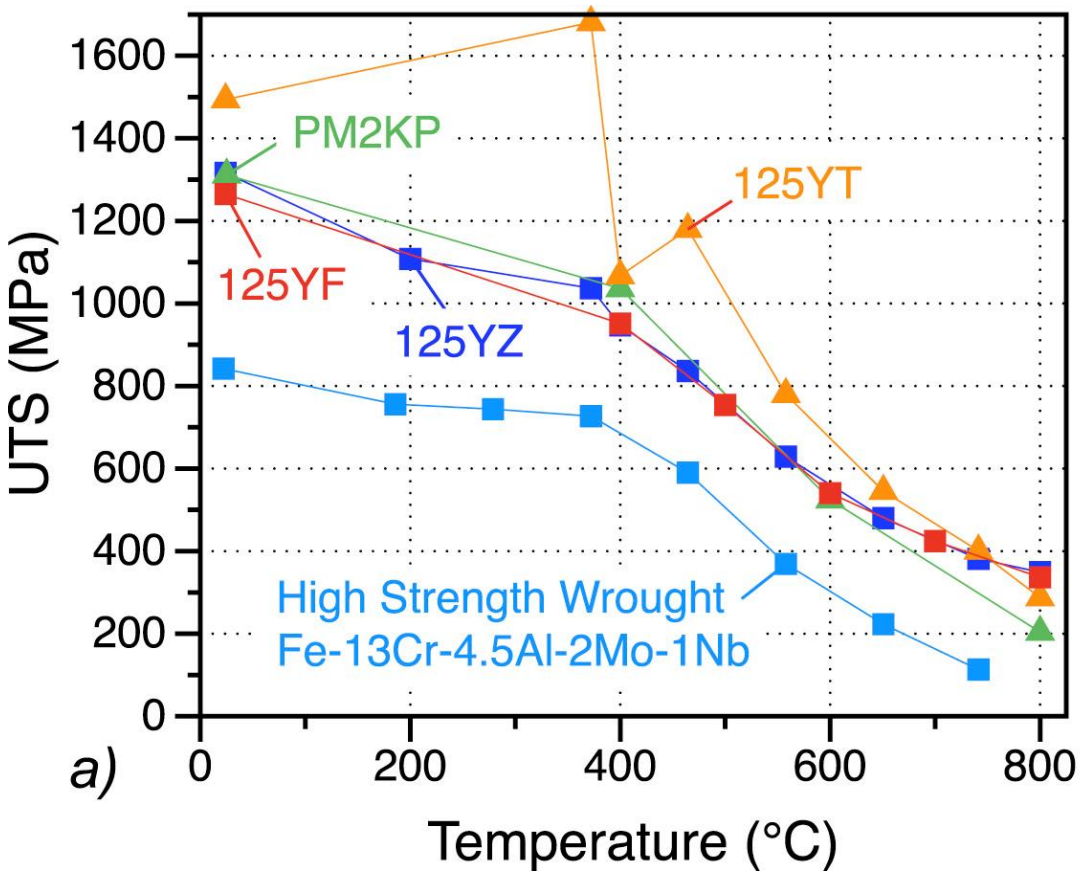

Figure 2.7: Strength comparison of ODS and non-ODS alloys up to 800 °C [9].

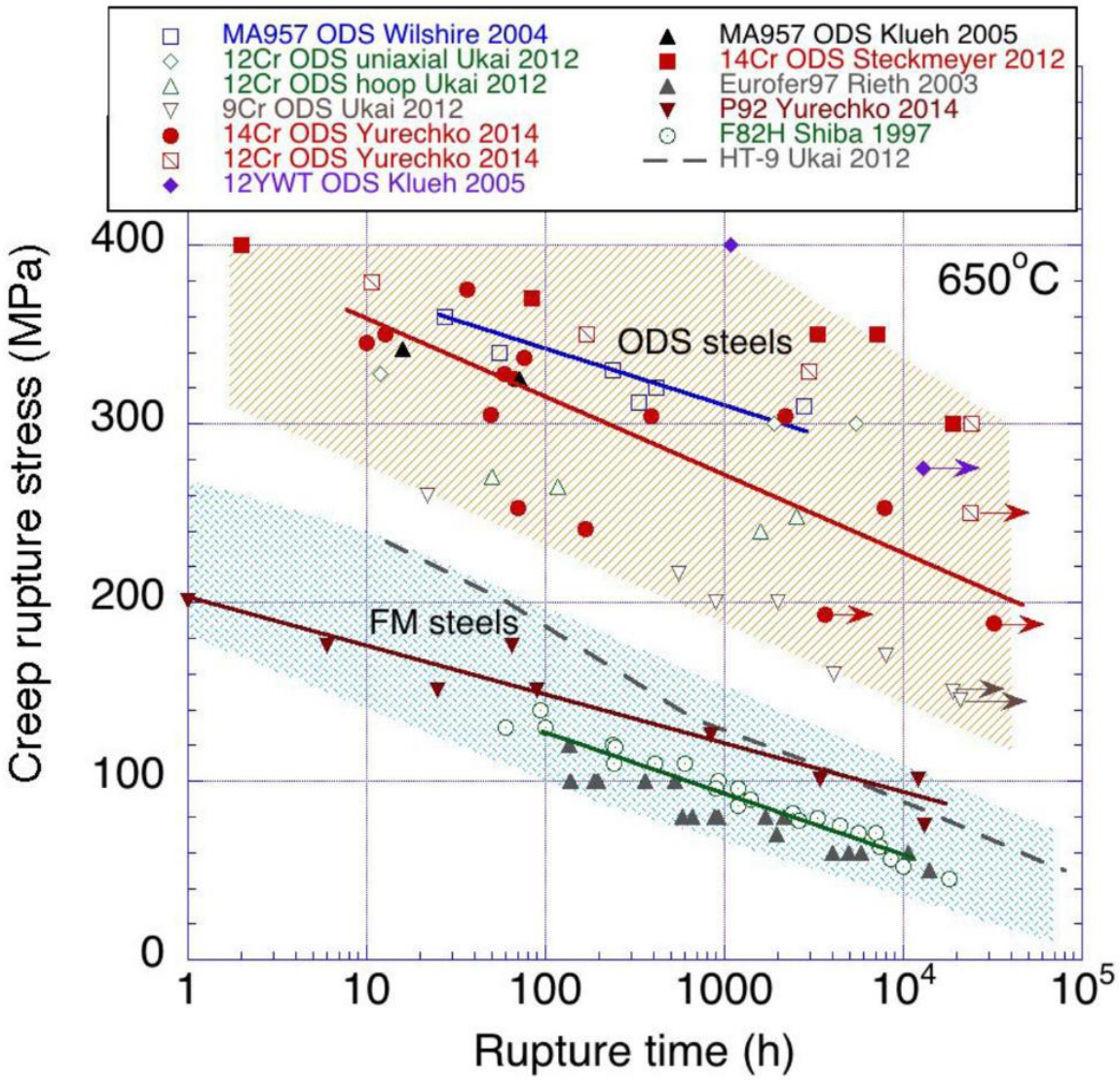

Figure 2.8: Creep rupture property comparison of ODS and non-ODS ferritic-martensitic steels [30].

2.1.2. Influence of Sinks on Irradiation Resistance

As explained in Chapter 1, material irradiation resistance greatly improves with the use of large numbers of sinks or a high sink strength. Interfaces provided by these sinks increases the number of locations for Frenkel pair defects to migrate to and recombine (when a self-interstitial atom or SIA comes in close proximity to a vacancy refilling an empty lattice position, also known as annihilation) as demonstrated in **Figure 2.1**. To determine how grain boundaries, dislocations, and precipitates affect irradiation resistance, their contribution to a material's sink strength can be calculated based on diffusion and reaction rate theory.

Grain Boundaries:

$$S_{gb} = \begin{cases} \frac{60}{d^2} \; ; \; for\ low\ total\ sink\ densities\ (S^{0.5}d \ll 1) \\ \frac{6S^{0.5}}{d} \; ; \; for\ high\ total\ sink\ densities\ (S^{0.5}d \gg 1) \end{cases} \tag{2.9}$$

Dislocations:

$$S_{i,v}^{disln} = Z_{disln} * \rho_n \tag{2.10}$$

Cavities and Precipitates:

$$S_{c,p} = 4\pi r N(1 + S_{tot}^{0.5} r) Z_{c,p} \tag{2.11}$$

where S is the sink strength provide by the type of sink in question, d is the average grain diameter, Z_{disln} is the bias of a dislocation to absorb an SIA or a vacancy (generally SIAs are favored by dislocations), ρ_n is the dislocation density, r is the radius of the cavity or precipitate, N is the number density, and $Z_{c,p}$ is the bias of the cavity or precipitate to absorb SIAs or vacancies (generally equal to one as precipitates do not typically have a bias) [16, 103]. The various parameters to calculate sink strength are determined using

either scanning electron microscopy (SEM) or transmission electron microscopy (TEM) techniques to measure and count their presence in a microcrusture. As demonstrated from the above equations, decreasing average grain diameter, increasing dislocation density, increasing precipitate number density, and decreasing precipitate size all have large impacts on total material sink strength, which is simply a summation of all individual sink strengths [16].

In high sink strength materials at temperatures below the threshold for vacancy mobility (~ 0.2 T_m), concentrations of SIAs and vacancies initially increase simultaneously at the onset of irradiation. At some time shortly after, SIAs begin to annihilate or absorb at sinks present in a system at a rate that creates a quasi-steady-state concentration. Vacancies continue to accumulate for a little longer. Eventually point defect concentrations reaches a threshold where a new vacancy is in close enough proximity to a sink that it will diffuse to it. This causes vacancies to also reach a quasi-steady-state concentration. The difference between steady-state times stems from differences between point defect diffusivities. SIAs are more diffuse and reach steady-state more quickly [90, 103].

As these defects annihilate or absorb at sinks, they are removed from a system and prevented from creating microstructural changes that can dramatically alter a system's material properties. This mechanism reduces radiation hardening and embrittlement that damages materials used in nuclear applications. Radiation hardening and embrittlement is a result of dislocations and defect cluster production that cause dislocation pinning or Orowan looping [16]. This is demonstrated in **Figure 2.9** below,

a

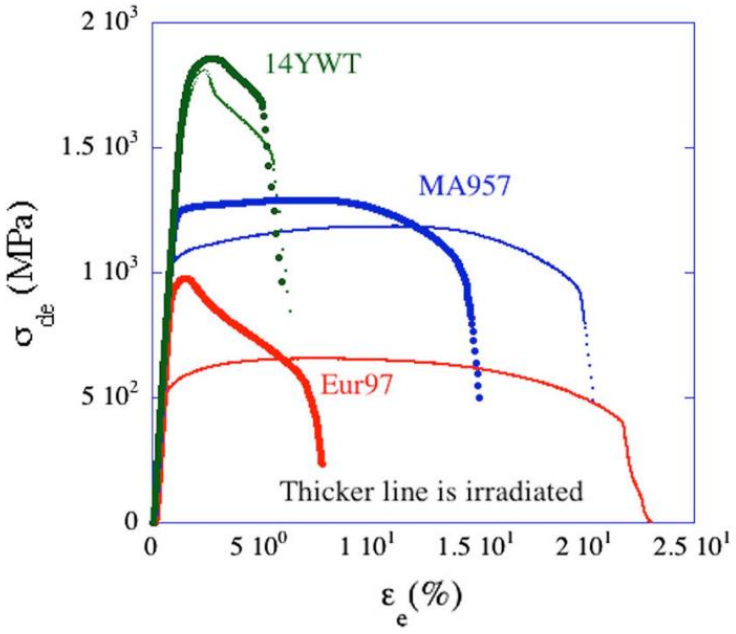

b

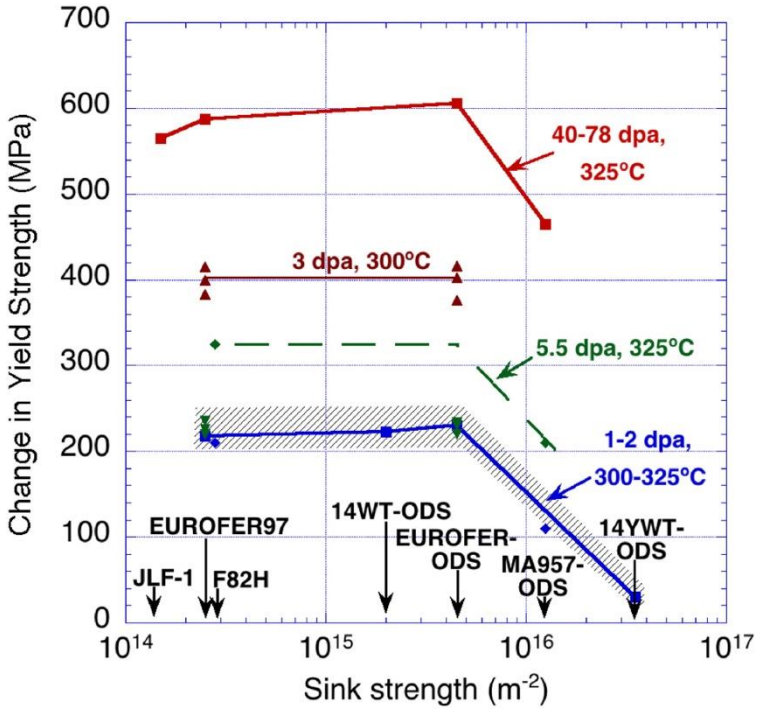

Figure 2.9: a) Presence of ODS precipitates in 14YWT and MA957 reduce the embrittlement experienced after irradiation [101]. b) Increases in sink strength and utilization of high sink strengths are responsible for the mitigation of hardening and embrittlement [30].

which shows that an increase in sink strength of a material leads to a reduction in resulting radiation hardening [30]. Increasing sink strength decreases the distance between sinks and increases the probability that any new self-interstitial atoms (SIAs) or vacancies (cumulatively known as point defects or Frenkel pairs) will be closer to a sink than another defect and inhibits defect clustering. In addition to minimizing hardening and embrittlement from irradiation, this prevention of defect clustering also restricts the amount of void swelling experienced under irradiation (**Figure 2.10**). This is particularly important at the higher operating temperatures of advanced nuclear reactor designs and fusion applications where vacancy diffusion is possible.

A large numbers of nanoscale precipitates attracts and traps He atoms produced during transmutation reactions. With a binding energy of 1.5 eV, these He atoms will initially reside inside oxide interstitial sites as suggested by DFT simulations and shown in **Figure 2.11** [101, 104]. He inside and at a precipitate surface facilitates vacancy accumulation along precipitate interfaces. This ultimately results in He bubble formation along the precipitate-matrix interface and prevents bubble formation and He embrittlement along grain boundaries that is particularly deleterious to a material's strength [16, 101]. Spreading out this He and voids prevents cavities from reaching a critical size for void swelling and protects a material. Smaller, more numerous precipitates yield smaller and more numerous He bubbles minimizing their influence on material properties. **Figure 2.11** demonstrates the relationship between bubble size and He/vacancy accumulation along the precipitate surface [101].

Just as irradiation can cause defects to form in a material, there is potential for irradiation to destroy or negatively alter the integrity of precipitates within an alloy.

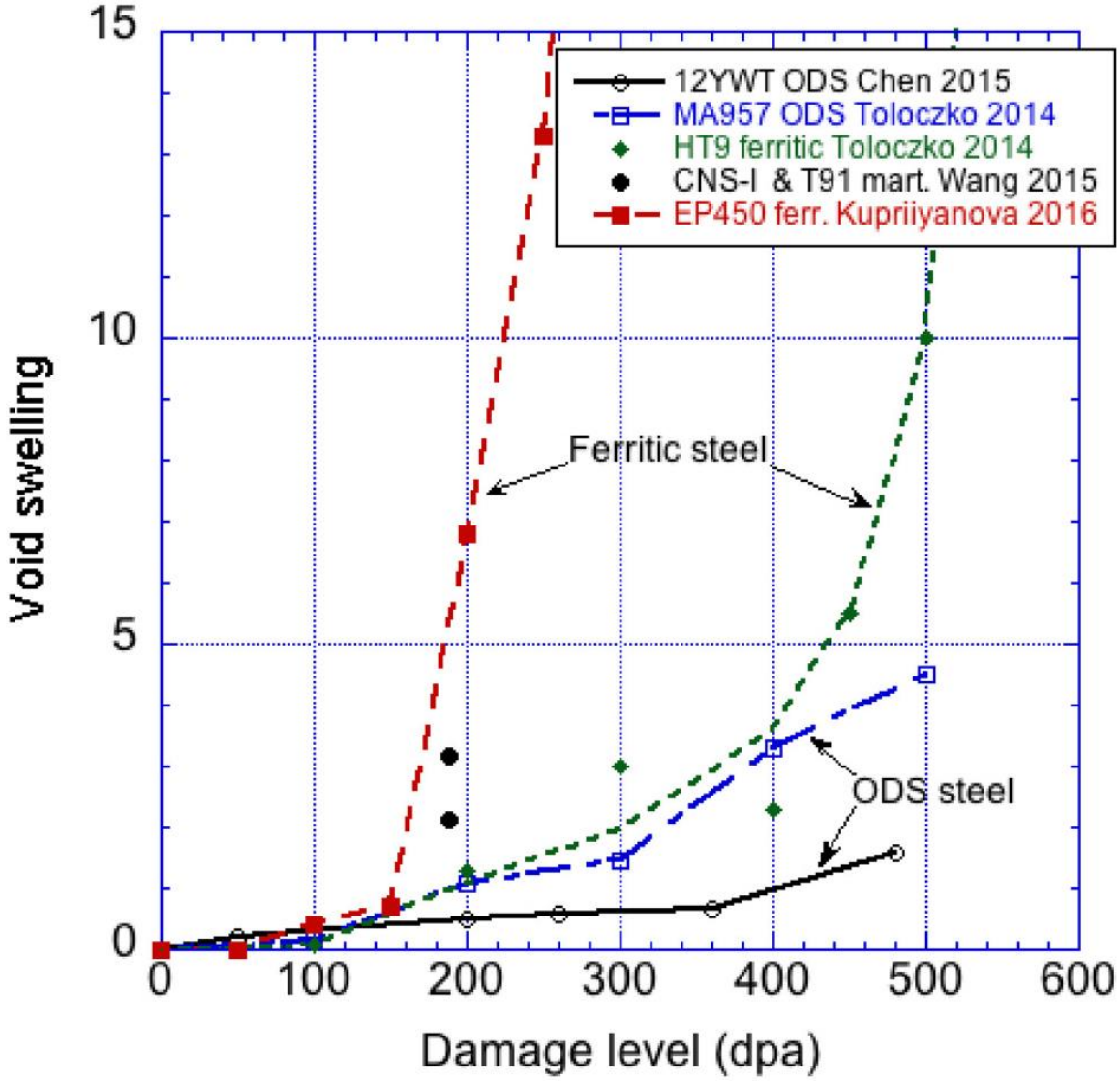

Figure 2.10: Presence of ODS precipitates reduces the amount of void swelling caused by irradiation [30].

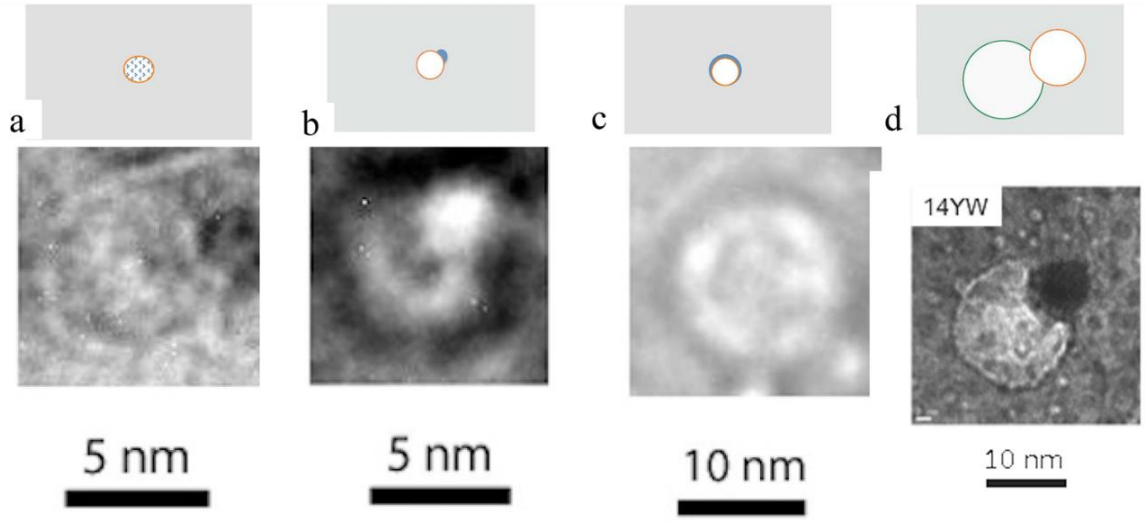

Figure 2.11: Cartoons (top) and TEM micrographs (bottom) showing the progressive states of accumulating He within oxides: a) helium residing inside an oxide interstitial, b) small helium bubble attached the surface of a small oxide, c) a large helium bubble spread over the surface of a small oxide, d) a large helium bubble trapped at the surface of a larger oxide [101].

Determining if these beneficial precipitates can also survive this extreme environment is critical to their viability for microstructural engineering. Work by Lescoat, et al., and Rogozhkin, et al., shows promise that ODS precipitate size and number densities remain relatively constant before and after irradiation. Their experiments used ion irradiation to examine how ODS precipitate structure and size changed with damage level or dpa at 500 ºC and 300 ºC respectively. Both studies showed that larger precipitates are less stable under irradiation and tended to shrink via radiation enhanced diffusion or ballistic dissolution [105, 106]. Smaller oxides, diameter < 10 nm, were resistant to the effects of ion irradiation and even increased in number during their experiments indicative of re-precipitation after ballistic dissolution or radiation enhanced diffusion of oxide elements away from larger precipitates. The belief is that the larger oxides were ballistically broken up during an irradiation cascade or dissolved from radiation enhanced diffusion and precipitated back out as smaller oxides at the increased numbers of dislocations created by irradiation [105]. This was further supported by Ribis and colleagues in 2021 through additional experiments using ion irradiation up to 150 dpa [107]. A diagram of these interaction is shown in **Figure 2.12**.

2.2. Oxide Chemistry

In general, ODS steels are simply a steel alloy that has had Y-based oxide precipitates added. Newer ODS steels often contain 9-20 wt% Cr, around 0.5 wt% Ti, and a few wt% Y_2O_3 [16, 101]. As mentioned in Chapter 1, Cr is added to improve the corrosion resistance of the alloy. Y-based oxides are chosen for ODS steels due to their high thermal stability. Of most oxides, Y_2O_3 has shown to have the lowest free energy of formation as demonstrated in the Ellingham diagram in **Figure 2.13** below. In addition to high

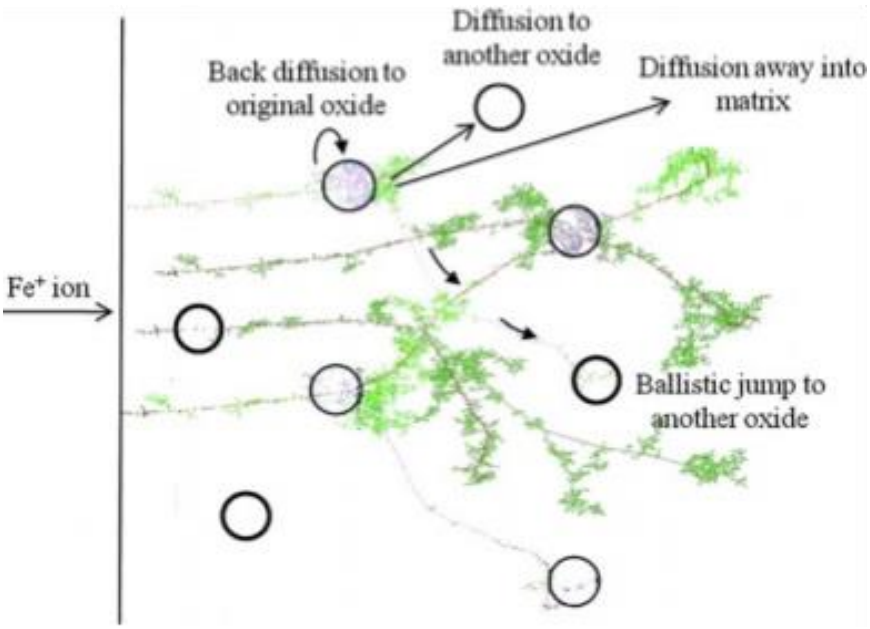

Figure 2.12: Schematic of the evolution of oxide particles dispersed in a steel alloy during irradiation [105].

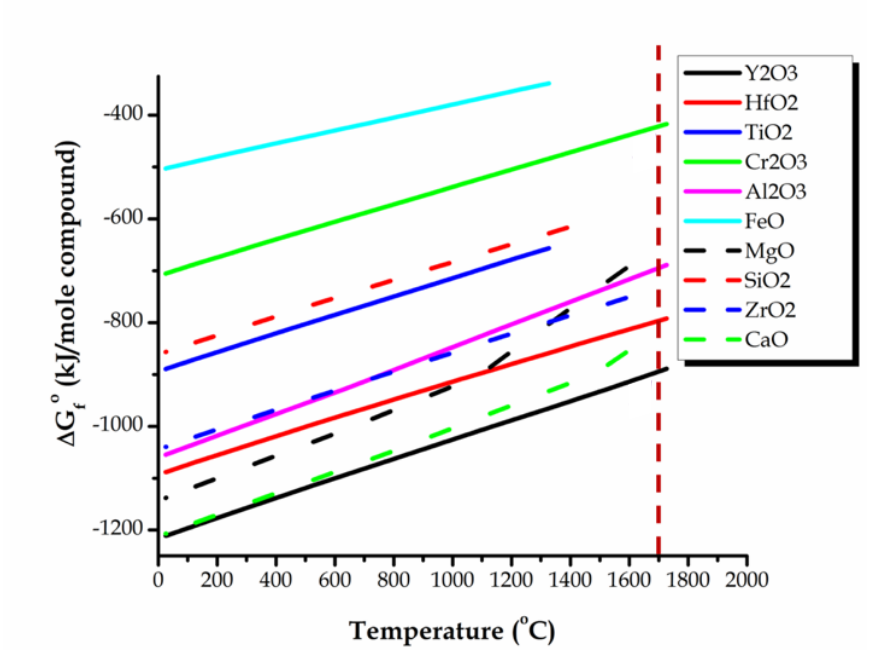

Figure 2.13: Ellingham diagram for common oxides showing free energy of formation (driving force or attraction of metals to O) for Y_2O_3 is significantly lower than FeO at the melting temperature [46].

thermal stability, a low free energy of formation and a high attraction of Y to free O as indicated by density functional theory calculations performed by Wang in 2018 indicate that the nucleation of Y-based oxides should be most strongly favored and encourage higher number densities of precipitates [46, 108].

Extensive work has been done examining modifications to oxide chemistry to minimize size and maximize number densities using conventional powder metallurgy manufacturing techniques. Additions of Ce, Hf, La, Sc, Ti, and Zr to or instead of Y on the formation of oxides have all been tested. Unocic et al. examined the use of Hf and Zr as an oxide refiner for an Fe-12Cr-5Al ODS alloy. They noted that $Y_3Al_5O_{12}$ (YAG) still formed in the base alloy and those with Hf and Zr additions and that the oxides present were of roughly equal size (~ 3 nm). No evidence of Y-Zr-O phases was found. Some complex Y-Hf-O phases were found and overall the precipitation was more complex. One possible reason for the lack of precipitate refinement was the consumption of Hf and Zr in the formation of highly stable carbonitrides[109]. Husák et al examined the addition of Cr, Hf, La, Sc, and Zr on the oxide formation in ODS EUROFER (Fe-9Cr-1W-0.5Mn-0.2V-0.1Ta-0.3Y_2O_3). Their work showed that Sc and Zr had the most profound influence on reducing precipitate size. Hf was less effective, and La and Ce were the least effective. The addition of Ti as an oxide refiner was initially examined by Ukai in 1993 and has been shown as a successful addition repeatedly since [16-18, 27, 41, 110, 111]. It is important to note that the relative amount of Ti added is important. Too much and larger TiO_2 form. Too little and refinement is not maximized as shown in **Figure 2.14**. A Y:Ti ratio of 0.4 was found to be optimal in minimizing oxide size [112].

As mentioned earlier in this section, Y-based oxides are chosen for their excellent

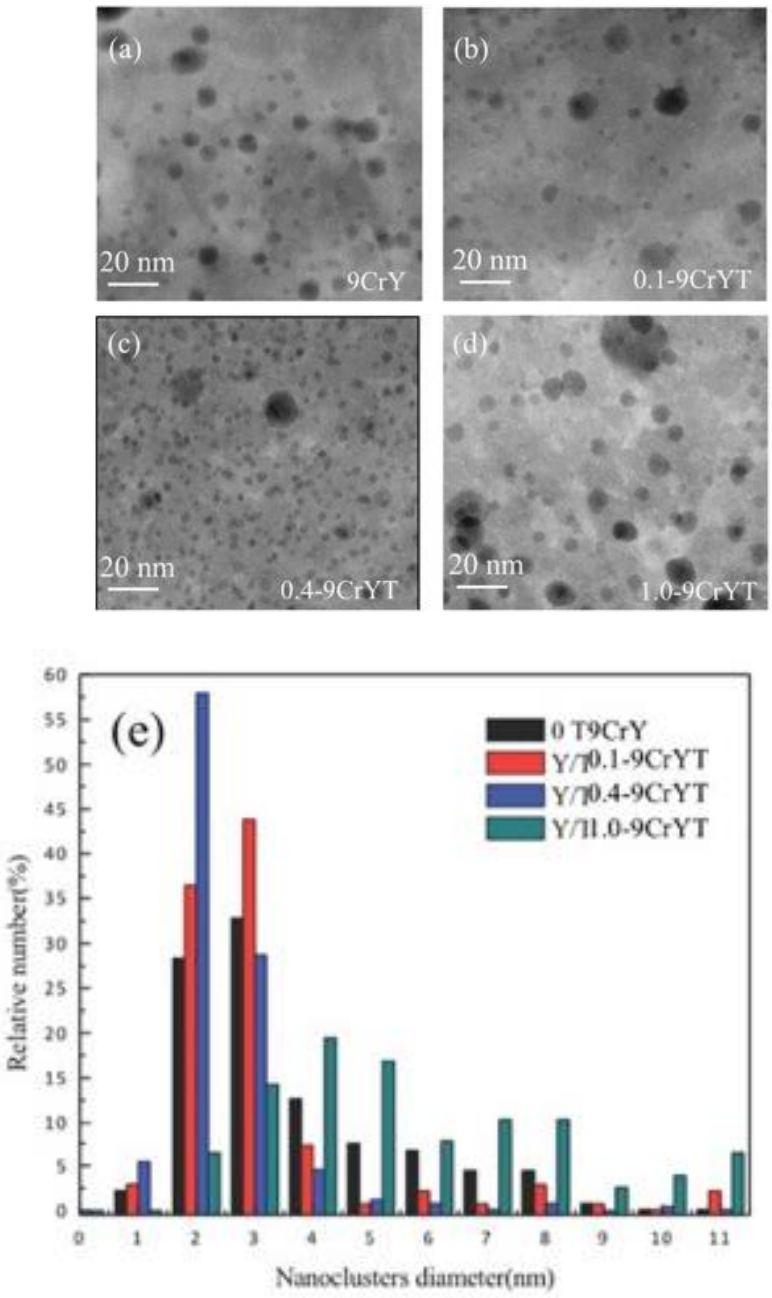

Figure 2.14: Oxide size distribution dependency on Y:Ti ratio for ODS steel produced using powder metallurgy [112].

thermal stability. Numerous studies have been performed to examine the coarsening and growth response of ODS precipitates across a variety of temperatures and timescales. Cunningham did extensive work looking at the thermal aging of MA957 (Fe-14Cr-0.9Ti-0.3Mo-0.25Y_2O_3) at temperatures between 800 °C and 1000 °C up to 32.4 kh. Using microhardness, small angle neutron scattering (SANS), atom probe tomography (APT), and transmission electron microscopy (TEM), Cunningham was able to monitor relative changes in material properties and oxide size and composition as a function of aging. It was found that no significant change in microhardness occurred when aged below 900 °C. Small reductions in strength occurred at 950 °C and 1000 °C (up to 13%) at almost 20 kh (**Figure 2.15**). It was not until aging temperatures were increased to ~1200 °C and above that the oxides tended to appreciably coarsen at a concerning rate (**Figure 2.16**) [113-115].

2.3. Conventional Manufacturing

Conventionally, ODS steels are fabricated using powder metallurgy techniques. Gas atomized base alloy powder, sometimes containing elemental Y and sometimes not, is mechanically alloyed in a high-energy ball mill with powder of some oxide phase (often Y_2O_3) for 20-40+ hours [27, 36, 38, 50, 111-114, 116-122]. During milling the metal and ceramic powders collided with each other, the milling media, and the sides of the mill at high velocities. This deforms the metal powders and breaks down the ceramic powder into smaller and smaller particles. Some of the ceramic powder cold welds to the metallic powder modifying its composition. Eventually sufficient plastic deformation occurs that the oxide powder dissolves and is incorporated into the metal matrix [16, 41, 123, 124]. During this process special care must be made to prevent gas infiltration and

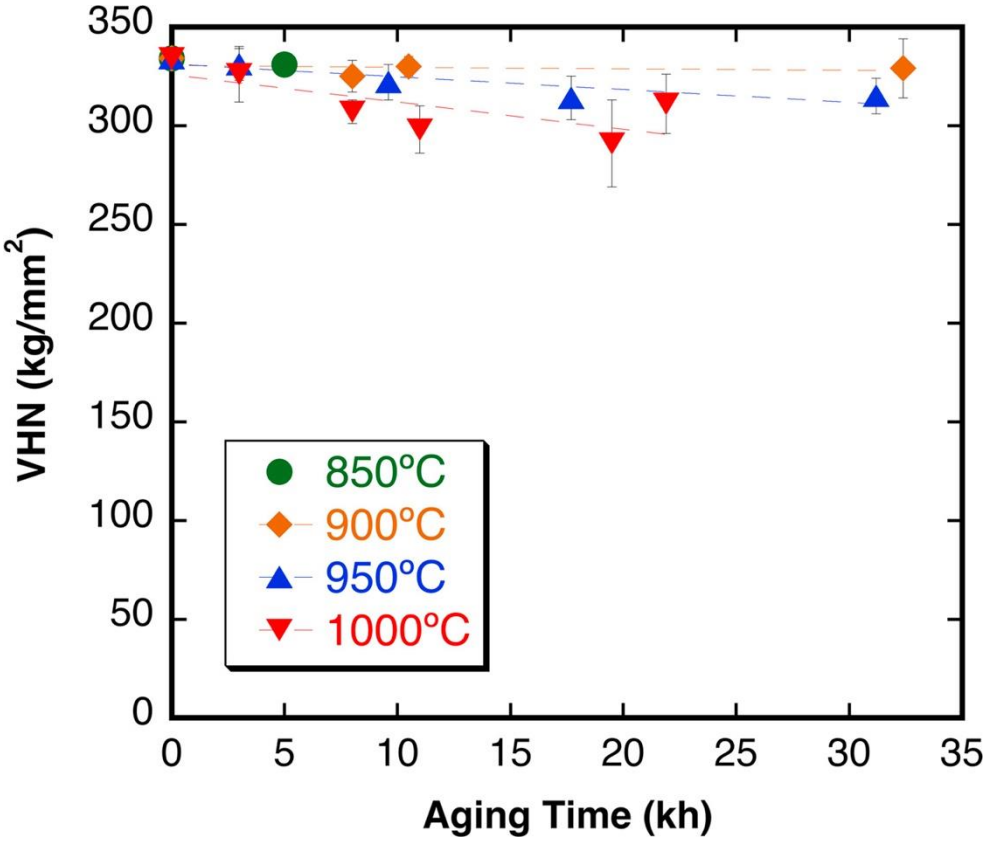

Figure 2.15: Effect of extensive thermal aging on microhardness of ODS MA597 [113].

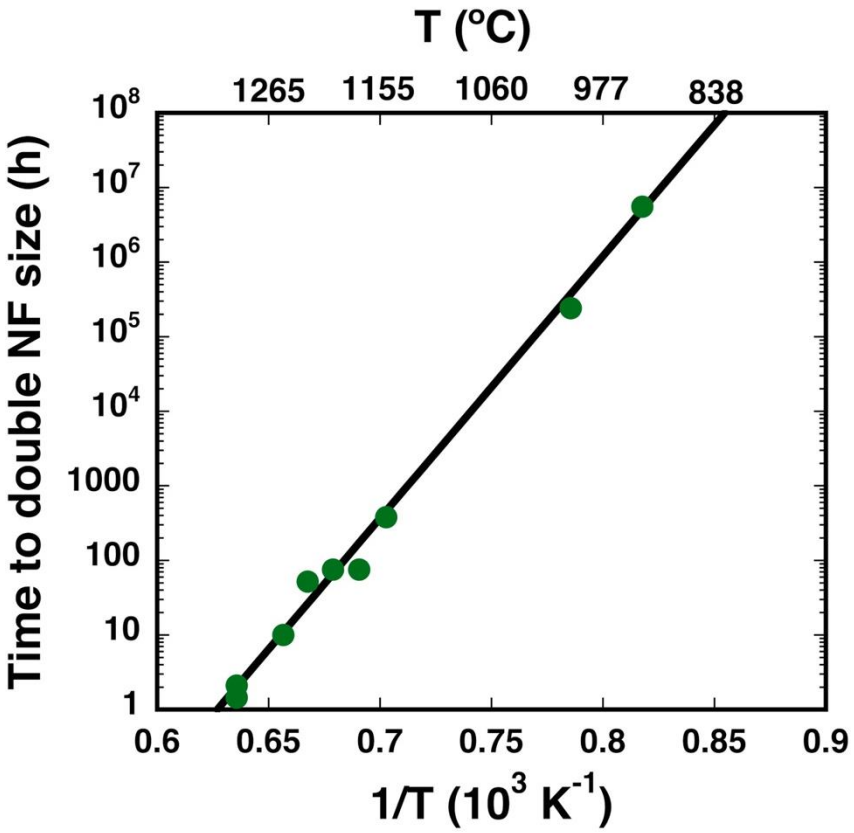

Figure 2.16: Effect of thermal aging at various temperatures on coarsening of precipitates in MA957 [115].

contamination of the powder via poor cleaning or the milling media [38, 46, 95, 125]. Poor control can lead to undesired increases in C, N, and O contents of an alloy that can greatly modify its properties.

After milling, the highly deformed powder is canned, degassed, and typically consolidated via either hot isostatic pressing (HIP) or hot extrusion (HE). Both processes consolidate the powder and fill in the gaps between particles by encouraging diffusion and plastically deforming powder particles using high temperatures and pressures. HIP achieves increases in specimen density by applying heat and high gas pressures uniformly across a specimen's surface. Increased temperature and pressure increases diffusion and encourages closure of gaps and porosity in a part. Combining elevated temperatures and pressures allows for using either at lower levels than when increased temperatures or increased pressures are used individually. This helps reduce grain growth during HIP [126, 127]. Typical HIP temperatures range between 850 °C and 1150 °C and with pressures on the order of 15 MPa [16, 17, 27, 41, 110, 114, 116]. HE heats up powder and forces the can through a small square or round die to achieve a similar effect while reducing the diameter of the material [38, 116, 128]. Precipitation can begin during a HIP or HE consolidation step and can be optimized through a subsequent heat treatment. Oxides produced by these methods are usually on the order of a few nm in diameter (1-5 nm) with number densities on the order of 10^{23} to 10^{24} m^{-3}. The main drawback to the extrusion process is the resulting elongation of the final grain structure. This results in extensive anisotropic mechanical properties comparing the extrusion and transverse directions and difficulties for further forming and machining leading to microcracks and premature failure under stress [16, 17, 101, 110, 129-131].

Any failure during this process requires restarting the process outlined in **Figure 1.3** and potentially an additional 40+ hours of milling time. Common technical challenges beyond the extensive time and effort for processing of ODS steels via conventional manufacturing are poor alloy homogeneity, heat-to-heat reproducibility, shaping and forming techniques for making intricate parts, and joining techniques that do not dramatically reduce the structural integrity of material [132]. The two former challenges stem from the use of mechanical alloying (MA) and have driven the search for alternative fabrication methods that avoid MA.

2.4. Gas Atomization Reaction Synthesis (GARS)

In an attempt to reduce the dependency on MA, as part of his dissertation work, Rieken developed the gas atomization reaction synthesis (GARS) process. This process impinges an oxygen-rich gas upon the liquid metal during the gas atomization process. The available gaseous oxygen primarily reacts with the Cr present in the steel alloys used and forms an oxygen-rich chromia shell on the surface of the gas atomized powder as it is cooled (**Figure 2.17**). Meanwhile, most of the Y present is in the interior of the powder particles. Due to the low solubility of Y in Fe, effectively zero at room temperature, Y has shown a propensity to agglomerate or precipitate out along grain boundaries [51, 133]. This proved true in the GARS produced powder too [46].

Generally, the solid-state consolidation processes mentioned above with MA powder (HIP and HE) are also typically used with GARS powders. The main difference is in how the precipitates are formed. During most of the MA related processes, the precipitates are formed from nucleation of oxide forming elements that are in solid solution in the alloy. For GARS produced powders, the O is already bound up in the

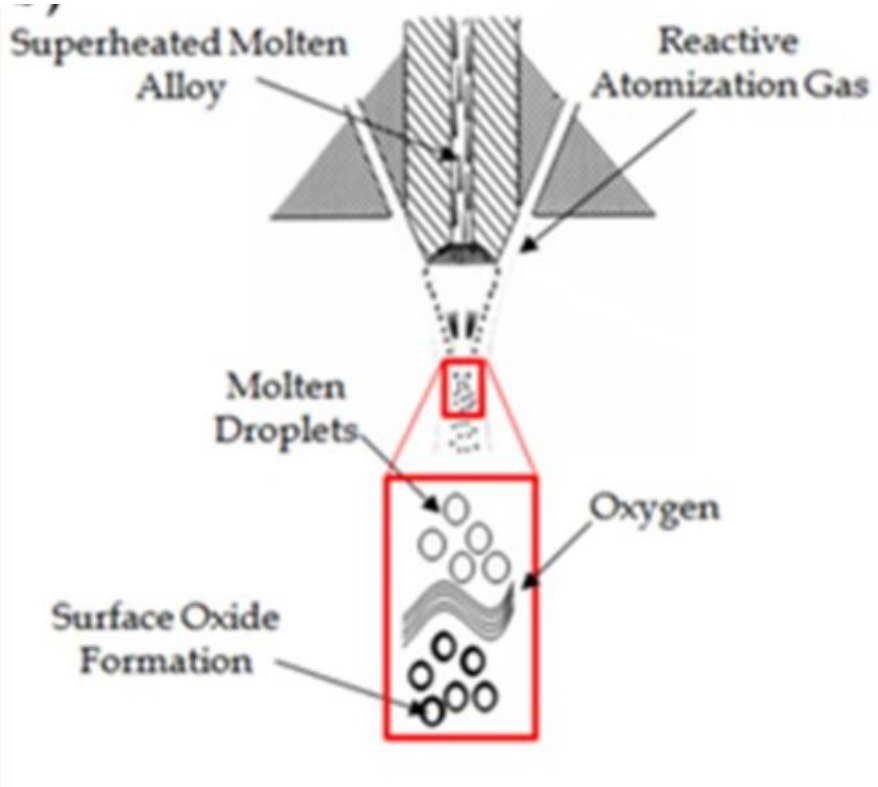

Figure 2.17: Schematic demonstrating the GARS process of introducing oxygen to metal powder [46].

chromia shell on the surface of the powder. During consolidation and subsequent heat treatments, the less stable chromia shell along prior particle boundaries begins to breakdown. As mentioned in Section 2.2, there is a large driving force for the formation of Y-based oxides. This driving force encourages this breakdown and subsequent precipitation of the more thermally stable Y-based oxide phases as described in **Figure 2.18** [46]. The typical precipitate size produce with GARS powder has shown to be slightly larger than their MA counterparts (4 to 15 nm) with slightly lower number densities ($\sim 10^{22}$ m^{-3}).

2.5. Additive Manufacturing of ODS Alloys Using Oxygen Containing Powder

Searching for alternative manufacturing methods to produce ODS alloys with better potential for shaping and forming intricate parts while avoiding the often deleterious effects of joining has driven many researchers to additive manufacturing (AM) technologies. Successful application of AM processes would allow for increased geometric complexity of ODS parts with potential for localized microstructure control while reducing the number of processing steps and need for joining [75-77]. The bulk of the research applying AM to consolidate ODS alloys has used powder already containing oxygen either via mechanical alloying or light blending/mixing.

Early work by Boegelein et al. looked at using powder bed fusion-laser beam (PBF-LB) to consolidate MA ODS PM2000 powder under an inert atmosphere. Nanoscale precipitation was achieved; however, average precipitate size was between 25-30 nm with a number density of 10^{21} m^{-3}. The authors noted that there was an appreciable amount of

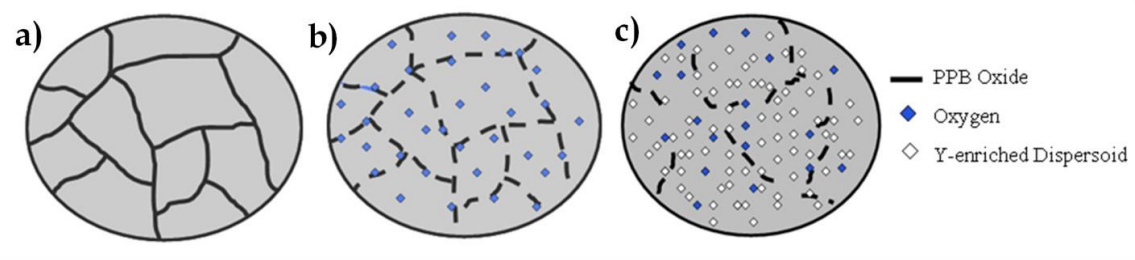

Figure 2.18: Chromia chemical reservoir at prior particle boundaries acts as an oxygen source for Y-oxide formation during consolidation and subsequent heat treatments [46].

Y-rich slag material along the edges of the built parts and some larger inclusions suggesting that precipitation was not maximized [62, 82].

In an attempt to avoid complete MA, Ghayoor et al. and Zhong et al. examined the use of lightly mixing or blending base metal powder with Y_2O_3 powder. Ghayoor et al. looked at using PBF-LB to consolidate 304L lightly blended with Y_2O_3 powder under an inert atmosphere. They were able to produce Y-Si-O phase nanoscale precipitates with a reported average size of 25 nm. No number densities were reported. The strength of the alloy was improved; however, the precipitates had poor thermal stability when aged at 1000 °C, 1100 °C, and 1200 °C for 100 h [80, 134]. Zhong et al. used PBF-LB to consolidate 316L with 0.5 wt% Si added and lightly milled with Y_2O_3 powder. The authors noted appreciable losses of Y_2O_3 in the finished parts compared to the blended powder. Some agglomeration occurred and precipitate sizes were generally between 10 – 70 nm albeit smaller than the 800 nm Y_2O_3 that was lightly milled with the 316L powder [135].

Recent work by Saptarshi et al. used PBF-LB to consolidate GARS fabricated 14YWT powder under an inert atmosphere. During the PBF-LB process, the chromia shell on the GARS powder was broken up and $Y_2Ti_2O_7$ precipitates formed between 17-57 nm in diameter. The precipitates were homogenously distributed with a number density of ~ $1.7x10^{20}$ m^{-3}. The authors claim that overall agglomeration was prevented [136].

2.6. Additive Manufacturing of ODS Alloys Using Reactive Atmospheres for *In Situ* Oxidation

In an effort to avoid the issues plaguing MA and the solid-state consolidation processes (HIP/HE), some researchers have attempted to leverage the high solidification velocities present in AM processes to capture O during consolidation using O-rich reactive

atmospheres for *in situ* oxidation. Using this method, O is dissolved in the liquid melt pool, captured during solidification, and precipitates out with the native deoxidizers present in the alloy. Saeidi et al. examined the use of PBF-LB to consolidate 316L under a reactive atmosphere with 0.1% O_2 present. Well dispersed 50 nm average diameter oxides comprised mostly of Si and O were reported [86]. Zhou et al. did a similar experiment consolidating 316L powder using PBF-LB while varying the residual O_2 present in the chamber. O_2 levels were examined at < 50 ppm, between 300-500 ppm, and between 1000-1200 ppm. < 50 ppm yielded no oxide precipitation. They found that as they increased the O_2 level in the chamber the distribution of oxides improved and refined further going from ~500 nm – 2 μm to 50 – 100 nm, respectively [137].

Springer et al. was one of the first to examine the possibility using a directed energy deposition-laser beam (DED) process. They consolidated 316L powder using minimal Ar shielding gas under air. O content of the as-built increased appreciably. Some larger oxides were formed (165 nm) with a number density of $8x10^{17}$ m^{-3}, and some slagging was noted [87]. Sridharan et al. did something similar in 2018. They found that there was significant Y loss during consolidation. As a result, they were able to achieve average precipitate of 97 nm with number densities ~ $2x10^{18}$ m^{-3}. In their mechanical testing, they found that reduction in tensile strength was more significant for the AM alloy vs. a wrought standard as tensile testing temperature increased from room temperature to 600 ^{0}C. There was a benefit of added ductility, however. It is also important to note that no TEM characterization was done in this study to confirm or deny the presence of finer precipitation [88]. The above results are summarized in **Table 2.1** and compared with literature on conventional manufacturing of ODS alloys as well as manufacturing using

Table 2.1: Comparison of ODS-Steel Fabrication Methods (PBF-LB = powder bed fusion – laser beam, MA = mechanical alloying, HE = hot extrusion, SPS = spark plasma sintering, HIP = hot isostatic pressing, GARS = gas atomization reaction synthesis, CR = cold rolling, FC = friction consolidation, N.R. = not reported) [9, 29, 38, 42-45, 47, 62, 80, 86-89, 136, 138, 139].

Group	Study	Nominal Composition	Manufacturing Method	Avg Diameter (nm)	Number Density (#/m^3)
Conventional Manufacturing	Dawson, 2015	ODS PM2000	MA (no consolidation)	2.1 to 2.5	$8x10^{23}$
	Dryepondt, 2018	Fe-12Cr-5Al+Y	MA + HE	2.2 to 2.9	$2x10^{23}$ to $6x10^{23}$
	Fu, 2021	ODS Eurofer	MA + SPS	4.13	$2.44x10^{23}$
	Massey, 2018	Fe-10Cr-6.1Al-0.3Zr	MA + HE	3.9	$1.8x10^{23}$
	Miller, 2004	ODS MA957	MA + HE	1.2	$2x10^{24}$
	Miller, 2006	14YWT	MA + HE	2	2 to $4x10^{23}$
	Xu, 2011	Fe–18Cr–8Ni–2W–1Ti–0.35Y_2O_3	MA + HIP	10 to 80	N.R.
GARS	Rieken, 2012	Fe-16Cr-0.31Y-0.12Hf	GARS + HIP + CR	15	$2x10^{22}$
	Zhang, 2022	Fe-15Cr-0.15Y-0.1Ti-0.09O	GARS + FC	4.33	$2x10^{22}$
Additive Manufacturing	Boegelein, 2015	ODS PM2000	MA + PBF-LB w/ inert atm	25 to 30	$1.8x10^{21}$
	Ghayoor, 2021	304L mixed w/ Y_2O_3	PBF-LB w/ inert atm	25	N.R.
	Saeidi, 2015	316L	PBF-LB w/ reactive atm	50	N.R.

Table 2.1 Continued

Group	Study	Nominal Composition	Manufacturing Method	Avg Diameter (nm)	Number Density (#/m^3)
Additive Manufacturing	Saptarshi, 2022	14YWT	GARS + PBF-LB w/ inert atm	17 to 57	$1.7x10^{20}$
	Springer, 2016	316L	DED w/ reactive atm	165	$8x10^{17}$
	Sridharan, 2018	316L	DED w/ reactive atm	75 to 100	$2.8x10^{18}$
	Zhong, 2012	316L + 0.5 Si mixed with Y2O3	PBF-LB SLM w/ inert atm	10 to 70	N.R.
	Zhou, 2017	316L	SLM w/ reactive atm	50 to 100	N.R.

GARS processes.

2.7. Oxygen Dissolution and Retention Under Additive Manufacturing

A critical component of being able to form high number densities of nanoscale oxide precipitates using AM with a reactive atmosphere to form oxides *in situ* is an ability to dissolve and retain O in a melt pool during consolidation. As demonstrated in the previous section, the use of AM processes has successfully been leveraged to capture O during the manufacturing process and allow for the formation of nanoscale oxides. Using an oxygen-rich environment during AM, additional oxygen can dissolve into an alloy system via two mechanisms: 1. O reacts with deoxidizers, like Cr, Al, Y, etc., in a melt pool to form oxides that are then captured during solidification as dispersoids or inclusions, or 2. O dissolves into a liquid melt pool that solidifies faster than O can diffuse away from a solidification front (i.e. solute trapping) forming a solid solution. The GARS process developed by Rieken utilizes the first mechanism. O in contact with a liquid metal quickly reacts with abundant Cr to form a chromia-rich shell around powder particles which breaks down during further processing allowing O to form more stable precipitation with Y [47]. Alternatively, increased solidification rates provided by DED AM processes could result in enhanced solute trapping of O during solidification leading to a potentially supersaturated solid solution via the second mechanism [75, 77, 83, 84]. This trapped O would either precipitate out with Y during any remaining build thermal cycles or during a post-build HT.

Kuo in *Welding Metallurgy* notes that the ability of O to dissolve into liquid metal is governed by Sieverts' Law where dissolution of gaseous O by liquid steel can be described by the following chemical reaction:

$$\frac{1}{2}O_2(g) = [\underline{O}] \tag{2.12}$$

where diatomic O is dissolved into liquid steel. An equilibrium concentration of O in liquid steel can then be described at any given temperature by relating Sieverts' law and a reaction equilibrium constant as shown in Equation 2.13.

$$\ln\left(\frac{[O]}{\sqrt{p_{O_2}}}\right) = \ln\left(K_{O_2}^{d}\right) = -\frac{\Delta G^{o}}{RT} \tag{2.13}$$

where [O] is the O concentration of the liquid metal in weight percent, p_{O2} is the partial pressure of diatomic O above the liquid metal in atm, $K_{O_2}^{d}$ is the equilibrium constant for the dissolution reaction, ΔG^{o} is the standard free energy of formation in cal/mol (assumed to be equal to -28000 – 0.69T for steel), R is the gas constant in cal/(K * mol), and T is the absolute temperature of the liquid metal in K [140].

As diatomic O passes by an energy source such as a laser, there is potential for the diatomic O to dissociate into monatomic O. As noted by DeBroy and David, monatomic species dissolve much more readily in liquid metal than their diatomic counterparts as demonstrated in **Figure 2.19** [141]. The dissolution of monatomic O can be described by an analogous chemical reaction and equation (equations 3 and 4).

$$O(g) = \underline{[O]} \tag{2.14}$$

$$\ln\left(\frac{\underline{[o]}}{p_O}\right) = \ln\left(K_O^{d}\right) = -\frac{\Delta G^{o}}{RT} \tag{2.15}$$

where p_O is the partial pressure of monatomic O above the liquid metal and ΔG^{o} is assumed to be -88064 + 15.045T [140, 141].

After dissolving O into a melt pool, it needs to be captured before escaping back into the build atmosphere. Aside from reacting in the liquid phase, O can be trapped in solid solution through solute trapping. As described by Aziz in 1982, solute trapping is the

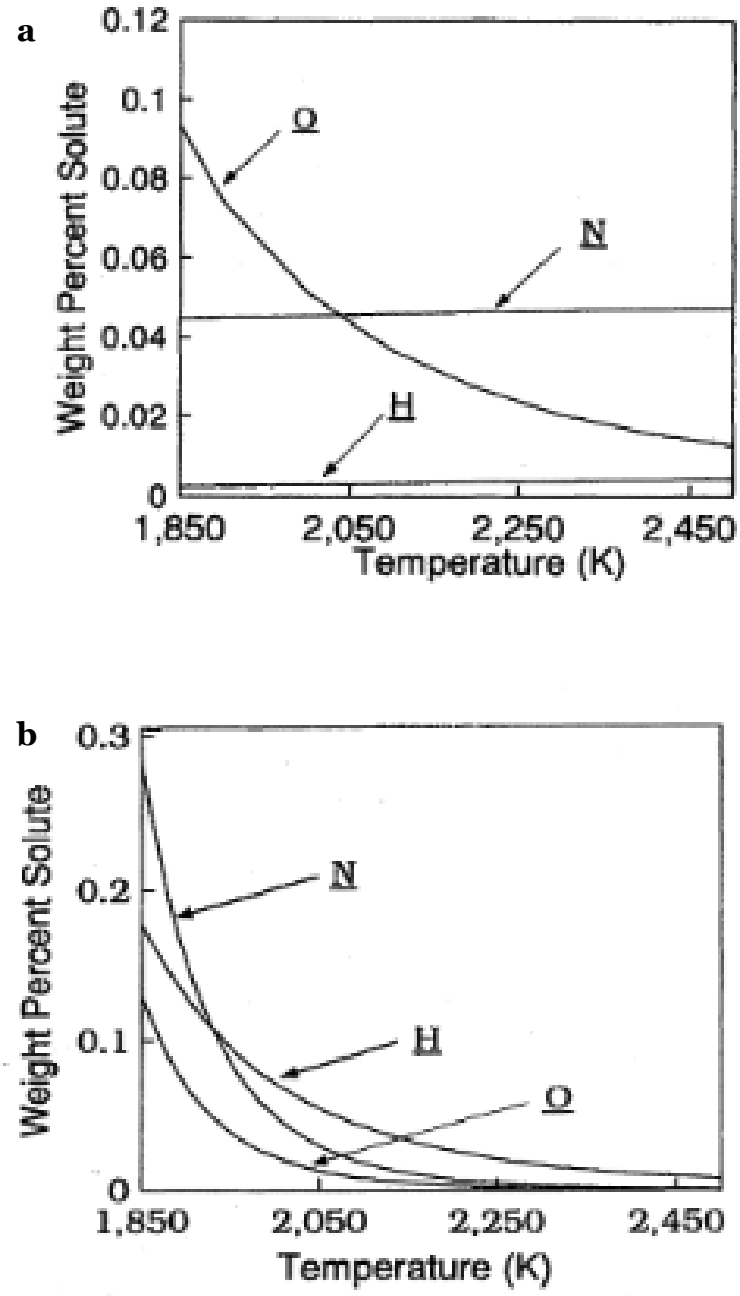

Figure 2.19: a) Equilibrium concentration of H, N, and O in Fe using a) diatomic and b) monatomic pure gas environments (p_i = 1 atm/5x10^{-2} atm, 1 atm/10^{-6} atm, 10^{-9} atm/10^{-8} atm, respectively) as a function of temperature [141].

ability of a solidification interface to move more quickly than solute atoms can diffuse away in the liquid phase. This allows for a solidification interface to overtake solute atoms and trap or lock them within a solid phase. Complete solute trapping requires a solidification velocity greater than a critical solute trapping velocity (u) as is determined by Equation 2.16.

$$u = \frac{D_i}{\lambda} \tag{2.16}$$

where D_i is the diffusivity of solute in the liquid and λ is the interatomic spacing of the solid [83]. Aziz notes that this not a binary process. If a solidification velocity is roughly within an order of magnitude of the complete trapping velocity, solute trapping may still occur albeit at a reduced efficiency[142].

2.8. Oxide Agglomeration

When comparing the relative size and number densities of oxide precipitates formed using MA with HIP/HE to any AM processes (**Table 2.1**), it becomes apparent that oxide dispersions produced using AM are generally sparser and contain larger oxides on average. The widespread belief in the literature is that these larger precipitates are a result of two phenomena: 1. low relative densities of oxides compared to liquid Fe resulting in floating oxide phases on a melt pool's surface, and 2. poor incorporation of oxides into steel matrices due to poor chemical compatibility as measured by oxide-alloy wettability or oxide-liquid steel interfacial energy causes oxides to be push in front of a solidification front instead of incorporating in a matrix [50, 60-62, 81, 82, 143-145].

As explained by Grong, oxide phases do not float on a melt pool's surface because of Stokes' law. Due to their relatively lower densities, oxide phases are readily swept up by a weld pool's convective currents and carried to its surface. As shown in **Figure 2.20**,

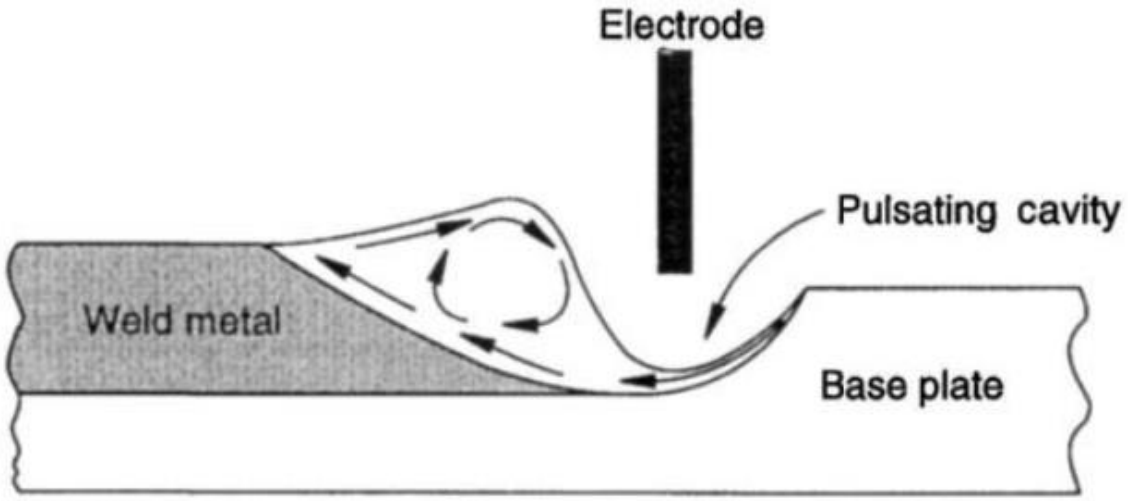

Figure 2.20: Schematic of melt pool turbulence [146].

these currents circulate material up from the bottom of a melt pool to the top and then back down. Once a lighter oxide phase is drug up by melt pool turbulence to its surface, they then float until they are ejected from the melt pool or captured by a solidification front as an inclusion [146]. While on a melt pool's surface, oxides can grow or coarsen three different ways: 1. accelerated diffusion of oxide forming elements in a liquid melt pool, 2. collision of oxide precipitates with one another while speeding around from melt pool turbulence, or 3. Ostwald ripening [143, 147]. To look at minimizing the effects of these, we must examine their relationships to oxide formation and melt pool phenomena.

2.9. Reducing Oxide Agglomeration

A method to minimize the effects of accelerated liquid phase diffusion is to decrease a melt pool's lifetime, which is a function of melt pool size and solidification velocity. Both are dependent on specimen operating parameters (namely laser power and tool speed). In this instance there are either hard machine limits (physical limitations of the device) or material limits (build quality limitations) that reduce the flexibility of changing operating parameters significantly. Alternatively, the effects of diffusion could be reduced by increasing the number of sinks for oxide forming elements to diffuse to. As described at the beginning of this chapter, the addition of numerous sinks inhibits the growth of voids or bubbles such that they cannot reach a critical size for void swelling to occur. Similarly, if the number of oxide nuclei is sufficiently large, the amount of growth and coarsening that any singular oxide can experience is minimized. Homogeneous nucleation of oxides is governed by the two following equations:

$$r^* = \frac{-2\gamma V_{m,ox}}{\Delta G_{nuc}} \tag{2.17}$$

$$\Delta G^* = \frac{16\pi\gamma^3 V_{m,ox}^2}{3\Delta G_{nuc}^2} \tag{2.18}$$

where r^* is the critical radius for a stable oxide, γ is the interfacial energy between the oxide phase and liquid Fe, $V_{m,ox}$ is the molar volume of the oxide, ΔG_{nuc} is the driving force for nucleation or the change in bulk free energy from the parent phase to the particle phase, and ΔG^* is the energy barrier for nucleation [143].

Additionally, precipitate collision in a liquid melt pool strongly influences coalescence or agglomeration. Work from Babu, David, and DebRoy examining how melt pool lifetime directly influences precipitate growth and number densities suggested that coarsening as a result of collision occurred much more rapidly than coarsening expected from Ostwald ripening [147]. Recent modeling work performed by Eo et al. gives some insight on how to minimize collision induced agglomeration. Their modeling noted that coalescence or agglomeration from collision was more severe for larger precipitates. Effectively, larger precipitates appeared to have a greater probability to strike or be struck by another precipitate and fuse [143]. Minimizing precipitate size and melt pool lifetime (i.e., time for potential collisions) appear to be the most effective methods to reduce precipitate coalescence. Alternatively, reducing melt pool turbulence could help.

The last method for oxide coarsening during AM would be Ostwald ripening. While not expected to be a primary contributor to agglomeration, it can still negatively influence precipitate sizes and number densities. Precipitate growth via this mechanism is governed by the Wagner Equation below.

$$d_v^3 \approx d_o^3 + \frac{64\gamma D_m C_m V_{m,ox}^2}{9RT} * \tau \tag{2.19}$$

where d_v^3 is the mean particle diameter after some time, d_o^3 is the initial particle diameter, D_m is the solute elemental diffusivity, C_m is the solute element in bulk concentration, and

τ is the retention time (a function of the distance from the point of maximum melt pool width and the tool speed) [146].

There is a common parameter shared by each of these equations: γ, the interfacial energy between oxide and liquid metal also known as the wettability of the oxide phase. Interfacial energy is considered an approximation for how strong a bond is between two dissimilar phases in a material and is believed to partially govern how different phases are distributed in a bulk matrix. Interfacial energy is commonly determined experimentally using a sessile drop test where a liquid sample of one of the phases is placed on a solid sample of the other phase being examined (e.g., a sample of liquid metal is placed on a sample of solid oxide). Measurements are taken on a liquid metal's surface tension, and the contact angle that forms between a liquid metal droplet and a solid oxide substrate is measured. An example of such measurement is included in **Figure 2.21**. These two pieces of information are then used to calculate a system's interfacial energy and give an indication of how different phases are interacting at their shared interface. Lower contact angles result in lower interfacial energies, demonstrate increased bonding between phases, and indicate better compatibility [148, 149]. Reducing the interfacial energy of an oxide-liquid metal system should reduce the critical oxide radius, decrease the energy required to nucleate an oxide, and reduce the amount of coarsening an oxide should experience in a melt pool as indicated by Equations 2.17, 2.18, and 2.19 [143, 146].

2.10. Research Objective Summary

Recently there has been a strong push to examine alternative methods of producing ODS alloys instead of traditional powder metallurgy techniques. Alternative means of producing ODS alloy powders like GARS and alternative processing techniques like PBF-LB and DED AM have been examined in some capacity to determine their

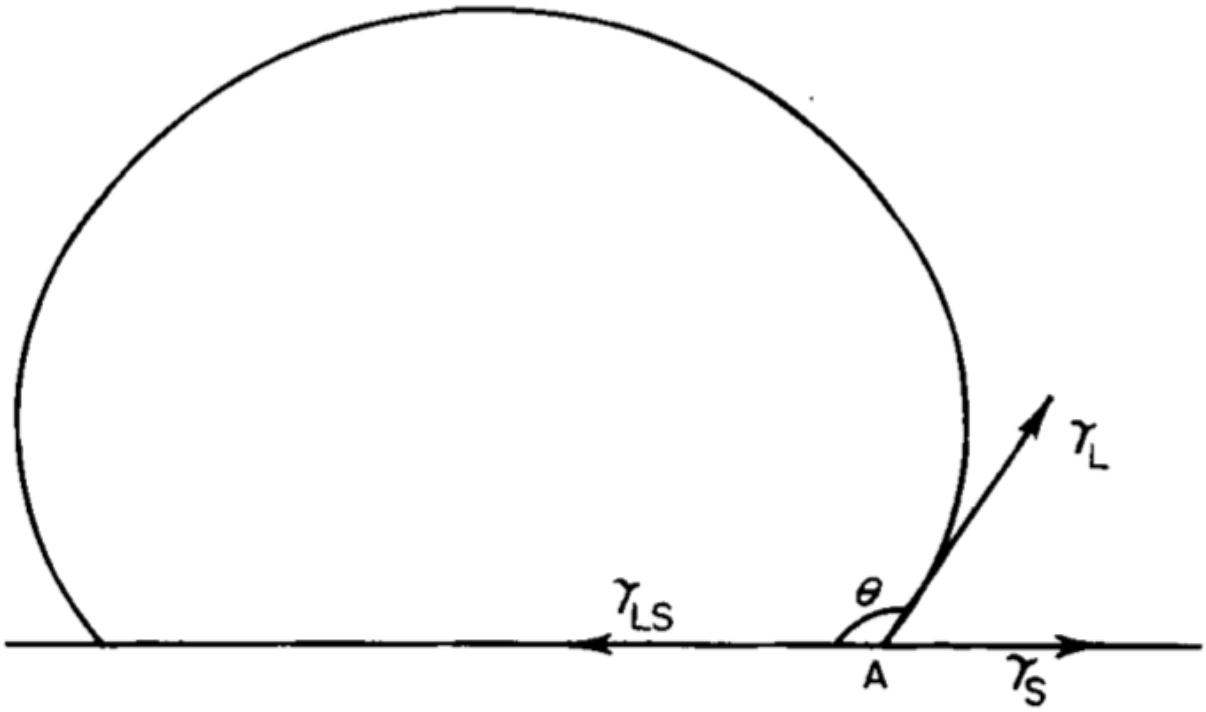

Figure 2.21: Sessile drop experiment to measure liquid metal-solid oxide contact angle [149].

feasibility at producing ODS alloys with finescale precipitation conducive to improved mechanical properties and radiation tolerance. Some researchers have examined if the use of an O-rich build chamber during AM can allow for production of ODS alloys without MA. However, there is a lack of literature examining how changes in AM operating parameters and conditions influence the potential to produce ODS alloys under a reactive gas environment. Further, much of the existing literature uses an off-the-shelf alloy system with added oxide forming elements to produce their ODS alloys. A comparison on how changes in alloy composition can influence characteristics of ODS alloy parts produced under a reactive gas environment has yet been performed.

This work focuses on demonstrating the feasibility of producing ODS alloys using DED AM methods while avoiding MA. This will be achieved by demonstrating that dispersoid number densities achievable using DED AM with a reactive gas environment approach those produced via conventional powder metallurgy methods. This requires developing an understanding for how DED AM operating parameters influence O dissolution and retention and the formation of deleterious oxide inclusions. Further, the influence of different alloying additions on deleterious oxide inclusion formation and precipitation will be evaluated. Formation of oxide inclusions wastes substantial amounts of oxide forming material better used to form nanoscale precipitates that would improve material properties instead of worsening them. Chapter 3 describes what methods and techniques were used in this work to examine how DED AM operating parameters and alloying additions influence production of ODS alloys without MA. Chapters 4 and 5 discuss the results from varying operating parameters and alloy composition,

respectively. Finally, chapter 6 presents the conclusions derived from this study and suggests future work.

CHAPTER THREE
MATERIALS AND METHODS

3.1. Characterization Methods

3.1.1. Inductively Coupled Plasma-Optical Emission Spectrometry (ICP-OES) and Inert Gas Fusion (IGF)

Inductively Coupled Plasma-Optical Emission Spectrometry (ICP-OES) and Inert Gas Fusion (IGF) were used to determine the bulk compositions of the as-received powders, as-built specimens, and substrates used for these experiments. Accurately determining these compositions was crucial to examining how varied additive manufacturing conditions influenced oxygen dissolution and retention as well as any changes in minor alloying element concentrations. ICP-OES works by grinding solid material and dissolving said material in some acid, typically nitric acid. This solution is then diluted to match some calibration standard before being ran through an ICP-OES system. In an ICP-OES system, a liquid solution is sprayed as an aerosol into contact with an argon plasma where electrons of elements in an aerosol solution can be excited. As these electrons de-excite, photons are released with a distinct wavelength correlating to specific elements and an intensity that correlates to an element concentration. These wavelengths and intensities are measured, compared to standards, and a sample composition is determined [150].

IGF takes piece of a specimen and melts it in a graphite crucible under He gas. C from the crucible and within a specimen reacts with specimen O forming CO or CO_2. This CO and CO_2 is captured in a carrier He gas stream and transported to a non-dispersive infrared (NDIR) cell. NDIR cells measure the absorption of infrared radiation by CO and CO_2 in a gas mixture and compare those to a reference gas of pure He. This comparison

allows for an oxygen concentration to be determined [151]. Dirats Laboratories performed compositional analysis using ICP-OES with IGF on all specimens in this work.

3.1.2. Optical Microscopy

Optical microscopy was used to examine overall specimen build quality. Each specimen was sectioned and polished using conventional metallography techniques. A Leica DM4000M optical microscope was used to capture optical mosaic micrographs of specimen cross-sections. FIJI was then used to determine specimen defect density (percentage of negative space, e.g. pores, cracks, inclusions, etc.) within a sample as described by Hallberg [152, 153]. This measurement also functions as a converse of part density as typically measured by Archimedes' method.

A similar method was used to examine how alloying additions influenced oxide agglomerate sizes. Scripts were written in Jython (a FIJI/ImageJ specific application of the Python language) and Python to systematically step through non-edge optical micrographs, count their oxide agglomerates, measure oxide agglomerate areas, and calculate oxide agglomerate equivalent diameters (as determined using equation 3.1).

$$D = \sqrt{w * h} \tag{3.1}$$

where D is the equivalent diameter of an agglomerate in microns, w is the width of a rectangular box bounding an irregularly shaped agglomerate in microns, and h is the height of a rectangular box bounding an irregularly shaped agglomerate in microns. To aid in filtering out non-oxide agglomerates and non-agglomerates, a raw threshold of 25 to 60 (unitless), an area range of $7x10^{-5}$ to 0.05 mm^2, and a circularity range of 0.06 to 0.8 were applied. Further, features with roundness values greater than 0.9 and aspect ratios greater than 8.0 were filtered out of the data sets. These filters were determined by

analyzing five optical micrographs from each specimen manually and determining what above parameters provided sufficient filtering out of cracks, pores, lack of fusion defects, and non-oxide agglomerates without excluding large numbers of oxide agglomerates. Features outside the raw threshold did not match the correct color of oxide agglomerates. Features smaller than $7x10^{-5}$ mm^2 were assumed to be noise. Features larger than 0.05 mm^2 tended to be lack of fusion defects. Features below the circularity range and above the aspect ratio threshold were primarily cracks. Features above the circularity range or roundness threshold were considered pores.

3.1.3. Microhardness

Microhardness measurements were taken on as-built and select post-build heat treated (HT) specimens using a Wilson® Hardness TUKON™ 1102 tester. No less than 18 measurements per specimen were taken using 300g of force and a hold time of 10 seconds using a diamond pyramid Vicker's microhardness indenter. Microhardness measurements were also performed on as-received powder as a reference. As-received powders were cold mounted in conductive epoxy and polished to a one-micron diamond solution finish to create a flat and smooth surface prior to indentation. Special care was taken to ensure that indents were performed on powder particles sufficiently large enough to contain each indent. Typical indent depth for powder particles was between eight and nine microns while average particle diameter was 65 microns. The microhardness data was compared to a reference alloy produced by vacuum induction melting, HT'd at 1150 °C for 1 h, hot rolled at 800 °C, and annealed at 1000 °C for 1 h [154].

3.1.4. Electron Microscopy

3.1.4.1. Scanning Electron Microscopy

Scanning electron microscopy (SEM) was used to examine the microstructure of these AM specimens. Either a Hitachi S4800 or a Zeiss EVO or a JEOL 6500 or a ThermoFisher Scientific Helios 5 Hydra DualBeam was used. All SEMs were equipped with energy dispersive x-ray spectroscopy (EDS) detectors; the latter three SEMs were equipped with electron backscatter detection (EBSD) detectors-SEM also. EDS systems allowed for local composition gradients to be examined as well as identification of large secondary phases. This works by incident electrons from an electron microscope scattering inelastically off an inner-shell electron of a given atom. As that inner-shell electron returns to its initial state, a characteristic x-ray is released indicative of an elemental species involved in an interaction [155]. EBSD uses high-energy electrons that backscatter from roughly 20 nm deep in a specimen to determine a crystal lattice's orientation with respect to a specimen surface [156]. This technique allows a user to gather information on specimen grain size, specimen texture, and possible cracking mechanisms.

3.1.4.2. Focused Ion Beam

A focused ion beam (FIB) was used to prepare specimens for characterization using scanning transmission electron microscopy (STEM) and atom probe tomography (APT). One of a Zeiss Auriga Crossbeam FIB/SEM, a ThermoFischer Scientific Helios 5 Hydra DualBeam plasma FIB (pFIB), or an FEI Nova 200 Dual Beam FIB operated by James Burns at Oak Ridge National Laboratory's Center for Nanophase Materials Science (ORNL CNMS) was used for these preparation steps. These machines were used to cut

small micron-sized sections from specimens and thin them down to either electron transparency (STEM) or to a fine needlepoint (APT). Conventional FIB techniques for sample preparation were used [157]. Samples were quickly placed under and maintained under vacuum after FIB preparation and prior to TEM characterization. Special effort was also taken to minimize time between FIB preparation and TEM characterization to minimize potential surface oxide formation.

3.1.4.3. Scanning Transmission Electron Microscopy

Scanning transmission electron microscopy was used to probe specimen microstructure on a sub-micron scale looking for nanoscale precipitation. A Zeiss Libra 200 STEM equipped with a mono-chromated EELS system, a JEOL NeoARM aberration-corrected STEM equipped with EDS detectors (operated by Raymond Unocic or Matthew Boebinger also at ORNL CNMS, and a Thermofisher Scientific monochromated and aberration corrected Spectra 300 TEM/STEM equipped with EDS and electron energy loss spectroscopy (EELS) detector systems were used for high-resolution STEM imaging, EDS mapping, and EELS characterization. All STEM characterization was performed at 200 keV for these experiments. EDS mapping as done with an SEM was used to examine compositions of sub-micron microstructural features like precipitates and grain boundaries. EELS analysis measures a change in electron energy as it passes through a thinned specimen and correlates resulting characteristic peaks to determine what elements an electron interacted with. EELS analysis was also used to determine how thick STEM lamellae were. This process uses a ratio of incident electron beam energy and post-specimen electron beam energy measured by an EELS detector combined with Z-effective

(a weighted measure of a material's atomic number) to approximate sample thickness [158].

3.1.5. Atom Probe Tomography

APT is a technique that takes sharp, nanoscale needles of specimens fabricated using a FIB and applies a high positive voltage at low temperatures to induce a high electric field at a needle tip. For these specimens, a high frequency laser was also focused on the needle tip. This causes atoms at a needle tip to be ionized and "evaporate" from a needle. In this high electric field, ions are then accelerated towards a time-of-flight detector that allows for the relative mass-to-charge ratios, detector location, and time-of-flight to be used to reconstruct a needle tip. These tip reconstructions allow for atomistic characterization of small specimen volumes to aid in identifying nanoscale precipitation and segregation along interfaces in addition to providing a three-dimensional representation of a material on the atomistic scale [159]. A Cameca LEAP 4000XHR was used to collect APT data on specimens in this work that were then reconstructed using IVAS reconstruction software. For more in-depth discussion on the intricacies of APT, please refer to *Atom Probe Tomography* by Baptiste Gault.

3.2. Experimental Design

3.2.1. Influence of Operating Parameters on *In Situ* Oxidation

For the first set of experiments, a DMD103D DED AM system (originally built by POM, now DM3D Technology) with a pneumatically conveyed powder system and a 1kW, 910 nm wavelength diode laser was used. Gas atomized Fe-12Cr-6Al-2Mo-0.18Y (wt%) metal alloy powder provided by ATI Powder Metals with an average powder size of 65 μm,

and unaltered powder O content (not altered in any way from the manufacturer's normal product levels, ~ 0.01wt%) was used.

As-received powder was consolidated under two different oxygen-rich environments to produce 20 mm by 20 mm by 20 to 30 mm rectangular prism specimens. The two experimental setups utilized different O sources to examine how different methods of providing O influenced O dissolution and retention. Variations in laser power, tool speed, available O concentration, build plate preheat temperature, and laser raster type (continuous raster and pulsed laser raster) were also examined for their influence on O retention and overall build quality. For these experiments, a powder flow rate of 5 grams per minute, total welding gas flow rate of 44 liters per minute, laser standoff distance of 12 mm, and laser spot diameter of 1.2 mm were maintained. A-36 steel plate served as the build substrate.

For the first experimental setup (**Figure 3.1a**; specimens 1-4), powder was consolidated under an oxygen-rich build atmosphere with a completely inert welding gas stream. The build chamber was continuously backfilled with air to maintain a 16 at% O concentration with the balance being a mixture of N, Ar, and He (at ~ 64%, 19.1%, and 0.9%, respectively). An Ar – 4.5% He welding gas mixture was used. This experimental setup was tested the effects of laser power and raster method (continuous raster or pulsed laser raster). For a pulsed laser raster, after irradiating an area for a desired pulse time, a laser is shuttered. A shuttered laser moves at a desired movement speed to the next position in a raster pattern. A shutter is then opened for a programmed dwell time before closing again and repeating the process for the remainder of a programmed raster pattern. A summary of the remaining varied operating conditions can be found in **Table 3.1**.

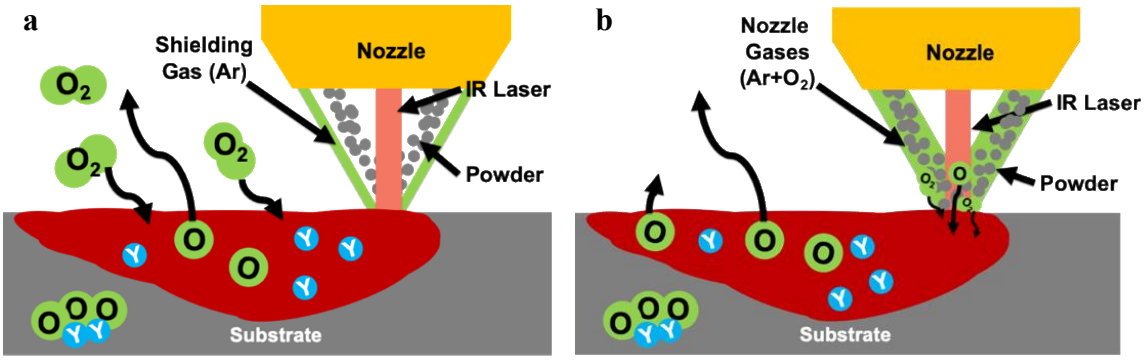

Figure 3.1: Schematic of DED AM process using *in situ* oxidation: a. consolidation under air, b. under Ar with Ar-O_2 blended gas stream.

Table 3.1: Sample processing parameters (atm = atmosphere, wg = welding gas, C = continuous raster pattern, P = pulsed raster pattern, * = HT'd specimen); * indicates specimen underwent a post-build heat treatment of 1 hr at 600 °C.

Specimen	Laser Power (W)	Oxygen Source (atm/wg)	Raster Type (C/P)	Pulse Dwell Time (s)	Raster Speed ($mm*min^{-1}$)	Available O_2 (at%)	Pre-heat Temp. (°C)
1	350	atm	P	0.1	720	16	20
2	350	atm	C	-	720	16	20
3	400	atm	P	0.08	720	16	20
4	400	atm	C	-	720	16	20
5	400	wg	C	-	720	0.1	20
6 *	500	wg	C	-	720	0.1	20
7 *	650	wg	C	-	720	0.1	20
8 *	500	wg	C	-	600	0.1	20
9	500	wg	C	-	720	0.5	20
10	500	wg	C	-	720	0.1	350

For the second experimental setup (**Figure 3.1b**; specimens 5-10), the build chamber was kept under an inert Ar atmosphere with a slight overpressure to inhibit ingress of ambient air. A welding gas mixture enriched in O to either 0.5 at% or 1 at% O_2 with a balance of Ar and He (93.3 at% and 5.7 at%, respectively for 1 at% O_2 specimens) was used. These specimens focused on further examining how varying laser power, tool speed, amount of available O, and continuous pre-heat conditions influenced O retention and build quality. Detailed operating parameters are also included in **Table 3.1**. **Figure 3.1a** shows the first experimental setup utilizing an oxygen-rich atmosphere. Metal powder was pneumatically conveyed through a nozzle and into a melt pool using an Ar-He gas mixture. A cone of Ar (denoted shield gas) surrounded the powder stream (like conventional welding systems). The build chamber was backfilled with ambient air to provide an O source for a melt pool. **Figure 3.1b** demonstrates the second experimental setup utilizing an oxygen-rich welding gas. Powder is instead pneumatically conveyed into a melt pool by an oxygen-rich gas stream providing melt pool/oxygen interaction at the hottest point. A cone of Ar gas still surrounded the powder stream (left out for clarity). The build chamber was backfilled with facility Ar. The laser and powder/gas stream were coaxially aligned for all experiments.

Select specimens (denoted by * in **Table 3.1**) showing the most promise for acceptable build quality and/or appreciable oxygen retention underwent a post-build heat treatment (HT) of 1 hour at 600 °C as suggested by Massey et al. [37] to promote additional dispersoid formation and examine if the AM process was sufficient for complete oxide precipitation.

3.2.2. Influence of Alloying on Agglomeration and Precipitation

For the last set of experiments, a focus was placed on examining how alloying changes influence oxide agglomeration and nanoscale precipitation of ODS FeCrAl produced using AM. The literature describes the formation of these large inclusions to be a result of poor oxide wettability, a low comparative density between an oxide and liquid steel, and collision of existing oxides within a melt pool [50, 60-62, 81, 82, 143, 145]. High interfacial energy between an oxide phase and liquid steel drops the wettability such that oxides in a melt pool are effectively repelled by the solidification front of liquid steel [144]. This combined with low relative density of most common Y-based oxides used in oxide dispersion strengthened (ODS) materials (shown in **Table 3.2**) makes them difficult to capture by the solidification front increasing the potential to grow from enhanced liquid-state diffusion or oxide collision as they are moved about by melt pool convection currents.

Changes in alloy composition provide a possible means to improve oxide wettability in liquid Fe or steel. Small additions of Si, Ti, and O have been shown in the literature to reduce the contact angle between Fe or steel and various oxide surfaces during simulations or sessile drop method tests, which corresponds to a decrease in interfacial energy [60, 61, 143, 148, 149, 160, 161]. Work by Verhiest et al., tested how additions of Cr and Si to Fe affected wettability of Al_2O_3 and Y_2O_3 at 1575 °C under vacuum and Ar atmospheres. They found that Fe with Cr content ranging from 9 wt% to 20 wt% fully wetted Al_2O_3. Any combination of Fe with Cr content ranging from 0 wt% to 20 wt% failed to wet Y_2O_3, and, in general, increases in Cr content increased the measured contact angle of FeCr on Y_2O_3. However, adding Si (up to 0.5 wt%) to Fe-9Cr reduced the

Table 3.2: Densities of common related oxides compared with liquid iron.

Phase	Density (kg/m^3)
Y_2O_3	5030
$YAlO_3$ (YAP)	5350
$Y_4Al_2O_9$ (YAG)	4510
$Y_3Al_5O_{12}$ (YAM)	4550
Y_2TiO_5	4750
$Y_2Ti_2O_7$	4930
$Y_2Hf_2O_7$	7640
$Y_2Zr_2O_7$	5500
Al_2O_3	4000
Liquid Iron	7800

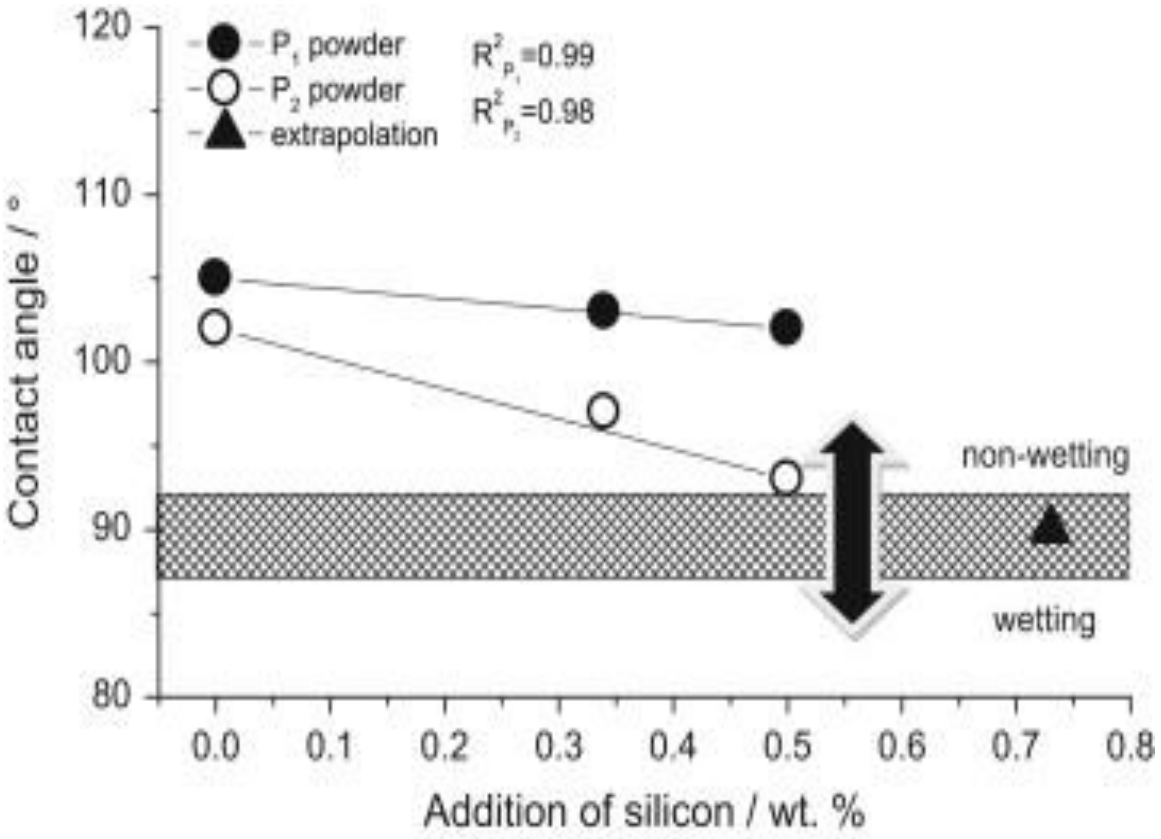

Figure 3.2: Effect of Si additions on the contact angle (wettability) of Fe-9wt%Cr on a Y_2O_3 substrate [61].

measured contact angle (**Figure 3.2**). Their work suggested that a concentration of Si greater than 0.7 wt% would be sufficient to achieve wetting of Y_2O_3 [61]. Work by Kingery on interfacial energy measurements of FeSi alloys on Al_2O_3 at 1550 ºC also showed that an increase in Si reduced the contact angle. Kingery's results suggest much higher Si contents may be required for complete wetting as they showed that Fe-9Si was unable to completely wet Al_2O_3 [148].

Work by Madzivhandila et al., examined how additions of Ti would influence the interfacial energy of a white cast iron (Fe-25Cr-2C-1Mn-0.3Si-.2Ni-0.06Mo-0.01S-0.04P) on an Al_2O_3 substrate. Sessile drop experiments were ran under an Ar atmosphere up to 1531 ºC with Ti concentrations of 0 wt%, 0.1 wt%, 0.7 wt%, and 1.5 wt%. Contact angle measurements were taken every ten minutes between droplet temperatures of 1440 ºC and 1340 ºC. **Figure 3.3a** shows that increased Ti contents resulted in decreased contact angles, and that increased temperatures increased contact angles. A Ti concentration greater than or equal to 0.7 wt% was required to achieve wettability at 1400 ºC. An addition of 1.5 wt% Ti provided complete wettability across all observed temperatures (**Figure 3.3b**) [60]. Work by Humenik and Kingery supports these results where an addition of 0.4 wt% Ti to electrolytic Fe dramatically reduced the contact angle on Al_2O_3 [149].

Work originally by Nogi and Ogino examined how additions of O, S, Se, and Te would influence deoxidation of molten Fe. Their results (**Figure 3.4a**) show that modest increases in O content can appreciably reduce the contact angle of molten Fe on Al_2O_3 at 1600 ºC [160]. Takuichi et al., performed an analogous study on the interfacial energy of liquid iron on alumina where both O concentration and temperature were examined

a

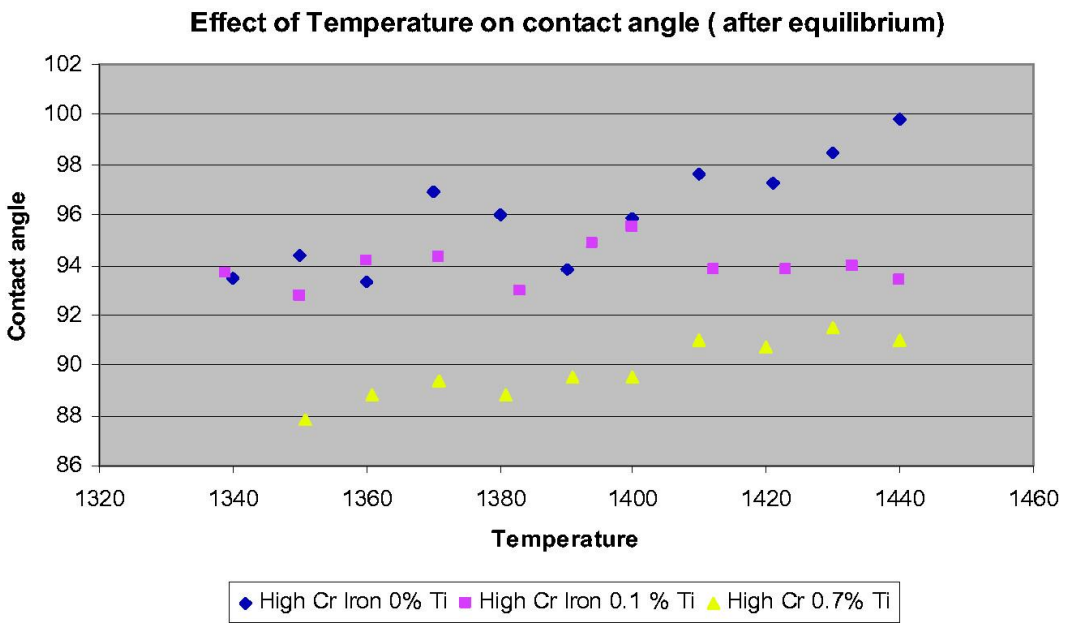

b

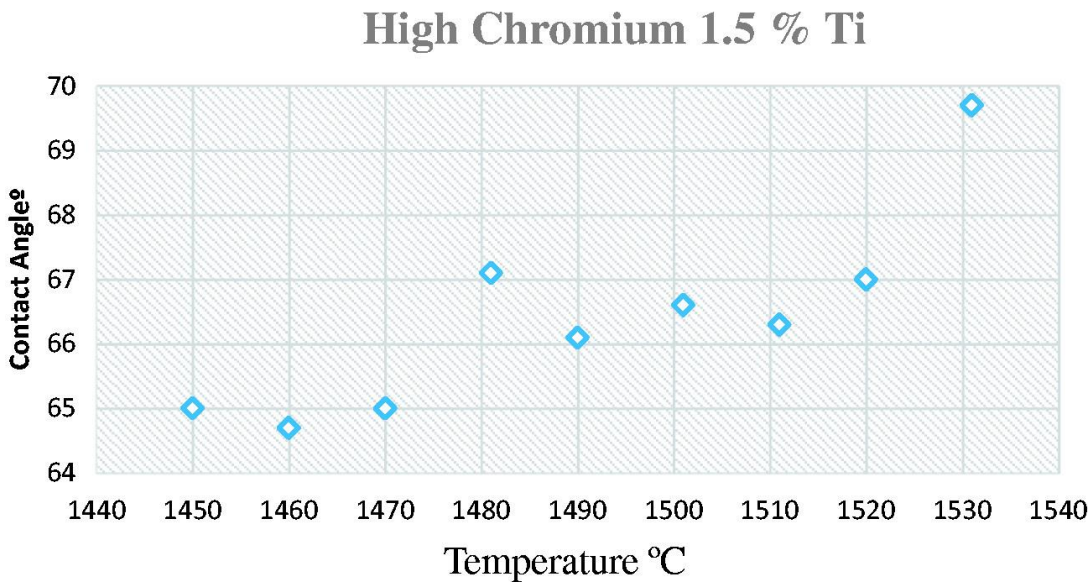

Figure 3.3: Effects of Ti additions (a. 0 wt% Ti to 0.7 wt% Ti; b. 1.5 wt% Ti) and temperature on the contact angle (wettability) of 25wt%Cr white cast iron on a Al_2O_3 substrate [60].

a

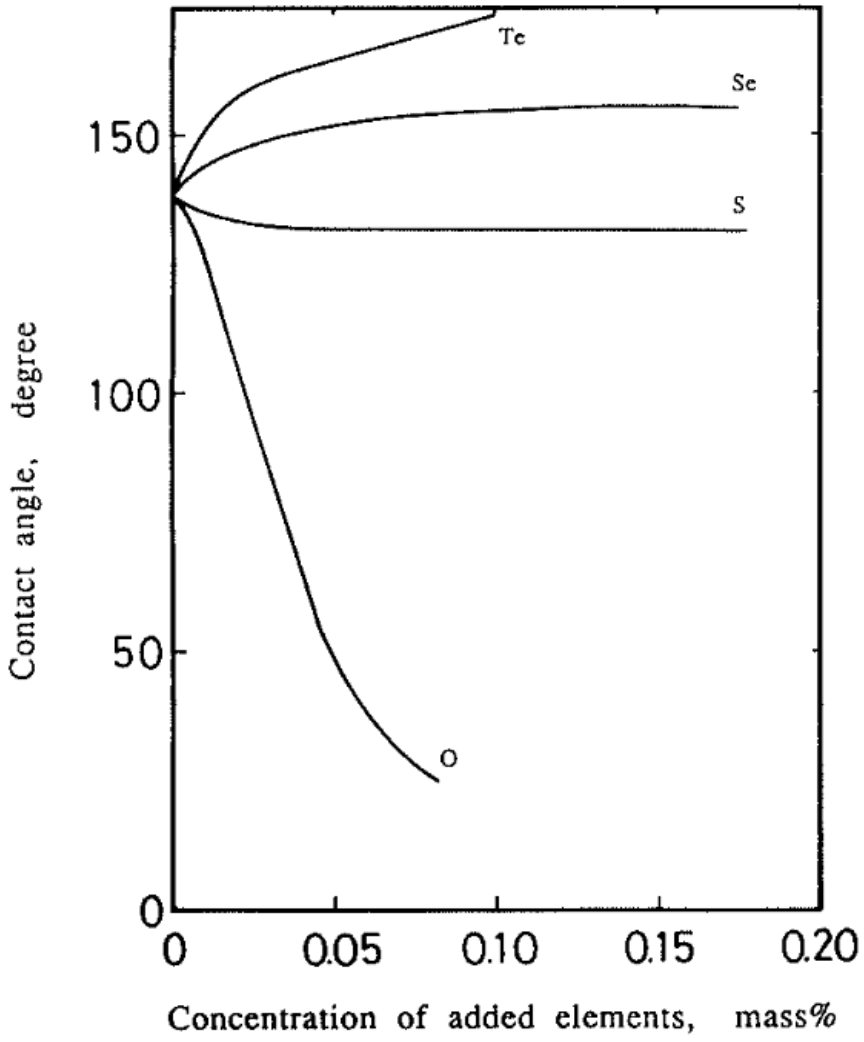

Figure 3.4: Effect of O content and temperature on the interfacial energy of liquid Fe on Al_2O_3. a) comparison of influence of O, S, Se, and Te content on contact angle. b) Changes in O content and temperature affect contact angle. Filled shapes are tested on Al_2O_3. Empty shapes are tested on ZrO_2 [160, 162].

b

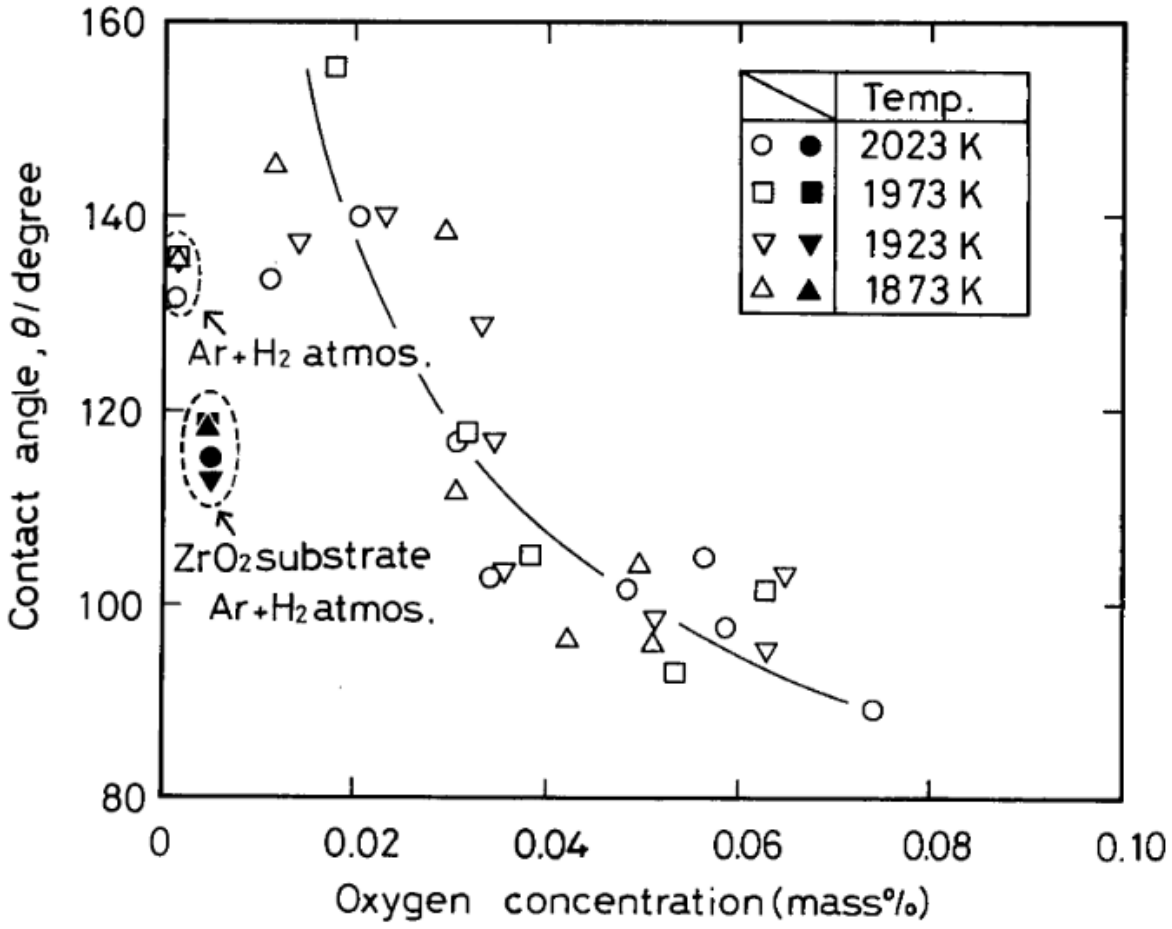

Figure 3.4 continued [161].

(**Figure 3.4b**). Their results agree that small increases in O concentration can have an appreciable effect on reducing contact angle [161]. These and other supporting results were later summarized by Eo et al., and Nakashima and Mori supporting that increases in alloy O content reduced interfacial energy between Fe alloys and oxides [143, 162]. Improving oxide wettability through small alloy additions as shown above should improve oxide incorporation into a Fe/steel matrix and inhibit excessive agglomeration that causes large oxide inclusions. Further, additions of Ti and O have shown repeatedly throughout the literature to be advantageous for refining ODS precipitate size distributions [18, 27, 50, 163].

To examine how alloying changes affect agglomeration and precipitation in ODS FeCrAl produced by AM, three alloying changes were considered: 1) a pre-build heat treatment of FeCrAl powder in air to induce formation of an oxide shell around powder particles and increase O concentrations, 2) an addition of TiC powder to increase Ti concentrations, and 3) an addition of SiC powder to increase Si concentrations. Gas atomized Fe-12Cr-6Al--0.33Y (wt%) metal alloy powder designed for use in DED AM systems provided by Powder Alloy Corporation (PAC) was used as the base material for these experiments. TiC powder with a particle size smaller than 44 microns was provided by Atlantic Equipment Engineers (AEE). SiC powder with an average particle size of 600 nm was provided by Washington Mills (WM).

Three different pre-build heat treatment conditions were examined, 200 °C, 350 °C, and 1000 °C. For this test, quartz ampules were filled with 10 g of ATI FeCrAl powder and sealed (no backfilling). In a tube furnace, ampules were heat treated at each temperature for one hour. Post heat treatment, the flowability of powder was observed. It

was found that powder heat treated at 1000 °C partially sintered during heat treatment and flowability was greatly reduced. Powder heat treated at 200 °C and 350 °C maintained their pre-heat treated flowability. To maximize oxide shell formation, a pre-build heat treatment at 350 °C was chosen.

A 27.22 kg lot of PAC FeCrAl powder was split up into six 4.54 kg batches. Half of the PAC FeCrAl powder was heat treated in 4.54 kg batches in a box furnace under air at 350 °C for one hour to form an oxide shell on the surface. Two 4.54 kg batches of PAC FeCrAl powder, one as-received and one with the pre-build heat treatment, were blended using a hand operated mixer for three minutes after adding approximately 30.5 g of AEE TiC powder. Similarly, two additional batches of PAC FeCrAl powder, as-received and heat treated, were blended with approximately 20.5 g of WM SiC powder. The amount of TiC/SiC powder added was determined by attempting to match an optimal Y:Ti atomic ratio for ODS precipitates as determined in the literature and shown in **Figure 2.13** [112]. Three minutes was chosen to achieve sufficient blending but avoid affecting powder morphology and thus flowability [164]. The above results in six different lots of powder to be consolidated: FeCrAl (base alloy), FeCrAl+HT, FeCrAl+TiC, FeCrAl+TiC+HT, FeCrAl+SiC, and FeCrAl+SiC+HT. From this point forward, these lots of powder are denoted as B1, B2, B3, B4, B5, and B6, respectively. Expected alloy compositions (not accounting for pre-build heat treatment) prior to consolidation are shown in **Table 3.3** for reference.

A BeAM Modulo 400 produced by AddUp was used to produce 21 x 21 x 25. mm sample cubes. All specimens were consolidated under the second experimental setup

Table 3.3: Varied alloying expected specimen composition (ignoring changes in oxygen content).

	Element							
Specimen	Fe	Cr	Al	Y	O	Si	C	Ti
B1/B2	81.65	12.01	5.71	0.33	0.046	0.030	0.009	-
B3/B4	81.17	11.94	5.68	0.33	0.046	0.030	0.148	0.537
B5/B6	81.35	11.97	5.69	0.33	0.046	0.349	0.148	-

shown in **Figure 3.1b** with a O-rich welding gas used. One difference was that an O-rich atmosphere was used in addition to an O-rich welding gas for all specimens due to machine limitations preventing an O-rich welding gas from being used with an inert build chamber atmosphere.

Operating parameters for all specimens are included in **Table 3.4**. The chosen laser power and tool speed for these experiments were determined using the results from the first set of experiments shown in **Section 4.2.2**. To develop these operating parameters, a Python script was built to cycle through all combinations of laser power (350 W to 550 W) and tool speed (1300 mm/min to 2200 mm/min) based on recommended operating ranges for steel alloys provided by the BeAM system operator. A heatmap of the simulation results is shown in **Figure 3.5**. A laser power of 350 W and a tool speed of 1300 mm/min were chosen to maximize a parameter called gas incidence fraction that correlated well with increased oxygen dissolution and retention as demonstrated in the results of the first set of experiments. The remaining operating parameters were chosen based on machine limits or best practice recommendations from operator experience. For these experiments, the Secondary gas stream was an Ar-10%O_2 mixture welding gas. Carrier gas and Central gas streams were facility Ar. This mixture of gas streams blended down the welding gas mixture and provided a 5 at% O_2 concentration at the melt pool surface, an increase from a 1 at% O_2 mixture used in the first set of experiments. Work performed by Horn et al. examined how different O2 concentrations influenced PBF-LB AM of ODS 14YWT, and a 5 at% O2 mixture provided the finest precipitate distribution [163]. It should be noted that after printing B3, the operator noticed soot beginning to build up on the interior of theBeAM system. Out of an

Table 3.4: Varied alloying operating parameters.

Specimen	Target Laser Power (W)	Measured Laser Power (W)	Laser Diameter (mm)	Tool Speed (mm/min)	Target Powder Flow Rate (g/min)	Measured Powder Flow Rate (g/min)	Programmed Layer Height (mm)	Hatch Spacing (mm)
B1	350	360.5	0.67	1300	7	7	0.42	0.4
B2	350	360.5	0.67	1300	7	-	0.42	0.4
B3	350	360.5	0.67	1300	7	-	0.42	0.4
B3F	350	360.5	0.67	1300	7	-	0.42	0.4
B4	350	360.5	0.67	1300	7	-	0.42	0.4
B5	350	360.5	0.67	1300	7	10	0.42	0.4
B6	350	360.5	0.67	1300	7	11.3	0.42	0.4

Specimen	Carrier Gas (L/min)	Central Gas (L/min)	Secondary Gas (L/min)	Exhaust Fan on? (Y/N)
B1	3	3	6	N
B2	3	3	6	N
B3	3	3	6	N
B3F	3	3	6	Y
B4	3	3	6	Y
B5	3	3	6	Y
B6	3	3	6	Y

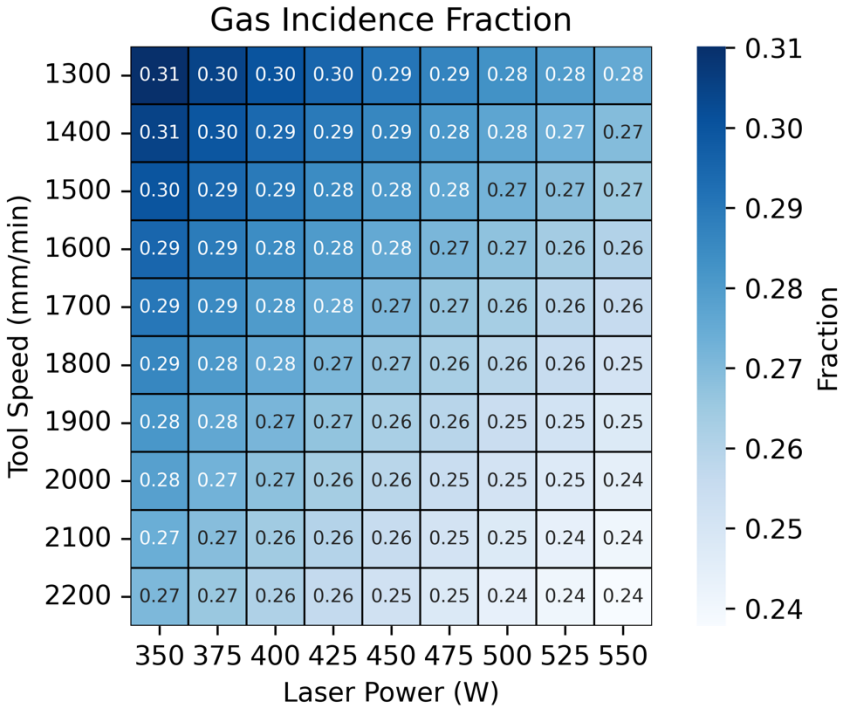

Figure 3.5: Gas incidence fraction heatmap used to determine the laser power and tool speed for the varied alloying experiments.

abundance of caution, the system interior was cleaned and B3 was reprinted with the exhaust fan turned on and noted as B3F. All further specimens were printed with the exhaust fan on. The exhaust fan pulls facility air into the build chamber and pushes system overpressure effluent through a bubbler. Post-build a portion of each specimen was heat treated at 600 °C for 1 h as performed in the first set of experiments.

CHAPTER FOUR
INFLUENCE OF OPERATING PARAMETERS ON *IN SITU* OXIDATION

4.1. Build Quality

4.1.1. Build Composition

Compositional analysis results of the as-received powder, all as-built specimens from this study, a steel substrate, a literature reference for an oxide dispersion strengthened (ODS) alloy produced using gas atomization reaction synthesis (GARS) powder, and a literature reference for an ODS FeCrAl alloy produced using mechanical alloying (MA) are provided in **Table 4.1** [38, 136]. As shown, minimal change occurred in across major alloying elements (Fe, Cr, Al, Mo) regardless of the operating parameters used. The amount of Y retained tended to decrease with increasing laser power. A literature review suggests that this could be a result of Y agglomeration or Y-oxide agglomeration in a melt pool during consolidation forming a slag that floats on a melt pool surface [62]. Marangoni convection combined with a lower density than the surrounding liquid Fe keeps these agglomerates on the surface [62, 81, 135, 146]. Poor wettability of oxides in liquid iron inhibits incorporation of these agglomerates furthering the issue [61, 143]. It is possible, though unlikely, that some Y vaporized during additive manufacturing (AM) resulting in a loss of Y [165]. Increasing laser power or a pre-heat temperature resulted in an increased melt pool lifetime and likely exacerbated these issues. Minimal uptake of C or N occurred suggesting a well-controlled build environment. Specimen 8 (500W, continuously rastered laser, welding gas oxygen source, 600 mm/min raster speed) retained the most O during production with a

Table 4.1: ICP-OES/IGF compositional analysis for varied operating parameters experiment (MA = mechanical alloying, GARS = gas atomization reaction synthesis).

	Species (wt%)											
Sample	Fe	Cr	Al	Mo	Y	Zr	W	Ti	C	O	N	P
As-Rec. Powder	79.57	12.14	6.09	2	0.18	-	-	-	0.003	0.0107	0.0004	-
1	79.56	12.04	6.16	2.03	0.17	-	-	-	0.004	0.0132	0.001	-
2	79.55	12.04	6.18	2.02	0.18	-	-	-	0.003	0.0079	0.0013	-
3	79.47	12.05	6.2	2.04	0.18	-	-	-	0.006	0.0267	0.0015	0.01
4	79.59	12.02	6.18	2.02	0.15	-	-	-	0.006	0.0064	0.001	0.01
5	79.78	12.05	6.01	2.01	0.11	-	-	-	0.004	0.0075	0.0003	0.01
6	79.72	11.99	6.04	2.03	0.14	-	-	-	0.015	0.0394	0.0003	< 0.01
7	79.79	11.99	6.02	2.03	0.12	-	-	-	0.003	0.0284	0.0002	< 0.01
8	79.65	12.05	6.06	2.01	0.13	-	-	-	0.006	0.067	0.0004	< 0.01
9	79.78	11.95	6.05	2.04	0.13	-	-	-	0.003	0.0254	0.0003	< 0.01
10	79.78	12.01	6.02	2.02	0.11	-	-	-	0.003	0.021	0.0004	0.007
MA [38]	83	10	6	-	0.21	0.28	-	-	0.014	0.135	0.051	-
GARS [136]	82.06	14.03	-	-	0.35	-	3.06	0.4	-	0.0981	-	-
Substrate	95.66	2.24	0.03	0.89	< 0.01	-	-	-	0.12	0.0012	0.097	0.01

six-fold increase over as-received powder. O retention approached half of that achieved by leading mechanically alloyed experimental ODS alloys while not using mechanical alloying demonstrating the promising potential of *in situ* oxidation as a production method for ODS materials [38].

4.1.2. Defect Density and Cracking

A continuous laser raster type resulted in the lowest porosity and cracking in as-built parts. Optical micrographs of Specimens 1/3 and Specimens 2/4 in **Figure 4.1** demonstrate an improvement in part quality comparing a pulsed laser raster vs. a continuous laser raster pattern, respectively. Overall relative build quality of all specimens is compared using defect density in **Figure 4.2**. Defect density was quantified as a percentage of negative space (pores, cracks, inclusions, etc.) within a sample determined using ImageJ or FIJI to analyze optical micrographs as described by Hallberg [152]. Specimen 8, the specimen with lowest defect density, is highlighted in green. Pulsed laser raster specimens exhibited the highest defect densities (1 and 3) due to their lack of fusion defects. Specimen 7 also showed a significant defect density comparable to its experimental setup counterparts (specimens 5-10), believed to be a result of some powder flowability issues while building.

More detailed characterization of the cracking phenomena present in as-built Specimen 8 is shown in **Figure 4.3**. Inverse pole figure (IPF) images show the presence of a few transgranular and intergranular cracks present even in the specimen with the lowest defect density (0.69%). Historical work examining the weldability of this and similar FeCrAl alloy systems suggested that this alloy contained an acceptable mixture

1.

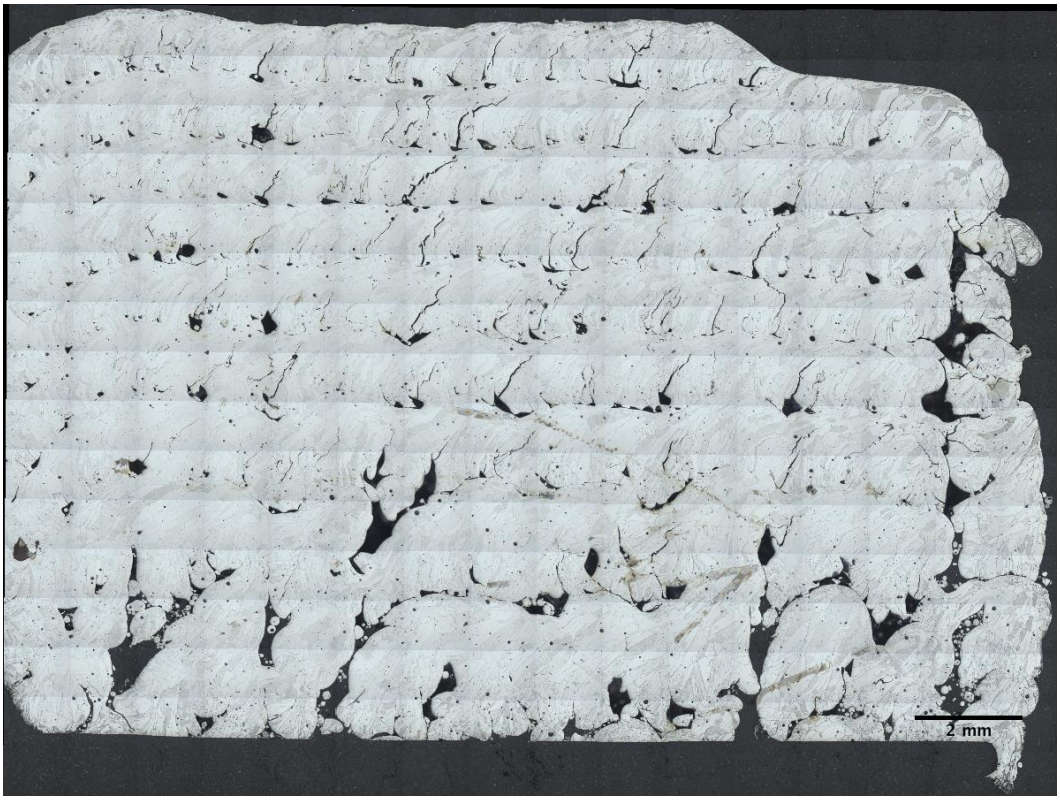

Figure 4.1: Optical mosaic micrographs of the as-built specimens (1 to 10; top to bottom) created in the preliminary work using a reactive atmosphere or a reactive welding gas. Z direction is up on each micrograph.

2.

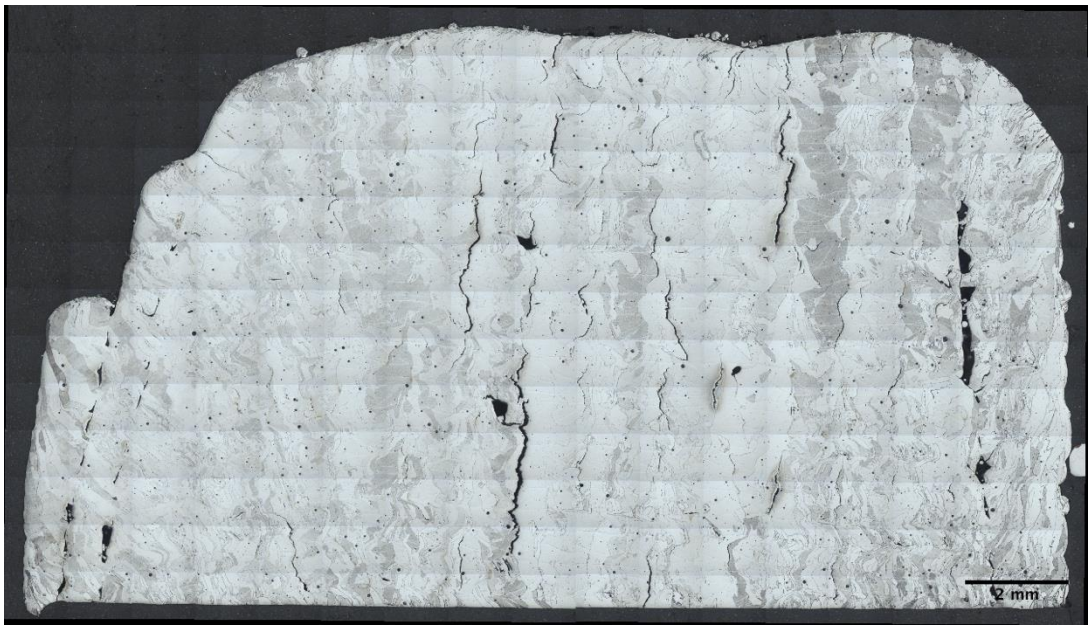

3.

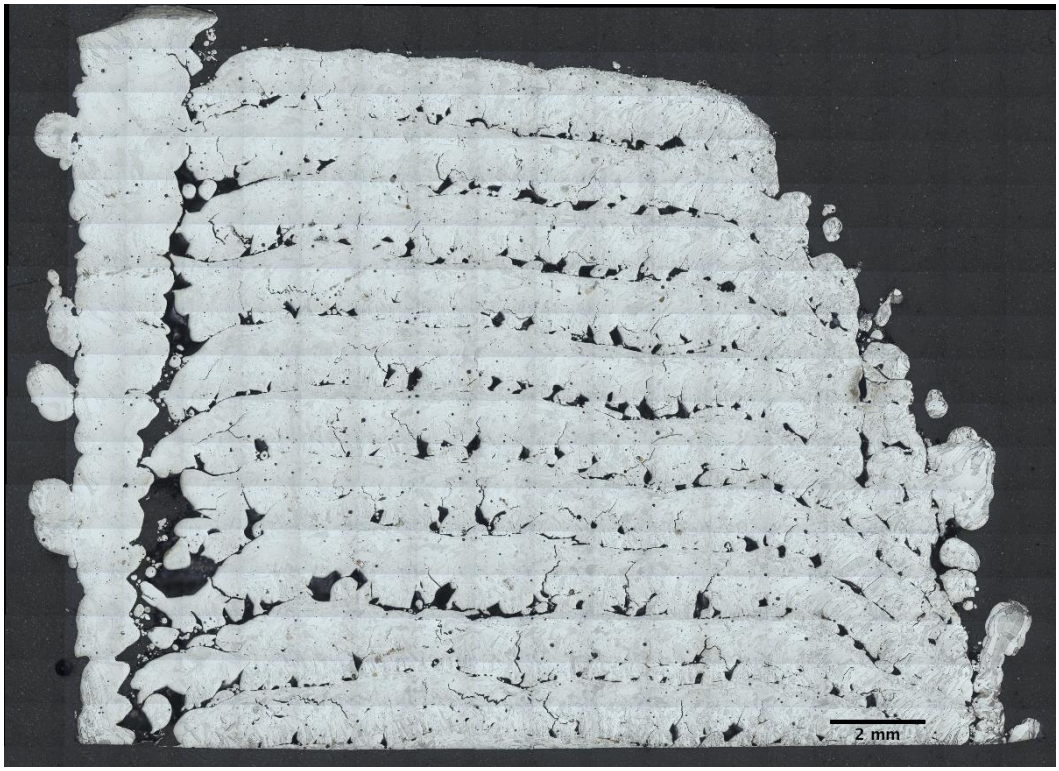

Figure 4.1 continued

4.

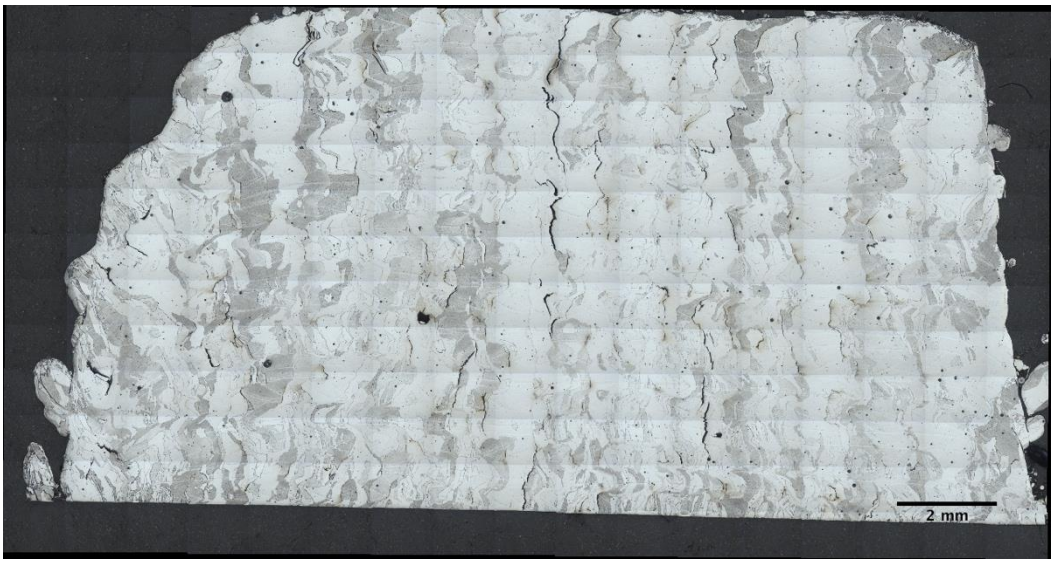

5.

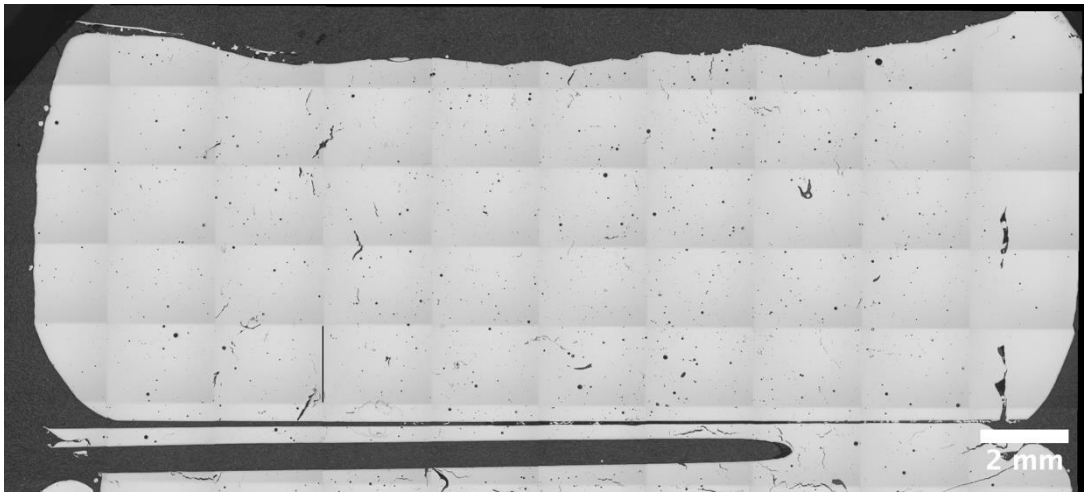

Figure 4.1 continued

6.

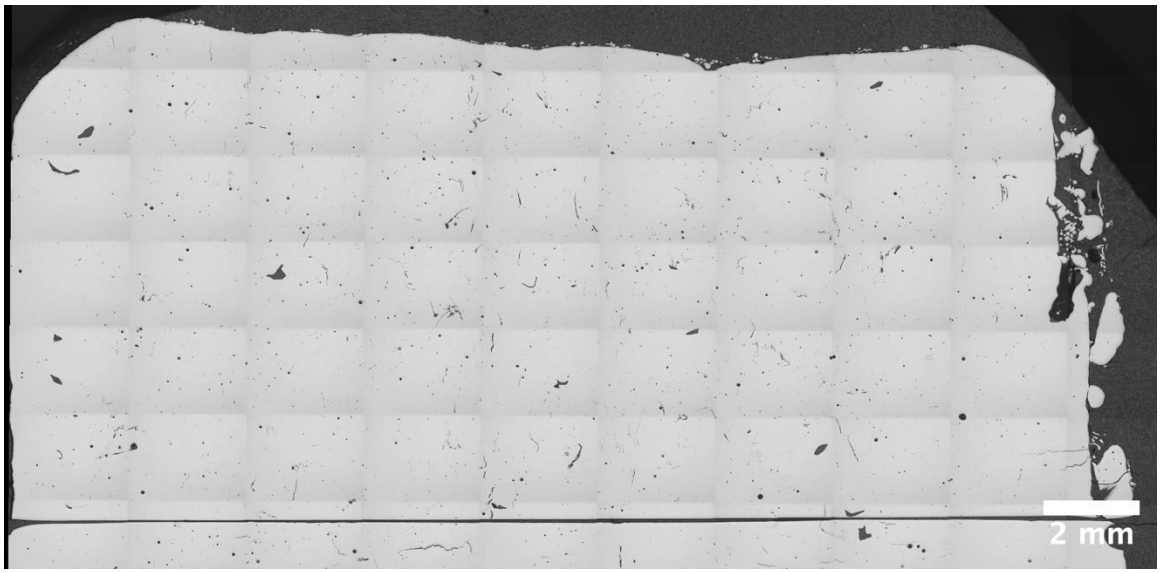

7.

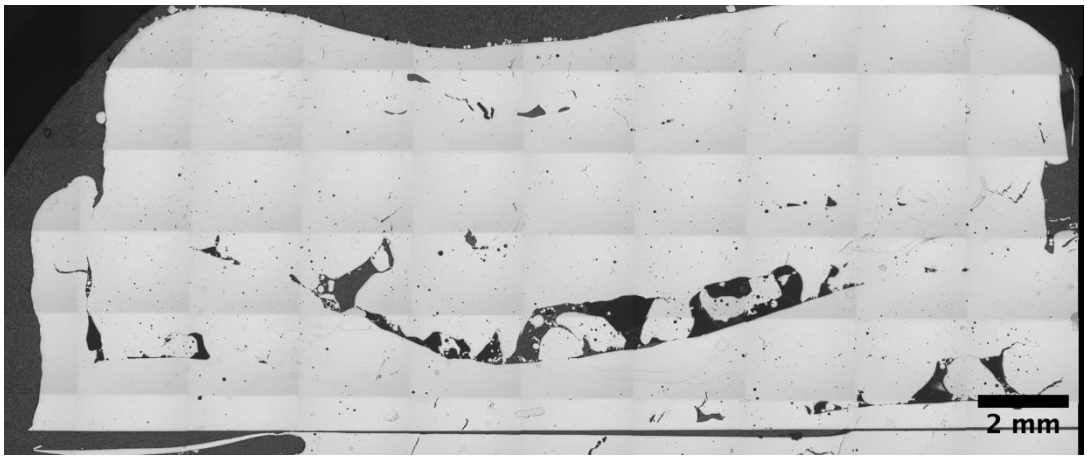

8.

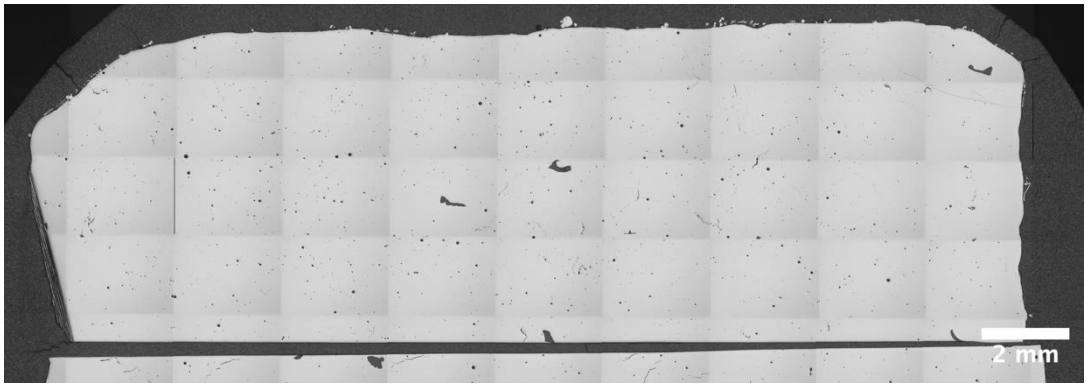

Figure 4.1 continued

9.

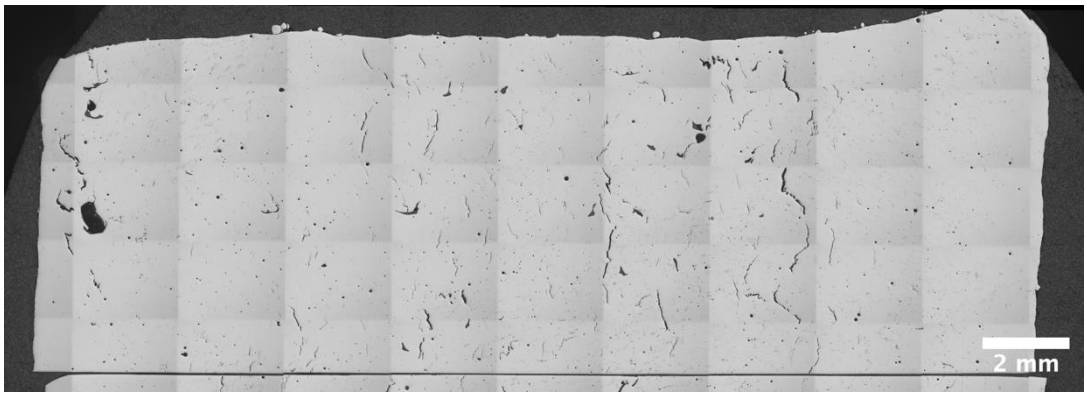

10.

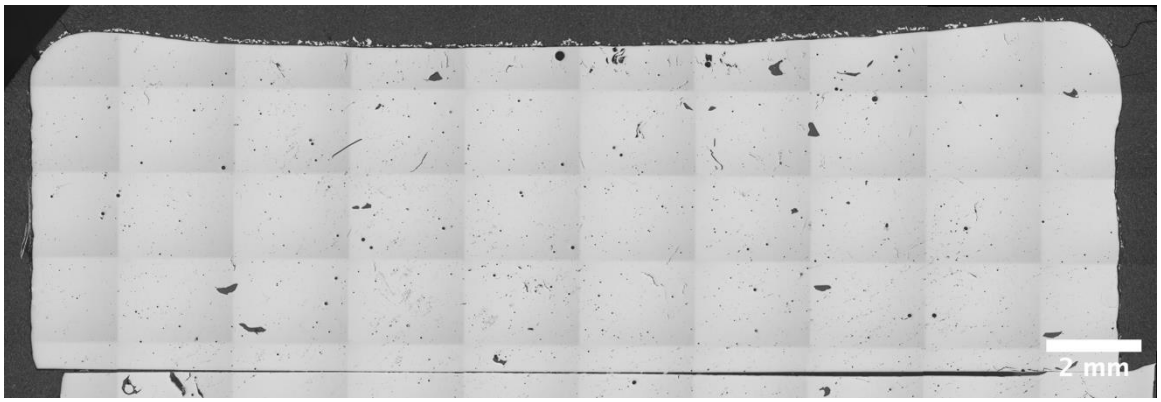

Figure 4.1 continued

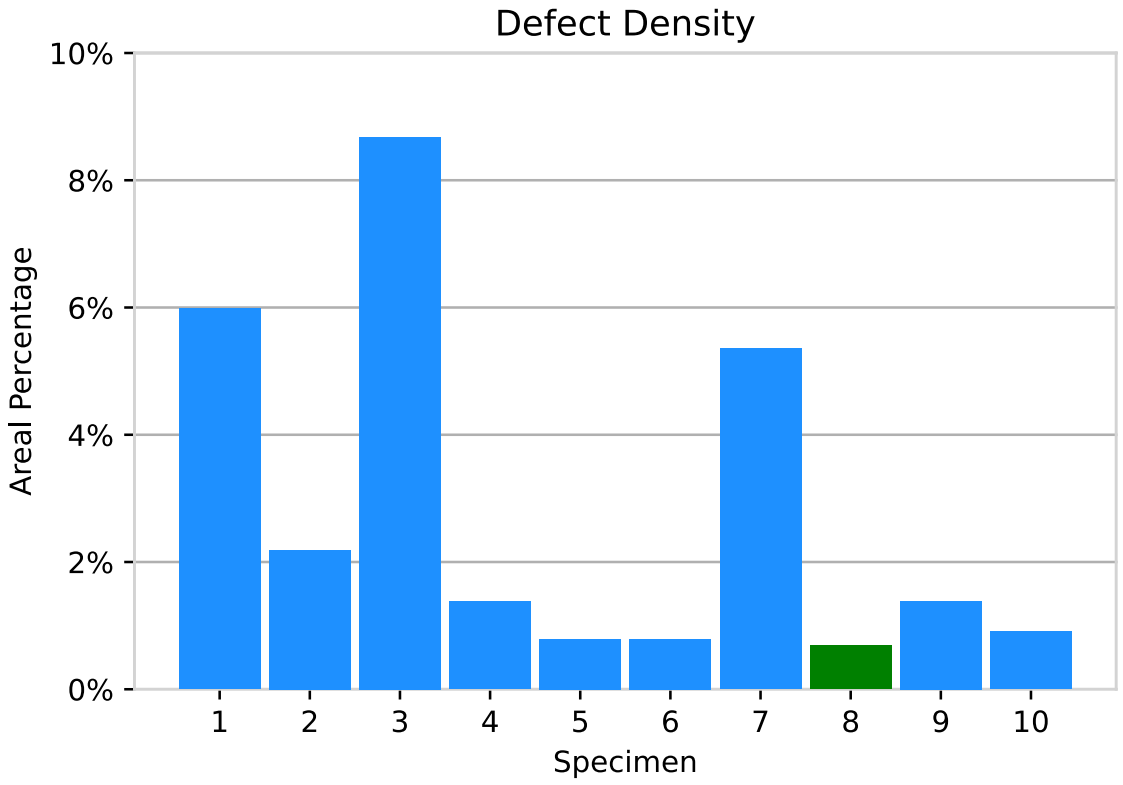

Figure 4.2: Comparison of the measured specimen as-built defect density.

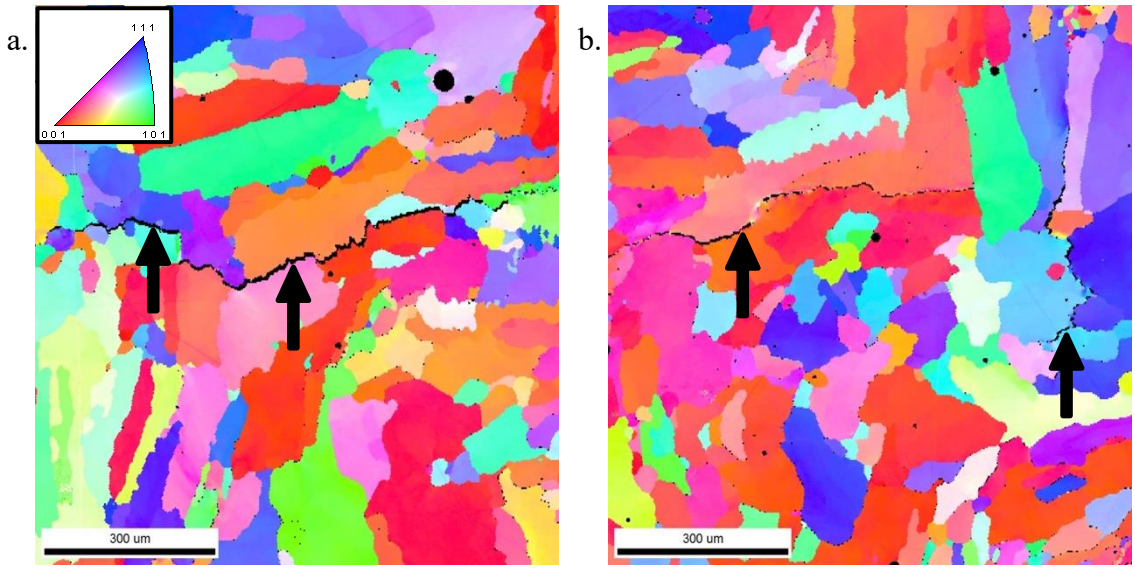

Figure 4.3: EBSD inverse pole figures of Specimen 8 showing a) intergranular (two left arrows) and b) transgranular (two right arrows) cracking mechanisms. Z direction is into the page.

of Cr and Al and that cracking should not be a concern [10, 11, 166-168]. However, the composition used in this study was near an edge of an acceptable range of alloy compositions identified in these earlier studies and, as shown in **Figure 4.1** and **Figure 4.3**, did crack. A welding study by Gussev et al. found that increasing Al concentration from 5wt% to 7wt% resulted in a transition from ductile to brittle fracture during tensile testing [11]. This was believed to be a result of increased ordering between Fe and Al to form intermetallic phases that were further embrittled by hydrogen produced during the welding process [166, 167]. Increasing the number of hydrogen sinks in the material through an addition of C or TiC reduced the impact of hydrogen embrittlement and allowed for crack-free welding. Ideally, formation of precipitates in this study would have done the same.

The prevalence of transgranular and intergranular cracking in these as-built specimens suggests that a possible cause is a difference between AM and general laser welding—increased residual stress accumulation—or an issue stemming from the specific operating parameters used during our study. Each specimen is built on a secured substrate. As a result, thermal cycling induced by layer after layer of laser rastering causes continuous cyclic expansion and contraction of each specimen. Partially immobilized by a substrate, continued expanding and contracting over dozens of layers causes stress accumulation. These cyclic thermal stresses potentially caused both types of crack formation. Built up residual stress put the solidification front under tension. This tension increases space between growing grains, and, with insufficient remaining liquid material to fill in the space, caused solidification cracking. This is supported by the Scheil simulation results in **Figure 4.4**. Large increases in slope as the fraction of solid

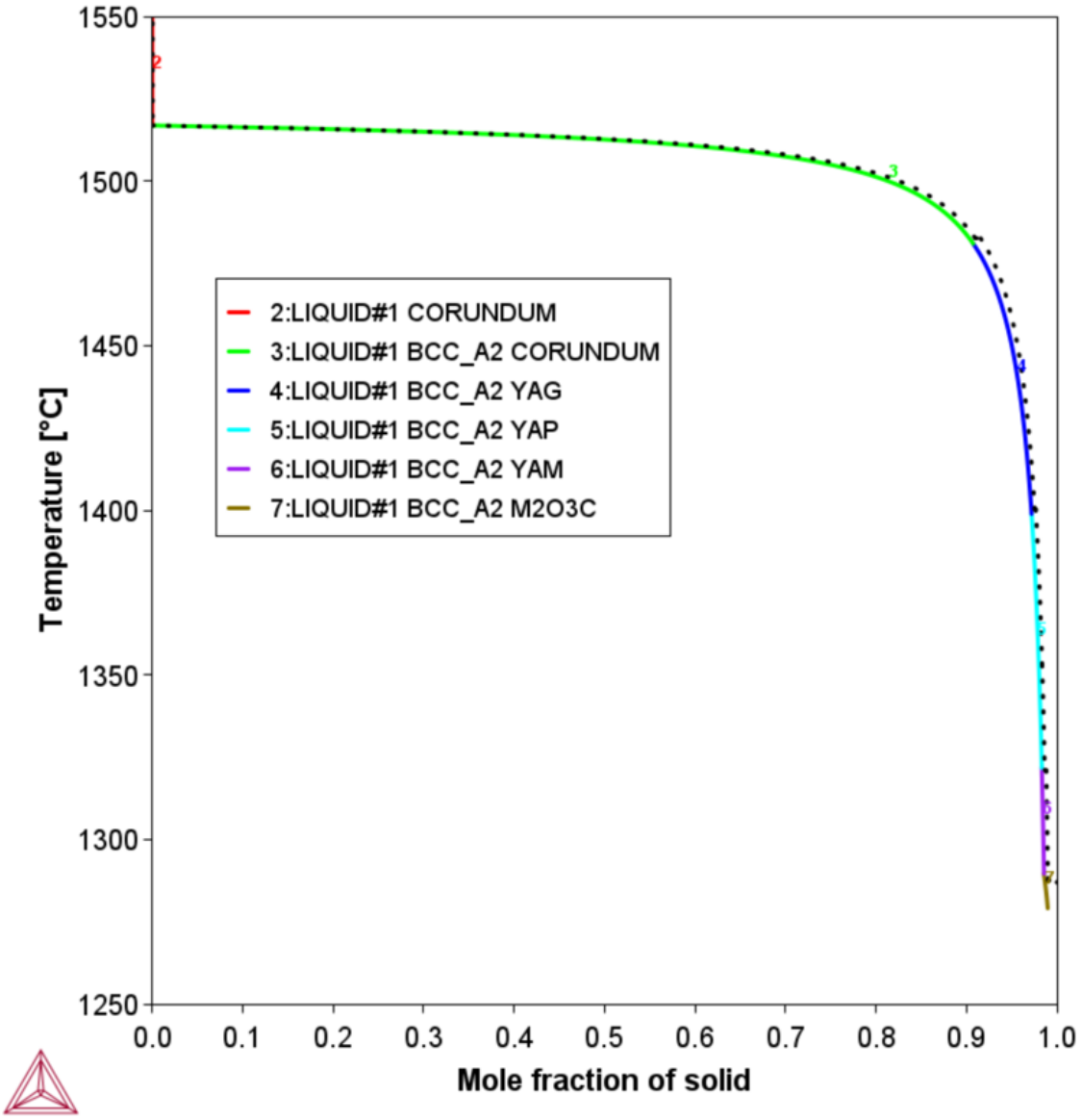

Figure 4.4: Scheil solidification simulation from ThermoCalc of the alloy used (M2O3C is Y_2O_3).

approaches one is indicative of a high probability of solidification cracking [169-171]. Additionally, total accumulation of local residual stress can exceed the local strength of an alloy system shown to be prone to brittle fracture. Potentially accelerated by hydrogen embrittlement or stress concentrators like voids/pores in the microstructure, cracks begin to form [11, 75, 77, 166, 167].

4.2. Agglomeration

4.2.1. Inclusion Formation

During manufacturing some yttrium-rich oxides formed either in the melt pool or as subsequent layers were being deposited. An example of an oxide inclusion from Specimen 8 is shown in **Figure 4.5**. Inclusions of various numbers and sizes were present in all specimens and can sometimes be seen in **Figure 4.1**. To better understand the nature of these inclusions, a FIB liftout STEM sample was made from the oxide inclusion pictured in **Figure 4.5**. A liftout was taken to ensure that only inclusion and no surrounding bulk was included. Inclusion EELS spectra were used to identify what phase was present. EELS results are summarized in **Figure 4.6**.

The EELS spectra suggest that these inclusions are monoclinic yttrium aluminate ($Y_4Al_2O_9$, YAM) as opposed to yttrium aluminum garnet ($Y_3Al_5O_{12}$, YAG), yttrium aluminum perovskite ($YAlO_3$, YAP) or yttria (Y_2O_3) phases. The primary peak of the Al K-edge of our sample was significantly smaller than of YAG or YAP. Its presence eliminated yttria as a possibility. The O K-edge of our sample only contained two leading dominant peaks unlike YAG (leading shoulder at 535 eV) or YAP (three well defined peaks at 536 eV, 540 eV, and 542 eV). The inclusion's Y L-edge contained an additional peak at 2100 eV and a shift of the fourth peak to 2155 eV ruling out YAG (no 2100 eV peak) and YAP

a.

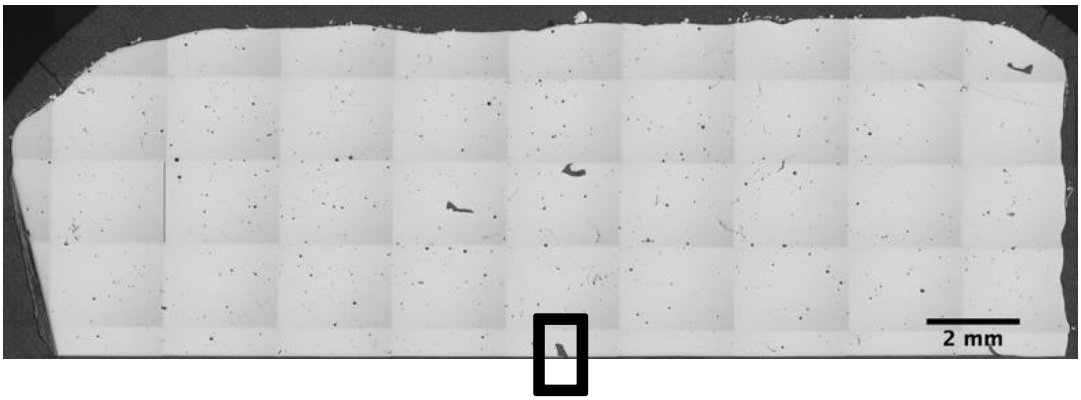

b.

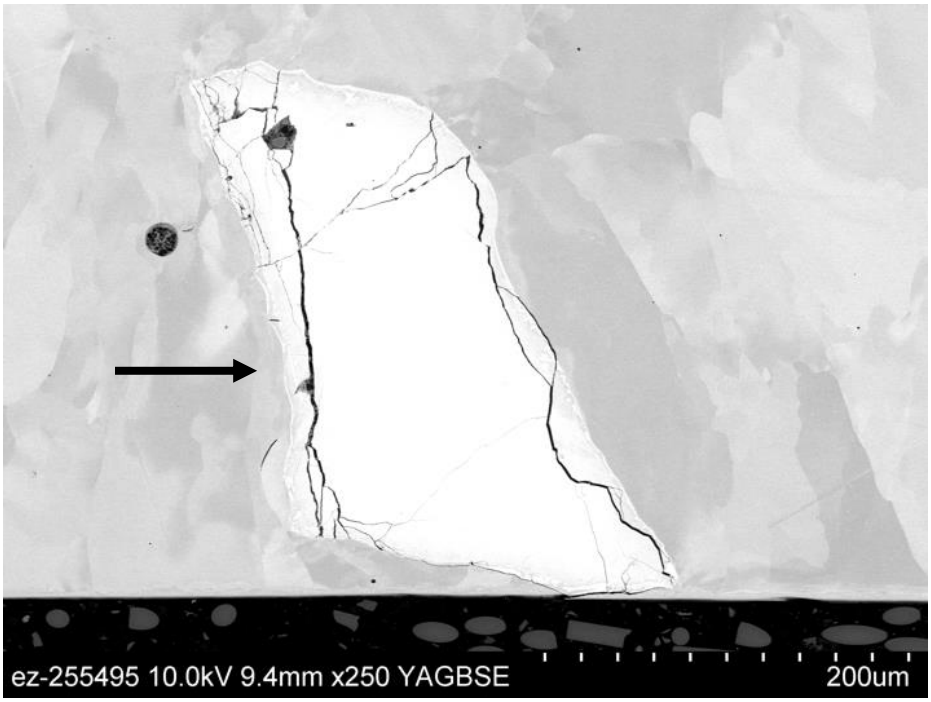

Figure 4.5: a. Optical micrograph of specimen 8, b. Backscatter electron image of an oxide inclusion in specimen 8 (indicated by the outline in a. and arrow in b.). Z direction is up in these micrographs.

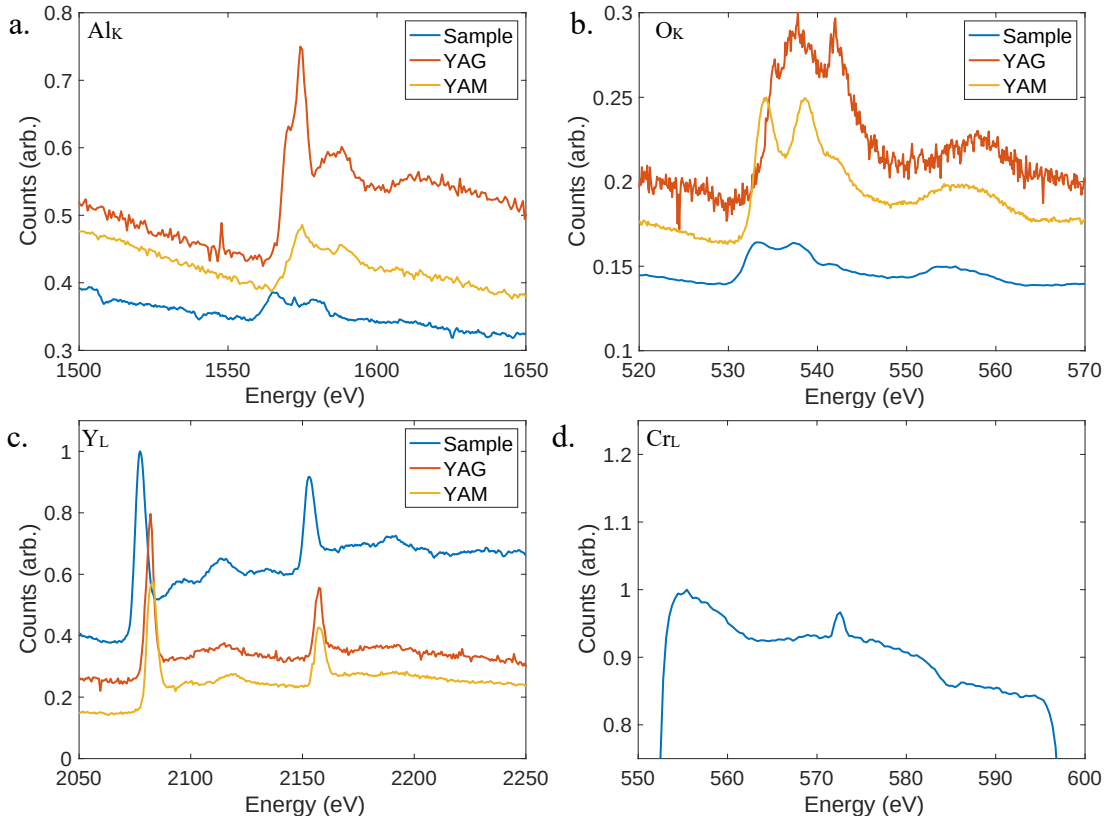

Figure 4.6: EELS spectra of the oxide inclusion from Specimen 8 with the a. Al K-, b. O K-, c. Y L-, and d. Cr L-edges shown in comparison to YAG and YAM reference spectra [172].

phases (peaks at 2095 eV and 2111 eV) [172-174]. Al K-, O K-, and Y L-edges are shown for YAG, YAM, and the sample (Specimen 8 inclusion) for comparison in **Figure 4.6**. Some Cr enrichment was also detected; the Cr L-edge is shown in **Figure 4.6d**.

Inclusion formation during welding or AM of ODS alloys is unfortunately a frequent observation [62, 81, 135, 146]. Oxides form by reaction of their constituent elements within a melt pool. Increased diffusion in a liquid state also allows for oxide growth [175]. Initiated by Marangoni convection and facilitated by Stokes' law due to a lighter oxide density compared to liquid Fe, these oxides make their way to the melt pool surface where they either float with the moving interface or are incorporated into the matrix [62, 81, 135, 143, 146, 175]. Increased time spent in a melt pool increases the chance for growth from diffusion or collision/coalescence [143, 146, 176]. This is partially blamed on poor wettability or high interfacial energy between non-metallic inclusions and liquid Fe. Poor wettability stifles incorporation of inclusions by a solidifying matrix resulting in increased undesired inclusion growth [50, 60, 143]. A combination of these phenomena was likely responsible for the coarse inclusions present in this study.

4.2.2. Wasted Y and O

The presence of these agglomerates represents a waste of valuable Y and O that could be better served forming nanoscale precipitation. To determine how much Y and O was wasted in larger than desired agglomerates, their contents were estimated. Using optical micrographs like in **Figure 4.1** and FIJI/ImageJ analysis, the area of agglomerates was measured. Assuming that agglomerates were homogenously distributed, this area approximation can be treated as a substitute for volume [142]. Given that said agglomerates are YAM as suggested by EELS analysis above, a mass for

agglomerates can be approximated using the density of YAM (4.38 g/cm^3). Using an approximate density for the alloy used in this study (7.01 g/cm^3), a corresponding mass of bulk material containing the above agglomerates can be determined. Lastly, using the stoichiometry of YAM ($Y_3Al_5O_{12}$) an approximation of Y and O lost to agglomerates can be made. Focusing on specimens with the largest amount of oxygen retained (specimens 6, 7, and 8), the results of these calculations are shown in **Table 4.2**. The amounts of Y and O in agglomerates were subtracted from the amounts of Y and O available as determined by ICP-OES and IGF by Dirats Laboratories to give an approximation for how much Y and O are available to form precipitates or in solution. While a significant amount of important oxide forming elements was lost, specimens 6, 7, and 8 still showed an appreciable amount of available Y and O remaining available to potentially form nanoscale precipitation (0.018 wt%, 0.012 wt%, and 0.031 wt%, respectively).

4.3. Precipitation

4.3.1. Characterization by Scanning Transmission Electron Microscopy

Because of appreciable amounts remaining O, specimens 6, 7, and 8 were chosen for further characterization using STEM and APT. Using FIJI/ImageJ, annular dark field (ADF) and high-angle annular dark field (HAADF) micrographs were characterized measuring precipitates diameters and calculating image number densities. ADF and HAADF micrographs were chosen to capitalize on the increased z-contrast provided by their focus on imaging using scattered electrons. Results from STEM characterization are shown in **Table 4.3**. Specimens 11, 12, and 13 are samples from specimens 6, 7, and 8, respectively, that underwent the post-build heat treatment (PBHT) mention in **Chapter 3**.

Table 4.2: Estimation of Y and O consumed by agglomerates and Y and O available for nanoscale precipitation (assuming YAM oxide phase).

Specimen	Total Y (wt%)	Y in Agglom. (wt%)	Y Available (wt%)	Total O (wt%)	O in Agglom. (wt%)	O Available (wt%)
6	0.14	0.0541	0.0859	0.0394	0.0219	0.0175
7	0.12	0.0408	0.0792	0.0284	0.0164	0.012
8	0.13	0.0894	0.0406	0.067	0.0362	0.0308

Table 4.3: STEM precipitate analysis of specimens with the largest amount of O available for nanoscale precipitation and their heat-treated counterparts.

Specimen	# of Micrographs	Avg Number Density ($\#/m^3$)	Avg Diameter (nm)
6	1	7.75E+17	200.75
11	2	1.00E+19	265.63
7	2	1.61E+18	114.89
12	4	1.77E+18	380.57
8	4	2.96E+18	157.21
13	5	4.45E+18	164.74
	Average:	3.60E+18	213.96

Precipitates across a wide variety of sizes and complexity were observed during STEM characterization. **Figure 4.7** shows a characteristic precipitate that would be found in specimens 6, 7, and 8, approximately 200 nm in diameter and sparsely dispersed throughout the matrix. **Figure 4.8** demonstrates some potential core-and-shell co-precipitation that occurred. In this precipitate there are what appears to be two or three smaller oxide precipitates surrounded by an area enriched in both Y and O. A linescan (**Figure 4.9**) was performed across the precipitate in **Figure 4.8** to give a better idea as to how the composition is evolving across the core- and-shell. Crossing the precipitate, concentrations of Y and O begin to increase as the darkest spot on the HAADF image is traversed. There is also a slight increase in Al at this spot giving it a rough stoichiometry of $Y_{15}Al_4O_{13}$. This does not match any known Y-Al-oxide phases. This could be due to thickness effects or a hypostoichiometric environment of O. If it is a result of thickness, it is likely a YAM phase oxide (Y3Al5O12) with an increased Y signal coming from additional Y-enrichment surrounding the oxide. This agrees with the phase identification of large oxide agglomerates performed in Section 4.2.1. **Figure 4.10** and **Figure 4.11** show a similar phenomenon occurring in specimens 12 and 13, respectively. Both show a Y-oxide precipitate surrounded by a Y-rich region. Co-precipitation is an expected possible outcome as the existing precipitate (likely the oxide in this instance) acts as a nucleation site for subsequent precipitates (likely the intermetallic shell in this instance) [177]. This is supported when considering the phase diagram shown in **Figure 4.12**. As a melt pool cools across most O concentrations, a region of Y-oxide phase formation is entered first. Upon further cooling, a melt pool eventually enters a region that includes the formation of a Y-rich intermetallic phase.

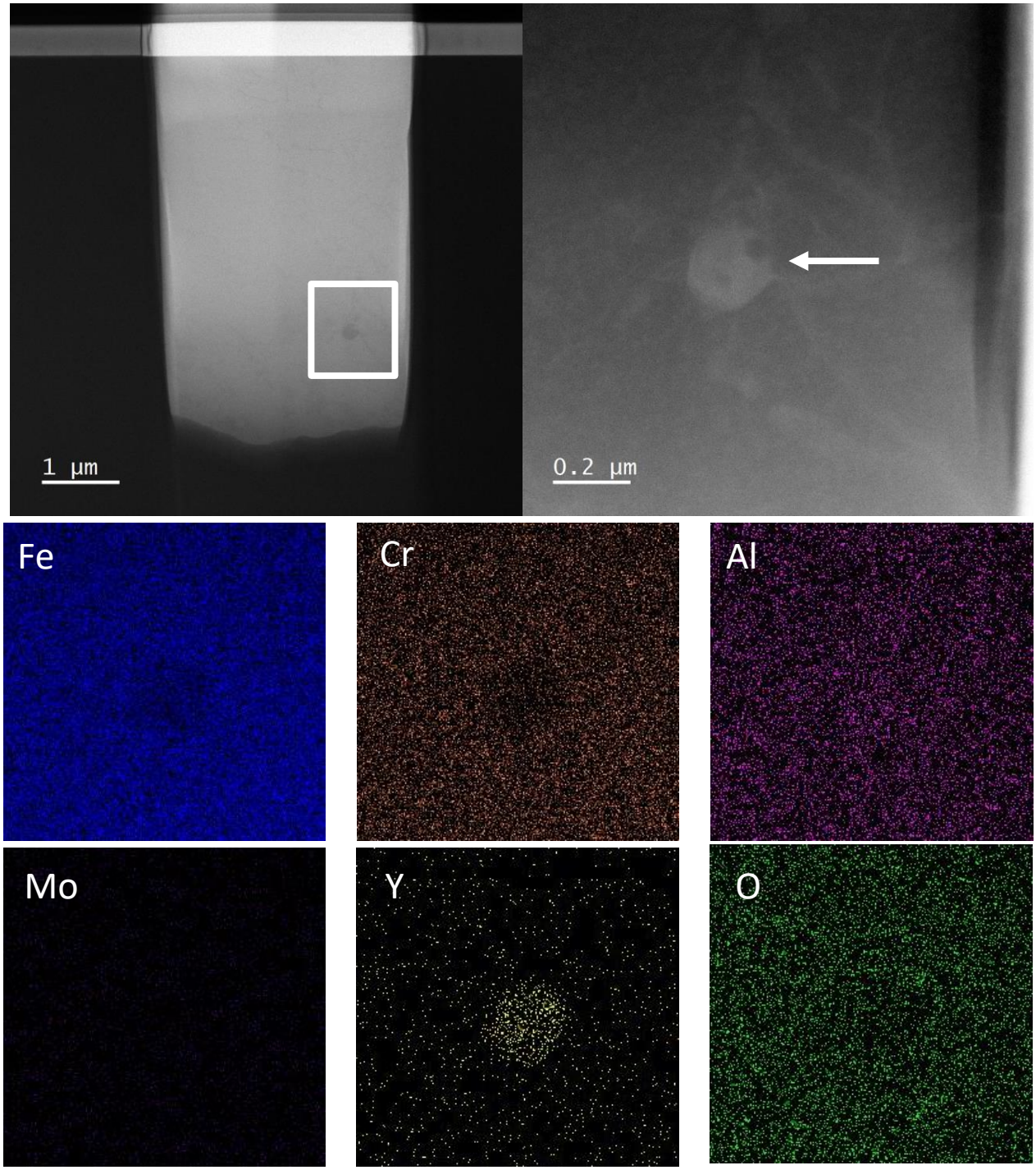

Figure 4.7: EDS maps of a large Y-rich precipitate found in Specimen 6.

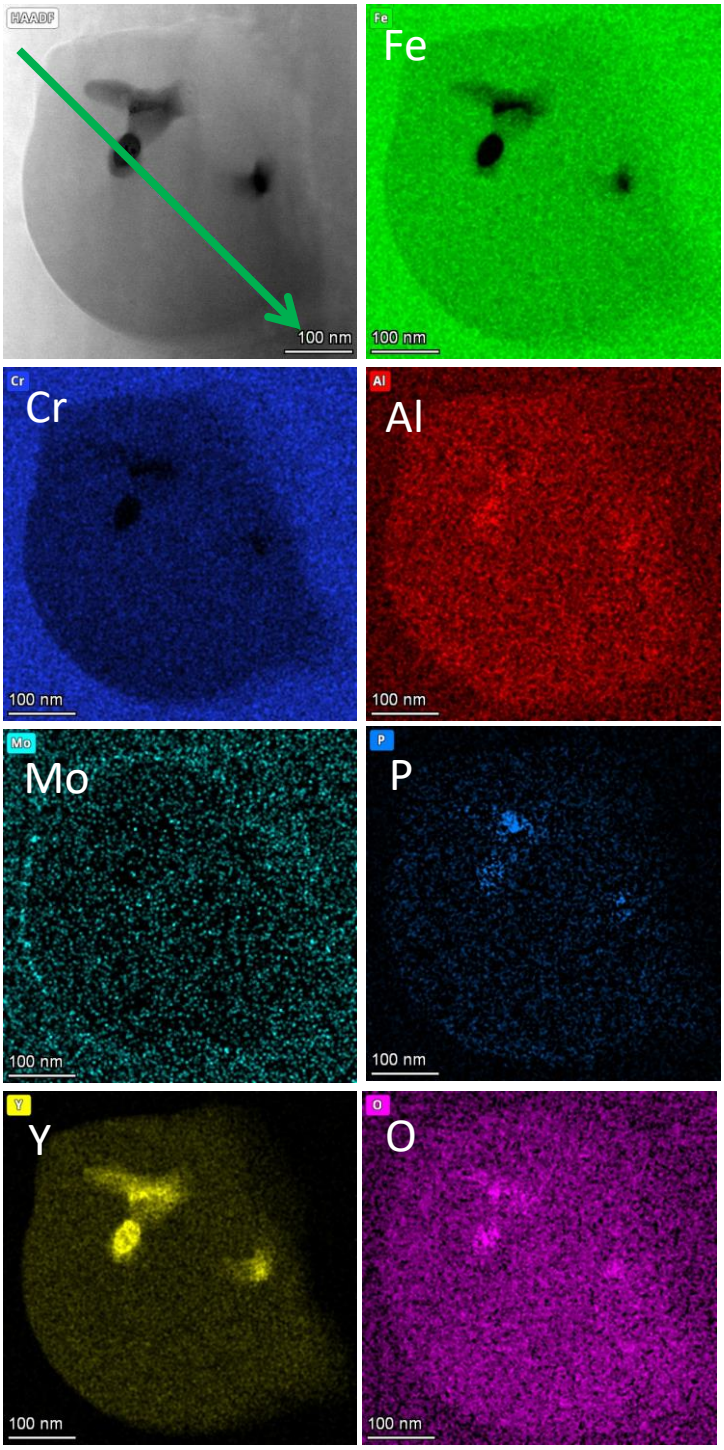

Figure 4.8: EDS maps of a large core- and-shell precipitate with oxides bound in a Y-rich shell. The linescan path is denoted by a green line.

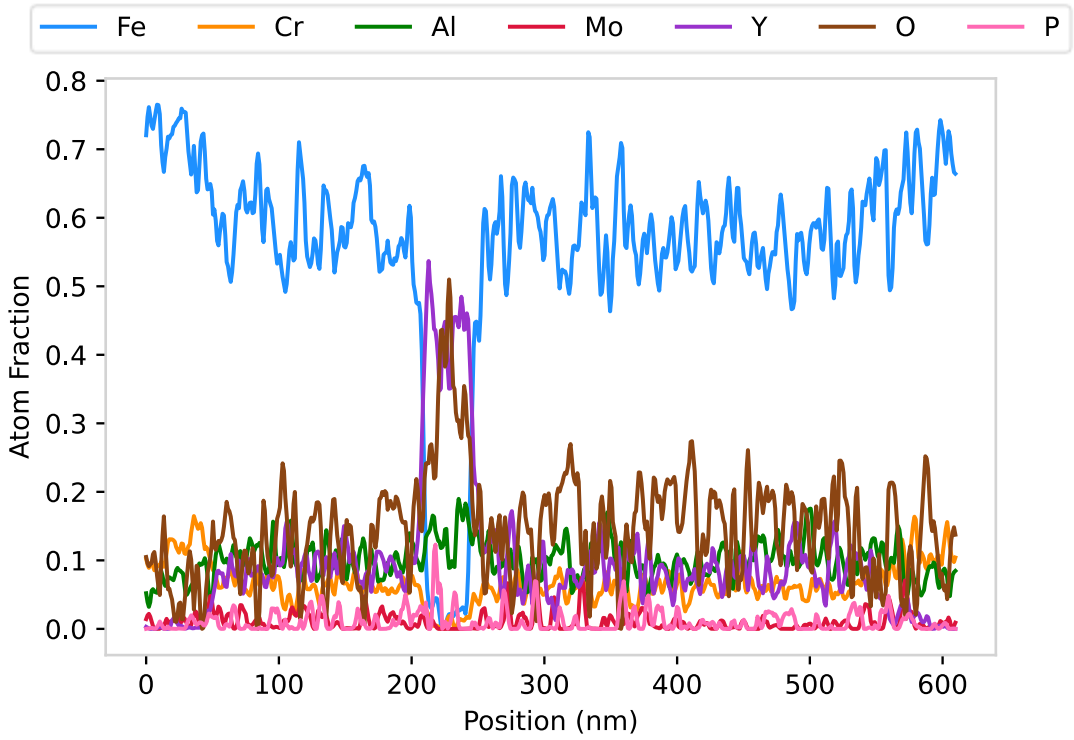

Figure 4.9: EDS linescan of core-and-shell precipitate in Figure 4.8.

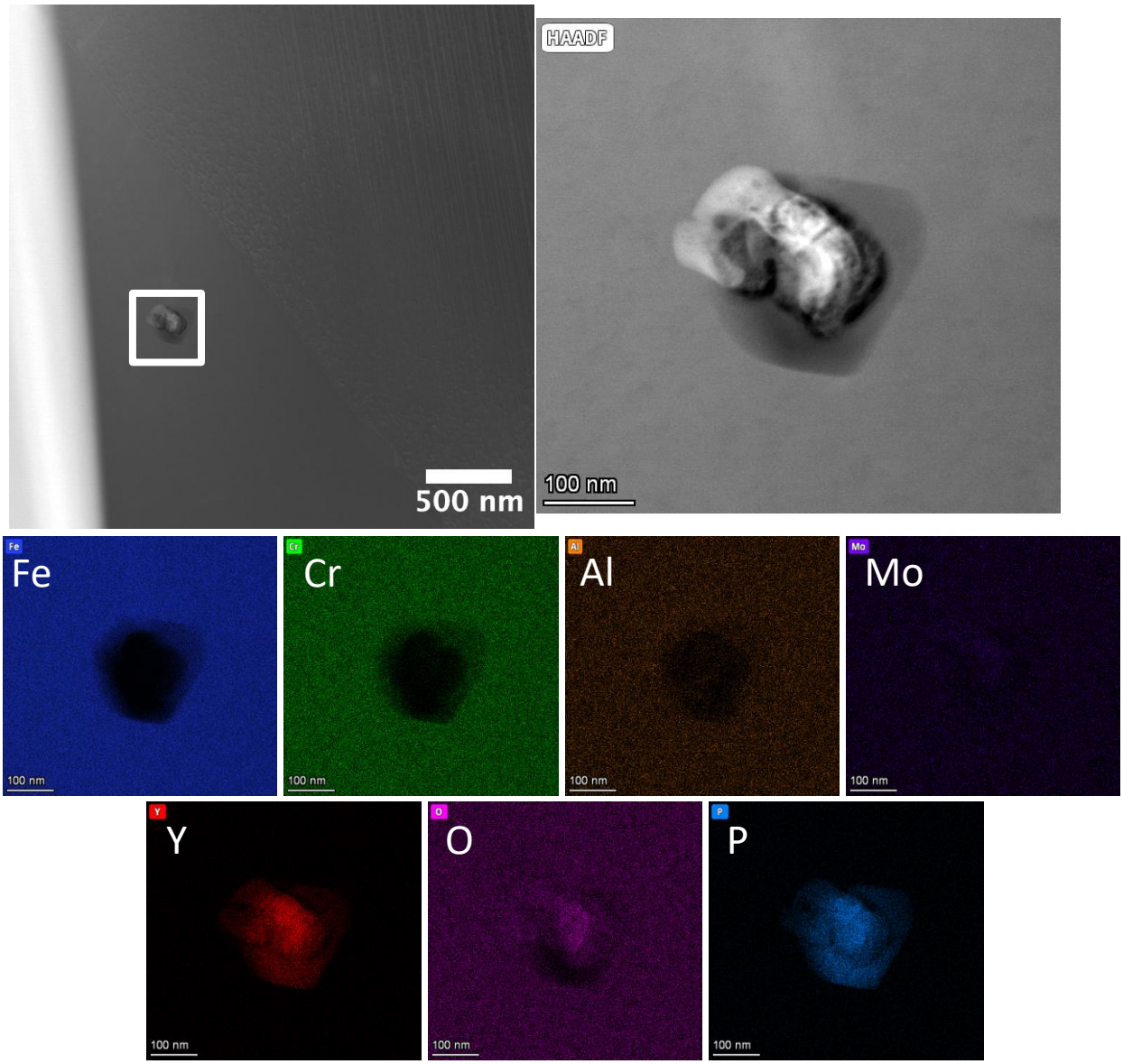

Figure 4.10: EDS maps of co-precipitation occurring in Specimen 12.

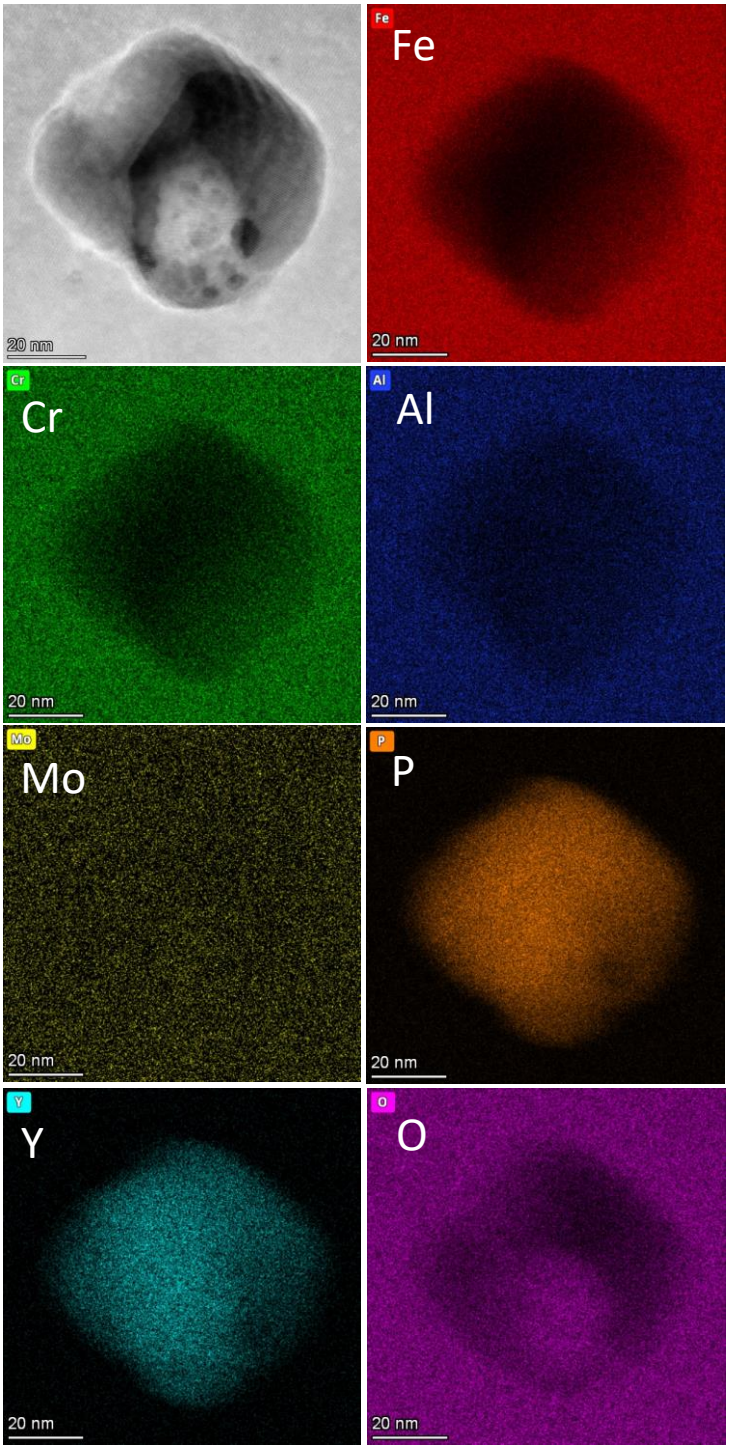

Figure 4.11: EDS maps of co-precipitation occurring in Specimen 13.

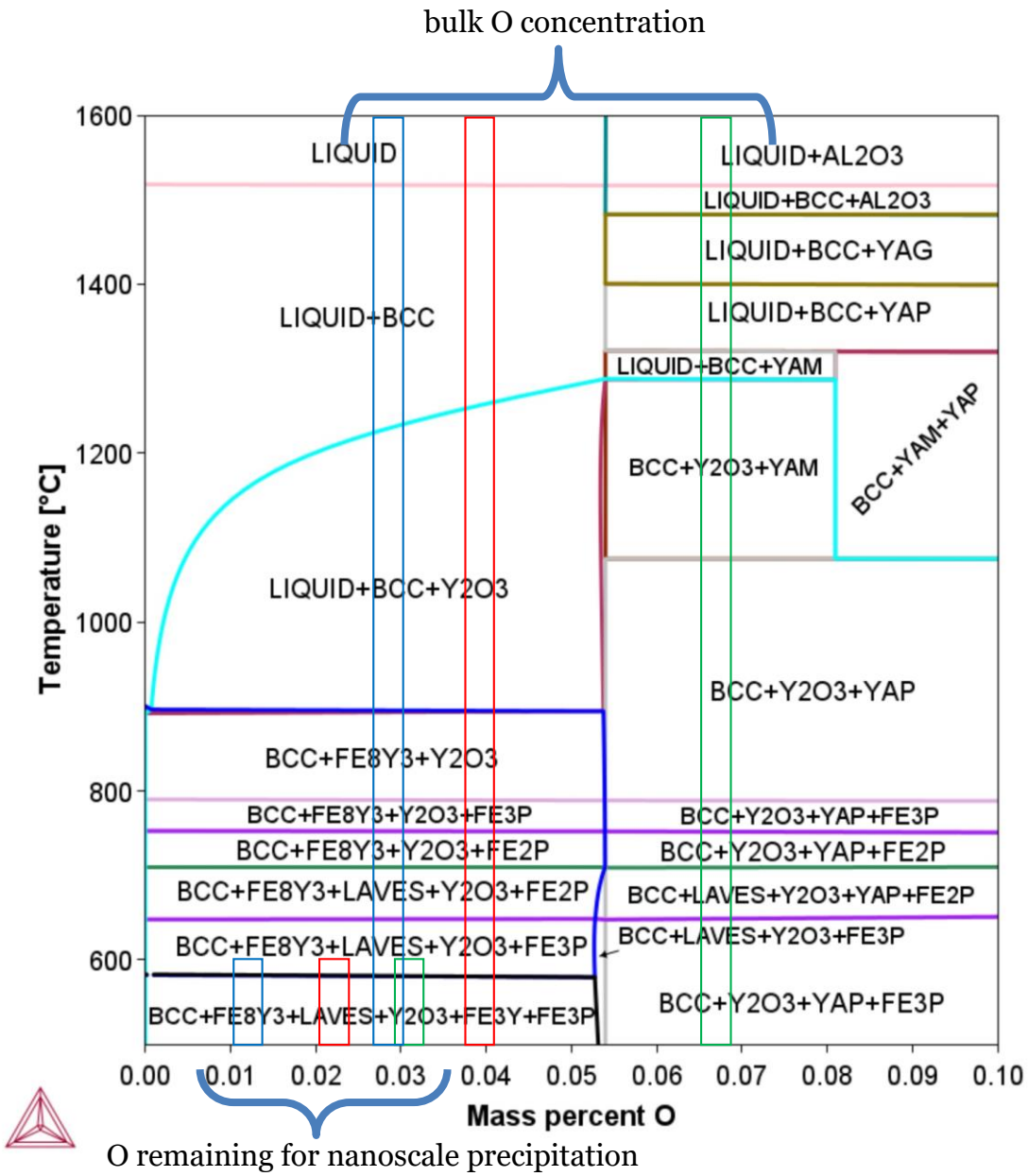

Figure 4.12: Temperature vs. O concentration phase diagram for our alloy. Region color = specimen before/after HT; Red = 6/11, blue = 7/12, green = 8/13. Bulk O concentrations and O left in solution are noted. TCFE9 was the database used for simulation.

Just as precipitates formed on one another, precipitates also formed along grain boundaries. This is shown in **Figure 4.13** where there are four or five oxide precipitates that formed along a grain boundary. Additionally, elemental Y has segregated along the grain boundary as is common in steels containing Y due to the near zero solubility of Y in BCC Fe [51].

As shown, number densities across all specimens characterized were similar. Intuitively, specimens 8 and 13 would be expected to have the most precipitates due to having the largest amount of O left in solution (O is a limiting factor for oxide production). This ended up being generally true except for Specimen 11. Precipitate number density increased by more than an order of magnitude from heat treating Specimen 6 into Specimen 11. This is believed to be a result of a non-oxide phase precipitating out of solution during the heat treatment. **Figure 4.14** shows that a Y-rich intermetallic phase potentially pops out of solution during the heat treatment in Specimen 11. **Figure 4.14** also shows an example of a Y-based oxide. Both precipitates are decorated by P, an unexpected result due to the low amount of P present in these experiments. Overall, it seems that a PBHT helped increase precipitate number densities; however, it also led to some coarsening across all specimens.

4.3.2. Characterization by Atom Probe Tomography

To better examine the composition of dispersoids a total of 10 APT needles were analyzed (2 from Specimen 11, 4 from Specimen 12, and 4 from Specimen 13). Reconstruction of two APT needles prepared from Specimen 11 (Specimen 6 post-HT) are shown in **Figure 4.15** and **Figure 4.16**. Moderate measured dispersoid number densities in our samples post-HT and limited analyzed APT volumes placed these samples

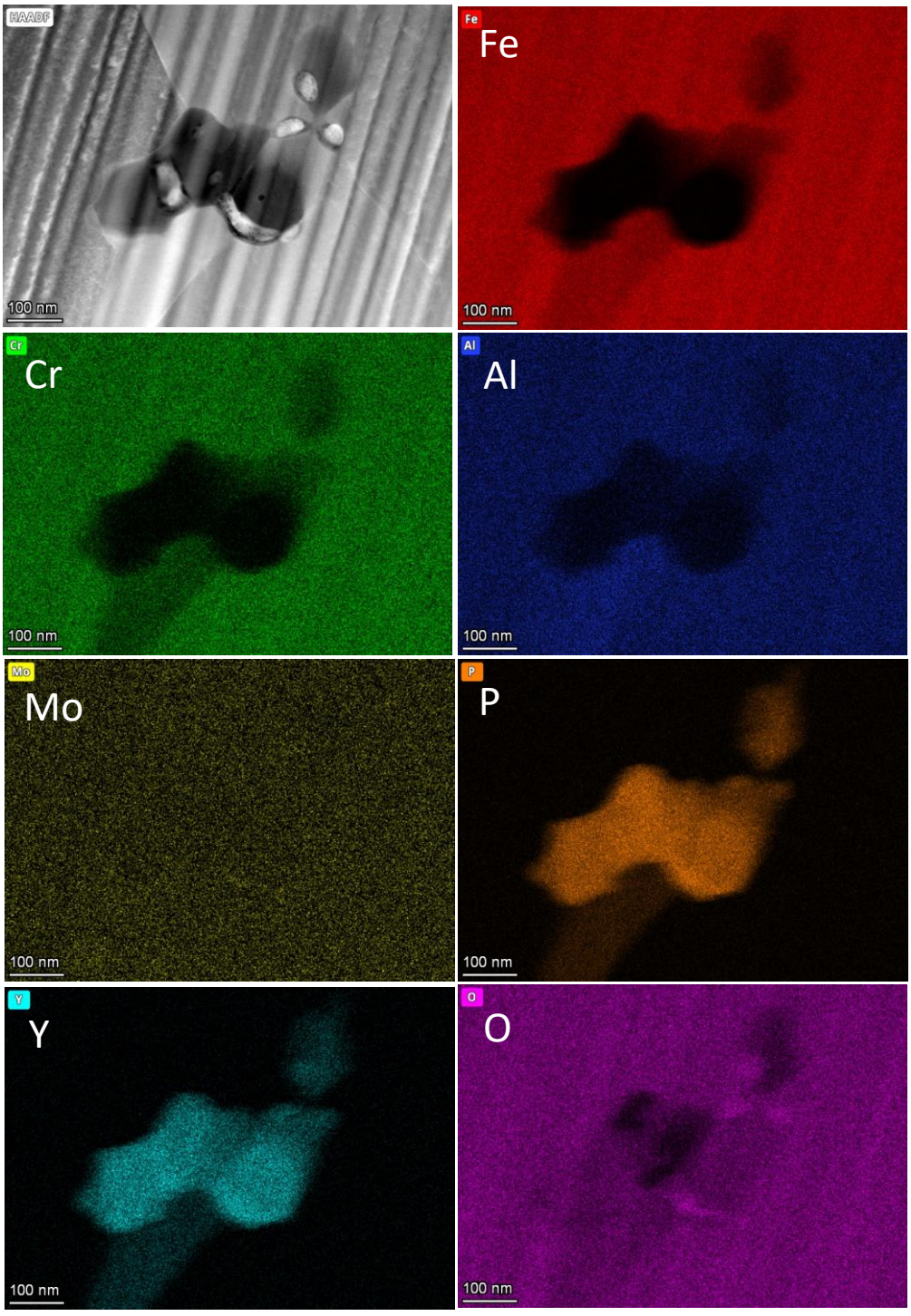

Figure 4.13: EDS maps showing precipitation and Y segregation along a grain boundary.

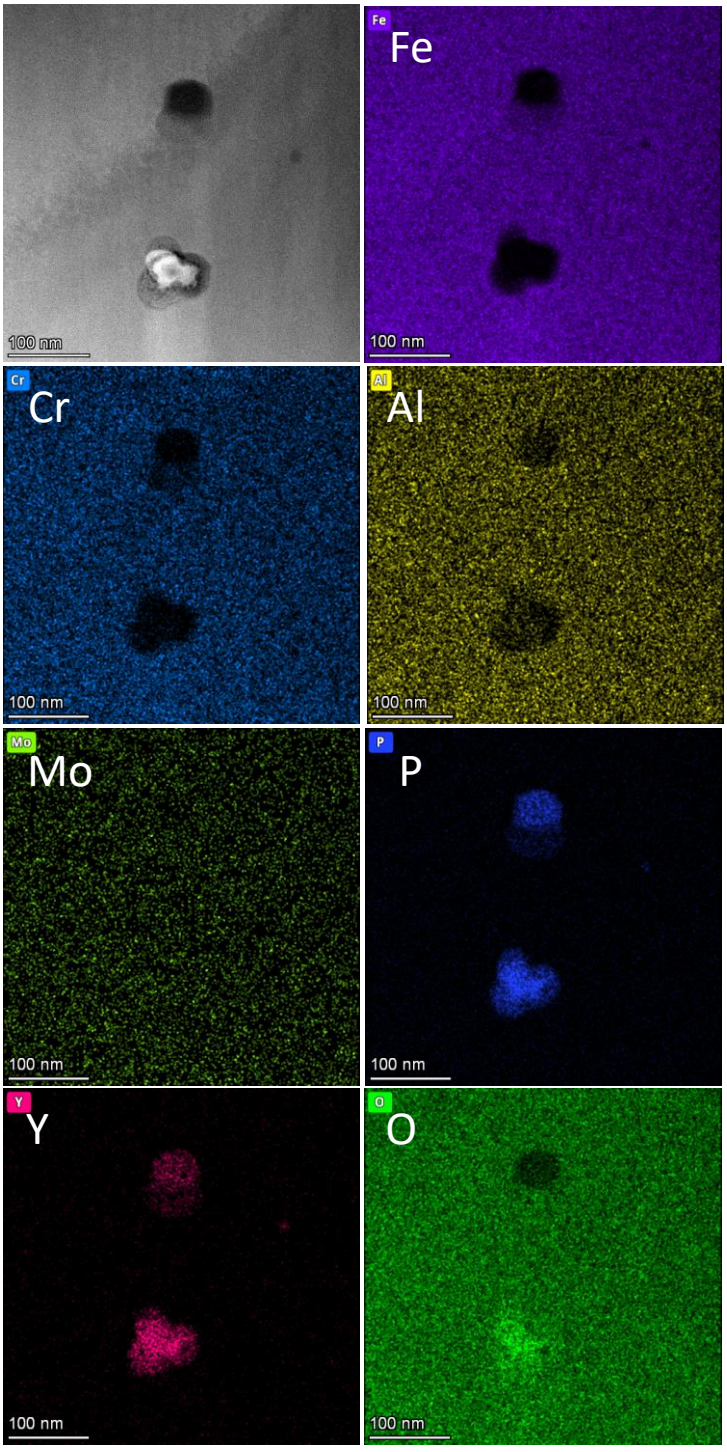

Figure 4.14: EDS maps of a Y-oxide and Y-rich intermettalic phase in Specimen 11.

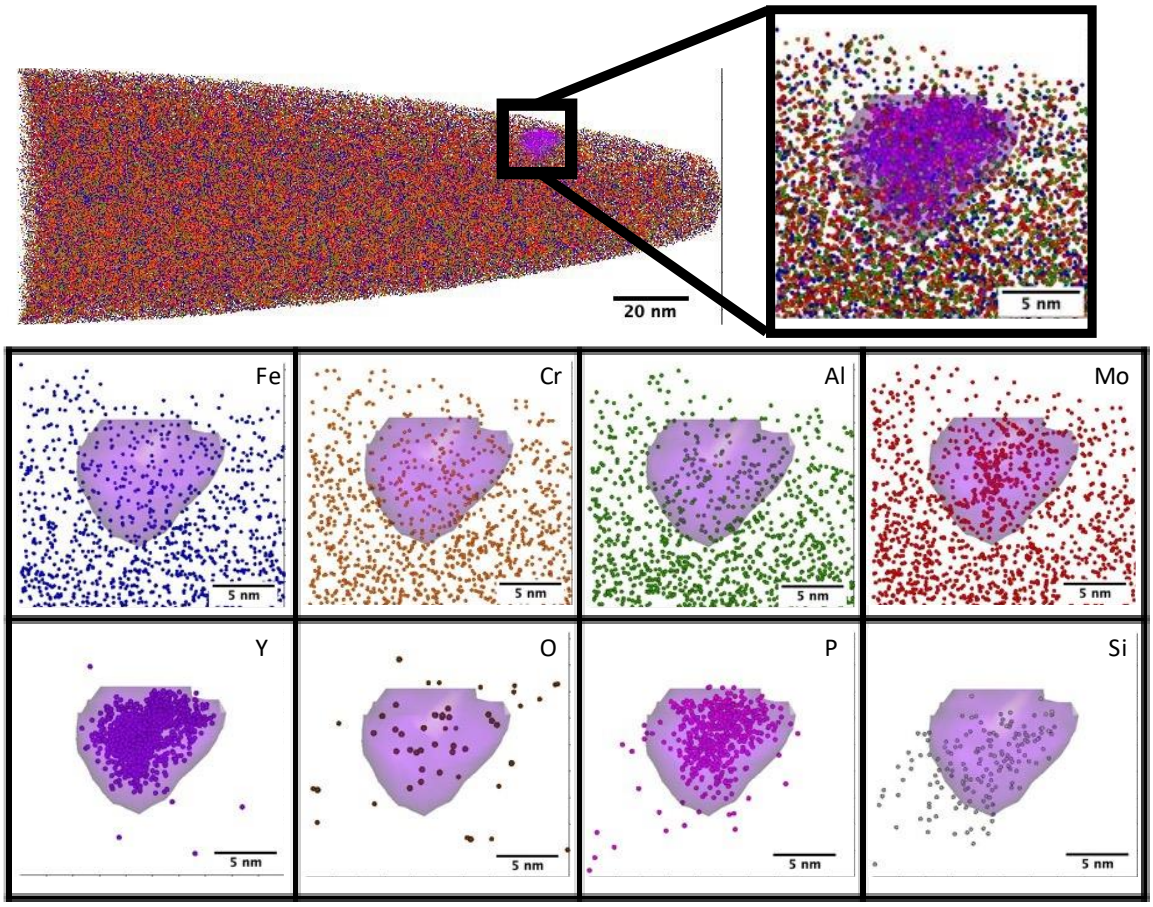

Figure 4.15: APT reconstructions of Needle 1 from Specimen 11 with a dispersoid. Isosurfaces outlined in purple with species of importance shown.

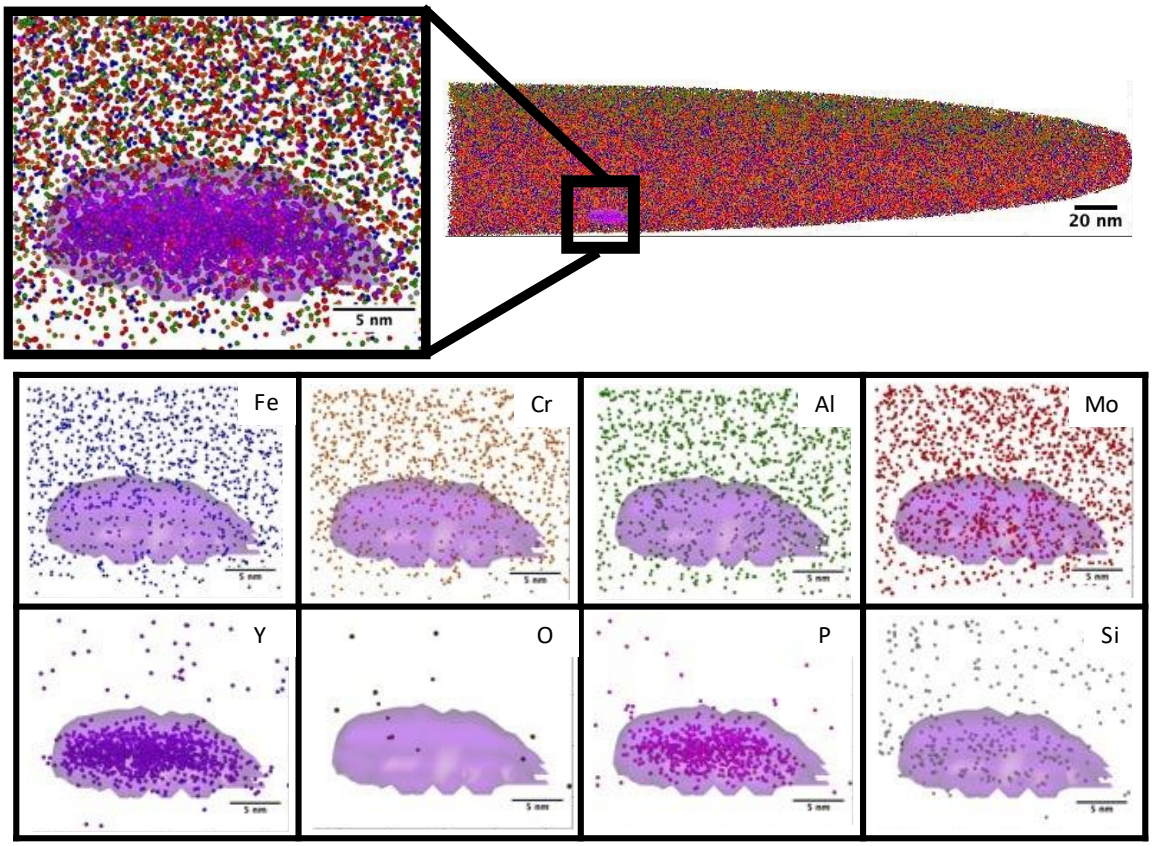

Figure 4.16: APT reconstructions of Needle 2 from Specimen 11 with a dispersoid. Isosurfaces outlined in purple with species of importance shown.

precipitates shown in **Figure 4.15** and **Figure 4.16** were the only dispersoids (shown by the purple isosurfaces) captured using APT. Proximity histograms were created for each (**Figure 4.17**). Needle 1 showed a clear decrease in Fe, Cr, and Al concentrations with corresponding increases in Mo, Y, and P. There was slight O enrichment. Needle 2 showed clear decreases in Fe and Cr with increases in Mo, Y, and P. There were no appreciable changes among other elements considered.

The presence of P in the STEM EDS and APT data was unexpected since the ICP-OES data did not detect P in the as-received powder and only detected amounts near the minimum detectable limit of P ($\leq$0.01%) in the as- built specimens (**Table 4.1**).Special care was given while ranging the APT data during reconstructions to insure the presence of P was not anomalous. A similar mass-to-charge ratio with singly-charged diatomic O (31 vs. 32) causing miss-labeling the representative peak was considered. Comparing the mass-to-charge ratios of more prominent species such as Fe, Cr, or Al with their references reinforced proper range file alignment and confirmed P presence. P contamination is believed to be due to mixing from the substrate (0.01 wt%). P has an affinity for grain boundaries and precipitates and likely segregated to precipitate surfaces in the melt pool or during the HT (600 ºC for 1 hr) as suggested by the nuclear reactor pressure vessel literature. Assuming a precipitate number density of 10^{18} m^{-3} and an average precipitate size of 200 nm, the maximum distance an atom of P needs to travel to a precipitate surface is 210 nm. P Diffusivity in solid steel is ~ $2.62x10^{-14}$ cm^2/s [178-182]. Using the simple relationship in Equation 4.1, P can diffuse up to 97 nm during the HT alone.

$$x = \sqrt{D * t} \tag{4.1}$$

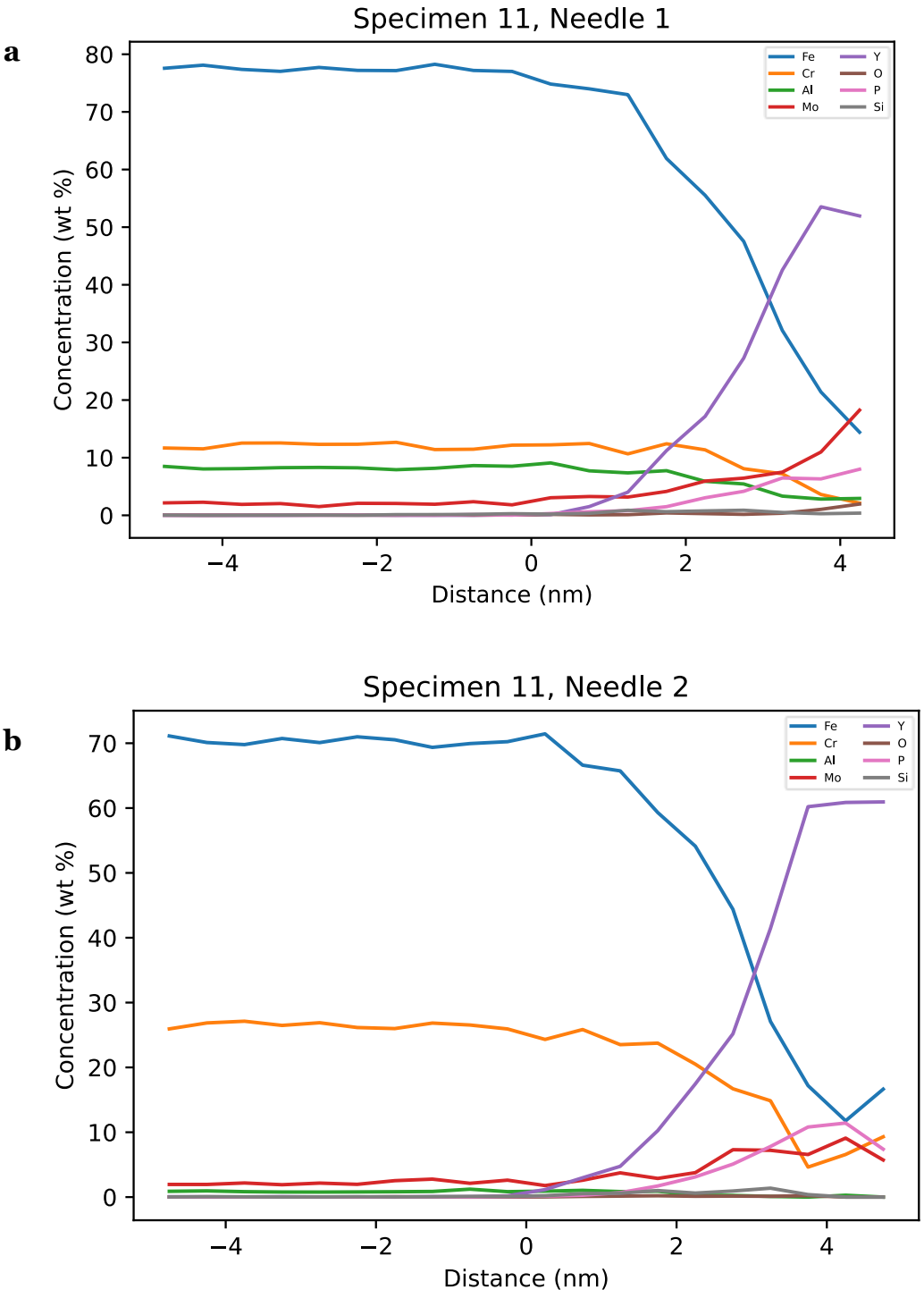

Figure 4.17: Proximity histograms of Specimen 11 Needle 1 (a) and Needle 2 (b).

where x is the diffusion distance, D is the diffusivity, and t is the time for diffusion. Thus, it is not unreasonable for some P atoms to segregate to precipitate surfaces.

Table 4.3 shows that precipitate number densities increased from Specimen 6 to Specimen 11 post HT. As mentioned in Section 4.3.1, this is believed to be a result of increased precipitation of a Y-rich phase as shown in the STEM EDS data. The APT data in **Figure 4.15**, **Figure 4.16**, and **Figure 4.17** supports this idea by also showing that some dispersoid compositions in Specimen 6/11 were in fact an Y-rich intermetallic phase. This suggests that the rapid cooling and high solidification velocities of DED AM potentially led to some unreacted Y being trapped in solid solution. A PBHT then provided sufficient energy to encourage the formation of these Fe-Y intermetallic dispersoids highly favored by the poor solubility of Y in BCC Fe [133].

To examine the potential for solute trapping of Y, a trapping velocity can be calculated as described by Aziz [83]. Using Equation 2.16 from Section 2.7, the trapping velocity for complete trapping of Y in BCC Fe was determined as ~ 8 m/s (diffusivity of Y was assumed ~ 2.03x10-5 cm2/s, BCC Fe interatomic spacing ~ 0.248 nm) [183]. Maximum solidification velocity for these specimens is 0.012 m/s or equal to the tool speed as suggested by Guo et al. [142], While complete trapping of Y is unlikely, being within two orders of magnitude, there is a chance for some Y to be trapped in solid solution. Mao et al. reported a similar phenomenon where Fe-Y intermetallic dispersoids formed in the as-fabricated and as-irradiated states of their FeCrAl alloy C35M (Fe-13Cr-5.3Al-2Mo-0.1Si-0.05Y) produced by vacuum induction melting and homogenized at 1200°C for 4 hours [184]. They showed a low density of relatively large Y-rich dispersoids

formed within this alloy system while not predicted by thermodynamic models like a Scheil simulation.

In the presence of O, it is expected that any unreacted Y not in agglomerates would precipitate out as an oxide. This likely did not happen because of an O-deficient environment as suggested by **Table 4.2**. Comparing the reported O availability to the reported Y availability shows that Y was available in quantities greater than stoichiometrically required to form an oxide like YAM. This is supported by Y's strong affinity to bind with available O as shown by the Ellingham diagram borrowed from Rieken, 2011 in **Figure 2.13** and the density functional theory simulations performed by Wang, 2018 where Y showed an attraction to O up to 10 nearest-neighbor distances away [46, 108]. This is further supported by the O v. Temperature phase diagram for this alloy predicted by ThermoCalc (**Figure 4.12**). At any available O concentration above 500°C, a Y-based oxide phase is stable and should form. Further, given the high relative diffusivity of O (on the order of 1.3-1.5x10^{-8} cm^2/s) in BCC Fe at our given HT conditions (600°C, 1hr), free O should have sufficient time to diffuse to free Y and react [185, 186]. However, as shown in **Figure 4.15**, **Figure 4.16**, and **Figure 4.17**, an oxide did not always form.

4.4. Mechanical Property Testing

4.4.1. Vickers Microhardness

To examine the bulk properties, microhardness measurements were taken of the as-received powder and each specimen (including specimens 11, 12, and 13). As-received powder (denoted as Specimen 0) was mounted into a conductive epoxy prior to hardness measurements and special care was taken to ensure that indents were performed on

powder particles sufficiently large to contain the entirety of the indent. Typical indent depth on powder particles was between 8-9 μm. Average particle diameter was 65 μm.

These results are shown in **Figure 4.18**. Hardness for a model FeCrAl alloy (Fe-12Cr-6Al) produced by vacuum induction melting, 1150 °C homogenization HT for 1 hr, hot rolling at 800 °C, and annealed at 1000 °C for 1 hr is provided for comparison (dashed horizontal line) [154]. All as-built specimens (1-10) showed a significant improvement (~ 10%) compared to the model reference alloy. The 1-hour HT at 600°C for specimens 11-13 did not result in significant increases in hardening over their as-built counterparts (specimens 6-8). The cause of the decrease in microhardness of Specimen 11 is currently unknown. No unexpected means of yielding was noticed during indentation of Specimen 11, but a large internal crack under the polished surface cannot be ruled out. Additional measurements were taken to minimize the effects of any anomalies present.

Increased dispersion homogeneity was expected to manifest as increased hardness during microhardness testing. The lack of change in microhardness data after a PBHT could indicate that chosen HT was insufficient to complete the formation of Y-Al-O precipitates. Alternatively, the number of build defects present in the specimens (possible explanation of the scatter in hardness data) may have inhibited a clear quantification of the strengthening effects of the observed nanoprecipitation. Lastly, if all oxide forming material was consumed during in the as-built state, a PBHT will not lead to an appreciable improvement in microhardness. All samples still showed a marked improvement in microhardness compared to model, well-annealed FeCrAl alloys from the literature, indicating some strength improvement by the AM alloys [10, 154].

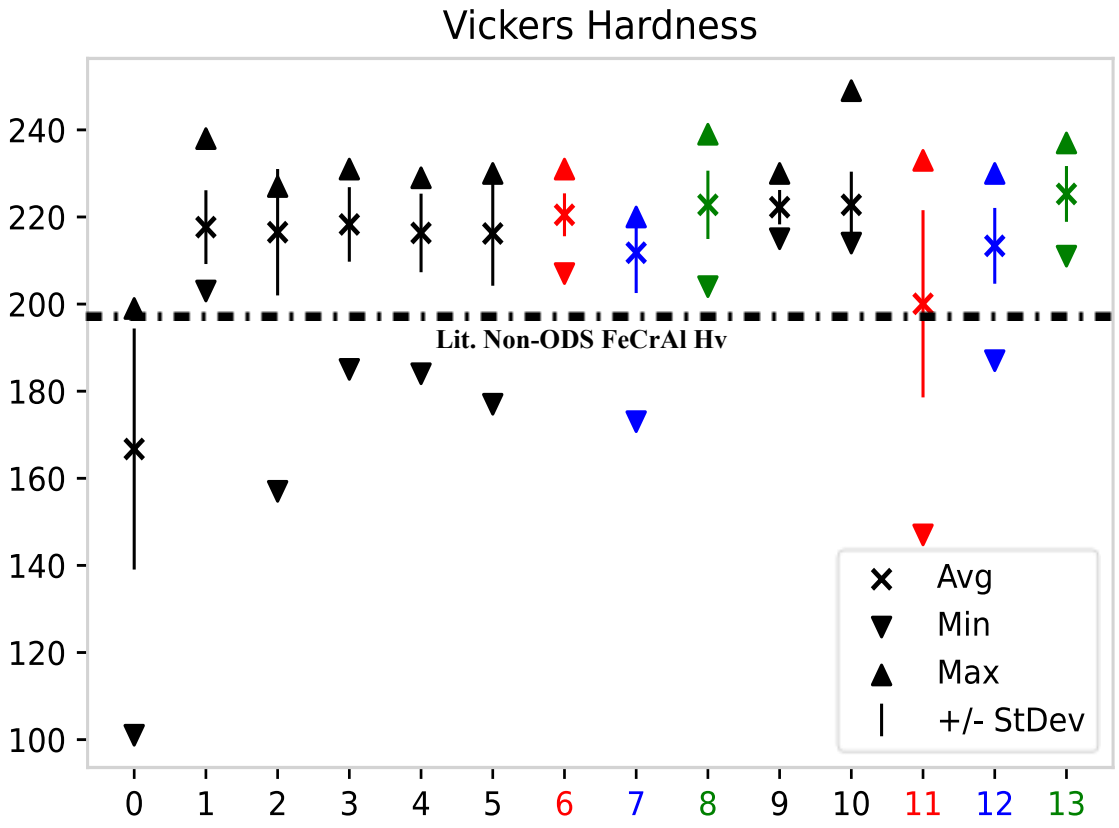

Figure 4.18: Vickers hardness measurements of all specimens including as-received powder (0) and HT'd samples of specimen 6, 7, and 8 (11, 12, and 13, respectively) compared with hardness values of non-ODS model FeCrAl alloys from literature (shown by the dashed line)[154].

4.4.2. Precipitate Strengthening

To further examine the effect of the dispersions on specimen strength, an increase in yield strength ($\Delta\sigma_y$) from a dispersion of spherical obstacles can be calculated by the Dispersed Barrier Model as shown in Equation 2.5 in Section 2.1.1. The Taylor factor (*M)* is assumed to be ~ 3 for BCC Fe. The shear modulus (μ) is ~100.4 GPa. The glide dislocation Burgers vector (b) is assumed to be 0.248 nm. The obstacle strength factor (α ~ 1.1) was calculated for each specimen using Equation 2.7 and related parameters as described by Tan and Busby. Average precipitate number densities (N) and diameters (d) are determined from analyzed micrographs and summarized in **Table 4.3** [10, 95-97]. For weaker obstacles, an alternative model by Friedel (Equation 2.6) accounts for dislocation shear through obstacles by increasing the inter-obstacle distance [99].

The dispersoid-matrix coherency affects the value of α [96]. Duo et al. and Hsiung et al. [2, 93] found that YAP/YAH precipitates in steel with diameters between 4.5 nm and 10 nm are semi-coherent [93] and that YAM precipitates with diameters less than 10 nm are either coherent or semi-coherent [2]. Dispersoids in our AM builds are significantly larger than typical coherent or semi-coherent oxide phases. This suggests that these dispersoids should be considered strong obstacles.

Using the respective data from **Table 4.3** and the constants for FeCrAl or BCC Fe, approximations of the contribution of precipitate strengthening to microhardness can be made. The results of these calculations are shown in **Table 4.4**. In addition to expected changes in microhardness and UTS, **Table 4.4** also contains two different reference alloys for comparison. Wang et al. is the previously mentioned alloy in **Section 4.4.1** (Fe-12Cr-6Al) and is also used as the base microhardness to calculate the expected

Table 4.4: Expected changes in microhardness and YS based on precipitate strengthening. Two model alloys are provided for comparison. Expected microhardness and YS values are calculated using the results of a hardening model and the microhardness value reported for Fe-12Cr-6Al as provided by Wang et al. [154].

		Dispersed Barrier Model				Friedel Model			
Specimen	Avg Hardness (Hv)	ΔVHN (Hv)	$\Delta\sigma_y$ (MPa)	Expected VHN (Hv)	Expected YS (MPa)	ΔVHN (Hv)	$\Delta\sigma_y$ (MPa)	Expected VHN (Hv)	Expected YS (MPa)
6	220.50	10.65	32.59	209.25	640.31	4.57	14.00	203.17	621.71
11	200.54	46.05	140.90	244.65	748.62	34.85	106.65	233.45	714.37
7	211.79	10.59	32.40	209.19	640.12	3.89	11.89	202.49	619.61
12	213.90	24.41	74.69	223.01	682.40	16.56	50.67	215.16	658.39
8	222.79	17.71	54.21	216.31	661.92	8.42	25.76	207.02	633.47
13	225.75	22.40	68.53	221.00	676.25	11.66	35.67	210.26	643.39
Average:	215.88	21.97	67.22	220.57	674.94	13.32	40.77	211.92	648.49
			Wang, 2021	198.60	607.72		Wang, 2021	198.60	506.43

microhardness values after accounting for precipitate strengthening.

Measured microhardness levels were ~ 215 to 220 Hv across all as-built and PBHT'd specimens. This shows a measured increase of 15 to 25 Hv (~ 10%) compared to model reference alloys (VHN ~ 195 to 200 Hv) [154]. The predicted increase in microhardness due to precipitate strengthening is 22 Hv (67 MPa) using a dispersed barrier model and 13 Hv (41 MPa) using the Friedel model. This corresponds to an expected increase in microhardness of approximately 10% of the typical hardness of a well-annealed Fe-12Cr-6Al alloy. These results and large average measured dispersoid size suggest that a classical dispersed barrier model like Equation 2.5 is a more appropriate fit to the data. This agreement with a dispersed barrier model supports the assumption of strong obstacles as based on the coherency data cited earlier in this section [2, 93]. It should be noted that expected microhardness values are converted to or from MPa to Hv using Equation 4.1, a conversion determined for BCC Fe alloys by Busby et al. [187].

$$\sigma_y = 3.06 * VHN \tag{4.1}$$

Differences in measured and expected microhardness could be attributed to unaccounted for Hall-Petch grain boundary strengthening, strain hardening from residual stress induced dislocation accumulation, vacancy point defect accumulation from rapid cooling in AM processes, and/or solid solution strengthening from additions of Mo, Y, or O to the matrix beyond the model FeCrAl alloy [3, 188]. These additional contributions would be combined with the dispersion strengthening and added to the base hardness using an appropriate root sum square and linear superposition relationships [100].

4.5. Build Property – Operating Parameter Relationships

4.5.1. Influence of Operating Parameters on Build Quality

Further examination of the effect of operating parameters on the overall build quality was also done. Increasing energy density resulted in an increase in build quality as has been described in the literature [189, 190]. Insufficient energy density has been shown to lead to poor melt pool penetration and poor bonding between layers (Specimens 1 and 3) causing lack-of-fusion defects and other types of porosity [75, 191, 192]. The typical PBF-LB correlation for energy density (Equation 4.2) was chosen to compare with part density (**Figure 4.19**).

$$E = \frac{P}{v*h*t} \tag{4.2}$$

where E is energy density (J/mm^3), P is power (W), v is tool speed or raster speed (mm/s), h is hatch spacing or the spacing between consecutive laser passes (mm), and t is the layer height (mm) [189, 190, 193]. Alternative relationships to compare operating parameters and build quality were examined; however, there was little useful correlation differentiating them from a simple correlation between build quality and laser power. So, a relationship that provided more a useful comparison was chosen. As shown in **Figure 4.19**, a clear positive correlation exists between this relationship and part density.

Analyzing the defect density results in **Figure 4.2** shows strong degradation effects from a pulsed laser raster pattern. Comparing specimens 1 and 3 to 2 and 4 demonstrates how increased thermal cycling produced from pulsing a laser, while improving oxygen retention of specimens 1 and 3, leads to increased residual stress and lack-of-fusion defects. Decreasing the time a laser impinges on a surface during a build

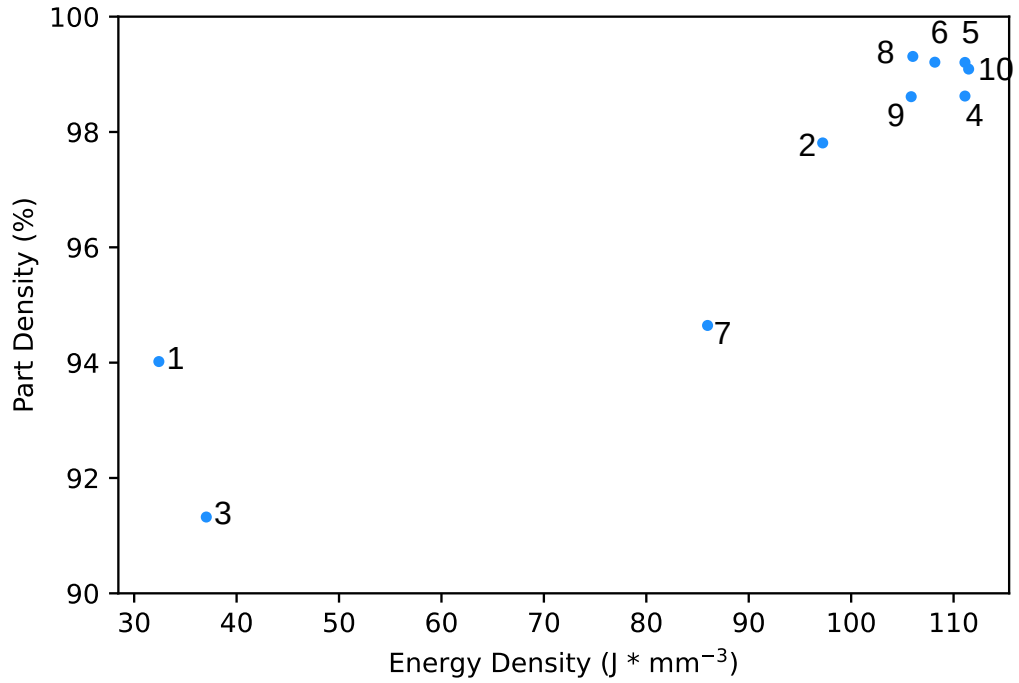

Figure 4.19: Energy Density v. Part Density of all as-built specimens.

process reduces the total energy delivered (as shown in **Figure 4.19**) to the specimen, reduces melt pool depth, causes insufficient bonding between layers, and thereby increases as-built defect density [75, 77, 194]. A pulsed laser raster was clearly effective in increasing O retention as shown in **Table 4.1**, so further research should still consider pulsed laser rastering as a potential raster pattern when dissolvable gas retention is a focus. Increasing the pulse frequency and decreasing pulse amplitude could potentially capitalize on increased O retention from the resultant surging solid-liquid interface while trying to minimize lack of fusion defects.

This is further supported by directly comparing the total energy deposited during one bead pass for a pulsed and continuous laser raster pattern at a 400 W laser power. Using data collected by a data recorder on the DED AM device used for these experiments, a power deposition with respect to time for a single bead pass was summed and normalized (shown in **Figure 4.20**). It was determined that Specimen 3 received 39% of the effective energy received by Specimen 4, an effective laser power of 155 W compared to 400 W. This reduction in energy deposition resulted in lack of fusion defects.

Unexpectedly high defect density was present in Specimen 7, which was built using the highest laser power of all samples. This is likely a result of machine malfunction. Near the end of this build, powder flow became inconsistent due to powder bridging across the feed hopper. Unpredictably, powder would cease flowing while the laser would continue to traverse its programmed raster pattern dumping large amounts of energy into the part without adding material to absorb the excess energy.

Examining the defect densities of specimens 6 and 9 gives some insight on how welding gas O concentration affects build quality. O being a surface-active element has a

a

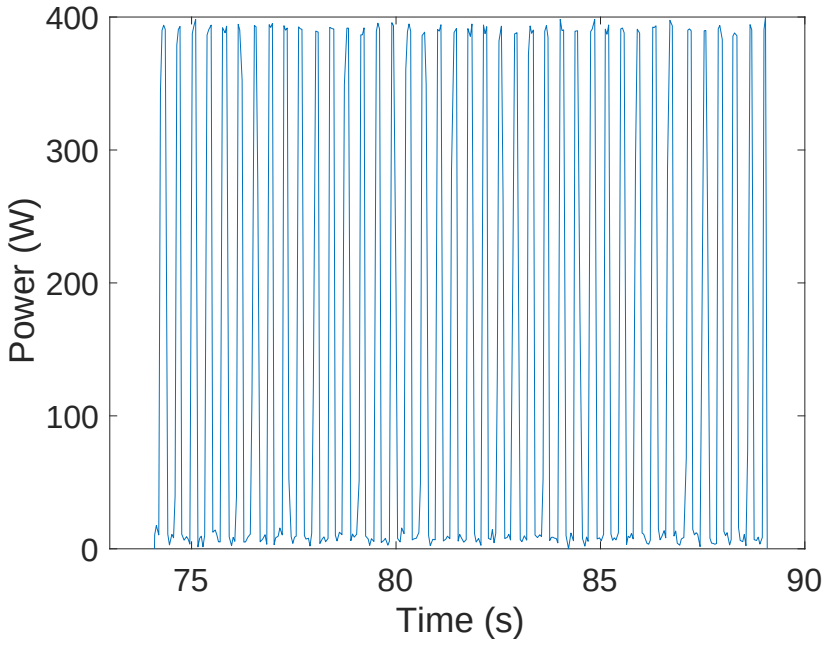

b

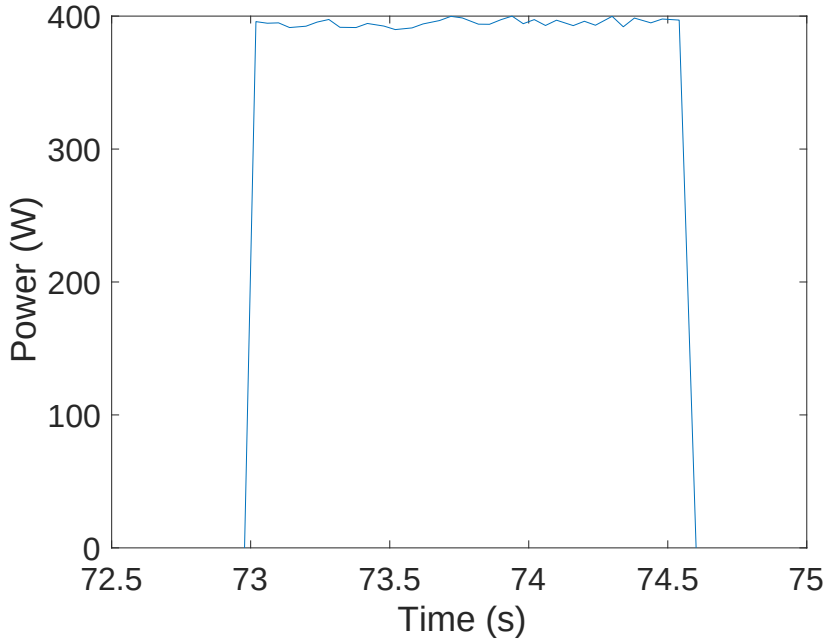

Figure 4.20: Power deposited for pulsed raster bead pass (Specimen 3; a) and continuous raster bead pass (Specimen 4; b).

direct effect on Marangoni convection and resulting melt pool shape. Increased in O in the welding gas between specimens 6 and 9 results in a shift from a wide and shallow melt pool to one deep and narrow (6 and 9, respectively) [195, 196]. This changed the solidification conditions in the melt pool and thus the propensity to form cracks and other defects.

As with conventional manufacturing of ODS alloys, there is a specific narrow window of operating conditions that yields a usable, good quality part when using techniques like laser-based DED AM. Applying too little energy to achieve complete melting leads to lack-of- fusion defects (specimens 1 and 3). Applying too much energy can yield keyholing instability and other subsequent defects [197]. This work has not found the perfect set of conditions for producing a good quality part. Focus was placed on producing large numbers of nanoscale dispersoids, however, a reasonable quality part was achieved.

4.5.2. Influence of Operating Parameters on O Content

Dissolution of gaseous O by liquid steel was described in Section 2.7 where it was assumed that O dissolution was dictated by Sieverts' law. Using the equilibrium reaction described in Equation 2.12 and the reaction rate equation established in Equation 2.13, an expected equilibrium concentration of dissolved O_2 in liquid steel can be calculated as a function of O partial pressure and liquid temperature. Should an O-rich gas stream interact with a high energy laser, however, diatomic. O molecules can dissociate into monatomic O. An analogous equilibrium reaction and reaction rate equation for dissolution of monatomic O is described in equations 2.14 and 2.15 [140, 141].

To better understand how much oxygen (re: what the oxygen partial pressure was) was available to be dissolved during a build process using an O-rich welding gas, a simple

dilution model was developed and solved. The build chamber was assumed to be a 6 ft by 6 ft by 4 ft rectangular prism initially containing a 100% Ar gas mixture at ambient temperature (72°F) and pressure (1 atm). This fully inert condition was assumed because the chamber was pumped down to a low-level vacuum and backfilled with facility Ar until a readout on an oxygen concentration sensor read less than 1% O_2 prior to starting a build. Incoming gas flow from the powder nozzle was 44 SLPM with a composition of 94.5% Ar, 4.5% He, and 0.1% O_2. It was assumed that the outgoing flow rate of gas was equal to in the incoming flow rate.

A differential equation describing our system is shown in Equation 4.3.

$$\frac{dA_{O_2}}{dt} = X_{O_2}^{in} Q_{in} - X_{O_2}^{out} Q_{out} \tag{4.3}$$

where A_{O_2} is the volume of oxygen present in the chamber, $X_{O_2}^{in}$ is the fraction of diatomic oxygen present in the inlet stream, $X_{O_2}^{out}$ is the fraction of diatomic oxygen in the exit stream, and $Q_{in} = Q_{out}$ is the volumetric flow rate of gas in/out of the system. It is known that a concentration of diatomic oxygen in the effluent gas stream

$$X_{O_2}^{out} = \frac{A_{O_2}}{V} \tag{4.4}$$

where V is total volume of the chamber.

Plugging Equation 4.4 into Equation 4.3 sets up a separable variables differential equation with an initial condition that the amount of oxygen in the build chamber at time $t = 0$ is also 0. Solving this equation yields the following relationship describing the amount of diatomic oxygen present in the build chamber at any given time:

$$A(t) = X_{O_2}^{in} V - X_{O_2}^{in} V e^{-\frac{Q}{V}t} \tag{4.5}$$

Dividing by the build chamber volume on both sides of the equation gives the concentration of diatomic oxygen present with respect to time.

$$[O_2]_{chamber} = X_{O_2}^{in} - X_{O_2}^{in} e^{-\frac{Q}{V}t} \quad (4.6)$$

Utilizing the assumptions given at the beginning of this section and an approximate build time for a given specimen (approximately 45 minutes), it was determined that a partial pressure of ~ 3.85x10^{-3} atm of diatomic oxygen would be available (partial pressure is equal to the fractional amount of a species multiplied by a system's total pressure). This corresponds to an equilibrium solubility of 7.87 wt% diatomic O in a melt pool at 2861 ºC according to Sieverts' law. Full dissociation of all O2 present would provide a partial pressure of 7.66x10^{-3} atm of monatomic O available for dissolution. This yields an equilibrium solubility of 5.46 wt% at 2861 ºC. The above relationships are demonstrated in **Figure 4.21**. Unfortunately, separate measurement of diatomic and monatomic O was not possible for this system. Comparing above theoretical results with compositional data provided in **Table 4.1** shows that all specimens were deficient at capturing the appreciable amounts of O that should have been available to them during solidification. Specimen 8 had the highest O uptake with concentration of 0.067 wt%, two order of magnitude less than what was predicted by Sieverts' law. This could be a result of either insufficient solidification velocity leading to poor solute trapping, conditions outside of what is generally accepted for Sieverts' law to apply, or both. Sieverts' law was written to describe the dissolution of diatomic gases in pure liquid metal when a dissolving gas is present in very low concentrations. Higher concentrations can cause inaccuracies [198]. The estimated partial pressures in these experiments are several orders of magnitude higher than those expressed in the literature for a similar O – steel system [140, 141].

Using a description of solute trapping from Aziz in 1982, the potential for solute trapping to influence dissolution and retention of O as described by Sieverts' law can be

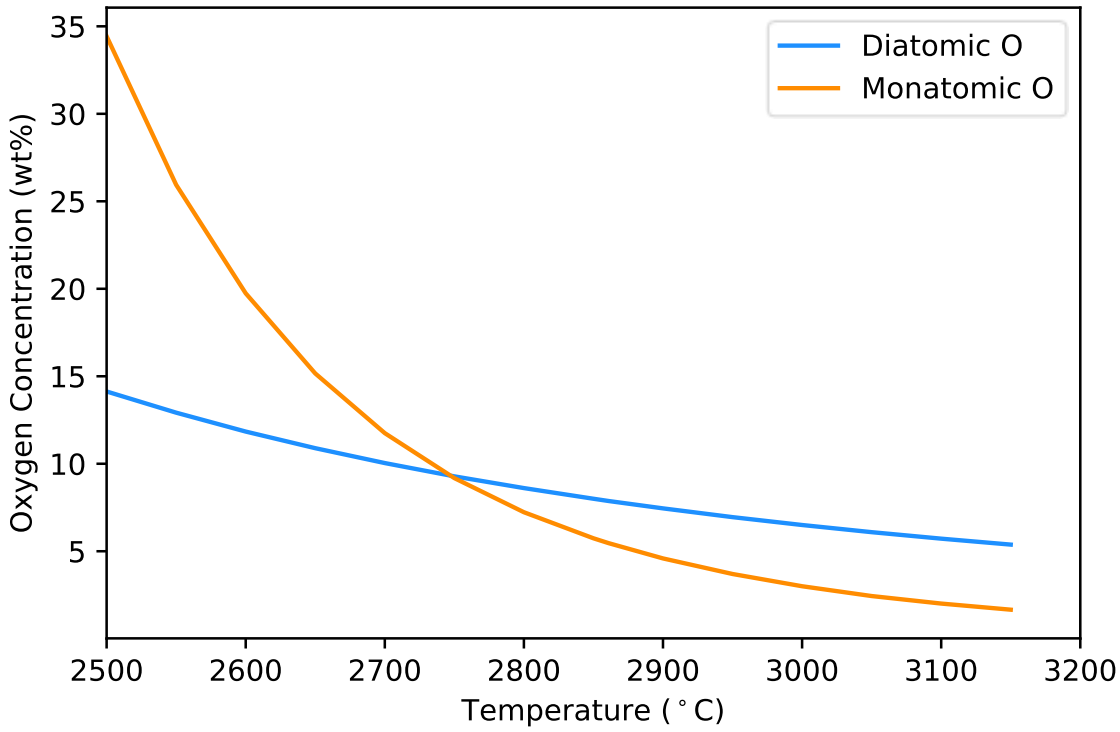

Figure 4.21: Equilibrium O concentration in liquid steel as a function of liquid temperature. Partial pressure of O was 3.85×10^{-3} atm for dissolution of diatomic O and 7.66×10^{-3} atm for dissolution of monatomic O.

examined [83]. Aziz described solute trapping as an ability of a solidification interface to move more quickly than solute atoms can diffuse away in a liquid phase resulting in the trapping or locking of solute atoms within a solid phase. For complete solute trapping, a solidification velocity needs to be greater than the trapping velocity. If a solidification velocity is within approximately one order of magnitude of that system's trapping velocity, some portion of solute trapping is said to still occur [83, 142]. For complete trapping of O in BCC Fe, a solute trapping velocity (u) was determined using Equation 2.16 as described in **Section 2.7**. A trapping velocity for O in BCC iron was determined to be approximately 9.6 m/s. This assumes an oxygen diffusivity in liquid Fe of 2.38×10^{-5} cm^2/s, and an interatomic spacing of solid BCC Fe of 0.248 nm [183, 199]. In this system, the maximum solidification velocity is the fastest tool speed of 720 mm/min or 0.012 m/s putting it approximately two orders of magnitude less than the trapping velocity. This is supported by the findings from Sieverts' law calculations where a two order of magnitude less concentration of O was measured compared to what was predicted (0.067 wt% vs. ~5-7 wt%).

Solute trapping does not appear to completely explain differences in measured O content between specimens, however. Specimen 8 maintained the highest O content while having the slowest tool speed (maximum potential solidification velocity). Before going further, it is important to remind the reader that reported O content values in this section would include oxide agglomerates in addition to any O trapped in solid solution. To further examine this unexpected result, melt pool thermal modeling was done to better understand melt pool characteristics and simulate theoretical solidification velocities. Calculating expected solidification velocities required an estimation of the temperature gradient and cooling rate for thermally unique build parameters (specimens 2, 5, 6, 7, 8,

and 10 were examined; pulsed laser rastering specimens were excluded for simplicity). The classic Rosenthal equation (Equation 4.7) for a point-source on a thick substrate was used to describe the thermal conditions and related melt pool characteristics at each set of operating parameters along both a centerline in an x-z plane and along a melt pool surface in an x-y plane[146].

$$T - T_o = \frac{q_o}{2\pi\lambda}\left(\frac{1}{R}\right)\exp\left\{\left(-\frac{v}{2a}\right)(R + x)\right\} \tag{4.7}$$

where

$$R = \sqrt{x^2 + y^2 + z^2} \tag{4.8}$$

q_o is the laser power, λ is the thermal conductivity (29.89 W/(m*K)), v is the tool speed, and a is the thermal diffusivity (4.334e-6 m^2/s) [10]. Heatmaps showing thermal profiles of specimens 2, 5, 6, ,7, 8, and 10 are shown in **Figure 4.22** below. A temperature upper bound at 2861 °C–the boiling point of Fe–was used to eliminate unrealistic temperatures predicted near the center of a melt pool. Each x-y plane heatmap included two contours marking 2861 °C and 1532 °C (assumed melting point of the alloy). Each x-z plane heatmap included one contour marking 1532°C and the edge of the melt pool. Each heatmap is a 6 mm x 6 mm plot.

Contours were used to determine the thermal gradient along the x-y plane. Distance (Δr) between the inner and outer contours was measured beginning perpendicular to and ending opposite of the laser's path of travel while rotating about the centroid of the inner contour in 3° increments. As the inner contour denotes the boiling point of Fe and the outer contour denotes the melting point of FeCrAl, a thermal gradient (∇T) as a function of angle (90° to 180°) about a melt pool was calculated. This is shown in **Figure 4.23**.

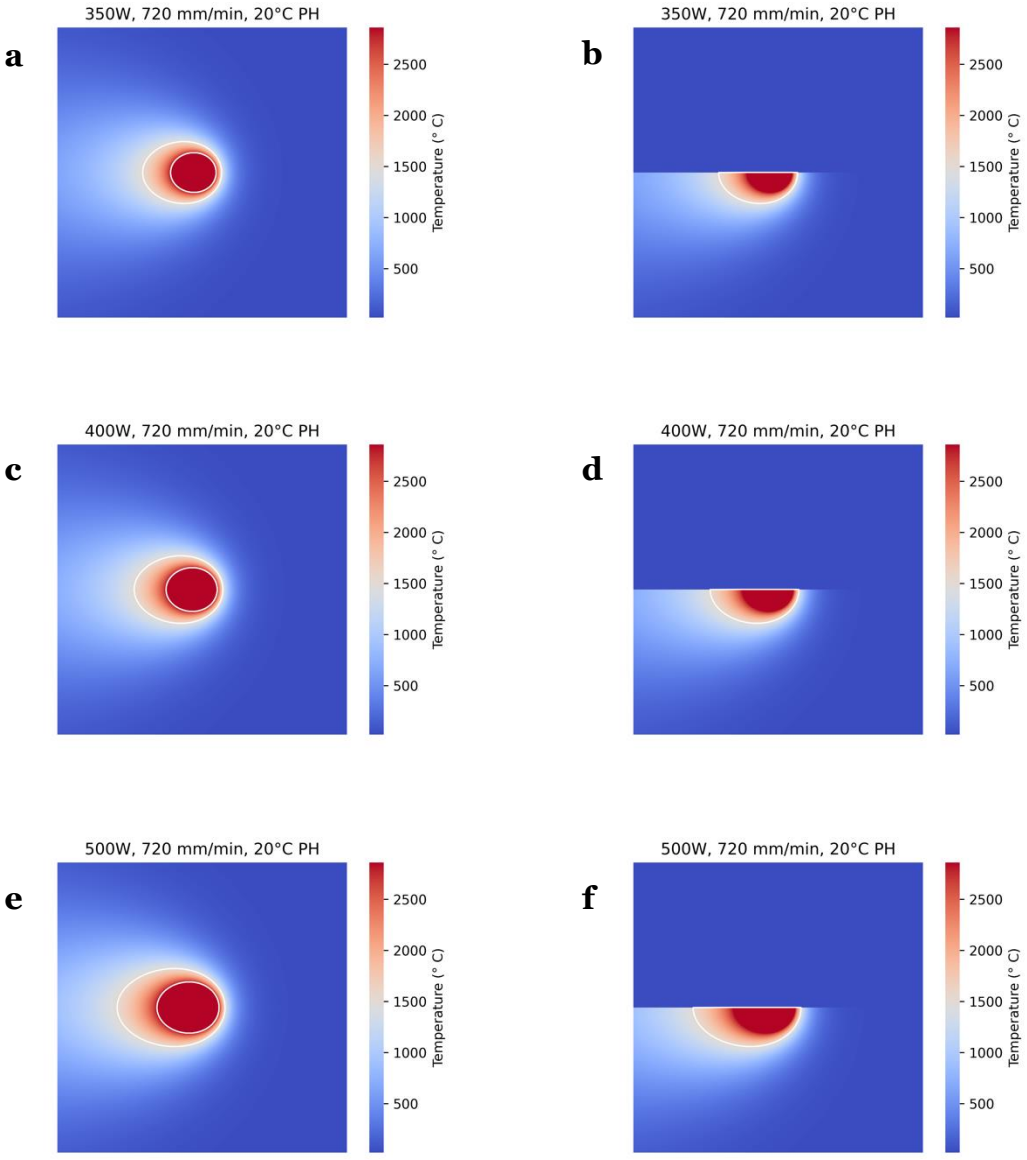

Figure 4.22: Thermal heatmaps for specimens 2, 5, 6, 7, 8, 10 with x-y plane on the left (a, c, e, g, i, k) and x-z plane on the right (b, d, f, h, j, l). The laser path of travel is to the right of each heatmap. Laser is traveling to the left of the page.

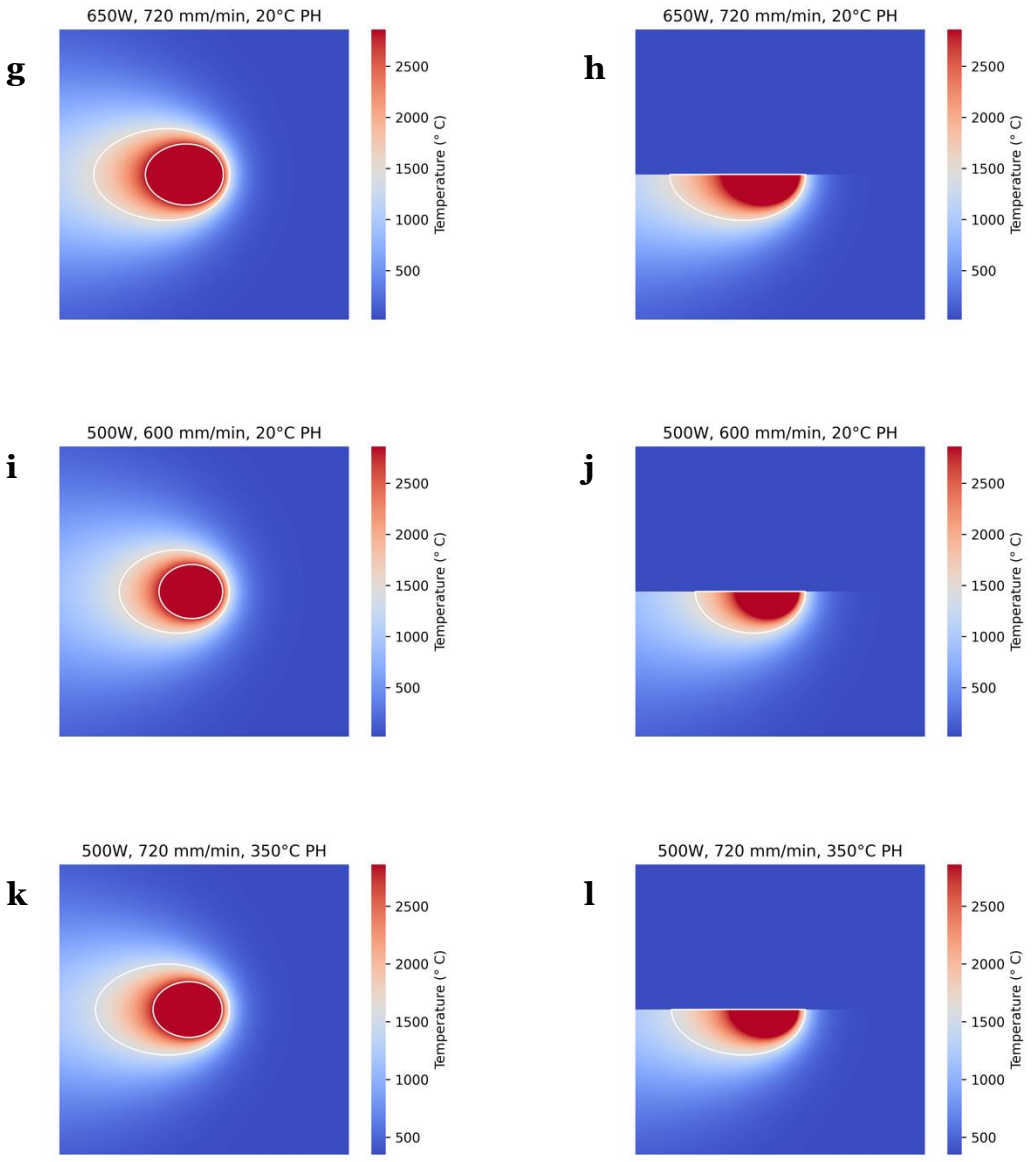

Figure 4.22 continued

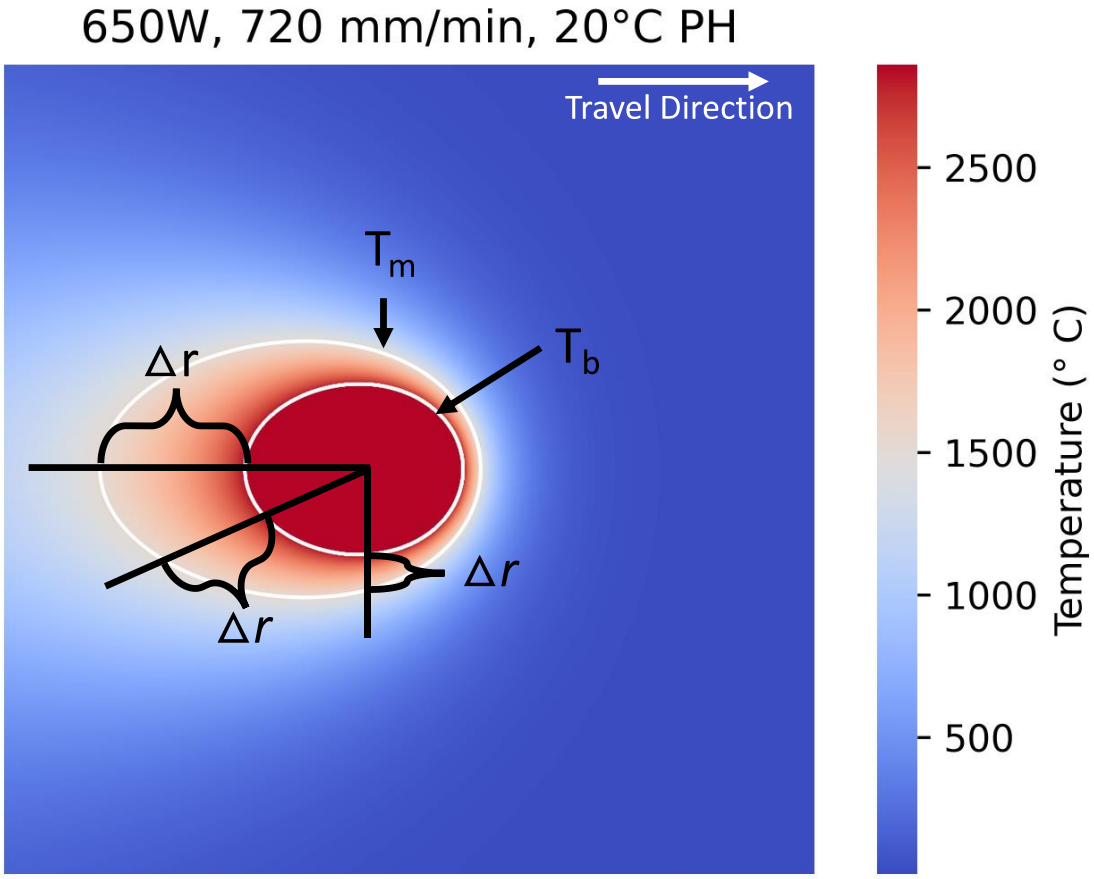

Figure 4.23: Diagram of contours being used for determining thermal gradient. Laser is traveling to the left of the page.

A cooling rate (*C.R.*; Equation 4.9) was then calculated for each specimen listed above using the following equation derived from Rosenthal's equation.

$$C.R. = \frac{2\pi\lambda}{\frac{q_o}{v}}(T - T_o)^2 \tag{4.9}$$

where T is taken to be the melting point (1532°C) [200] and T_o is taken to be the pre-heat temperature (20°C or 350°C, depending on the specimen) [146]. This gives a *C.R.* at a solid-liquid interface of each melt pool. Solidification velocity around a melt pool was calculated using this simple relationship:

$$\text{Solidification Velocity} = \frac{\text{C.R.}}{\nabla T} \tag{4.10}$$

where ∇T is the thermal gradient.

Average solidification velocity was plotted as a function of laser power in **Figure 4.24**. In general, an increase in laser power correlated with a decrease in the average solidification rate. Specimens 8 and 10 stood out as changes in the tool speed (Specimen 8 tool speed was 600 mm/min vs 720 mm/min) and pre-heat temperature (Specimen 10 pre-heat temperature was 350°C vs. 20°C), respectively, also occurred. A decrease in tool speed caused a decrease in the average solidification velocity. An increase in the pre-heat temperature did the same. Increases in the energy deposited reduced the driving force for solidification. Overall, total deviation in solidification velocity across the tested operating conditions was small (~ 25%).

Maximum and average solidification velocities were plotted with respect to O content to examine how solidification velocity influences O retention. O delivery method and available concentration were constant for all but Specimen 2 (350 W consolidated under oxygen-rich atmosphere instead of oxygen-rich welding gas). These results are shown in **Figure 4.25** with marker size showing relative laser power. Generally, an

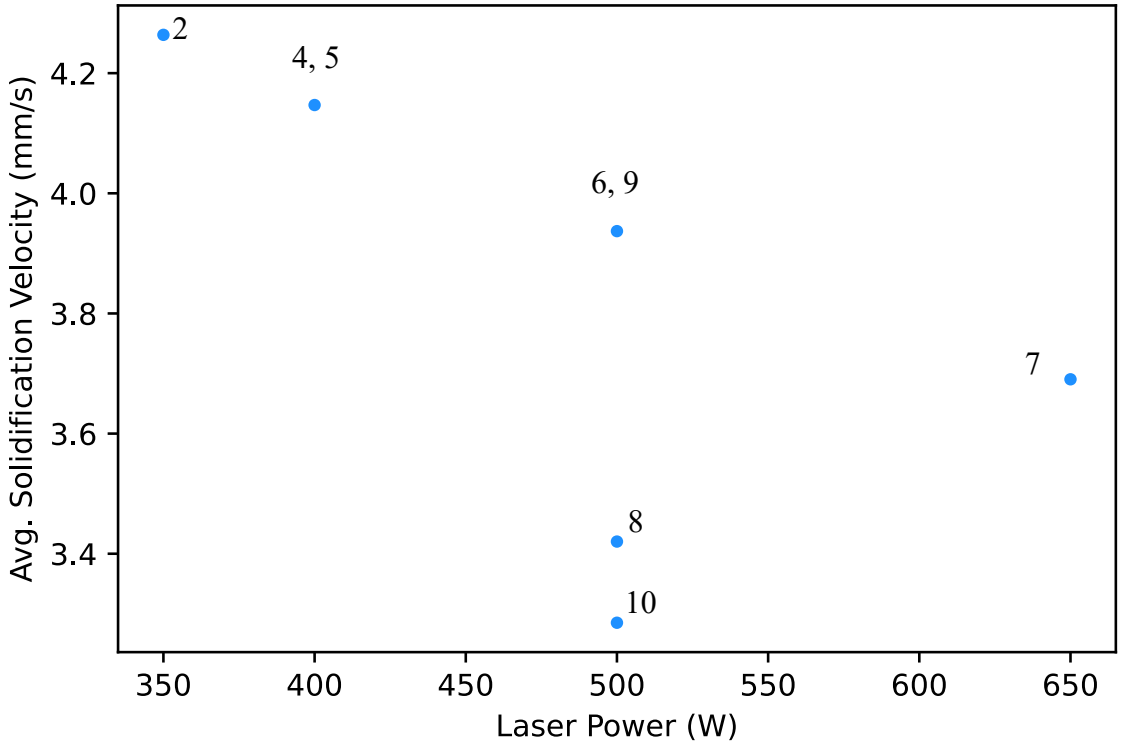

Figure 4.24: Comparison of laser power to average solidification velocity of listed specimens.

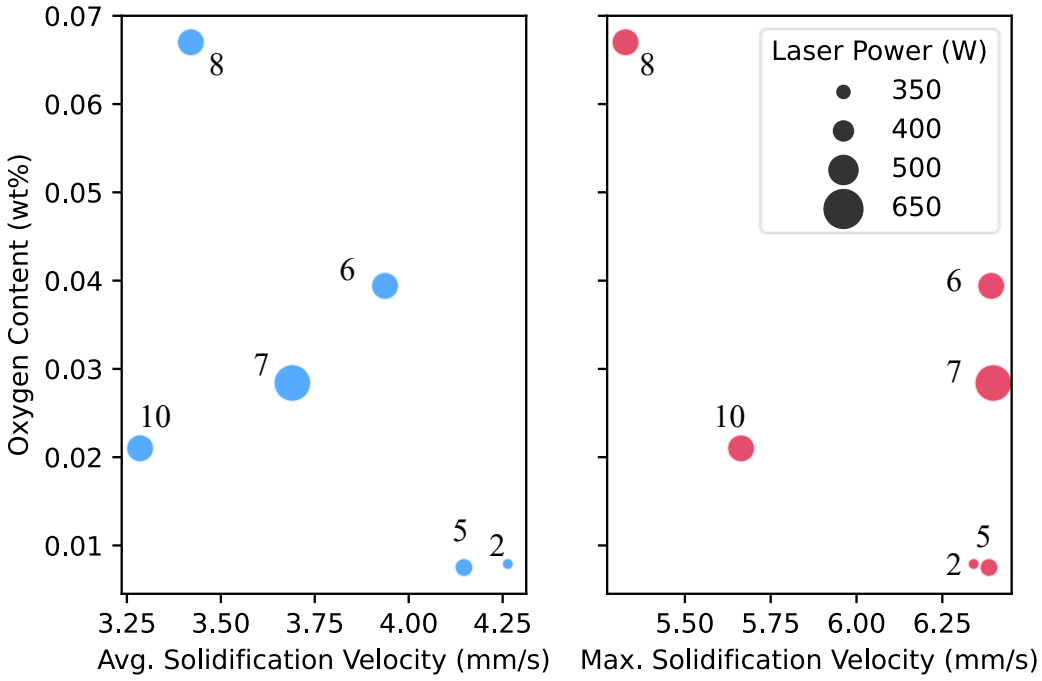

Figure 4.25: Comparison of average (blue) and maximum (red) solidification velocities to specimen O content. Note: the data point for Max. Solidification Velocity of Specimen 2 is shifted to the left 0.04 mm/s to prevent its overlap with Specimen 5.

increase in solidification rate negatively correlated with O dissolution and retention. This was most strongly evident comparing maximum solidification velocity and O content. The same trend was apparent for average solidification velocity too.

Results in **Figure 4.25** contradict the logic that increasing solidification velocity increases solute trapping potential and maximizes O retention. This suggests that either solute trapping was not the only controlling mechanism for O retention in these experiments. Other possible influences could be: 1. Melt pool lifetime or time available for O to diffuse the depth of the melt pool, or 2. Gas incidence time or the time the oxygen-rich gas stream was in contact with the surface of the melt pool, or 3. Decreased solidification velocity provided extra time for oxide forming elements to react and bind oxygen to the system [140, 141, 193]. It is important to note that for the second possible influence to be a limiting step, gas incidence time must be less than melt pool lifetime. Otherwise, melt pool lifetime would be the limiting factor.

The O delivery method and available O concentration for all specimens compared, aside from Specimen 2, was kept constant. Specimen 2 was consolidated under the first experimental setup, while the remainder were consolidated under the second experimental setup. Aside from a possible change in relative concentrations of diatomic and monatomic O from laser interactions, the concentration of O above the melt pool should not be a factor. As demonstrated above, this relationship is very sensitive to small changes in relative concentrations of diatomic and monatomic O species, especially as melt pool temperatures drop. If an increase in laser power resulted in an increase in dissociation of diatomic O, then the amount of dissolved O at lower melt pool temperatures would increase due to more readily dissolvable monatomic O being present as suggested in the literature [140, 141]. As a result, one would expect an increase in O

content in a build as laser power increased from Specimen 5 to Specimen 6 to Specimen 7 (400 W, 500 W, and 650 W, respectively). However, this was not the case. O content increased from Specimen 5 to Specimen 6 but decreased from Specimen 6 to Specimen 7. This could be a result of O's strong retrograde solubility in liquid Fe-increased laser power increases melt pool temperatures while also increasing the likelihood of dissociation of diatomic O into monatomic O-or an effect of decreasing solidification velocity from Specimen 6 to Specimen 7 [140, 141].

To better examine the mechanism controlling oxygen dissolution in a melt pool, the dimensions of a melt pool were determined. Using an algorithm that enclosed a hemi-elliptical contour of the edge of a melt pool in an x-z plane, a length and depth of each melt pool was measured. To calculate melt pool lifetime, the following equation was used:

$$melt\ pool\ lifetime = \frac{melt\ pool\ length}{average\ solidification\ velocity} \tag{4.11}$$

Figure 4.26a shows a relationship between melt pool lifetime and O content of the examined specimens. There was not a clear relationship between the two. To further confirm that melt pool lifetime was unlikely to be the controlling factor in specimen O content, a required diffusion time for O to diffuse the total depth of each melt pool was calculated using standard diffusion theory.

$$\frac{C_x - C_o}{C_s - C_o} = 1 - \mathrm{erf}\left(\frac{x}{2\sqrt{Dt}}\right) \tag{4.12}$$

where C_x is the target concentration of oxygen at the bottom of the melt pool, C_o is the initial concentration of oxygen in the as-received powder, C_s is the concentration of oxygen at the surface of the melt pool, x is the melt pool depth as calculated using the Rosenthal Equation, D is the diffusivity of oxygen in liquid Fe (taken to be approximately 4×10^{-5} cm^2/s [199]), and t is the time required for the concentration at depth x to reach

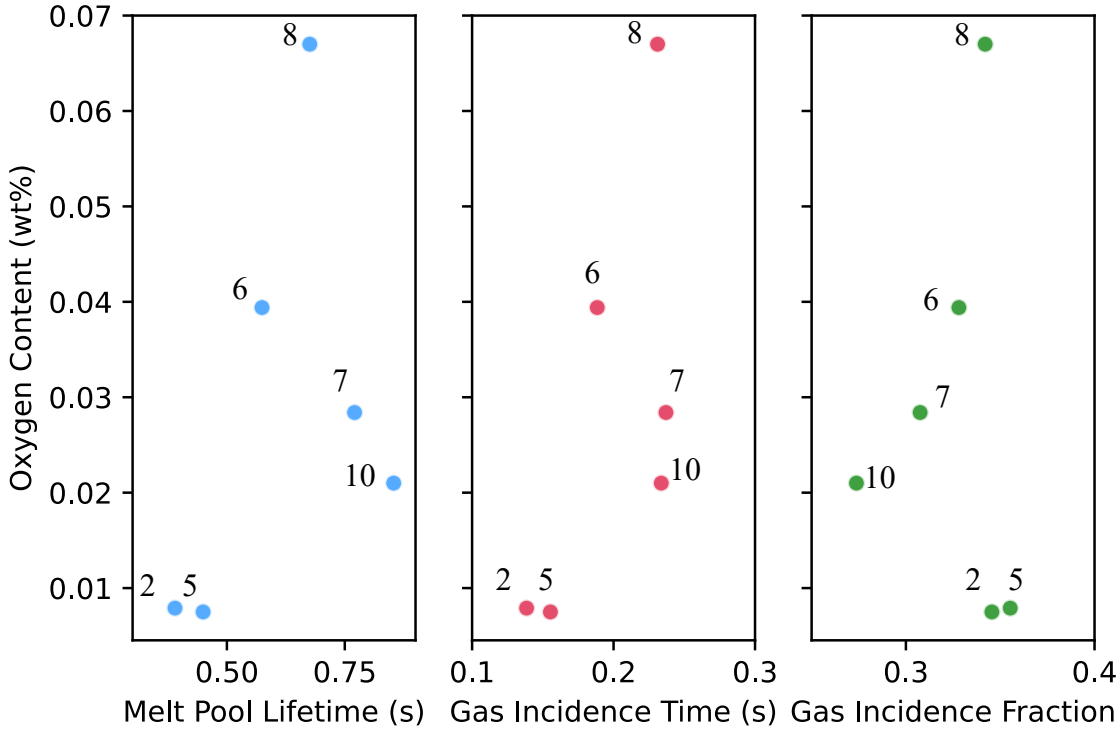

Figure 4.26: a. Comparison of melt pool lifetime (blue), b. gas incidence time (red), and c. gas incidence fraction (green) to specimen O content.

C_x [201]. Erf is a Gaussian error function. Solving Equation 4.12 for t for each melt pool depth while keeping all other conditions constant yielded required diffusion times on the order of 100 s, two orders of magnitude larger than calculated melt pool lifetimes. Thus, melt pool lifetime was unlikely to be the sole controlling factor for O dissolution and retention in these experiments.

Differences in surface O concentrations and melt pool lifetimes did not appear to explain a differences in O content between specimen builds. Equation 4.13 was used to calculate gas incidence time and examine how contact time between a melt pool and oxygen-rich gas stream influenced O retention.

$$gas\ incidence\ time = \frac{melt\ pool\ length}{tool\ speed} \tag{4.13}$$

The results are shown in **Figure 4.26b**. Specimen O content appears to correlate positively with increases in gas incidence time. This suggested that a mixture of solidification velocity and interaction time between a liquid melt pool and reactive gas stream was possibly controlling O content.

Again, gas incidence time does not cleanly correlate with O retention. Specimens 7 and 10 have longer gas incidence times than Specimen 8; however, Specimen 8 retained significantly more O. Examining the relative amount of time that a melt pool was under a reactive gas stream (denoted as the gas incidence fraction) may help rationalize the difference. Equation 4.14 shows how gas incidence fraction was calculated.

$$gas\ incidence\ fraction = \frac{gas\ incidence\ time}{melt\ pool\ lifetime} \tag{4.14}$$

The effect of gas incidence fraction on O retention is shown in **Figure 4.26c**. Ignoring Specimen 2 due to having a different gas delivery method (atmosphere instead of welding gas), a reasonably strong positive correlation between gas incidence fraction

and O content appears. Specimen 5 also seems to be an outlier. It is unclear as to why Specimen 5 was poor at dissolving and retaining O with its high gas incidence fraction and high solidification velocity. Specimen 5 was the first produced under the second experimental setup, so perhaps there was a delay in oxygen availability at the melt pool surface after startup. **Table 4.5** summarizes these calculations.

A few points of interest stand out when comparing how other operating parameters affected O retention. Comparing continuous laser raster specimens 2 and 4 to their pulsed laser rastering counterparts, specimens 1 and 3, demonstrated the importance of solute trapping and its connection to rastering method. The literature suggests that pulsed laser rastering can lead to an increase in solid-liquid interface velocity. This would improve the rate of O solute trapping [202, 203]. Examining the effective energy deposited during a singular laser pass of a pulsed laser raster pattern vs a continuous laser raster pattern reinforces this idea. As mentioned in **Section 4.5.1**, Specimen 3 received 39% of the effective energy received by Specimen 4, an effective laser power of 155 W compared to 400 W. This significant reduction in energy absorbed from a pulsed raster type led to an appreciable increase in solid-liquid interface velocity as demonstrated in **Table 4.5** when comparing like specimens with different laser powers such as specimens 5, 6, and 7.

As summarized in **Table 4.1**, pulsed rastering specimens 1 and 3 retained 2 to 3.5 times more O compared to the continuous raster specimens 2 and 4. In principle, increased O retention is desirable for creation of a high density of ODS particles. In these exploratory tests pulsed raster specimens contained unacceptably high defect densities (figures 2 and 3). Therefore, pulse raster operation may not be a promising approach for this alloy system.

The O delivery mechanism is also important. Comparing specimens 4 and 5, the

Table 4.5: Rosenthal's equation simulation results of thermally unique build conditions (excluding pulsed rastering).

Specimen	Laser Power (W)	Tool Speed (mm/min)	Pre-Heat Temp. (°C)	Avg. Solid. Velocity (mm/s)	Melt Pool Lifetime (s)	Gas Incidence Time (s)	Oxygen Content (wt%)
2	350	720	20	4.26	0.39	0.14	0.0079
5	400	720	20	4.15	0.45	0.16	0.0075
6	500	720	20	3.94	0.57	0.19	0.0394
7	650	720	20	3.69	0.77	0.24	0.0284
8	500	600	20	3.42	0.68	0.23	0.0670
10	500	720	350	3.29	0.85	0.23	0.0210

only difference is O delivery method. O-rich welding gas impinging on a melt pool nearest the laser provided an increase in O retention in Specimen 5. This is likely due to potential laser induced dissociation of O_2 within the welding gas leading to increased monatomic O which improves dissolution into a liquid phase [140]. It is also likely that a non-reactive welding gas for Specimen 4 inhibited contact between the melt pool and oxygen-rich atmosphere long enough to reduce O uptake. Melt pool lifetimes are on the order of 0.5 s, and gas incidence time for a non-reactive welding gas is 0.16s. Therefore, a significant portion of a melt pool lifetime is under an inert environment that pushes O away from a melt pool, further minimizing time spent under a reactive atmosphere. In future experiments, examining if a combination of an oxygen-rich atmosphere and oxygen-rich welding gas would further improve O dissolution and retention could prove worthwhile. Combining both sources would maximize melt pool time spent under a reactive environment encouraging dissolution of O by maintaining a chemical driving force necessary to encourage O dissolution and retention in a melt pool.

Comparing specimens 6 and 10 gives insight regarding an effect of a pre-heat on a solid-liquid interface velocity and solute trapping. The only different operating parameter between specimens 6 and 10 is an addition of a 350 °C pre-heat. A preheat was intended to reduce residual stress buildup by reducing thermal gradients caused by rastering. However, doing so led to an appreciable decrease in the solid-liquid interface velocity (3.94 mm/s to 3.29 mm/s), hindered solute trapping, and allowed more time for O to diffuse away from the solidification front [75, 77, 202, 203]. Gas incidence time for Specimen 10 did increase compared to Specimen 6. However, the fraction of Specimen 6's melt pool lifetime spent under contact of a reactive welding gas was comparably larger (gas incidence fraction shown in **Figure 4.26c**). The melt pool of Specimen 6 spent more

of its lifetime under a concentration gradient encouraging oxygen dissolution than Specimen 10.

4.6. Summary

The feasibility of using *in situ* oxidation during DED AM to produce ODS FeCrAl alloys was examined in this work with mixed results. Two different oxygen delivery methods were examined across a matrix of operating parameters to investigate the effects of laser power, available oxygen concentration, preheat temperature, and rastering types on oxygen retention and build quality. Key observations are as follows:

2. Feasibility of using DED AM with *in situ* oxidation to produce ODS alloys, alloys with nanoscale dispersions approaching 10^{21} m^{-3}, with a moderate number density of homogenously distributed nanoscale dispersoids has been demonstrated. This approach shows potential as an alternative to conventional mechanical alloying processes for ODS alloys but considerable work needs to be done to overcome a multiple orders of magnitude difference in dispersoid number densities between DED AM and conventional powder metallurgy techniques.
3. Solidification velocity and gas incidence fraction were critical factors in maximizing oxygen dissolution and retention using *in situ* oxidation
4. Considerable optimization of alloy design and operating conditions are needed to reduce cracking and inclusion formation during DED AM of ODS FeCrAl and increase dispersoid number densities. Reduction of inclusion formation and nanoparticle refinement provides a clear path to improving achievable number densities.
5. Appreciable improvement in material hardness was achieved through the addition of precipitates using DED AM with *in situ* oxidation.

CHAPTER FIVE

INFLUENCE OF ALLOYING ON AGGLOMERATION AND PRECIPITATION

5.1. Build Quality

5.1.1. Build Composition

Compositional analysis of samples of as-received powder, all as-built specimens, and a steel substrate are provided in **Table 5.1**. Expected compositions of B3/B4 and B5/B6 (ignoring changes in oxygen content) are also provided for reference. As expected, there was minimal change across major alloying elements (Fe, Cr, Al) between the powder and consolidated AM blocks, similar to what was observed in the first set of experiments. Changes in Y content seemed to correlate inversely with changes in O content. This is particularly noticeable in specimens using pre-build heat treated powder (B2, B4, and B6). This is again likely a result of agglomeration of Y-oxides in the melt pool during AM, forming slag that floats along the melt pool surface and is poorly incorporated into the Fe matrix due to poor wettability [61, 62, 81, 135, 143, 146]. Increasing O content is expected to improve wettability as predicted by simulations from Eo et al., which should help incorporate these oxides [143]. However, there may be a competing phenomenon. According to Le Chatelier's principle, an increase in reactants (O in this instance) would encourage formation of more Y-oxides, an already strongly favorable reaction due to Y's affinity for O [46]. Formation of more oxides would reduce the amount of O in a melt pool thus reducing wettability and incorporation of oxides. There is also a possibility of Y vaporization during AM; however, it is considered to be unlikely [165].

Si and C content of as-built B5 and B6 were approximately half of the expected values as shown in **Figure 5.1b**. This is likely a result of powder stratification after

Table 5.1: ICP-OES/IGF Compositional analysis of as-built specimens for varied alloying experiment.

	Species (wt%)								
Sample	Fe	Cr	Al	Y	O	Ti	Si	C	P
As-Rec. Powder	81.650	12.010	5.710	0.330	0.046	-	0.030	0.009	0.007
B1	81.510	12.120	5.760	0.330	0.059	0.040	0.030	0.006	0.010
B2	81.630	12.040	5.720	0.320	0.076	0.040	0.030	0.003	0.010
B3	80.860	12.050	5.750	0.330	0.051	0.630	0.030	0.160	0.010
B3F	80.830	12.040	5.760	0.350	0.067	0.640	0.030	0.150	0.010
B4	80.940	12.060	5.710	0.300	0.099	0.580	0.030	0.140	0.010
B5	81.320	12.100	5.790	0.340	0.064	0.040	0.160	0.068	-
B6	81.480	12.040	5.670	0.270	0.110	0.040	0.180	0.069	0.010
B3/B4 Expected	81.17	11.94	5.68	0.33	0.046	0.537	0.030	0.148	-
B5/B6 Expected	81.35	11.97	5.69	0.33	0.046	-	0.349	0.148	-
B1 Substrate	98.200	0.120	-	-	0.004	-	0.220	0.190	0.010

blending. Specimens B5 and B6 were the last two specimens produced in this set of experiments., so there was additional time for separation of the FeCrAl and SiC powders. It is possible that a more complex mechanism is at work here. During a basic oxygen furnace (BOF) steelmaking process, Si precipitates out of molten steel at high temperatures. This could lead to formation of a Si-rich slag layer and preferential removal of Si from the melt pool. Further, as in BOF steelmaking, O that is present can react with available C to create CO or CO_2 gas that will off-gas from the melt pool [204]. The nearly identical 2:1 ratio of expected Si content to measured Si content and expected C content to measured C content makes the former cause more likely. Future experiments should blend powders immediately prior to use. B3, B3F, and B4 did not seem to suffer from a similar issue (**Figure 5.1a**). Particle size differences between the PAC FeCrAl powder and the AEE TiC or WM SiC powders could also have had an influence. AEE TiC powder was closer in size to PAC FeCrAl and should separate less.

Addition of a pre-build heat treatment contributed appreciably to increasing as-built specimen oxygen content as shown in **Figure 5.2**. B2, B4, and B6 all showed increased O dissolution and retention over their counterparts (B1, B3/B3F, and B5, respectively) that did not receive a pre-build heat treatment. This process utilizes the chemical reservoir phenomenon used by Reiken et al. and Ordás et al. in their respective works on producing ODS alloys without mechanical alloying by forming oxide shells around powder particles [47, 205]. It also appears that the presence of Ti and Si (additional oxide forming elements and improvers of oxide-liquid steel wettability) accentuated O dissolution and retention. Increases in O content from specimens B3/B3F to B4 and B5 to B6 were larger than those observed from specimen B1 to B2. This increase has specimens B4 and B6 achieving O contents higher than their respective solubility

a

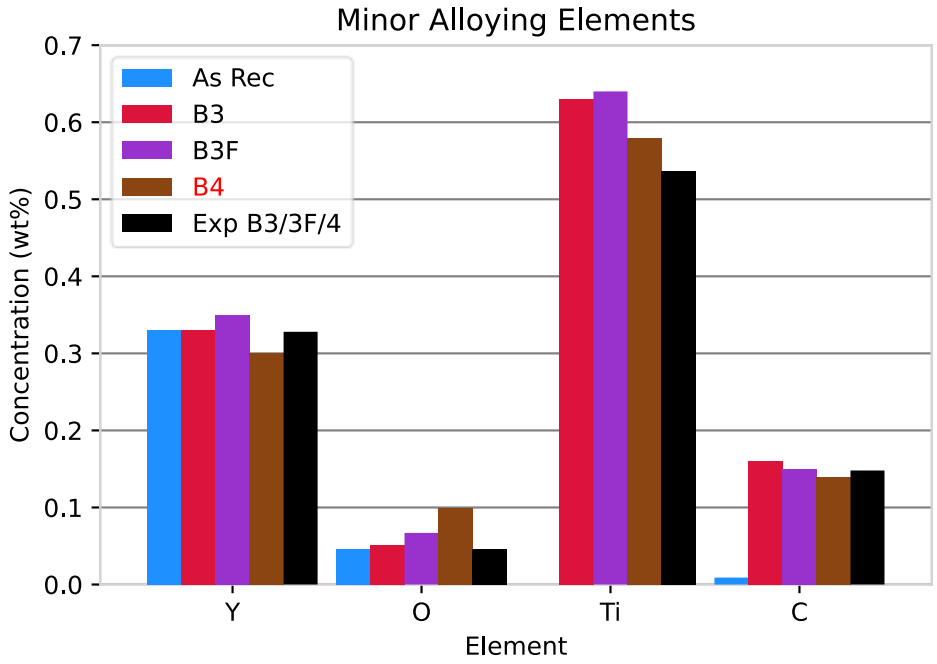

b

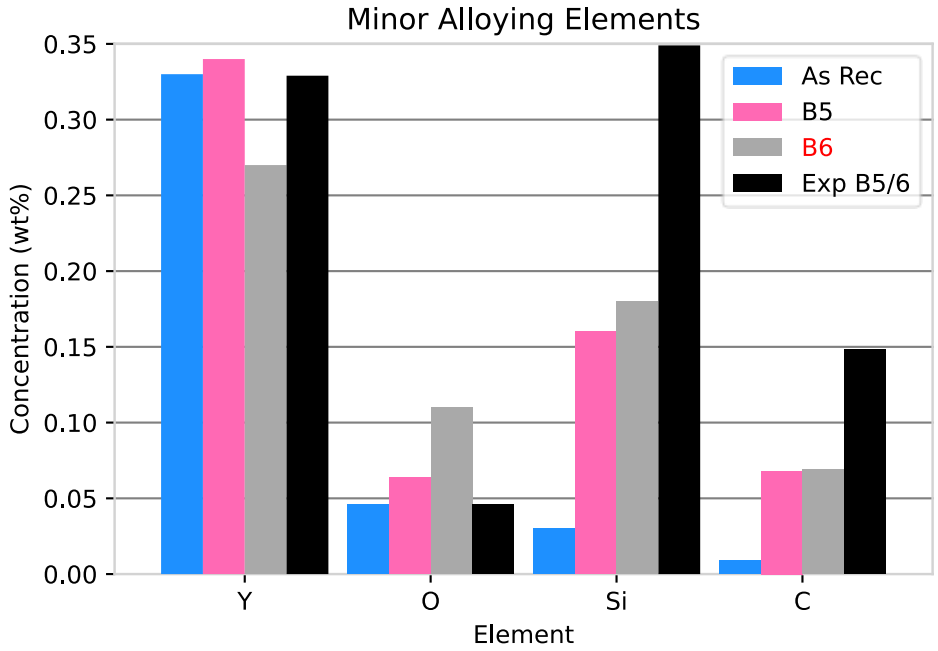

Figure 5.1: Comparison of minor alloying element concentrations of TiC (a) and SiC (b) added specimens to as-received powder and expected concentrations.

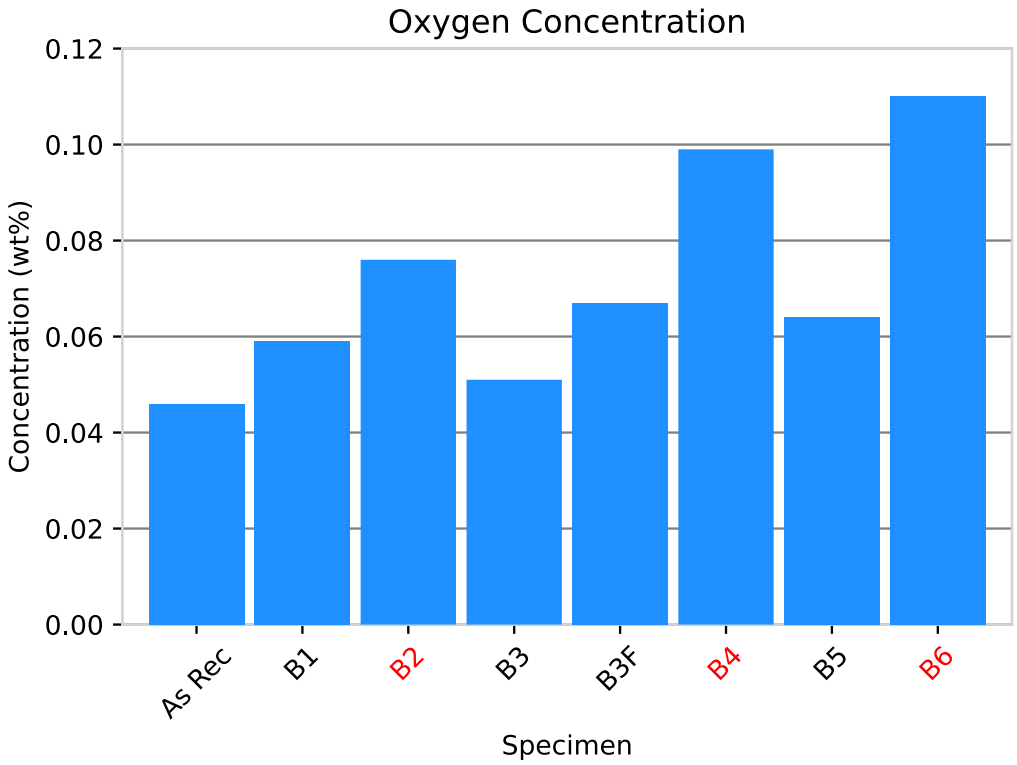

Figure 5.2: Comparison of as-built specimen O concentration. Specimens labeled in red used FeCrAl powder after a 350 °C, 1 h pre-build heat treatment.

limits as predicted by Thermo-Calc phase diagram simulations as shown in **Figure 5.3**, **Figure 5.4**, and **Figure 5.5** (as-received powder/B1/B2, B3/B3F/B4, and B5/B6, respectively).

5.1.2. Defect Density and Solidification Cracking

Mosaics of optical micrographs of each specimen are provided in **Figure 5.6**. These optical micrographs show what appears to be some defect repeated in layers as z increases (z direction is up on the micrograph). Upon closer inspection, those defects are primarily oxide agglomerates (shown in greater detail in **Figure 5.7**). In addition to oxide agglomerates (green), there are some lack-of-fusion defects, porosity, cracks, and TiC agglomerates where applicable (shown in black, white, red, and blue, respectively). Every specimen also shows a column of defects roughly the same distance from the edge of the part. This column of defects is from the perimeter pass of the raster pattern which was offset from the infill portion of the raster pattern by 0.4 mm. These columns of defects were cropped out of defect density analysis.

The relative amount of defect area-referred to as defect density-was measured for every specimen mosaic optical micrographs and FIJI following the methods described by Hallberg [152]. The results of these measurements are shown in **Figure 5.8**. Adding Ti or Si seemed to correlate directly with increases in defect density aside from Specimen B4.This effect seems most pronounced for SiC additions. Literature suggests this is a potential result of microsegregation of Si or Ti to grain boundaries during solidification, which provides a brittle interface for crack formation and propagation [206-208]. Carbon has also shown to be responsible for this issue [207]. Specimen B4 may have a reduced defect density as a result of a combination of available TiC and high O content. Given sufficiently small TiC particles, sufficiently high temperature, and sufficient time, TiC

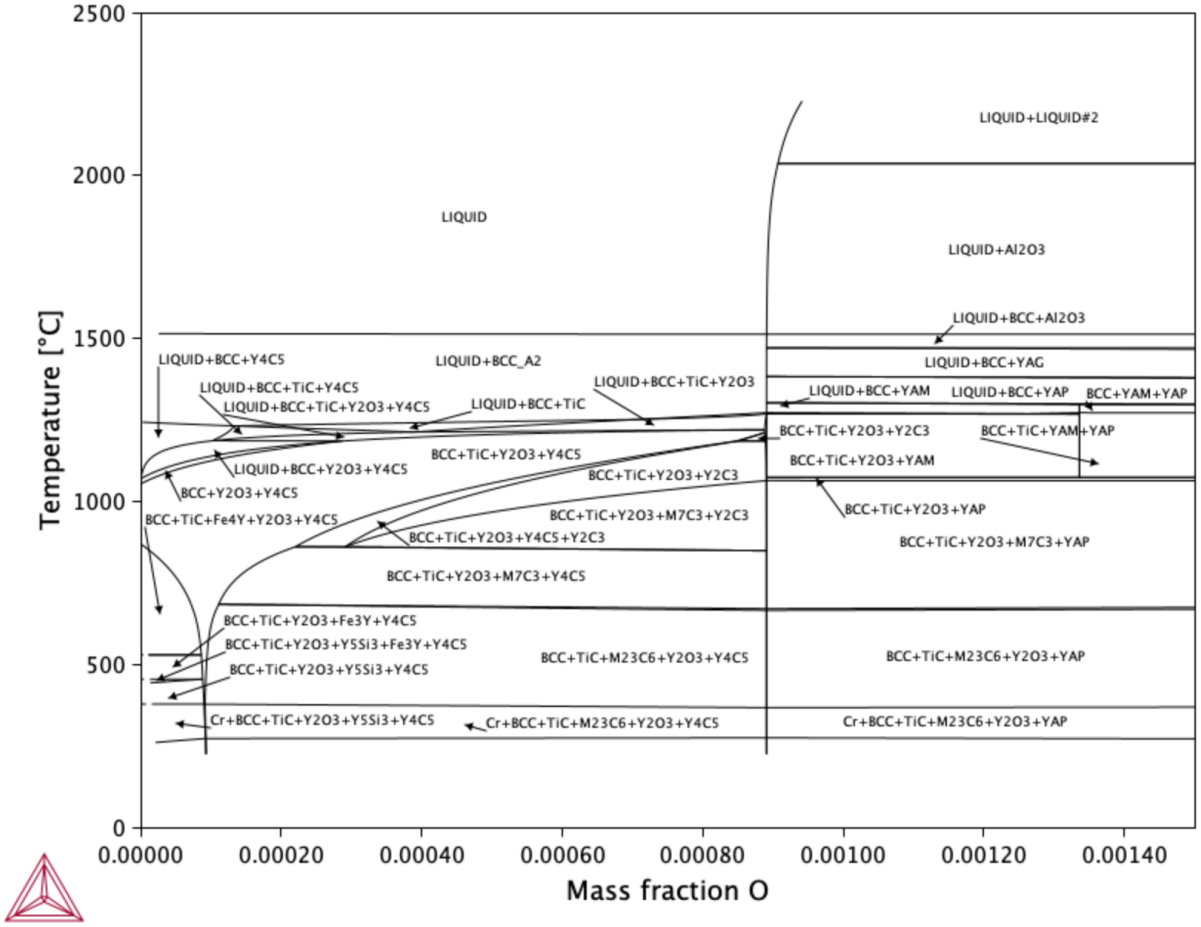

Figure 5.3: Phase diagram for as-received powder, B1, and B2 as predicted by Thermo-Calc.

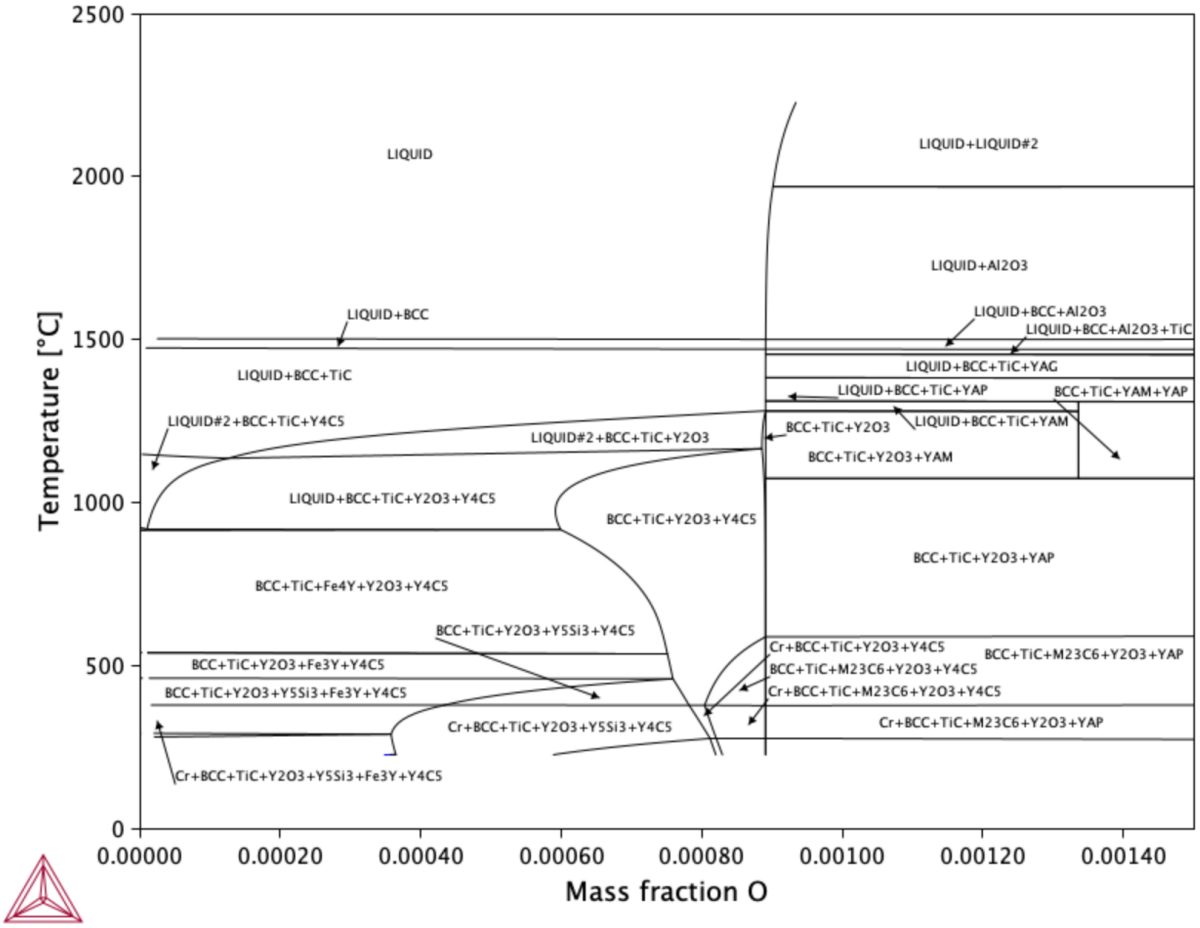

Figure 5.4: Phase diagram for B3, B3F, and B4 as predicted by Thermo-Calc.

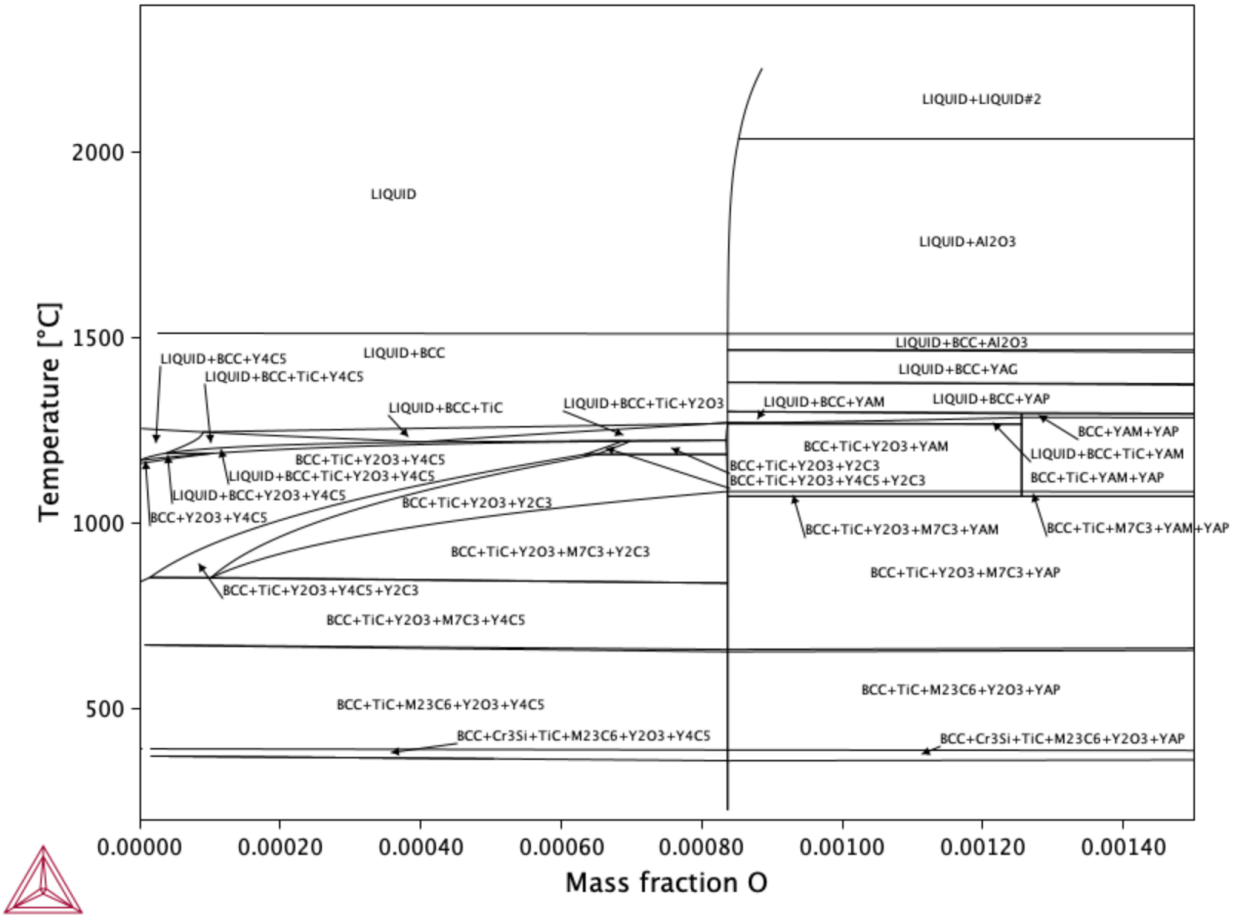

Figure 5.5: Phase diagram for B5 and B6 as predicted by Thermo-Calc.

B1

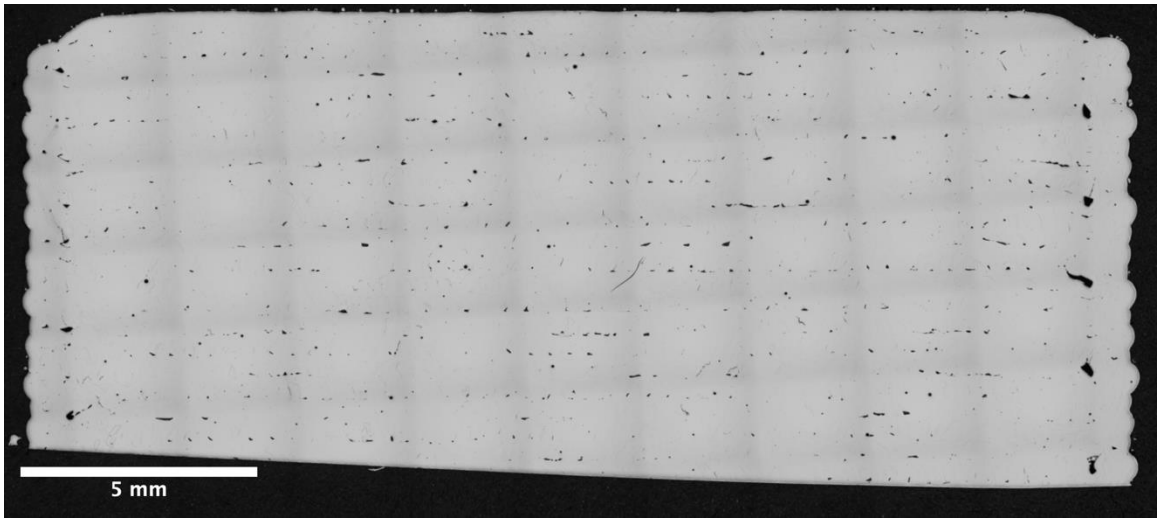

B2

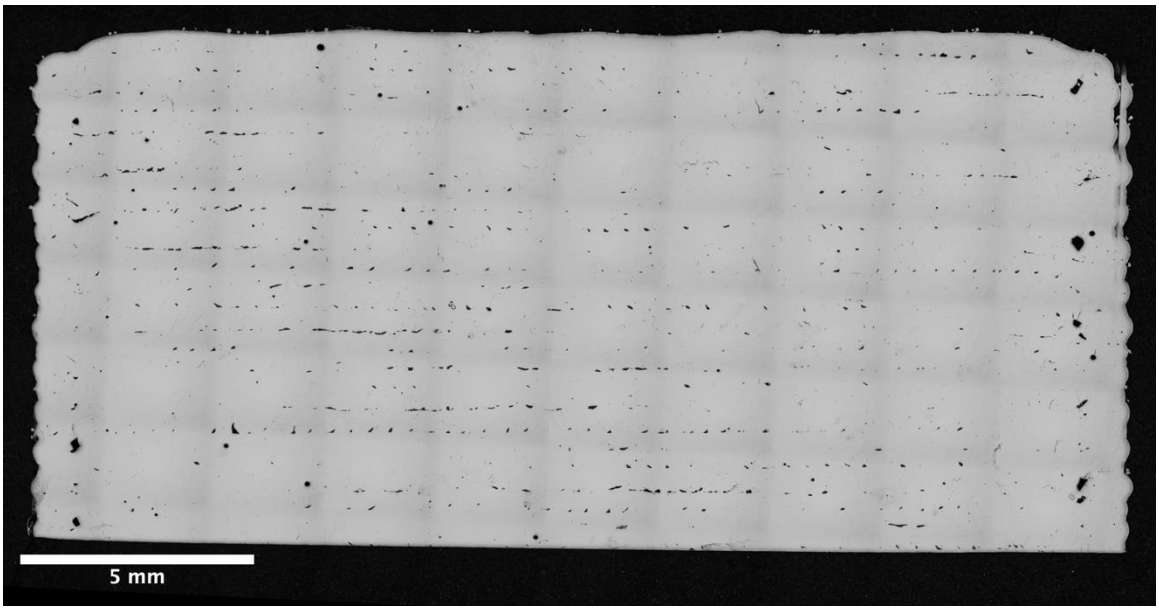

Figure 5.6: Mosaics of optical micrographs of the as-built specimens (B1 to B6; top to bottom) created from varied alloying additions. Z direction is up.

B3

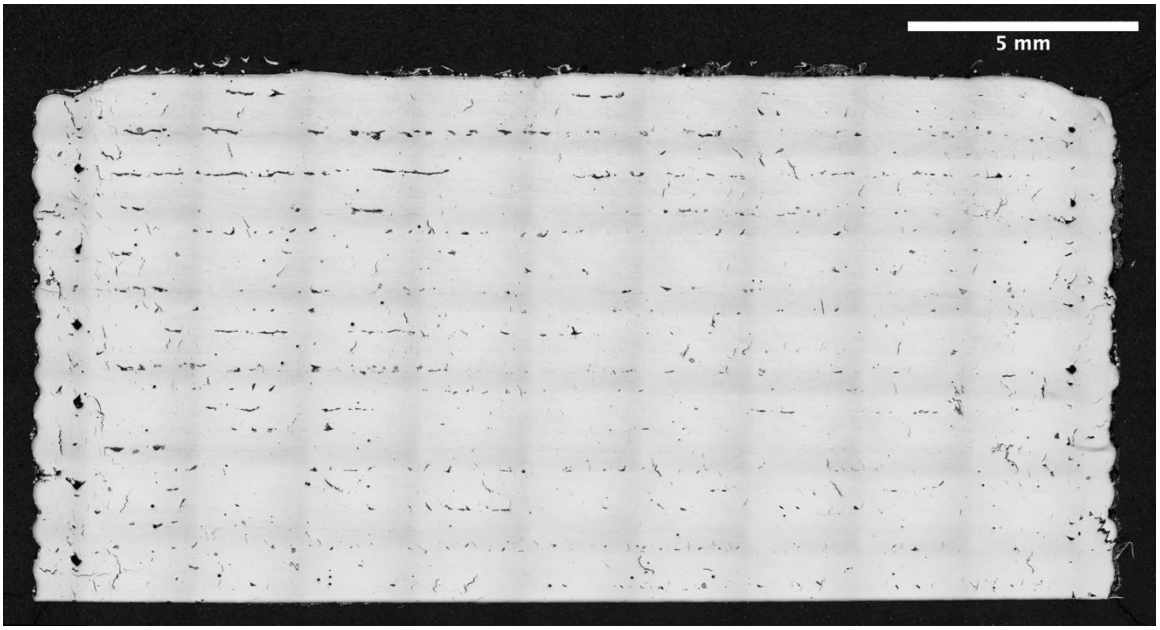

B3F

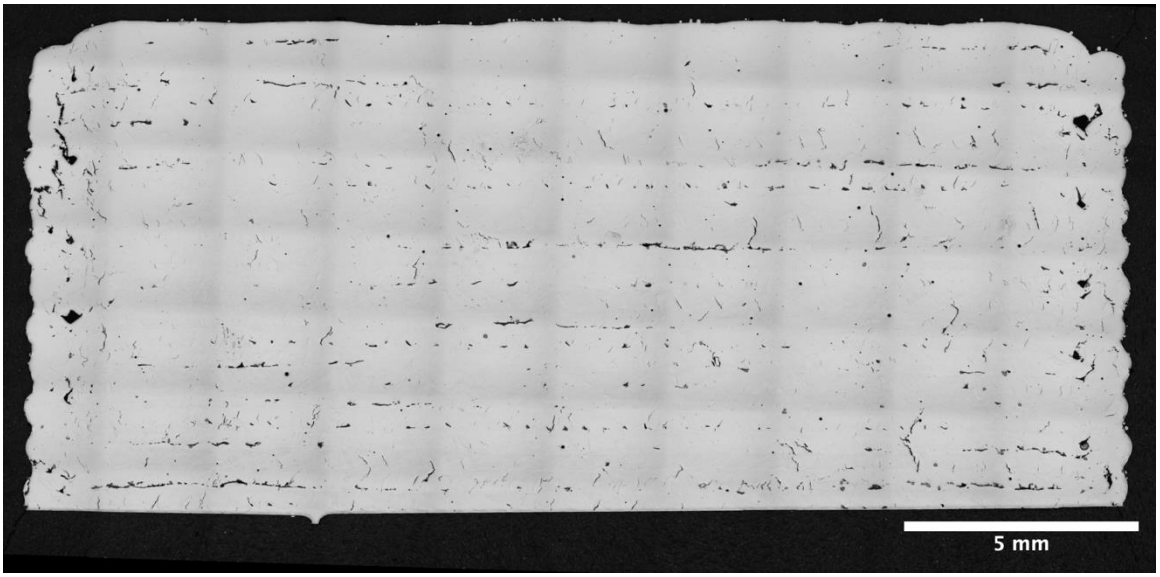

Figure 5.6 continued

B4

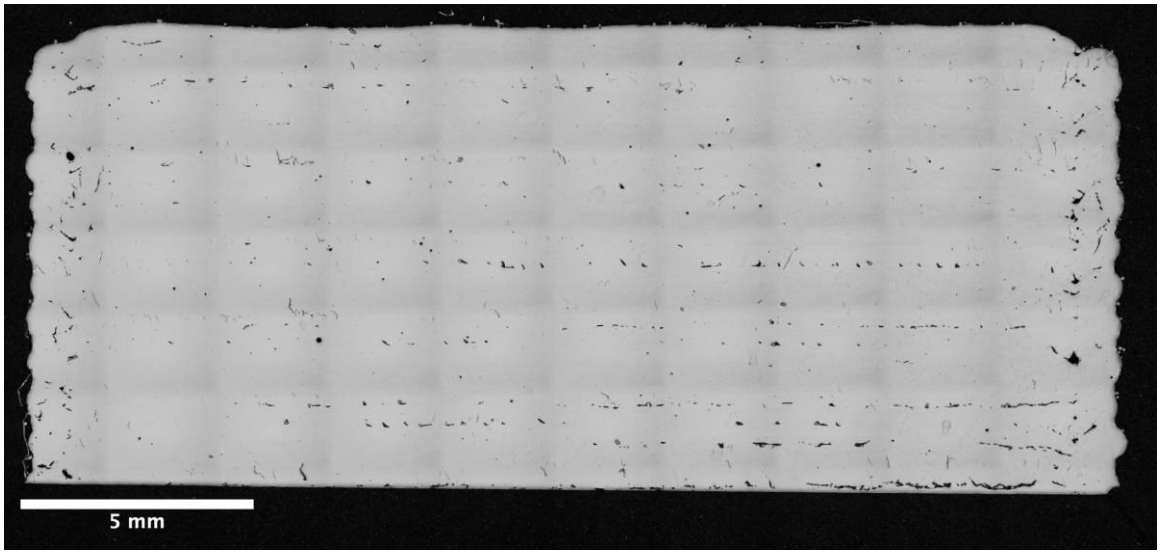

B5

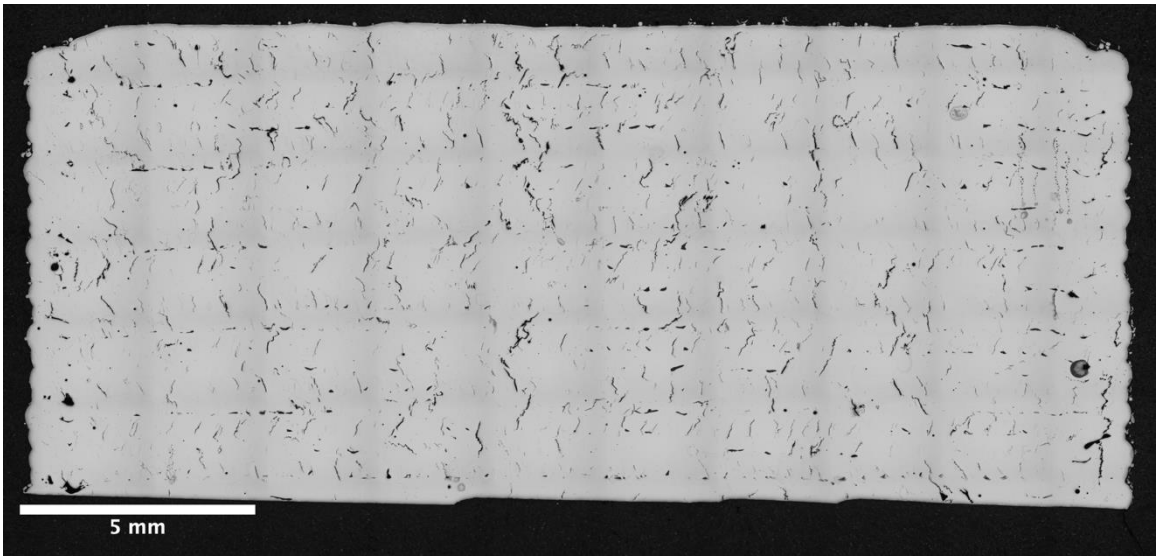

Figure 5.6 continued

B6

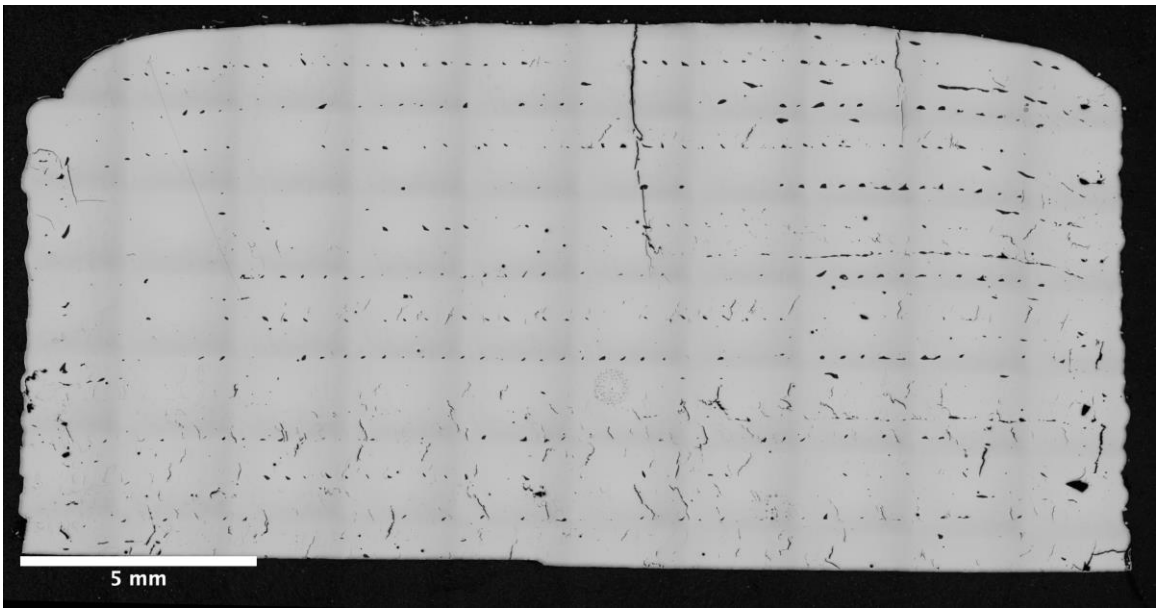

Figure 5.6 continued

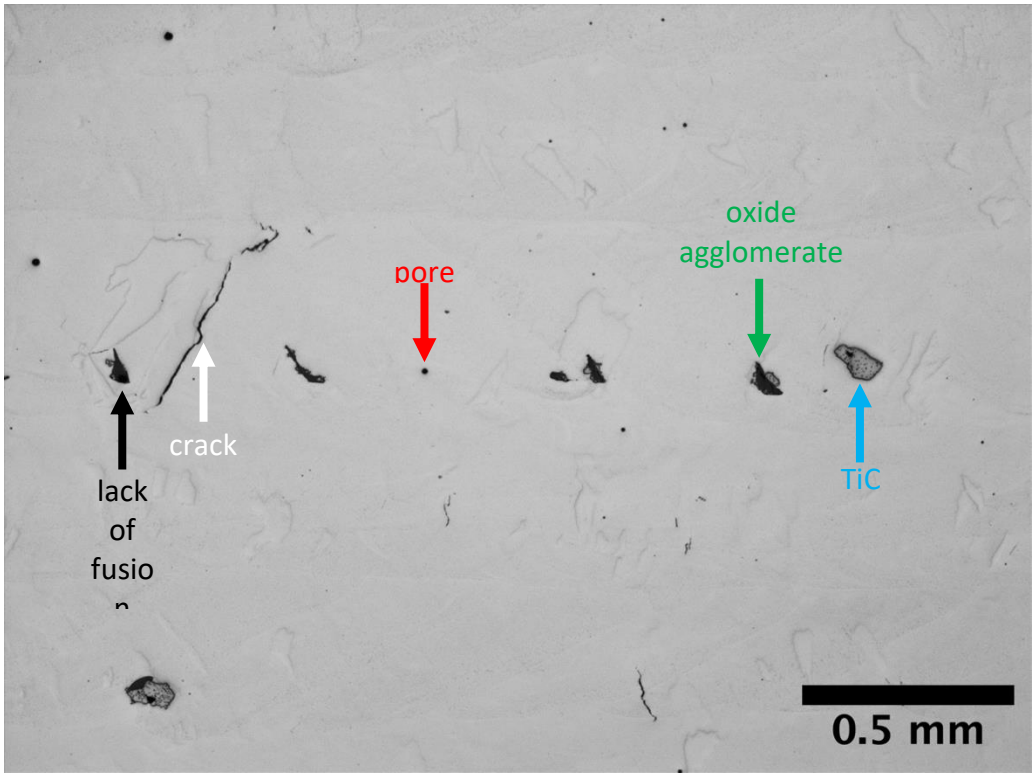

Figure 5.7: Optical micrograph from B4 showing what types of defects are present. The lack of fusion defect is attached to an oxide agglomerate. Z direction is up.

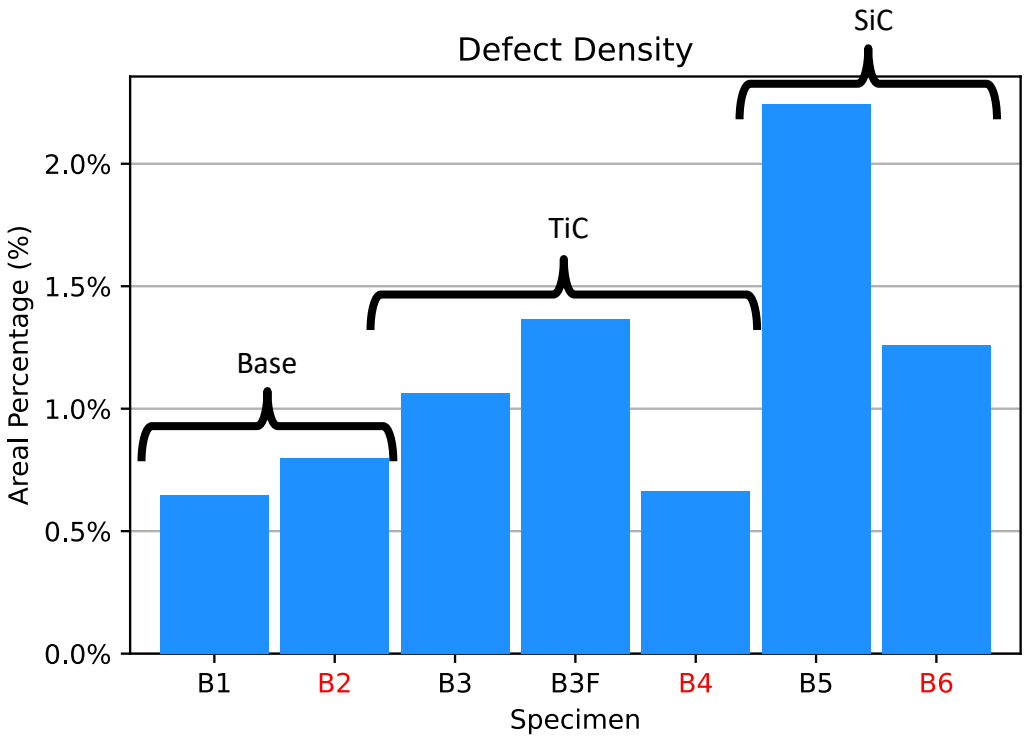

Figure 5.8: Comparison of as-built specimen defect density across different alloying conditions.

particles can oxidize and fill in cracks in a microstructure [209, 210]. This would also reduce the size of TiC agglomerates present in as-built B4. There is potential that a similar phenomenon occurred with B6 compared to B5. An increase in O availability improved the potential for oxidation of any SiC that failed to dissolve in the melt pool [211]. Another potential cause of reduced defect density of specimen B4 is its finer grain structure. Incompletely dissolved TiC particles act as inoculants for refined grain formation and welding of finer grained structures results in a reduction of solidification cracking probability [11, 212]. DICTRA simulations from Thermo-Calc support this possibility. **Figure 5.9** below shows a) TiC powder particle dissolving in liquid FeCrAl and b) SiC powder particle dissolving in liquid FeCrAl. **Table 5.2** provides the conditions used to set up the simulation. Inverse pole figures of each specimen showing the refined grain structure of specimens containing TiC in both the longitudinal and transverse cross-sections are shown in **Figure 5.10** below.

In general, alloy compositions used in this experiment have poor resistance to solidification cracking as indicated by a sharp increase in slope as the fraction of solid approaches one. Kou in 2015 identified that increased slope of a Scheil solidification curve as the square root of the fraction of solid approaches one was a reasonable criterion for solidification cracking [171]. Classical Scheil simulation data, generated using Thermo-Calc, for each specimen is included in **Figure 5.11a**. **Figure 5.11b** includes a direct comparison of Kou's solidification cracking criterion across all specimens. Plots comparing the solidification cracking criterion across the unique differences of the various alloying compositions are included in **Figure 5.12**. **Figure 5.12a** demonstrates how increasing O content results in a decrease in solidification crack probability. **Figure 5.12b** demonstrates how increasing alloying of FeCrAl through additions of Ti, Si, and C

a

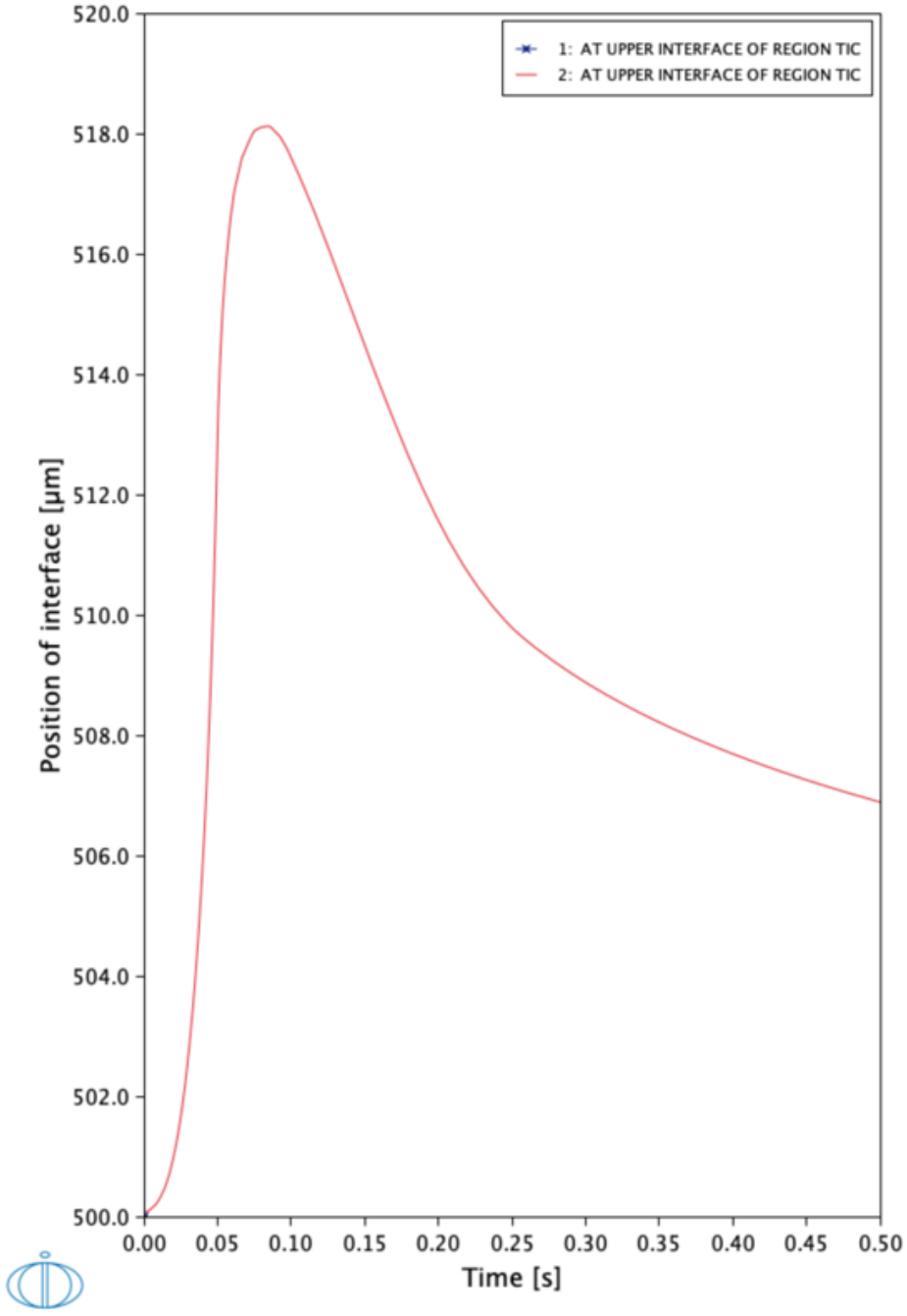

Figure 5.9: DICTRA simulations to predict the potential for complete dissolution of a) TiC and b) Si @; T = 1500 °C, right: T = 2345 °C) powder particles.

b

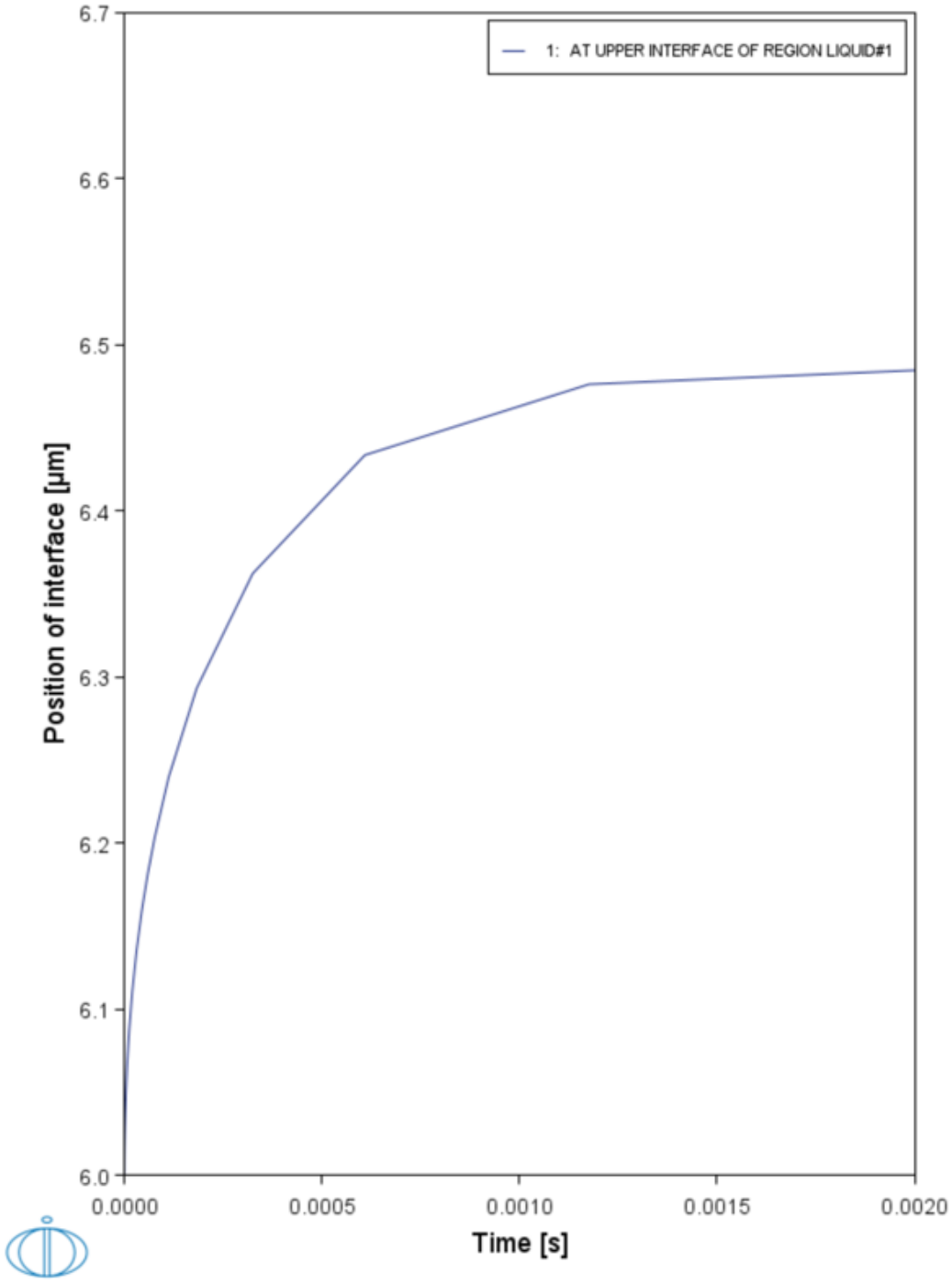

Figure 5.9 continued

c

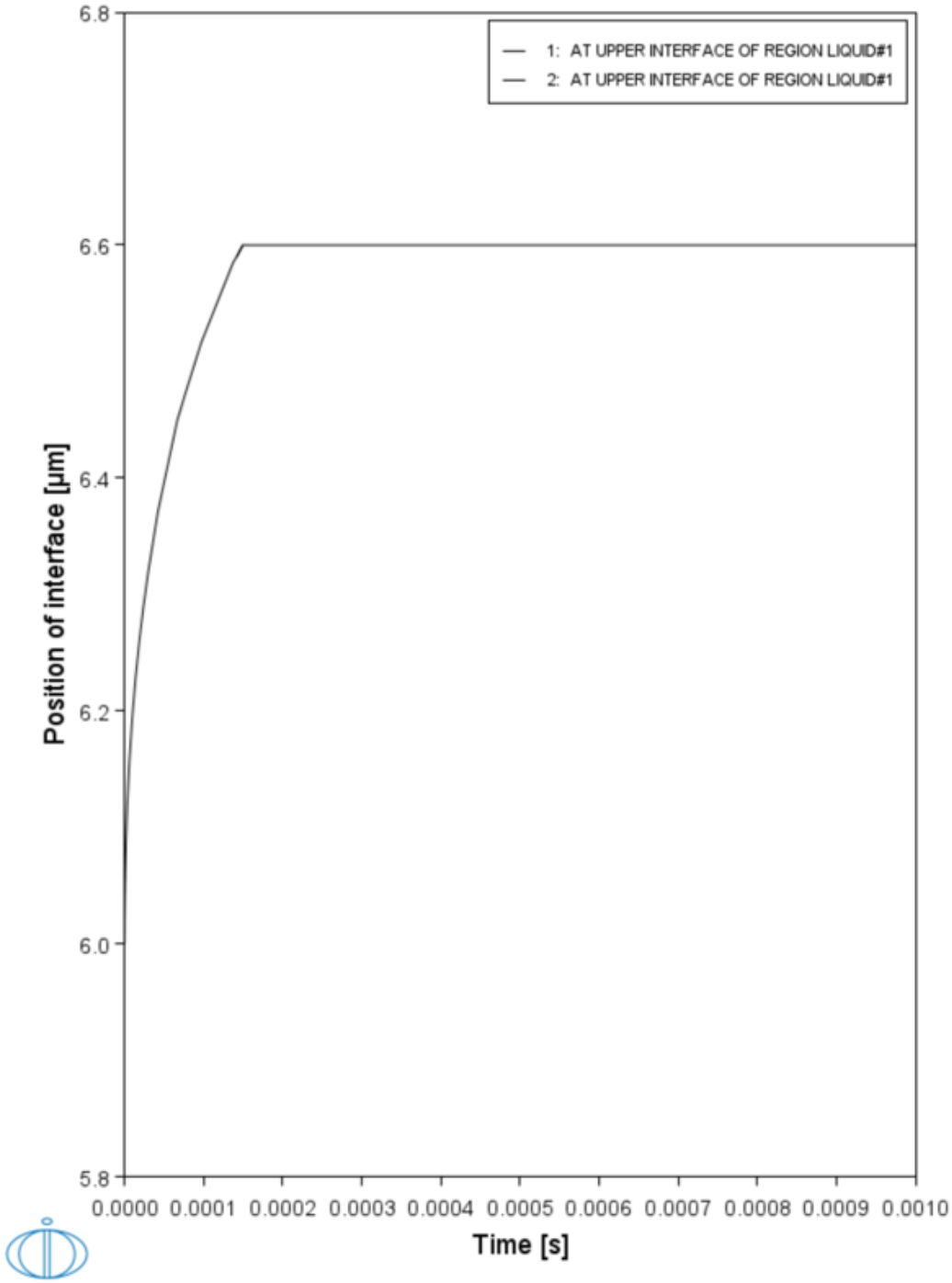

Figure 5.9 continued

Table 5.2: DICTRA simulation input parameters for TiC and SiC dissolution.

TiC

Phase	Composition	Phase Size	Phase Geometry	# of Nodes	Node Spacing	Temperature Profile
Liquid	Fe-12.01Cr-5.71Al-0.33Y-1e-4Ti,C	500 um	-	50	linear	non-isothermal
TiC (FCCA1#2)	Ti-18C-1e-4Fe,Cr,Al,Y	50 um	spherical	50	linear	

Temperature Profile				
Time	0	0.05	0.25	0.5
Temperature	1500 °C	2900 °C	1500 °C	1400 °C

SiC

Phase	Composition	Phase Size	Phase Geometry	# of Nodes	Node Spacing	Temperature Profile
Liquid	Fe-12.01Cr-0.01C-0.001Si	6 um	-	50	geometric	isothermal
SiC (SiC)	Si-30C-1e-4Fe,Cr	600 nm	spherical	50	geometric	

Temperature (left)	Temperature (right)
1500 °C	2345 °C

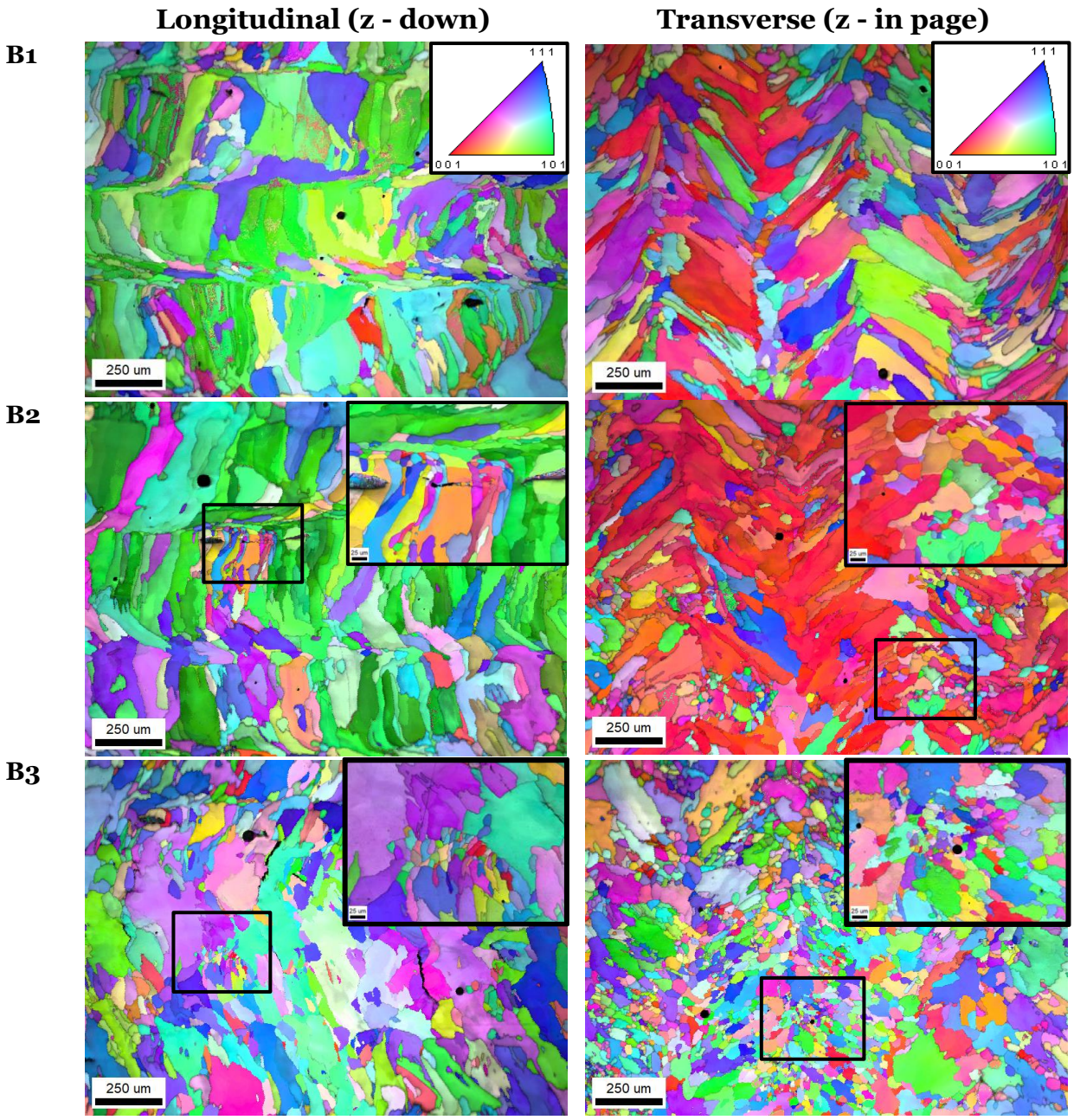

Figure 5.10: Inverse pole figures of longitudinal and transverse cross-sections from the top 10 mm of each specimen. Insets, when provided, show increased magnification of finer grained areas outlined in black on the main micrograph. White arrows mark examples of solidification cracking.

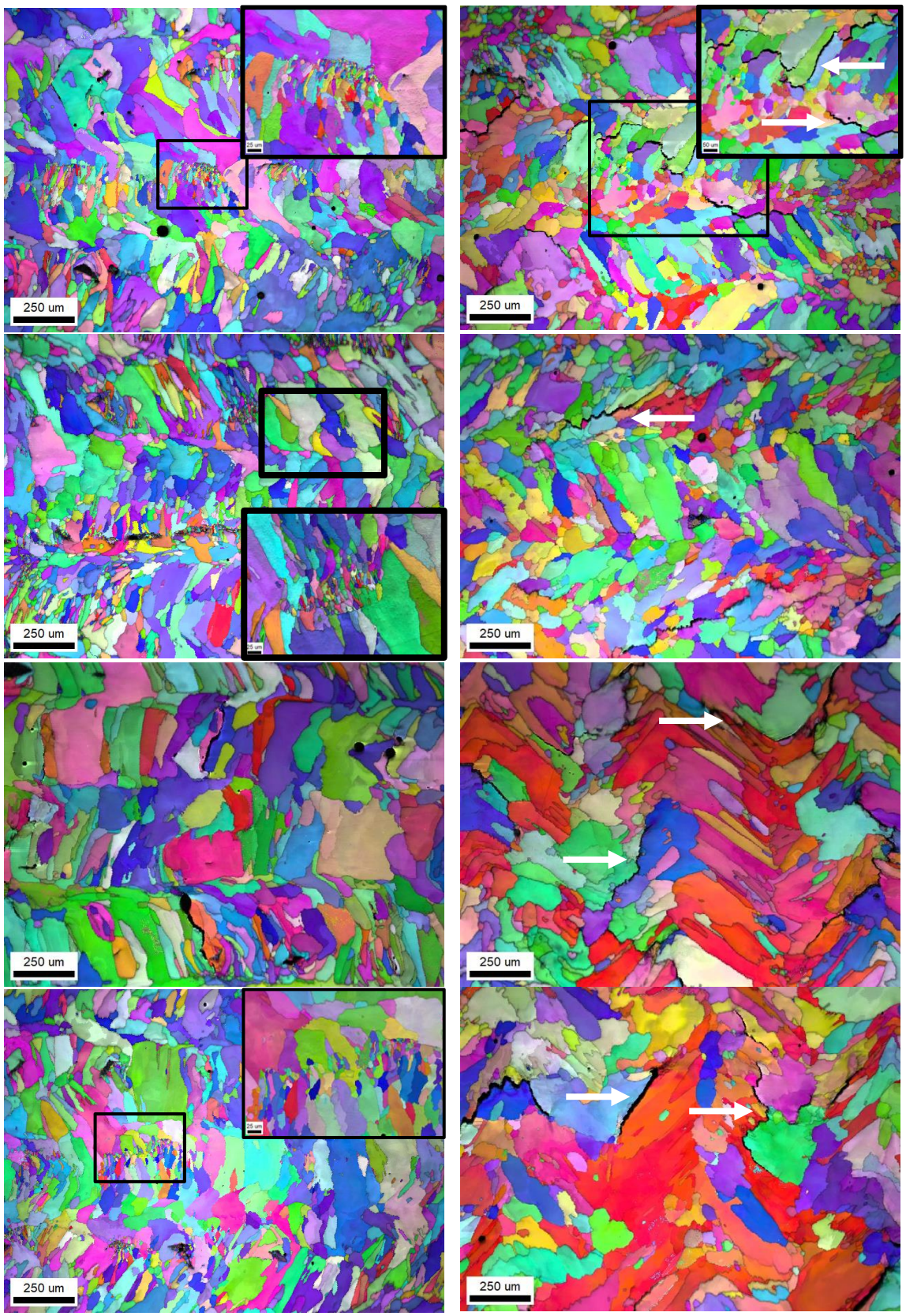

Figure 5.10 continued

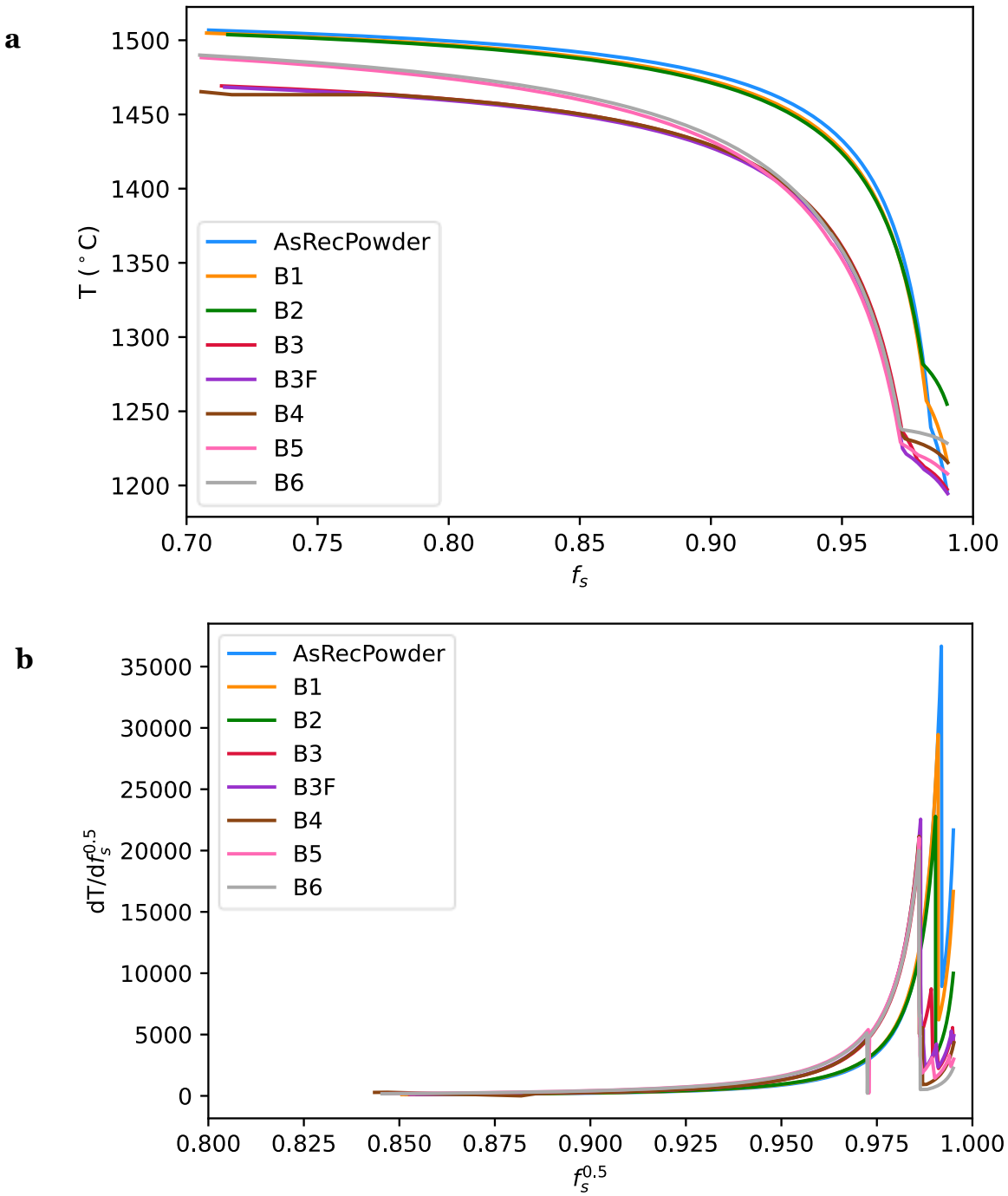

Figure 5.11: Solidification cracking criterion analysis: a) Scheil simulation approaching $f_s = 1$, b) derivative of Scheil simulation as $f_s^{0.5}$ approaches 1.

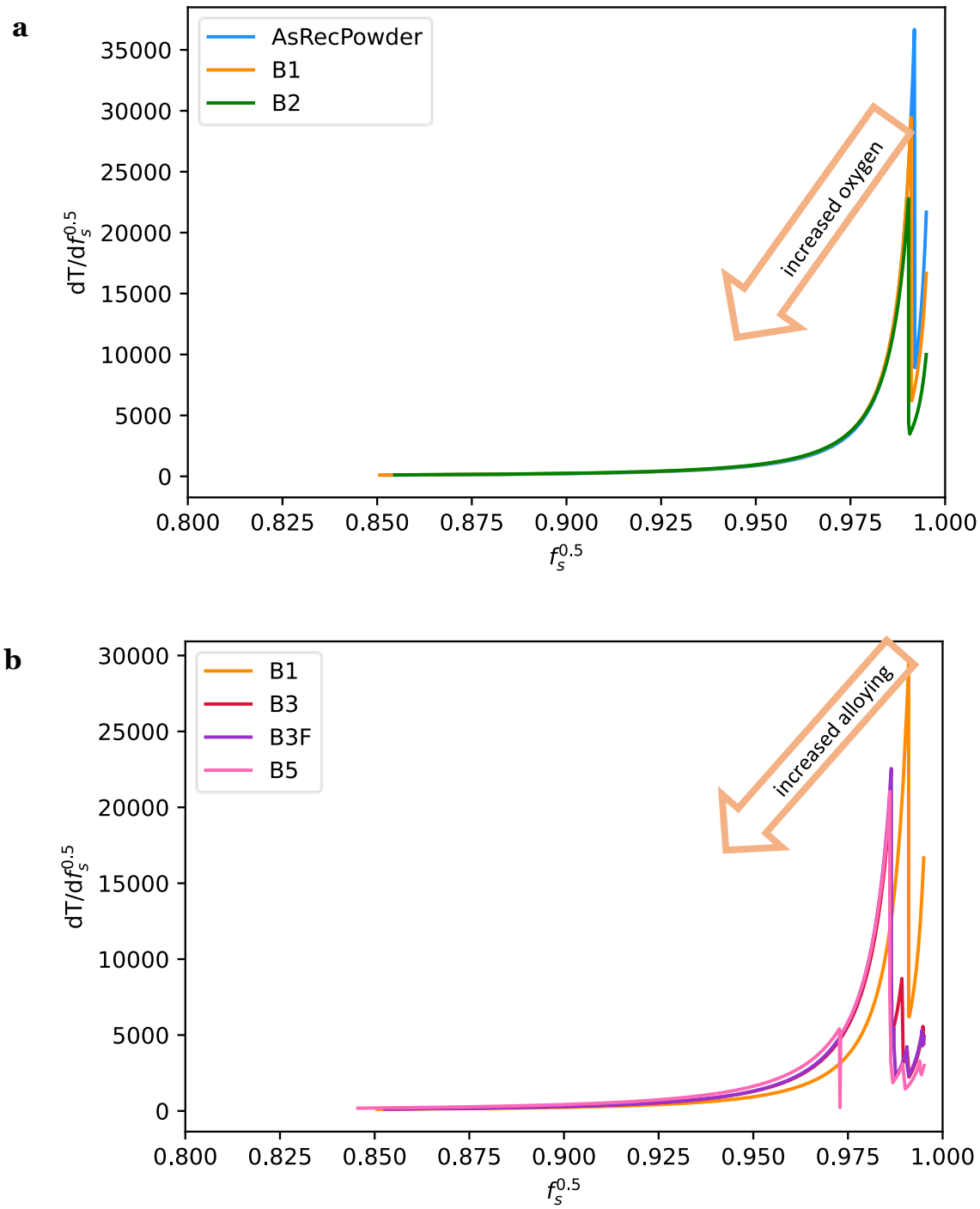

Figure 5.12: Solidification cracking criterion analysis showing the influence of a) increased oxygen content and b) increased alloying.

also results in a decrease in solidification cracking probability. Some examples of solidification cracks along the centerline of a raster path are shown in **Figure 5.9** and marked with white arrows on the transverse cross-section inverse pole figures.

5.2 Agglomeration

In order to better understand how changing alloy composition would influence deleterious oxide agglomeration, a careful automated analysis of all non-edge optical micrographs from each specimen was performed. The total number of oxide agglomerates measured and their total area for each specimen are presented in **Figure 5.13**. Specimen B3F had the most oxide agglomerates identified while specimen B6 had the most area covered by oxide agglomerates. B6 has the highest oxygen content potentially causing increased precipitation, agglomeration, more total agglomerate area. Given that B5 does not have the largest agglomerate total area or number of agglomerates with the number of cracks present in its mosaic of optical micrographs supports the choice of filtering parameters. Looking at the mosaic of optical micrographs for B3, B3F, and B5 provides a possible explanation for their high number of agglomerates but comparatively lower agglomerate total area. All three specimens optically show increases in vertical cracking compared to the remaining specimens. This suggests that there is still some room for improvement in the chosen filtering parameters; however, it is possible that filtering out more cracks would reduce the ability to correctly identify agglomerates.

Comparisons of oxide agglomerate average area (a) and average equivalent diameter (b) across all specimens are shown in **Figure 5.14**. In general, there appears to be little influence of alloying on average agglomerate size. B5 having a lower average area, lower average equivalent diameter, higher total area, and higher number of agglomerates

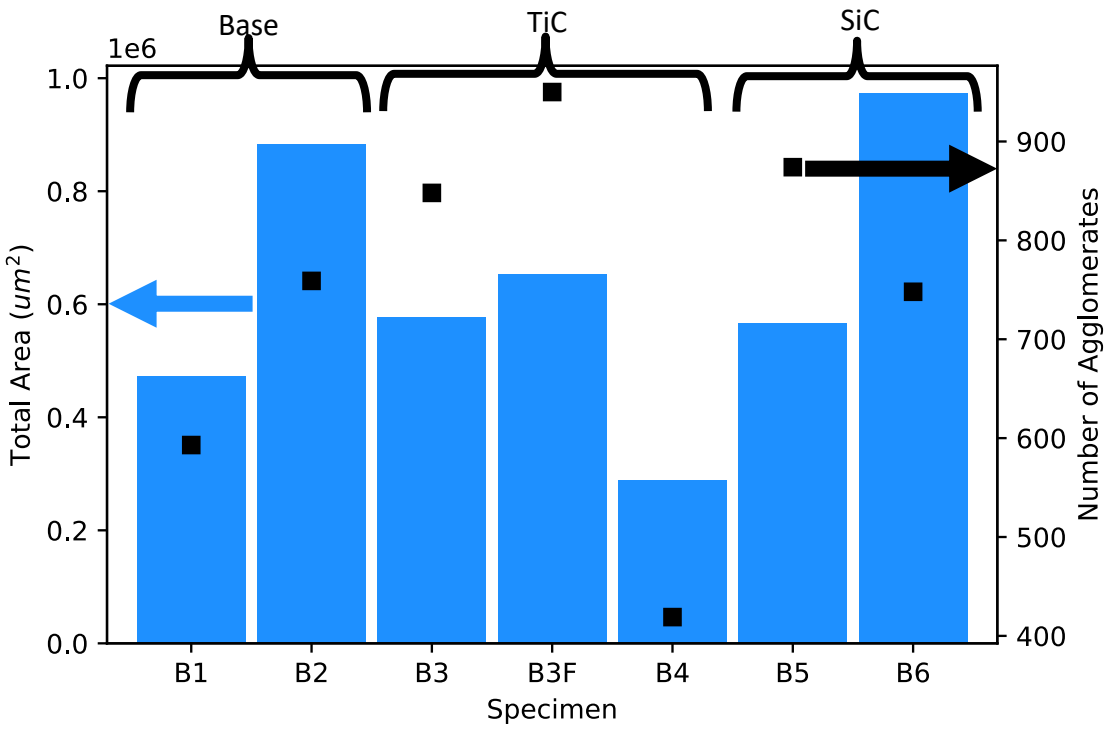

Figure 5.13: Comparison of specimen agglomeration with respect to changing alloying, total area (blue bars, left) and number of agglomerates (black squares, right).

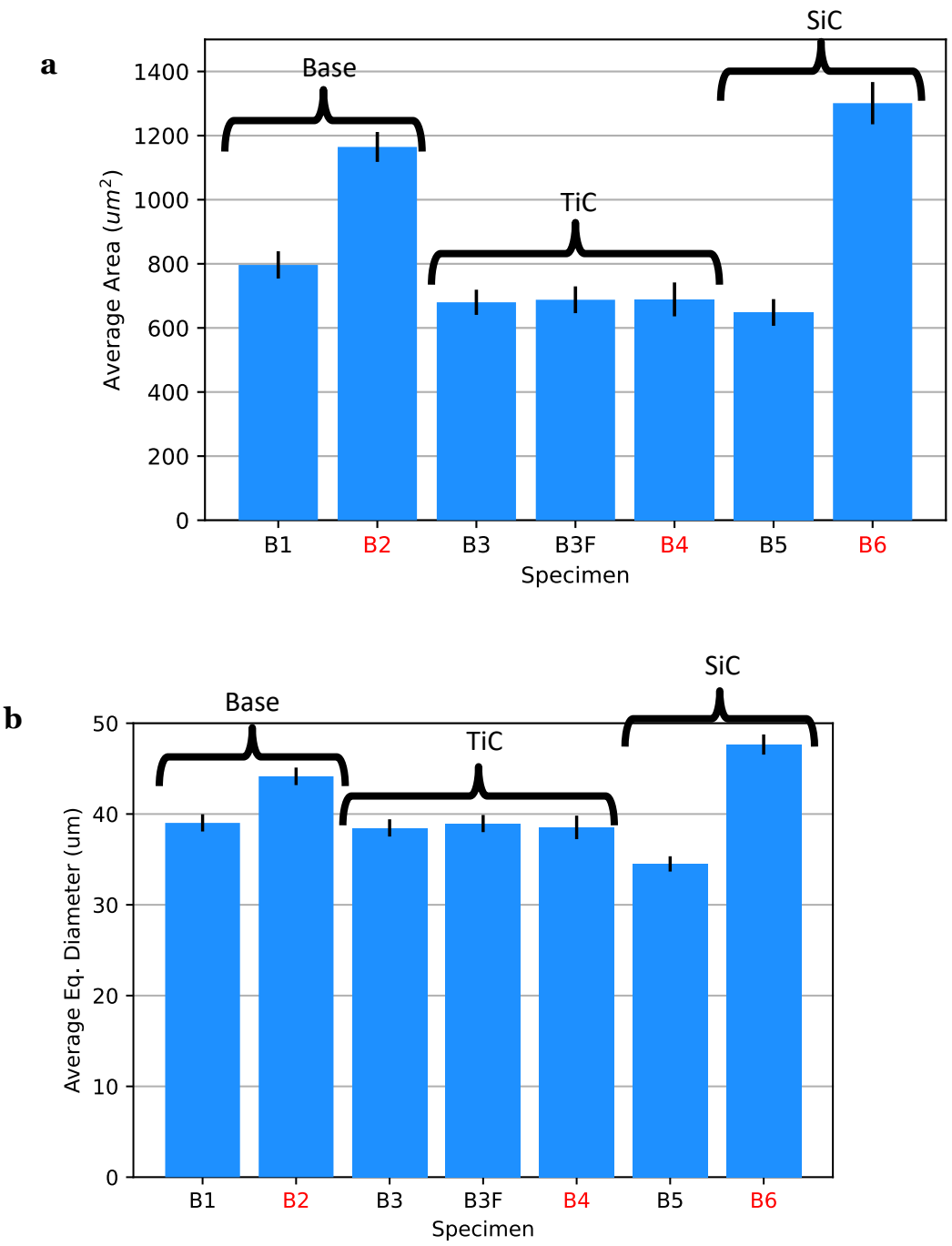

Figure 5.14: Comparison of average agglomerate area (a) and average agglomerate equivalent diameter (b). Error bars represent the Standard Error of the mean of each dataset.

than B4 again suggests that there is some counting of cracks or other non-agglomerate defects. Cracks being long and slender but just outside of the aspect ratio filter would still count towards the number of agglomerates and total area while driving down the average area and average equivalent diameter. For a better perspective of how alloying may influence agglomeration, histograms of area and equivalent diameter for all features labeled as oxide agglomerates for each specimen are shown in **Figure 5.15**.

Looking at both the area distributions and equivalent diameter distributions, an increase in oxygen content for the same base alloy composition results in an increase in oxide agglomerate size (both areal and equivalent diameter). Ignoring the results from B5 because of the likelihood of counting cracks as oxide agglomerates, it appears that the addition of TiC resulted in an overall reduction of oxide agglomerate size. Comparing histograms for B2 and B6 demonstrates that SiC additions also reduced overall oxide agglomerate size, although at a reduced effectiveness compared to TiC. This reduced effectiveness can be explained when considering the composition of specimens with TiC additions vs. specimens with SiC additions. As shown in **Figure 3.2**, a Si concentration of approximately 0.75 wt% was required to achieve wetting of a Y_2O_3 substrate by an Fe-9Cr alloy [61]. B5 and B6's Si concentrations are 0.16 wt% and 0.18 wt%, respectively. Still well below the threshold for oxide wettability. **Figure 3.3** shows that a Ti concentration of approximately 0.7 wt% was needed to achieve wettability while B3, B3F, and B4 had Ti concentrations of 0.63, 0.64, and 0.58 wt%, respectively [60]. The concentration of Ti in specimens with TiC added is 80% to 90% of the value reported in the literature for wetting. The concentration of Si in specimens with SiC added is 20 to 25% of the value reported in the literature for wetting. This was not wholly expected. The amount of TiC and SiC decided to be added to their respective batches was determined

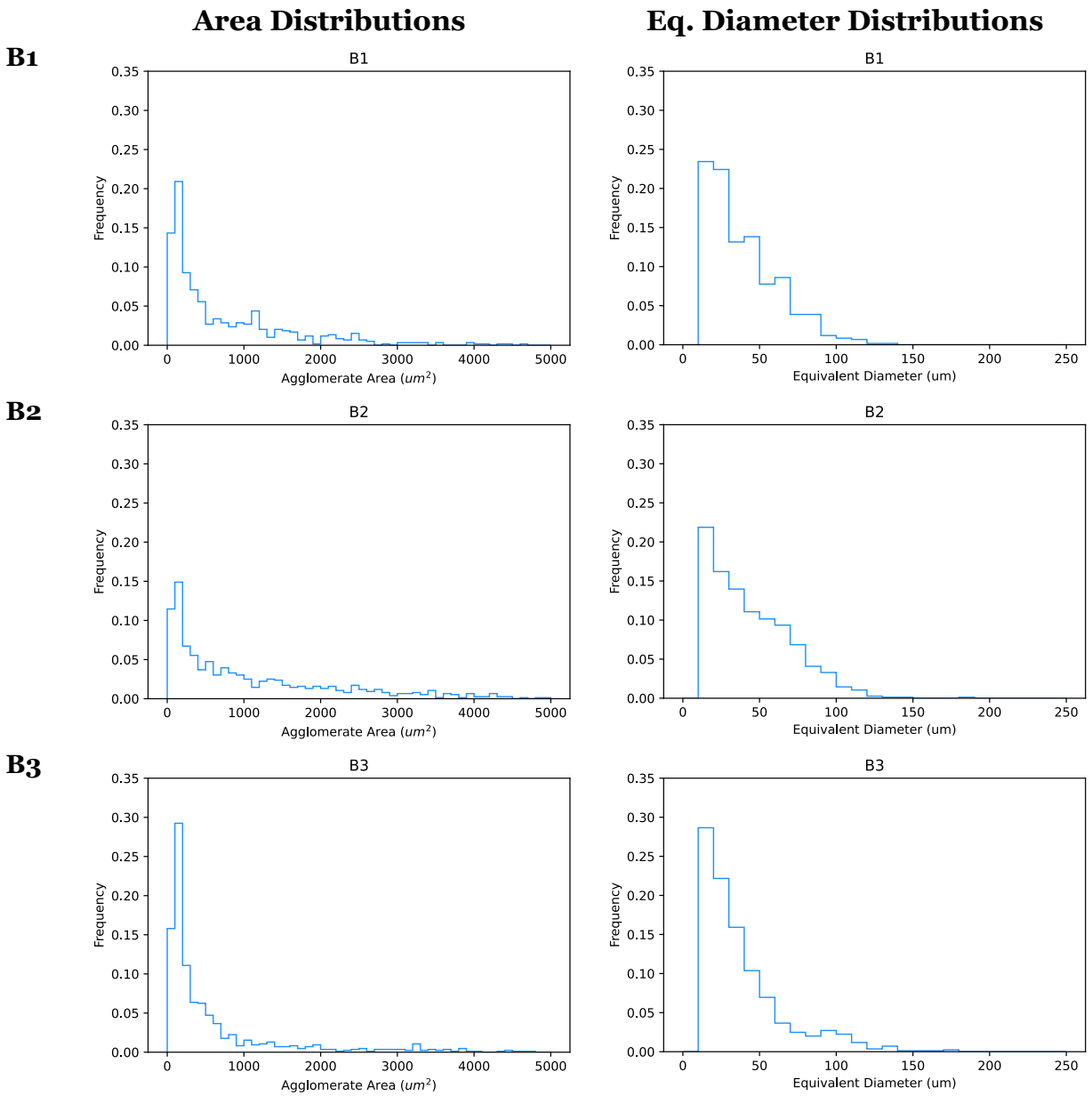

Figure 5.15: Agglomerate area (left) and equivalent diameter (right) distributions for each specimen.

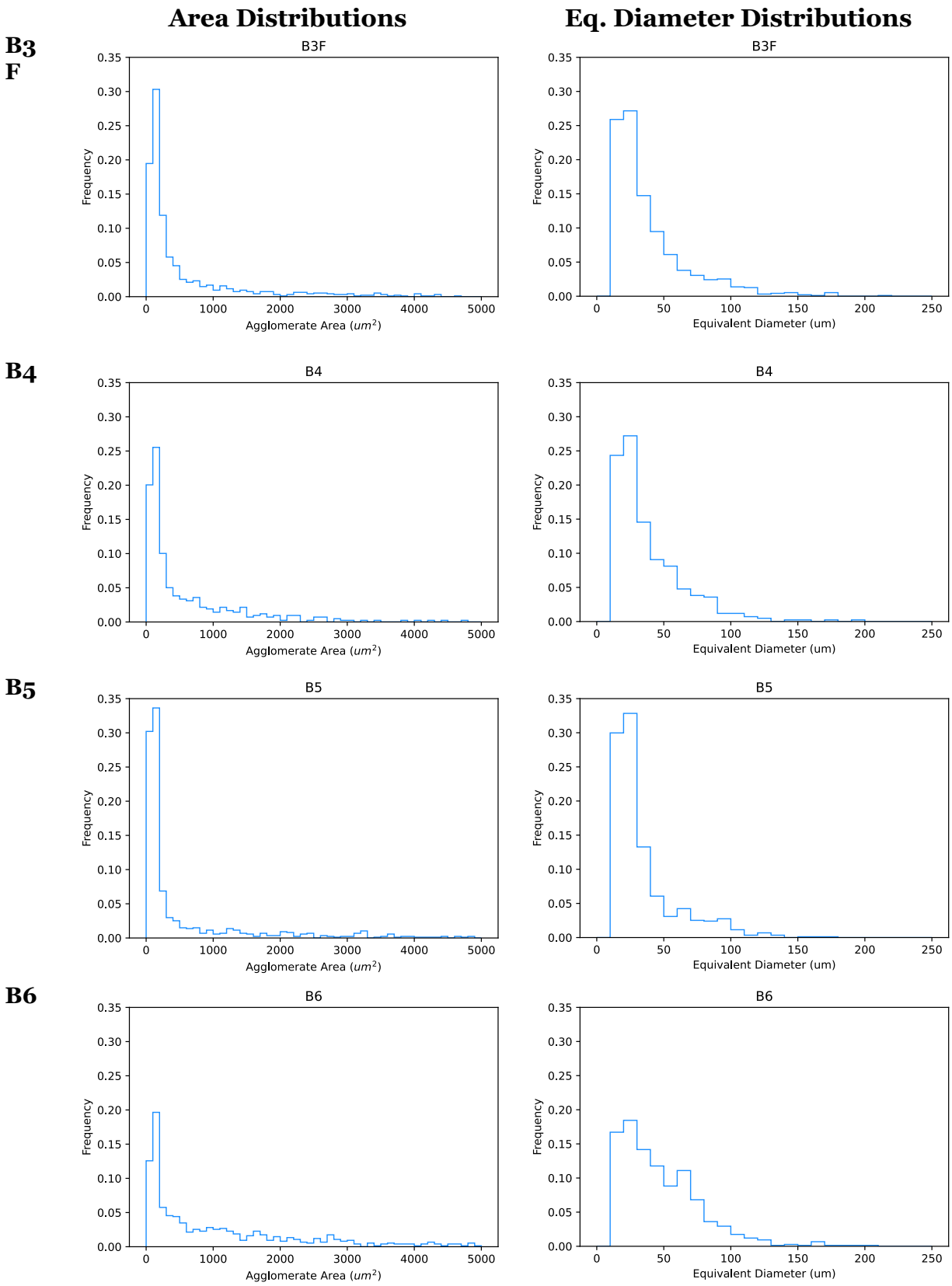

Figure 5.15 continued

using data from Lu et al. on the optimal atomic ratio of Y:Ti for minimizing ODS precipitate size. The authors determined the optimal atomic ratio to be 0.4 [112]. This ratio was used for both TiC and SiC additions to maintain consistency.

5.3. Nanoscale Precipitation and Grain Boundary Segregation

5.3.1. Scanning Transmission Electron Microscopy

STEM characterization was performed on all specimens. For the purposes of this analysis, B1, B2, B4, and B6 specimens will be focused on. B1 serves as a reference case for as-received powder. B2 examines the influence of a pre-build heat treatment to add more O prior to AM. B4 serves as a comparison of adding TiC compared to B2. Lastly B6 serves as a comparison of adding SiC compared to B2. In addition to these as-built samples, post-build heat treated samples from B2, B4, and B6 (referred to as B2HT, B4HT, B6HT from here forward) were characterized to determine if precipitation had completed during the build and if a post-build heat treatment would be beneficial.

Using FIJI, multiple high-angle annular dark-field (HAADF) micrographs from each specimen at various magnifications were analyzed and precipitates measured. For most specimens, two separate lamellae were characterized: one near a grain boundary and one in grain. Targeted TEM liftouts were made targeting the (100) zone axis in order to facilitate better imaging conditions [213]. HAADF micrographs were chosen to utilize the increased z-contrast they provide to differentiate objects with different relative elemental compositions. Results from that analysis are shown in **Table 5.3**. As shown, the number densities are similar across all compositions examined. Si additions appeared to reduce the number of nanoscale precipitates and potentially causing a slight increase in size. In general, a post-build heat treatment was not beneficial for enhancing precipitate formation. Instead, average precipitate number densities were slightly

Table 5.3: STEM precipitate analysis of unique alloyed specimens.

Specimen	# of Micrographs	Avg Number Density (#/m^3)	Avg Diameter (nm)
B1	7	6.81E+19	73.37
B2	5	1.25E+19	107.38
B2HT	6	1.94E+19	127.67
B4	9	6.22E+19	74.68
B4HT	7	5.66E+19	56.82
B6	6	6.12E+18	113.19
B6HT	7	4.68E+18	119.24

reduced comparing the as-built to post-build heat treated counterparts**.** The average diameter of precipitates increased in the B2 and B6 builds as a result of a post-build heat treatment. The decrease in average precipitate diameter from B4 to B4HT is likely a result of a small sample size and potentially more TiC precipitates being captured in those lamellae. Generally, average precipitate diameter and average precipitate number density are inversely correlated. Larger precipitates contain more precipitate-forming elements, leaving less reactants to form smaller precipitates.

STEM EDS was used to give some insight as to what kinds of precipitation formed across the varied compositions. In B1, the specimen with the lowest O content, Y-rich intermetallic phases form (**Figure 5.16**). These results are similar to experimental results shown in **Section 4.1.4** where an insufficient amount of O was present to completely react with all available Y. Precipitation of Y-rich phases result due to the near zero solubility of Y in BCC Fe [133].

The increased O content of B2 allows for Y-oxide formation in addition to Y-rich precipitates. This is shown in **Figure 5.17** where two Y-oxides are attached to a Y-rich intermetallic phase. The micrographs and maps shown are from B2HT. Additional co-precipitation occurred in the remaining specimens (B4, B4HT, B6, and B6HT) characterized too. These results are shown in **Figure 5.18** and **Figure 5.19**. For brevity, micrographs and maps from B4HT and B6 are shown as representative for their respective alloy compositions as their non-post-build heat treated counterparts have similar co-precipitation. B4 and B4HT show Y-oxide precipitates decorated by TiC particles. B6 and B6HT show Y-oxide precipitates surrounded by a Cr-carboxide phase. Looking at **Figure 5.5**, there is no clear Cr-oxide phase predicted by the B5/B6 phase diagram. However, there are multiple potential Cr-carbide phases predicted (e.g., M_7C_3

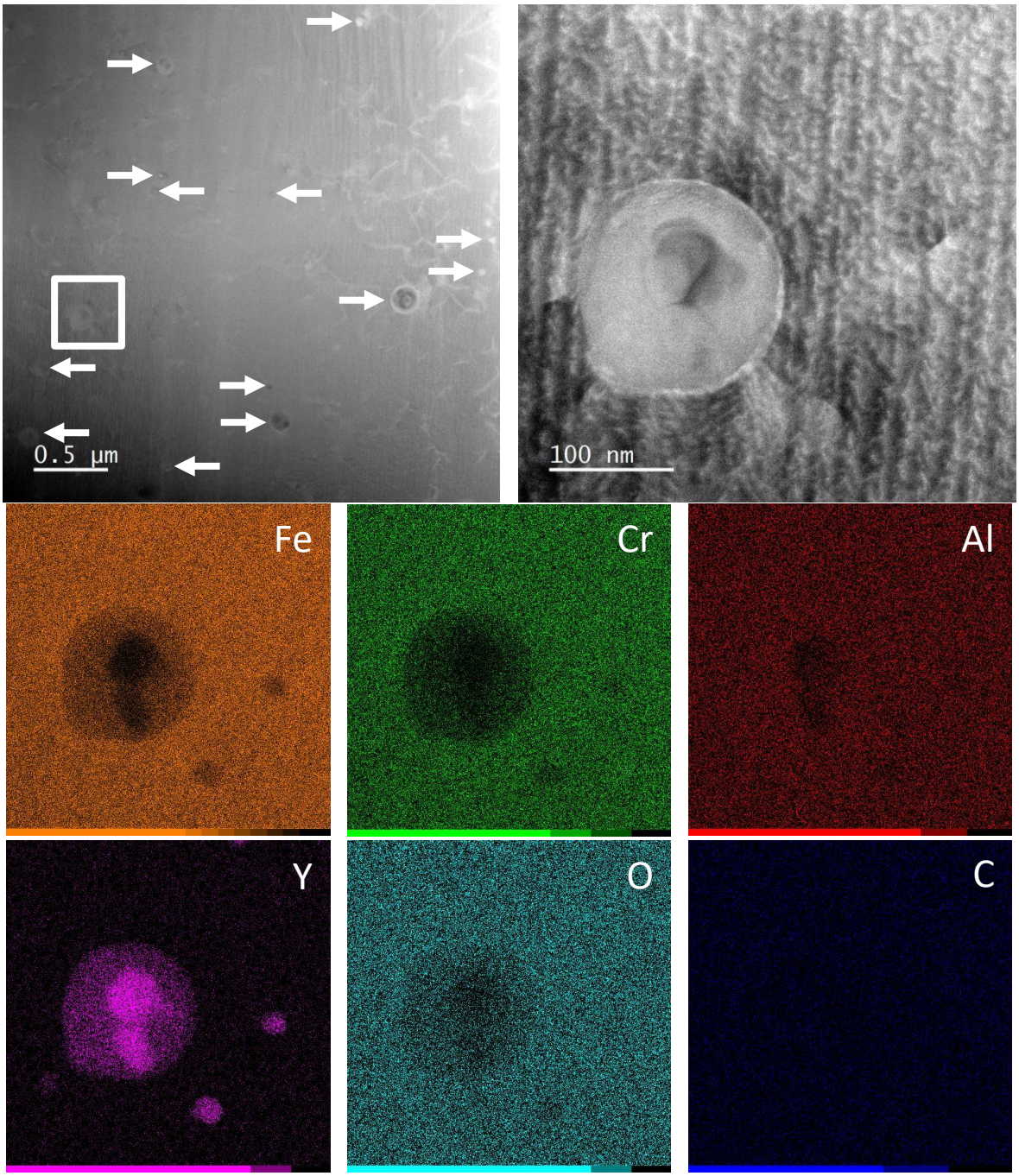

Figure 5.16: STEM EDS maps of Y-rich intermetallic precipitation in as-built B1. White arrows are pointing to other precipitates present in the matrix.

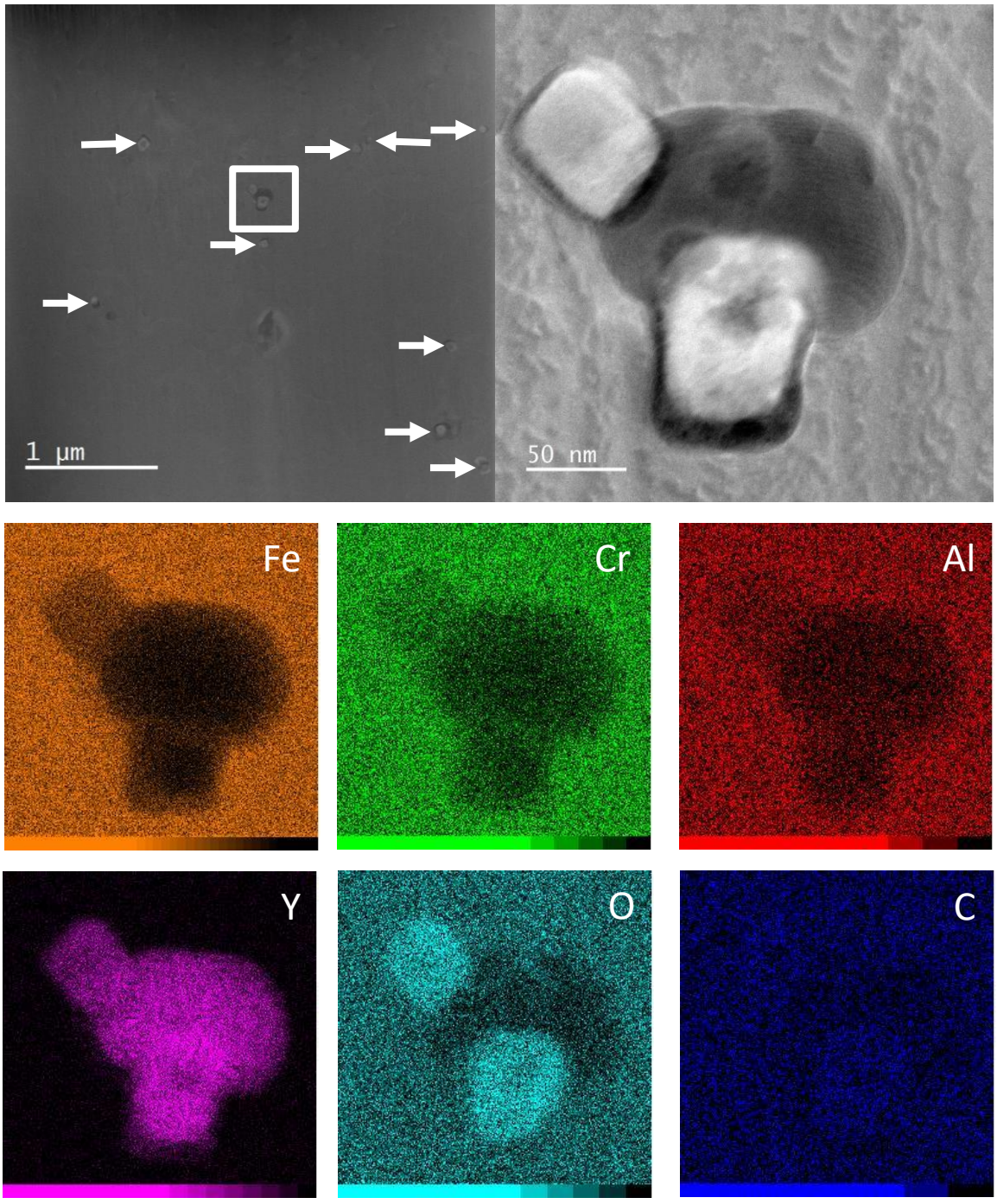

Figure 5.17: STEM EDS maps of co-precipitation of Y-oxides and Y-rich intermetallic precipitation in B2HT. White arrows are pointing to other similar precipitates present in the matrix.

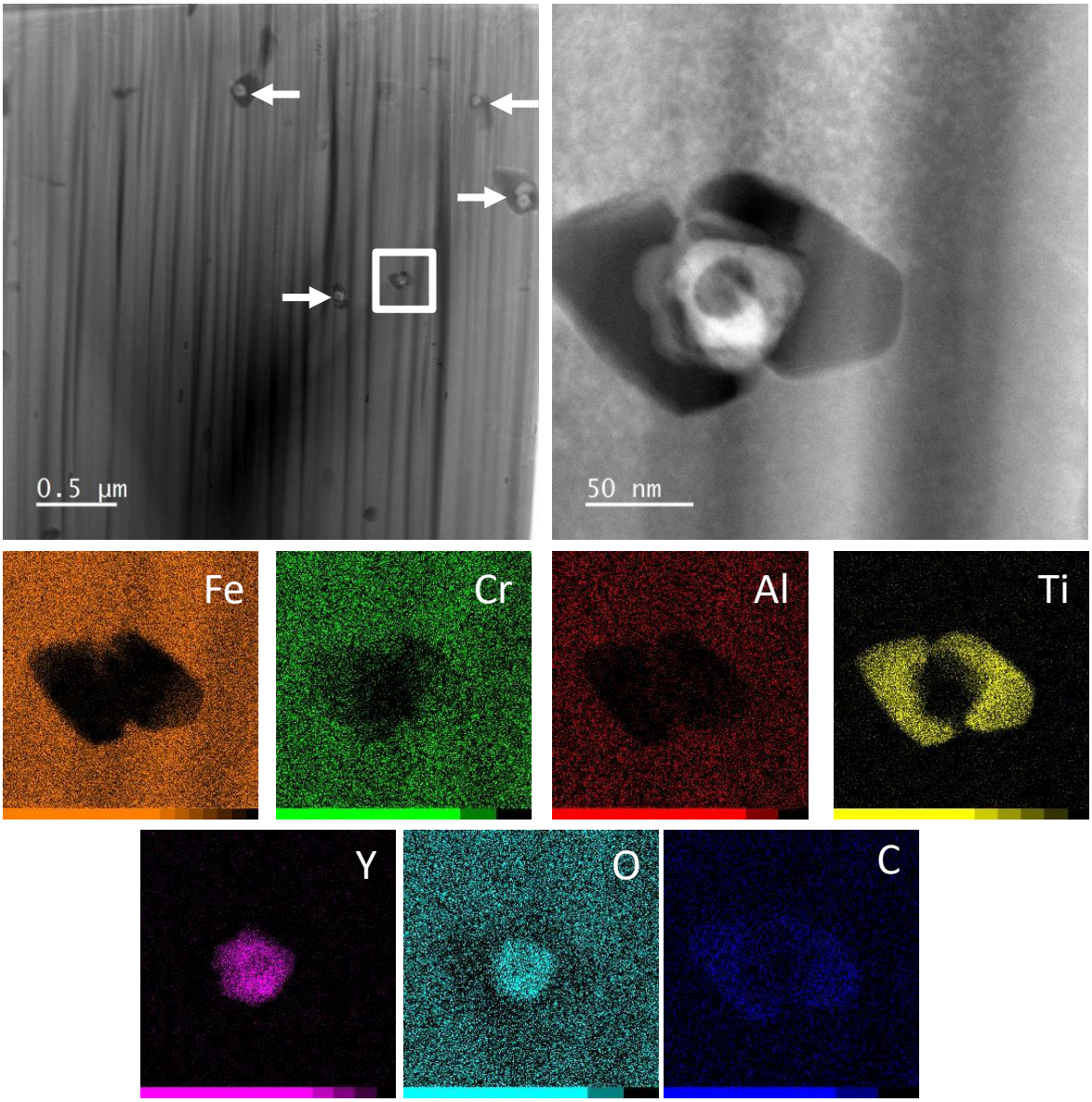

Figure 5.18: STEM EDS maps of co-precipitation of Y-oxides and TiC in B4HT. White arrows are pointing to other similar precipitates present in the matrix.

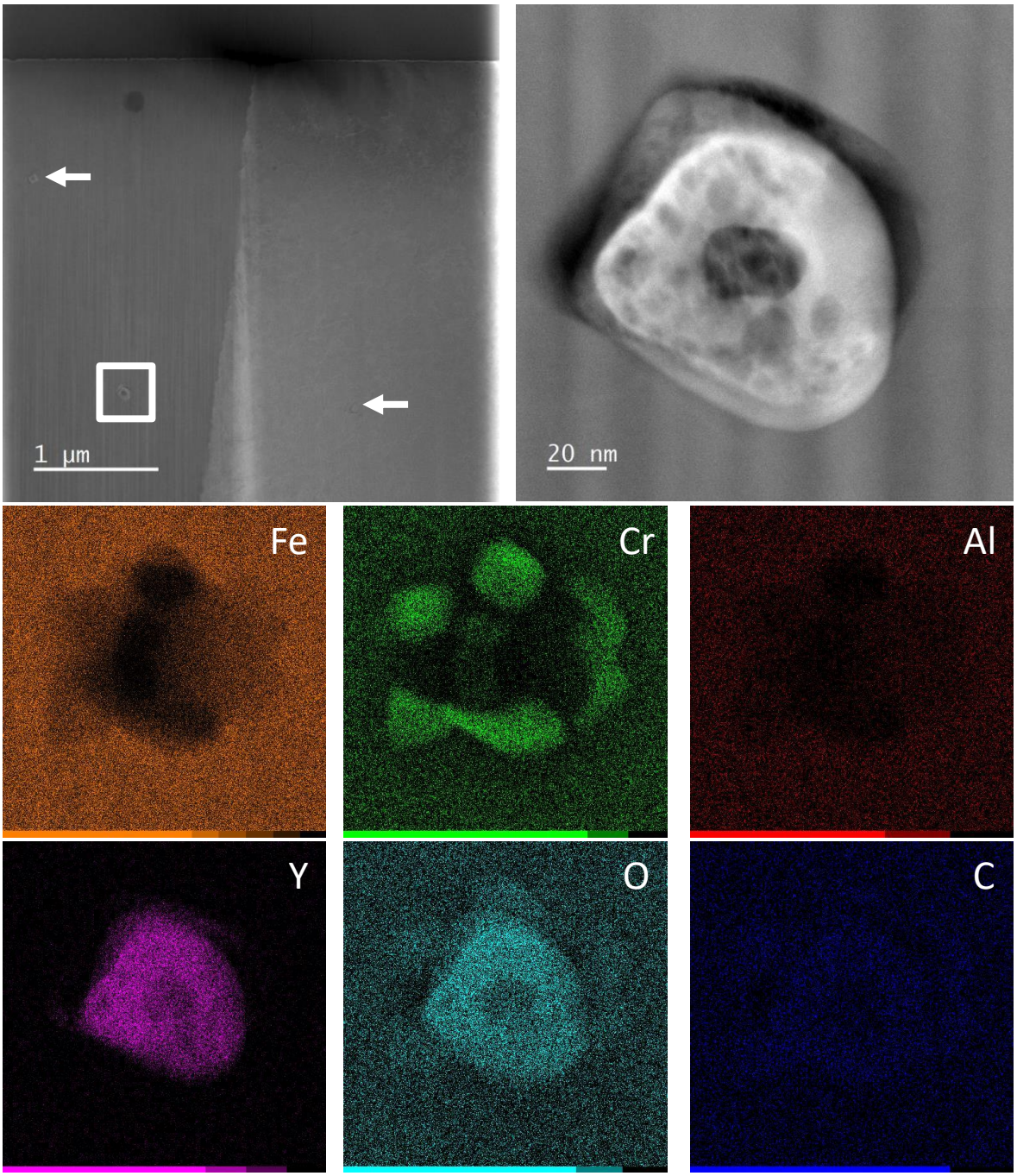

Figure 5.19: STEM EDS maps of co-precipitation of Y-oxides and Cr-carboxides in B6. White arrows are pointing to other similar precipitates present in the matrix.

and M23C6).

Singular TiC-enriched precipitates are also present in B4 and B4HT. These smaller, pill-shaped precipitates are not necessarily purely TiC, however. Looking at **Figure 5.20** shows that there is Cr enrichment present in the interior of TiC precipitates. A grain boundary was also analyzed from B4 (**Figure 5.21**). Microsegregation of Y, Ti, and C to grain boundaries occurred leaving the grain boundary devoid of Fe and Al while being deficient in Cr. As mentioned in **Section 5.1.2**, this microsegregation has the potential to weaken grain boundaries and result in premature failure under loading conditions or residual stress forming cracks [206-208].

5.3.2. Atom Probe Tomography

To better understand the precipitation complexity occurring in these specimens, a total of 17 APT needles were analyzed from specimens B2 (4 needles), B4 (5 needles), B4HT (4 needles), and B6 (4 needles). Identifying precipitates present in each needle was done using concentration isosurfaces looking for high densities of specific ionic species present within a volume. Proximity histograms were used to analyze select captured precipitates. The precipitates captured in **Figure 5.22** and **Figure 5.23** closely resemble what was observed in **Figure 5.20**: TiC precipitates with some Cr enrichment. These TiC precipitates are either reprecipitated or capture of powder particles with incomplete dissolution as predicted by the phase diagram in **Figure 5.4** and the DICTRA simulation in **Figure 5.9a**. **Figure 5.24** shows an APT example of the types of complex co-precipitation occurring in these specimens (qualitatively similar to that shown in **Figure 5.18** and **Figure 5.19**). An Y-Si-Ti intermetallic phase is shown in contact with a TiC precipitate. Co-precipitation is often observed in weld metal where multiple secondary phases are possible, like these AM alloys [177]. From specimen B6, two different

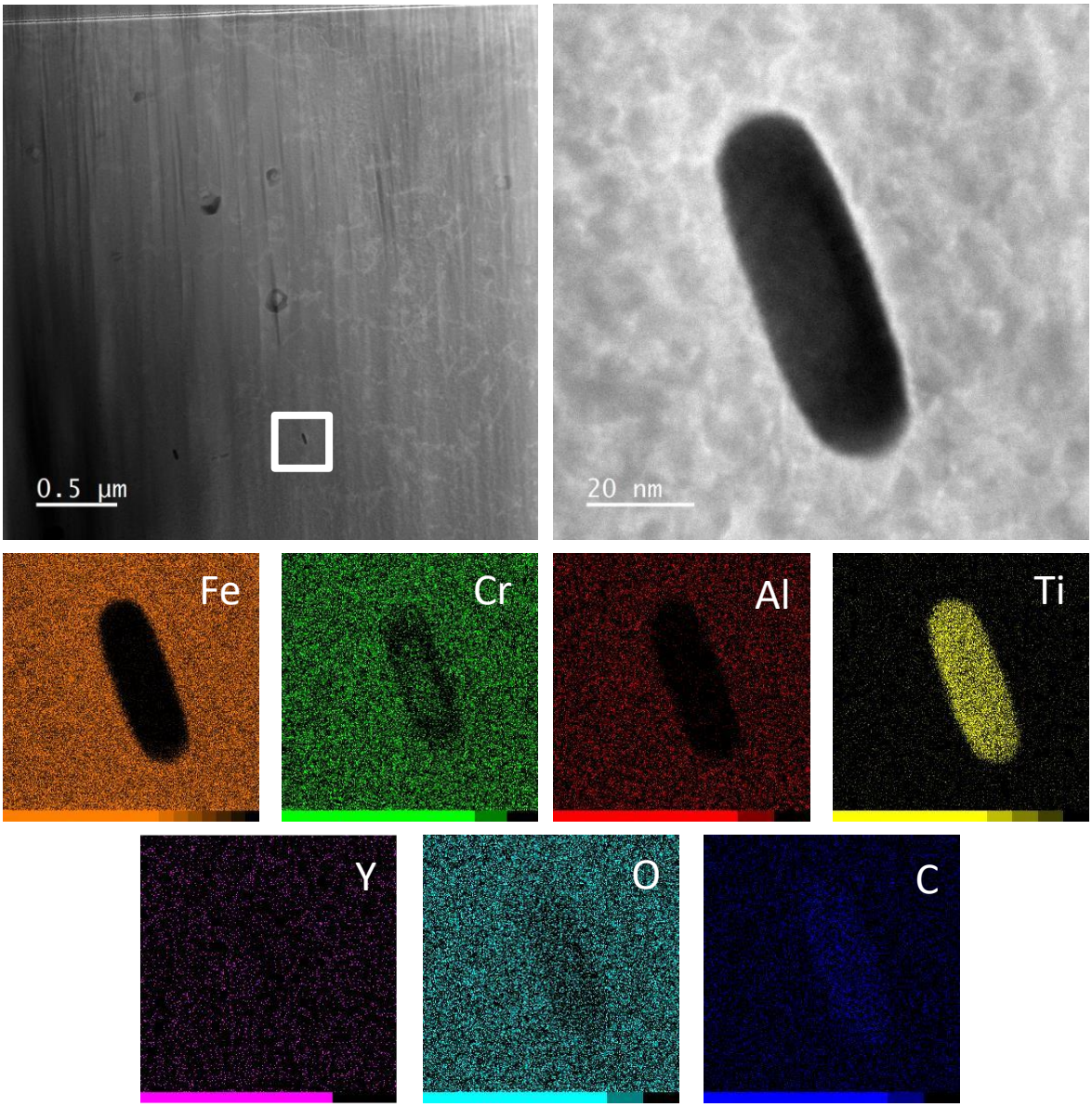

Figure 5.20: STEM EDS maps of TiC enriched in Cr from B4.

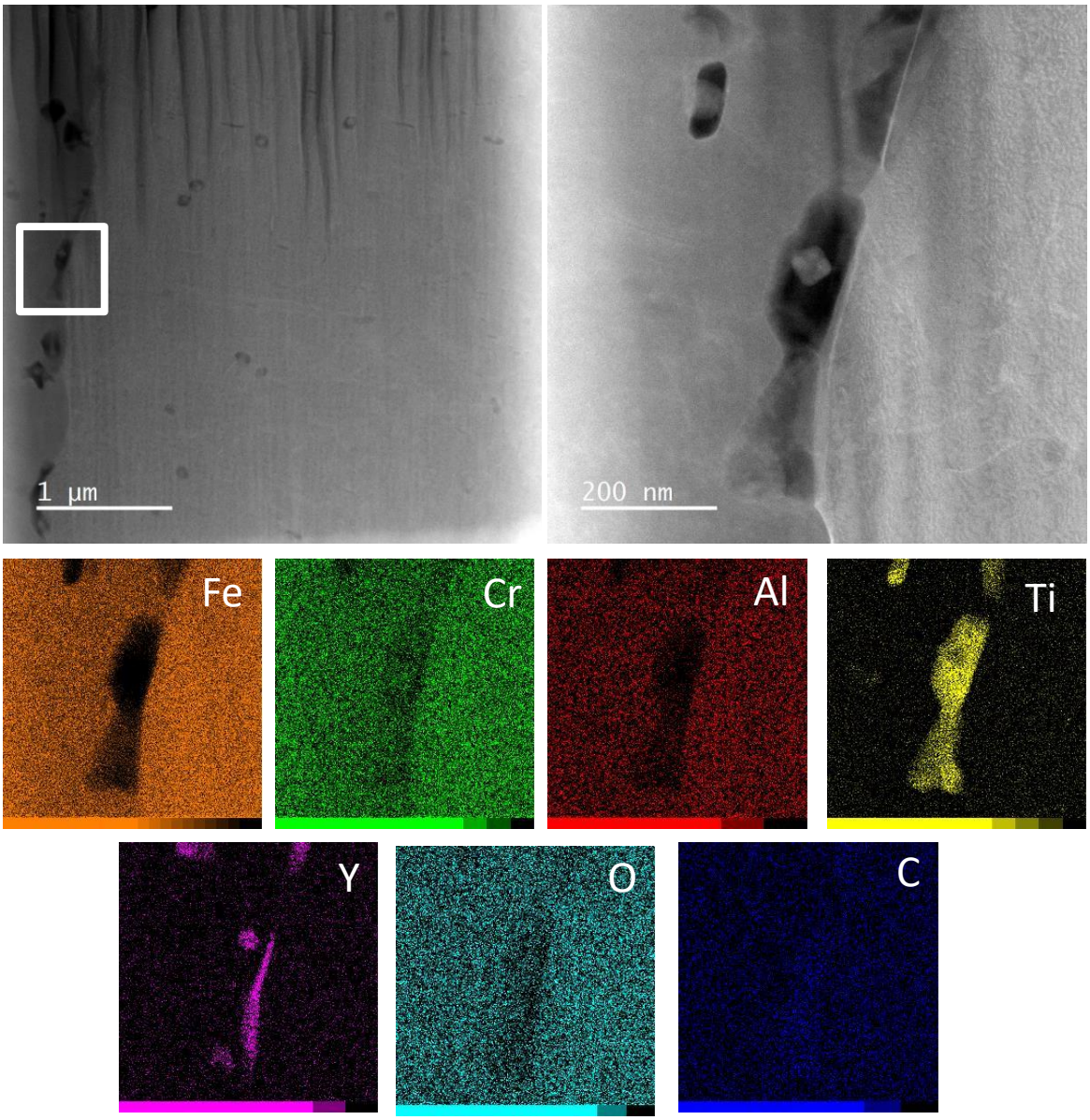

Figure 5.21: STEM EDS maps of a grain boundary from B4 showing Y, Ti, and C enrichment.

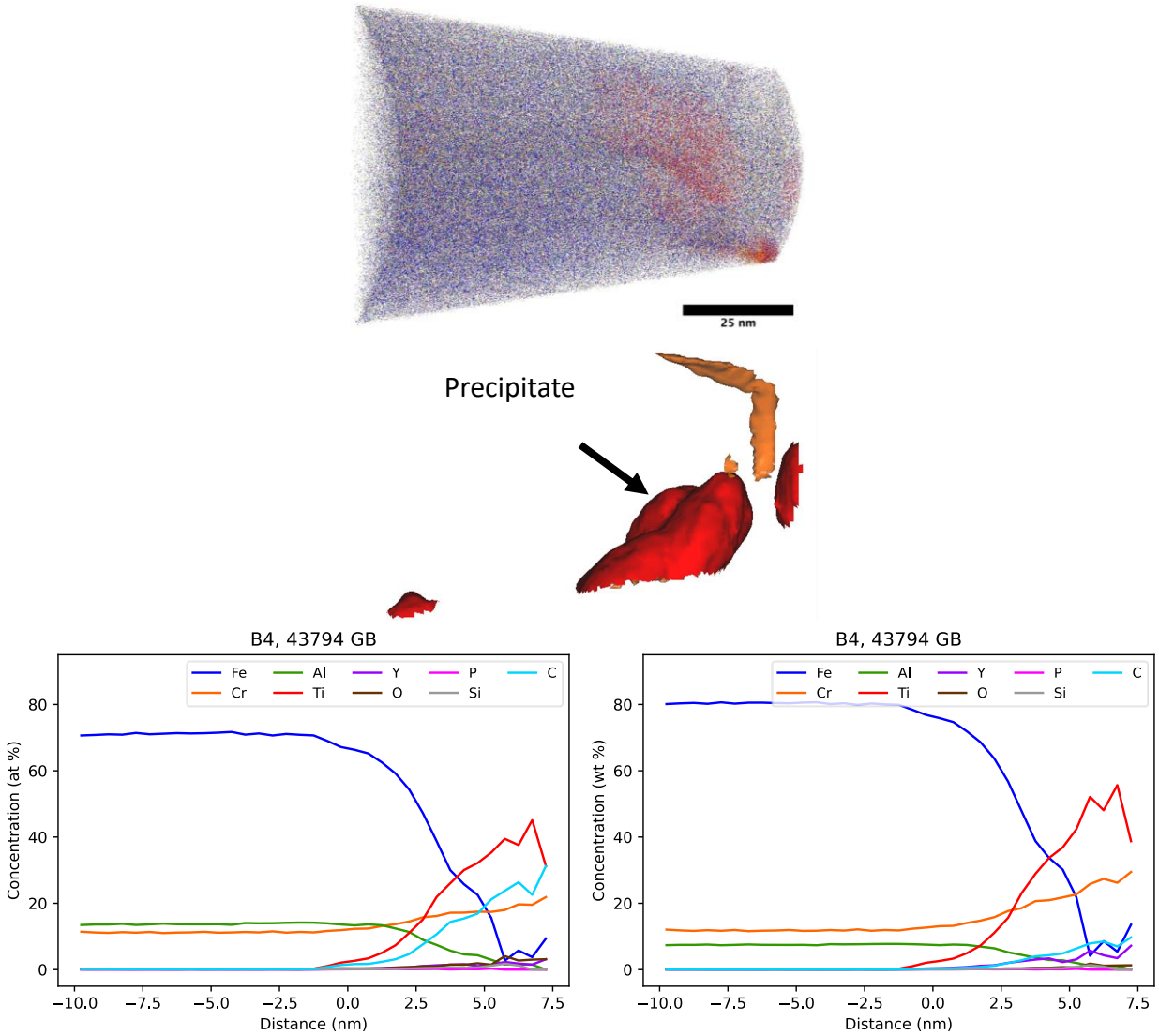

Figure 5.22: APT reconstruction of Needle 43794 from Specimen B4 with parts of a grain boundary and multiple precipitates captured. Proximity histograms of the large TiC precipitate marked with a black arrow are included.

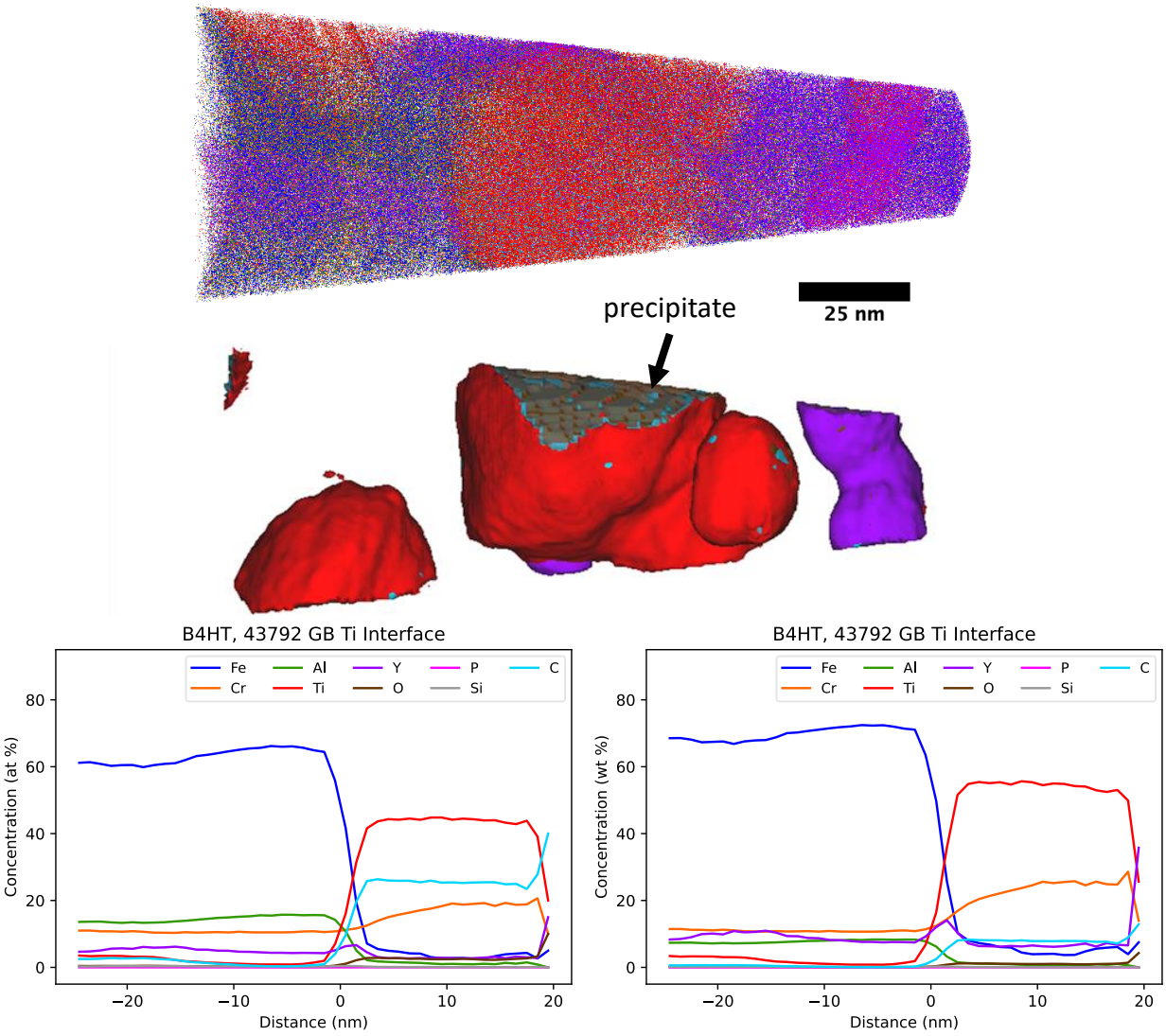

Figure 5.23: APT reconstruction of Needle 43792 from Specimen B4HT with parts of a grain boundary and multiple precipitates captured. Proximity histograms of the large TiC precipitate marked with a black arrow are included.

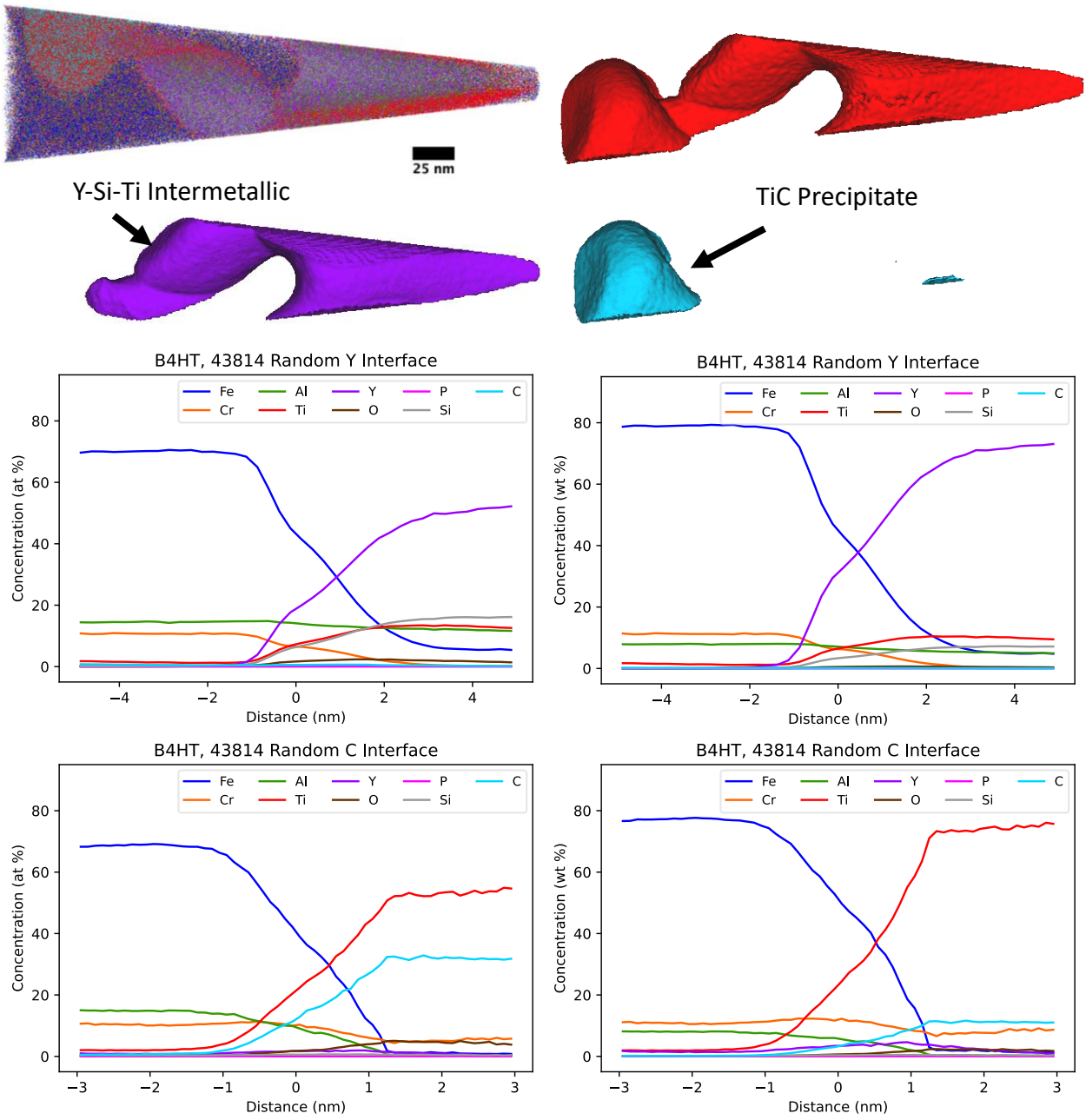

Figure 5.24: APT reconstruction of Needle 43814 from Specimen B4HT. Proximity histograms of a large Y-rich intermetallic phase (top) and a TiC precipitate without Cr infiltration (bottom) are included with the referenced precipitates marked by a black arrow.

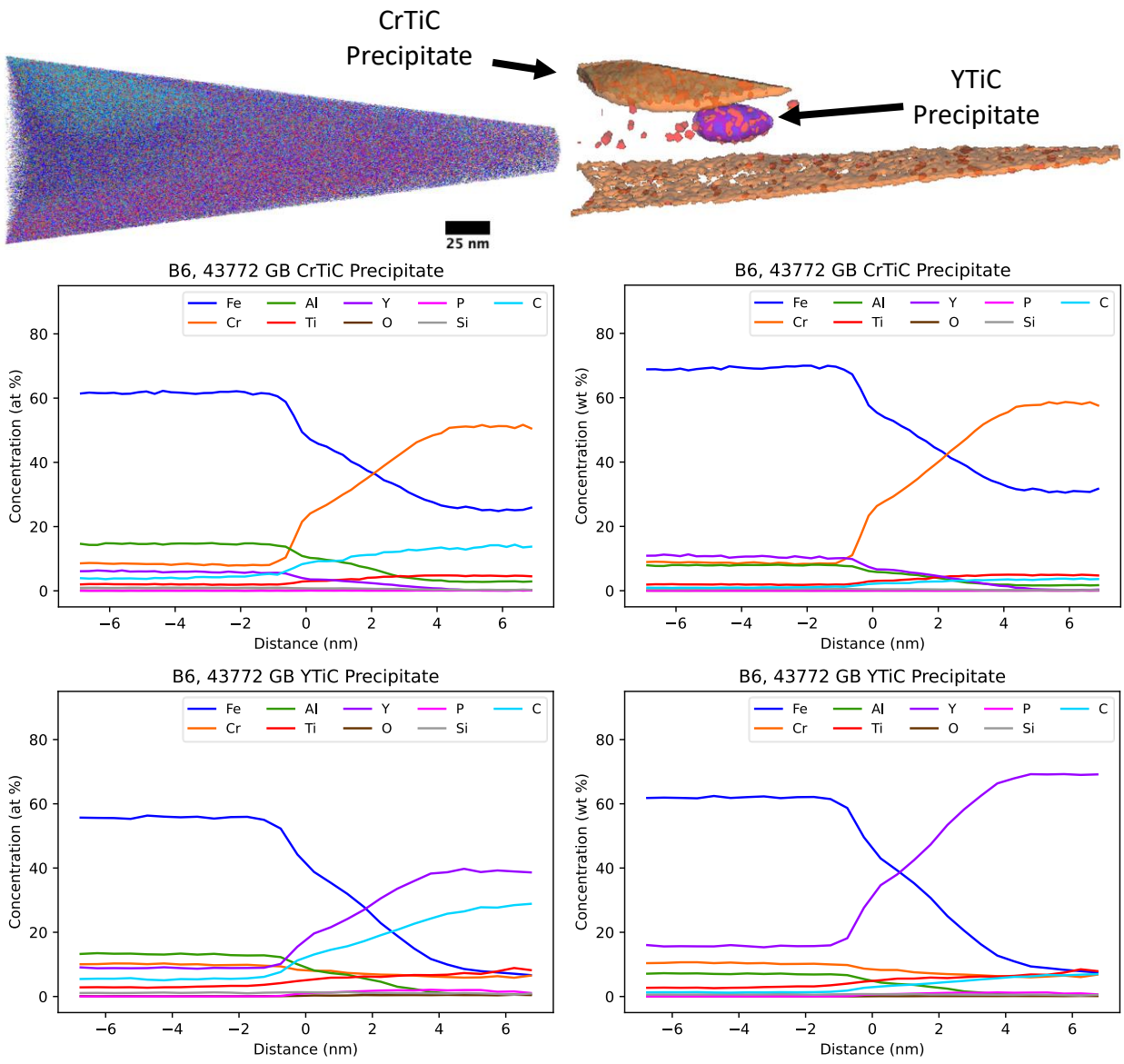

Figure 5.25: APT reconstruction of Needle 43772 from Specimen B6. Proximity histograms of a CrC precipitate enriched in Ti (top) and a YC precipitate enriched in Ti (bottom) are included with the referenced precipitates marked by a black arrow.

precipitates were captured. As shown in **Figure 5.25**, a YC precipitate and CrC precipitate were located in and on a grain boundary. Both precipitates surprisingly contained small concentrations of Ti. This is likely due to contamination. Specimens B5 and B6 were produced last and immediately after B4, which was blended with TiC powder. It is likely that some of the fine TiC powder was trapped in the pneumatic powder delivery system and was eroded away during subsequent builds. The CrC precipitate present has a Cr:C ratio similar to M23C6 (approximately 3.3:1 vs. 3.8:1). It is important to note that C and O concentrations captured from APT should not be considered 100% accurate. Concentrations of C and O have been shown in APT literature to be underestimated [214-218].

For each specimen at least one needle included a grain boundary. The remaining needles were taken at random. 1-dimensional concentration profile cylinders were placed across each grain boundary to examine if any grain boundary segregation occurred. Some level of grain boundary segregation was found in specimens B4, B4HT, and B6 (**Figure 5.26**, **Figure 5.27**, and **Figure 5.28**, respectively). For the grain boundary captured from B4, local Cr concentration nearly tripled (approximately 10 at% to 30 at%) while C and O concentrations also increased appreciably (approximately 0 at% to 7 at% and 13 at%, respectively). The B4HT grain boundary captured was significantly enriched in Y and lightly enriched in Ti and C. This closely reflects the STEM EDS data in **Figure 5.21**. Y segregation like this is common in ODS alloys due to low solubility of Y in an Fe matrix [51]. Instead of clipping a grain boundary as with B4 and B4HT, the needle from B6 in **Figure 5.28** transverses a grain boundary. The grain boundary is enriched in Y, C, Ti, and Si. The interior of the grain boundary contains a precipitate further enriched in Y, C, and to a lesser extent Ti. As shown, there is a thin layer of Cr enrichment along the edge

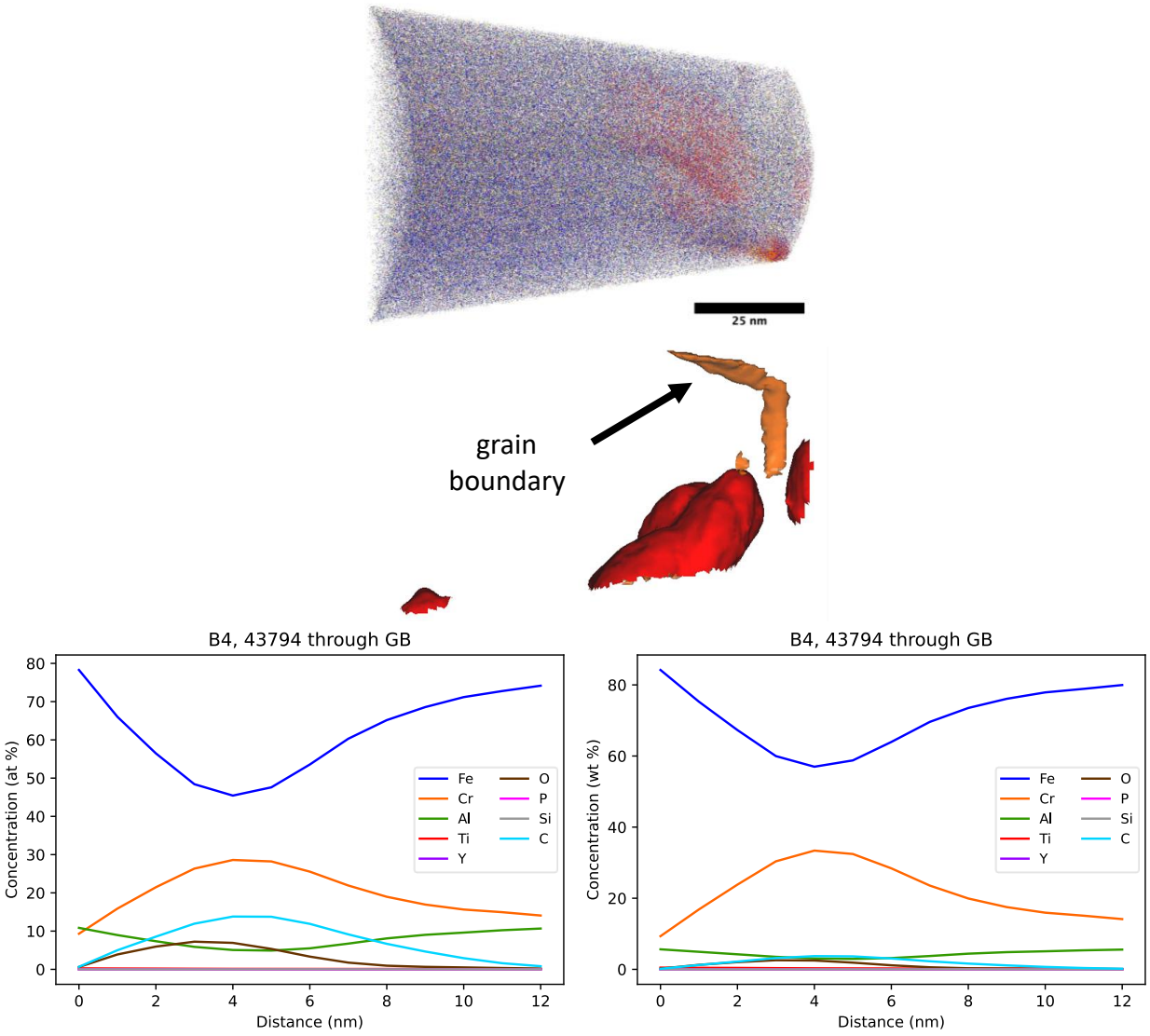

Figure 5.26: 1-dimensional concentration profile through an edge of a grain boundary (marked with black arrow; Cr-rich angled region) captured in B4.

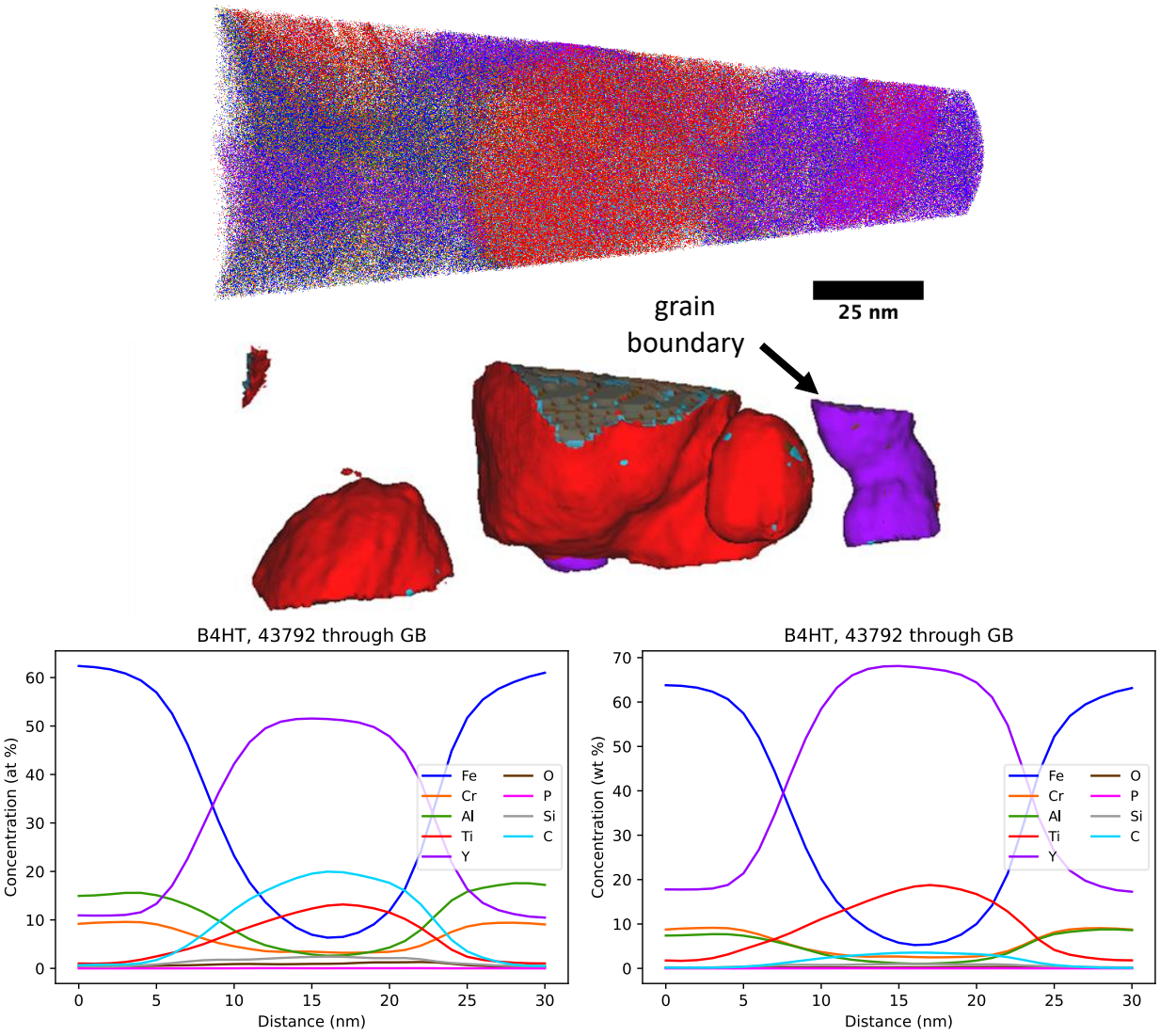

Figure 5.27: 1-dimensional concentration profile through an edge of a grain boundary (marked with black arrow; Y-rich region across needle tip) captured in B4HT.

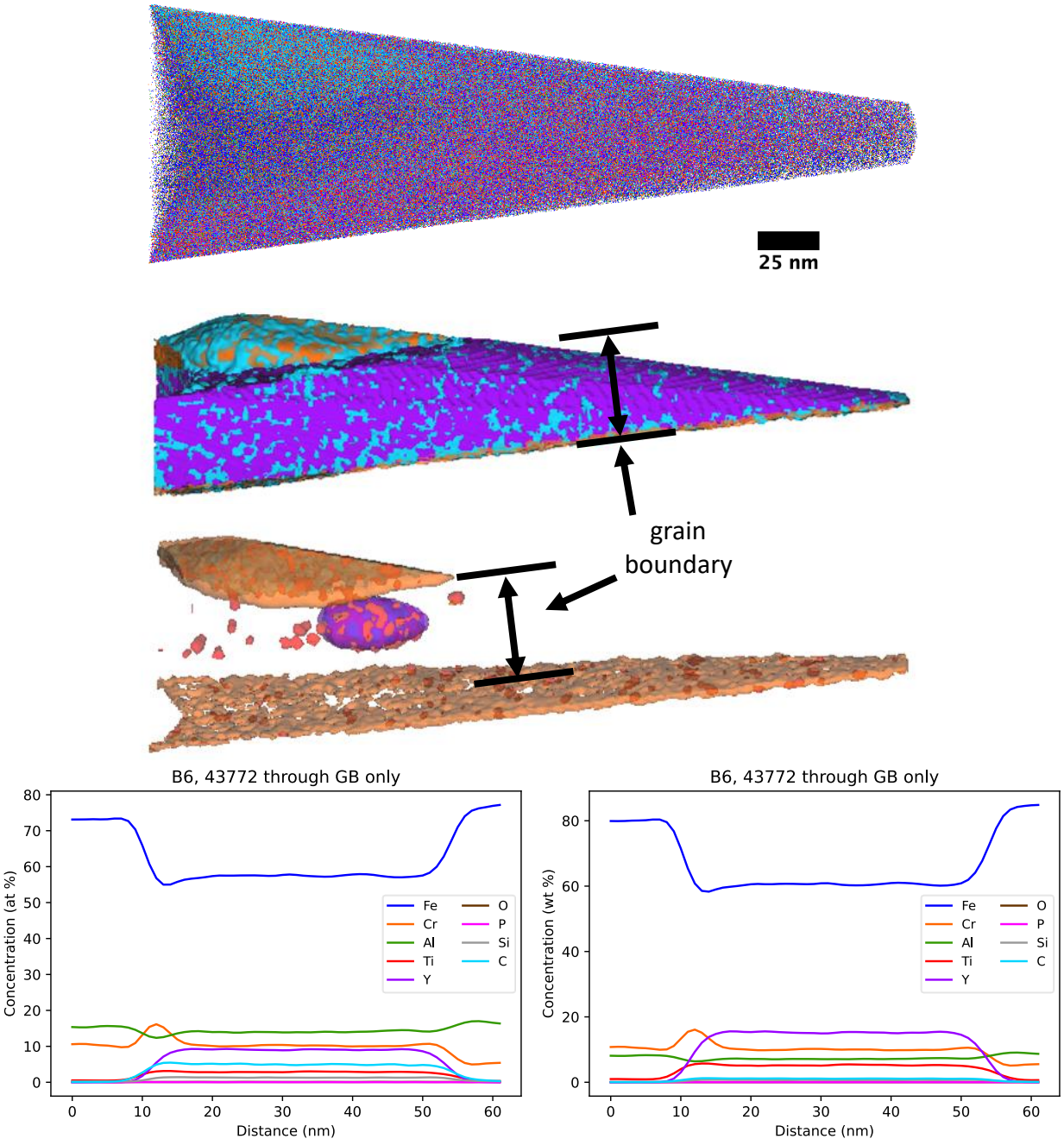

Figure 5.28: 1-dimensional concentration profile through a grain boundary (marked with black arrow; bounded Y-rich region) captured in B6.

of the grain boundary. On the opposite side of the grain boundary, there is a precipitate enriched primarily in Cr and C adjacent to the grain boundary.

5.4. Mechanical Properties

5.4.1. Vickers Microhardness

To examine how changes in alloy composition influenced mechanical strength, Vickers microhardness measurements were taken. The results from those measurements are shown in **Figure 5.29**. To minimize the influence of as-built defects like those shown in **Section 5.1.2**, the Grubbs' method of identifying outliers was used to remove outlier datapoints. As shown, the SiC and TiC alloying additions led to >10% increase in microhardness compared to B1/B2. This is expected to be via grain size refinement and solid-solution strengthening as the differences between precipitation across the as-built specimens are minimal [3].

5.4.2. Precipitate Strengthening

The microhardness for the reference alloy used in **Section 4.1.5** was approximately 195 Hv. An increase of ~ 20 Hv was measured compared to the reference alloy specimens B1 and B2. This increase is similar to what was seen with specimens from the previous experiment (current: ~ 212 HV vs. previous: 216 Hv). For B3, B3F, B4, B5, and B6 an increase of approximately 45 Hv was measured over the reference alloy. B1 and B2 should give the best comparison for how precipitation influenced mechanical properties given that precipitation was similar across all as-built specimens and B1 and B2 did not have any additional alloying aside from O. An estimate of how much precipitate strengthening contributed to the increase in hardness over the reference alloy can be calculated using the Friedel model from **Equation 2.6** with $M = 3$, $\mu = 100.4$ GPa, $b = 0.248$ nm, N equal to the average precipitate number density in the builds, d equal to the

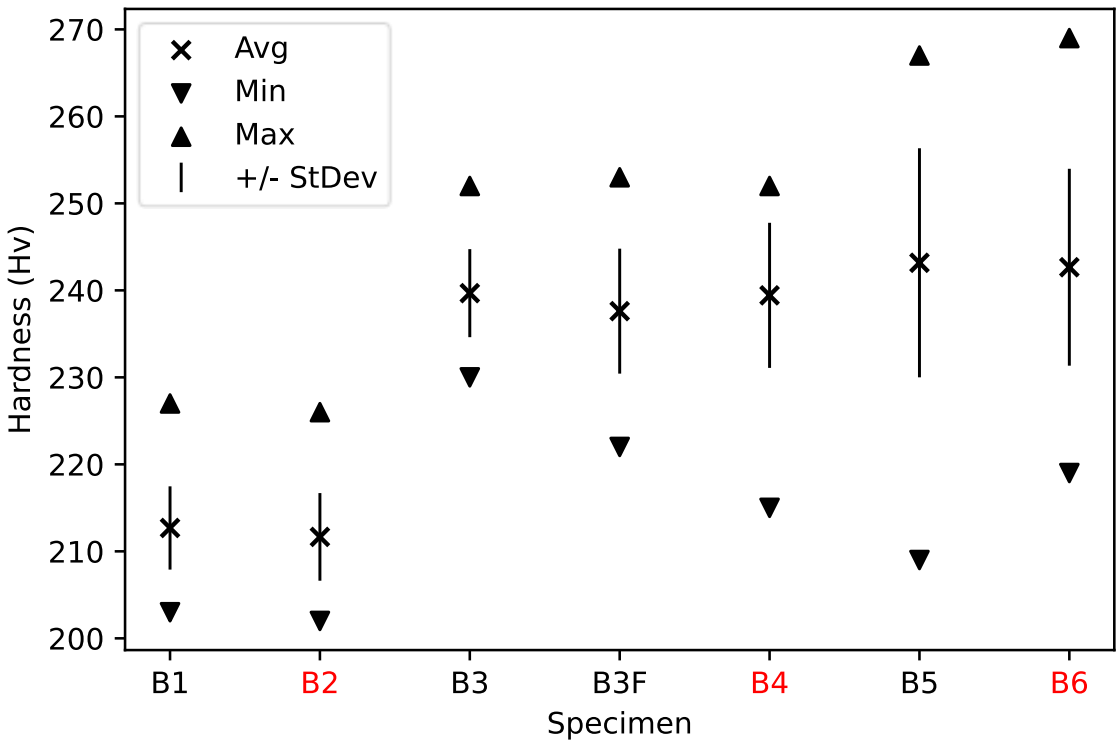

Figure 5.29: Vickers microhardness measurements of all specimens.

average diameter, and α (calculated using the relationship established by Tan and Busby; Equation 2.7) some value between 0.88 to 1.03. The predicted increase in microhardness is between 8 Hv and 28 Hv (25 and 85 MPa). Using the general dispersed barrier model (**Equation 2.5**) gives a predicted increase in microhardness between 19 Hv and 51 Hv (57 and 155 MPa) [10, 95-97, 99]. The microhardness values are calculated from predicted increases in yield strength via the conversion outlined in Equation 4.1 determined for BCC Fe alloys by Busby et al [187]. **Table 5.4** includes a comparison of these results across specimens with characterized precipitation. This, like in the previous experiment, suggests that the dispersed barrier model is better at approximating the strengthening contribution of precipitates in this system.

The further increase in microhardness by B3, B3F, B4, B5, and B6 compared to B1 and B2 is unlikely to be influenced by precipitation alone as B3, B3F, B4, B5, and B6 had similar precipitate distributions as B1 and B2 (**Table 5.3**). Grain refinement and solid-solution strengthening are potential causes of this dramatic increase in hardness [3]. This is further supported when looking at a study by Gussev, Field, and Yamamoto where TiC was added to a FeCrAl alloy (Fe-13Cr-5Al-2Mo; C35M) in varied amounts, autogenously welded, and mechanically examined via tensile testing. The authors added 0.1, 0.3, and 1.0 wt% TiC to the base alloy. The relevant results of their experiments are summarized in **Table 5.5** [11]. The strength of C35M067TC is estimated using a TiC addition that was used in these experiments and a linear regression of the relevant specimens from Gussev et al.'s study. The measured change in hardness between their base alloy and the estimated C35M067TC is 23.6 Hv, very similar to the measured microhardness difference between B1/B2 and B3/B3F/B4/B5/B6. The authors noted that

Table 5.4: Expected changes in UTS based on precipitate strengthening.

		Dispersed Barrier Model				Friedel Model			
Specimen	Avg Hardness (Hv)	ΔVHN (Hv)	$\Delta\sigma_y$ (MPa)	Expected Hardness (Hv)	Expected YS (MPa)	ΔVHN (Hv)	$\Delta\sigma_y$ (MPa)	Expected Hardness (Hv)	Expected YS (MPa)
B1	212.69	50.71	155.17	249.31	762.89	27.76	84.94	226.36	692.65
B2	211.66	28.18	86.22	226.78	693.93	14.07	43.04	212.67	650.76
B2HT	--	39.44	120.69	238.04	728.41	23.10	70.69	221.70	678.40
B4	239.43	49.06	150.11	247.66	757.83	26.68	81.66	225.28	689.37
B4HT	--	38.72	118.47	237.32	726.19	18.08	55.34	216.68	663.05
B6	242.66	20.43	62.51	219.03	670.23	9.30	28.44	207.90	636.16
B6HT	--	18.50	56.62	217.10	664.33	8.26	25.29	206.86	633.00
			Wang, 2021	198.60	607.72		Wang, 2021	198.60	607.72

Table 5.5: Summarized relevant results on the influence of TiC additions to FeCrAl weld strength from Gussev, Field, and Yamamoto. C35M067TC is an approximated strength of an alloy with a TiC addition as in this experiment using a linear regression of the literature data [11].

Alloy	Amount of TiC Added (wt%)	UTS (MPa)	Expected VHN (Hv)
C35M	0	601.6	235.9
C35M01TC	0.1	623.8	244.6
C35M03TC	0.3	650.9	255.3
C35M10TC	1	683.4	268.0
C35M067TC	0.67	661.7	259.5

the grain size along the weld centerline of the C35M10TC alloy were 3x to 5x smaller than those of C35M.

5.5. Summary

The feasibility of using *in situ* oxidation during L-DED AM to produce ODS FeCrAl alloys has been demonstrated in the scoping AM parameter study outlined in **Chapter 4** and also in the alloying study outlined in this chapter. Six different alloy combinations were tested to examine how additions of Ti, Si, and/or O prior to consolidation by AM influenced oxide agglomerate formation and nanoscale precipitation. The key conclusions are as follows:

- Addition of a pre-build heat treatment on powder significantly increased the amount of O dissolved and retained.
- Addition of TiC and SiC led to appreciable grain size reduction and defect reduction of the as-built block when in the presence of significant amounts of O.
- Addition of Ti led to a reduction in agglomeration. A firm conclusion on the efficacy of Si additions reducing agglomeration could not be obtained due to unexpectedly low Si content in the as-built specimens.
- Additions of TiC and SiC had little effect on nanoscale precipitate distributions. They did complicate the precipitation chemistry by providing the necessary ingredients for more varied precipitate compositions. The presence of C appears to be a key bad actor and should likely be avoided in future studies. It is also possible that increased alloying with Ti or Si is necessary for a more noticeable change in precipitate distributions.

CHAPTER SIX

CONCLUSIONS AND FUTURE WORK

6.1. Summary of Experimental Results

In this work examining the feasibility of using L-DED AM with a reactive atmosphere to produce ODS FeCrAl, it was found that significant increases in specimen O content were achievable without using MA. Simulations based on Rosenthal's equation were performed to determine how varied operating parameters affected AM melt pool characteristics and then compared to as-built specimen O content. It was discovered that both solidification velocity and gas incidence fraction (fraction of a melt pool's lifetime spent underneath a reactive atmosphere) were both important in controlling O dissolution and retention during L-DED AM under a reactive atmosphere. Including the fraction of a melt pool's lifetime spent under a reactive atmosphere takes into consideration how long a positive or negative driving force for is influencing O dissolution.

Using TEM and APT, it was discovered that moderate precipitate number densities were achievable in an as-built state (approaching 10^{20} m^{-3}) and that a HT at 600 °C for 1 h did not significantly contribute to furthering precipitation. Specimens analyzed post HT showed minor increases in precipitate number densities at best, and more often showed decreases in precipitate number densities and coarsening. This suggests that either prior to or during HT that the system's precipitation state has shifted from a nucleation stage to an undesired growth and coarsening stage. As evidenced, precipitation formed using this process is often complex with various core-shell or co-precipitation present.

Comparison of precipitate characteristics in this work and those in the literature are provided in **Figure 6.1**. This work has achieved better precipitate dispersions than historically achieved using L-DED (nearing 10^{20} m^{-3}). While these results were an improvement on what was previously achieved using this technique, PBF-LB has shown potential to achieve number densities on the order of 10^{21} m^{-3}. Experiments using GARS powder and powder metallurgy techniques achieve number densities on the order of 10^{22} m^{-3}. The current standard using MA powder and powder metallurgy techniques has shown an ability to achieve number densities on the order of 10^{24} m^{-3}. So, the results from these experiments, while an improvement on previous literature, show L-DED AM is still one order of magnitude behind PBF-LB, two orders of magnitude behind GARS methods, and four orders of magnitude behind mechanically alloyed powder. This suggests that using L-DED to produce ODS alloys with number densities on the order of 10^{23} m^{-3}, as desired for fusion energy system, is unlikely to be successful without significant process improvements [219]. In the case of non-fusion energy systems focused on improving material creep resistance (desired number densities of 10^{21} m^{-3}), there is some promise that more manageable process and alloy refinements can overcome the order of magnitude difference in number densities [145, 220].

Work by Wassermann et al., suggests that ~ 10^{21} m^{-3} number densities may be a current theoretical limit for AM processes. After characterizing Ni-20Cr + 1 wt% Y_2O_3 specimens produced using a PBF-LB under varied laser powers and tool speeds, they modeled oxide evolution characteristics during AM. Their results showed that precipitate number densities correlated inversely with solidification velocities. They noted that lower solidification velocities increased melt pool residence times for oxides causing increased potential for coarsening via oxide collision [145]. This agrees with work performed by Eo

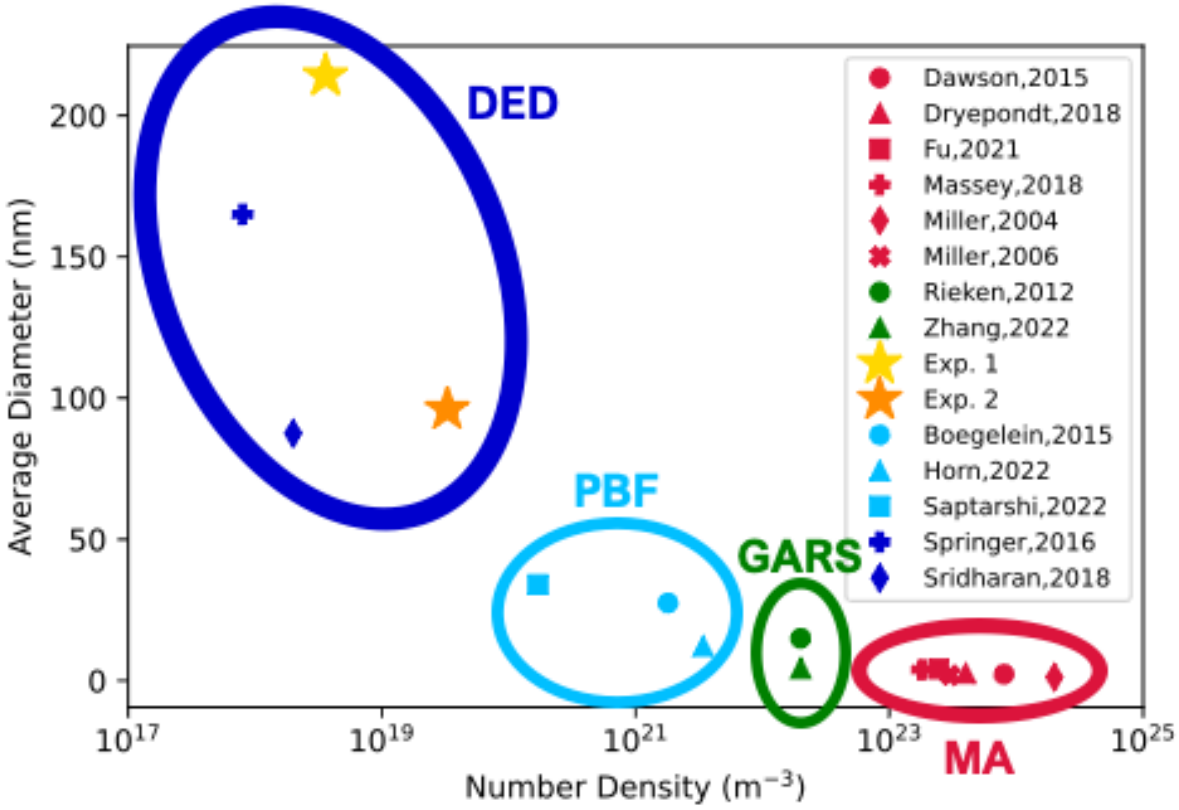

Figure 6.1: Comparison of this work's precipitate characteristics to literature values of other methods for producing ODS alloys. DED = directed energy deposition, PBF = powder bed fusion, GARS = experiments using gas atomization reactions synthesis powder and powder metallurgy techniques, and MA = experiments using mechanical alloyed powder and powder metallurgy techniques. This work's experiments are shown by the starred results.

et al., where they modeled oxide evolution of ODS alloys produced via PBF-LB and L-DED. Coarsening via collision was a primary mechanism for increased oxide size and is supported in the welding literature on oxide inclusion growth [147].

Solidification velocities in this work are on the order of 10^{-3} to 10^{-2} m/s while typical solidification velocities for PBF-LB systems are on the order of 0.5 to 1 m/s. This leads to an increased melt pool residence time for any oxides formed during AM allowing for appreciably longer times for collision driven coarsening. This is compounded by poor compatibility between melt pool oxides and the solidifying alloy where work has shown that oxides will ride along in front of a solid-liquid interface further increasing the time an oxide spends in a melt pool [144].

A means of avoiding collision driven coarsening would be to limit precipitation in a melt pool in favor of precipitation during a post-build heat treatment. However, solute trapping of O is difficult. As discussed in Section 4.5.2, the trapping velocity for complete trapping of O is ~ 9.6 m/s. As L-DED solidification velocities are on the order of 10^{-3} to 10^{-2} m/s, this suggests that small amounts of O are likely getting trapped in solid solution. As a result, it is likely that significant proportions of O (and other important oxide forming elements) are forming oxides in a melt pool as suggested by Wassermann et al. and supported in **Table 4.2** of this work. As mentioned above, formation of precipitates in the melt pool further drives coarsening by collision and restricting the potential of manufacturing ODS alloys via these methods. This is further compounded because large amounts of dissolved O are needed to achieve desired oxide number densities (10^{23} m^{-3}) via this method as shown in **Figure 6.2**.

Additions of TiC and SiC were studied to examine their influence on agglomeration and precipitate dispersions. As shown in **Figure 3.2** and **Figure 3.3**, adding Si and Ti

Table 6.1: Oxygen content required (wt%) required for various precipitate sizes, number densities, and phases relevant to ODS FeCrAl. Red cells are O concentrations near or above those achieved using PM techniques.

	[O] at Select Precipitate Number Densities (wt%)											
	1E+21			1E+22			1E+23			1E+24		
Diameter (nm)	Yttria	YAM	YAG	Yttria	YAM	YAG	Yttria	YAM	YAG	Yttria	YAM	YAG
1	7.76E-06	8.51E-06	1.07E-05	7.76E-05	8.51E-05	1.07E-04	7.76E-04	8.51E-04	1.07E-03	7.76E-03	8.51E-03	1.07E-02
2	6.21E-05	6.81E-05	8.54E-05	6.21E-04	6.81E-04	8.54E-04	6.21E-03	6.81E-03	8.54E-03	6.21E-02	6.81E-02	8.54E-02
3	2.10E-04	2.30E-04	2.88E-04	2.10E-03	2.30E-03	2.88E-03	2.10E-02	2.30E-02	2.88E-02	2.10E-01	2.30E-01	2.88E-01
4	4.97E-04	5.45E-04	6.83E-04	4.97E-03	5.45E-03	6.83E-03	4.97E-02	5.45E-02	6.83E-02	4.97E-01	5.45E-01	6.83E-01
5	9.70E-04	1.06E-03	1.33E-03	9.70E-03	1.06E-02	1.33E-02	9.70E-02	1.06E-01	1.33E-01	9.70E-01	1.06E+00	1.33E+00
6	1.68E-03	1.84E-03	2.31E-03	1.68E-02	1.84E-02	2.31E-02	1.68E-01	1.84E-01	2.31E-01	1.68E+00	1.84E+00	
7	2.66E-03	2.92E-03	3.66E-03	2.66E-02	2.92E-02	3.66E-02	2.66E-01	2.92E-01	3.66E-01			
8	3.97E-03	4.36E-03	5.47E-03	3.97E-02	4.36E-02	5.47E-02	3.97E-01	4.36E-01	5.47E-01			
9	5.66E-03	6.20E-03	7.78E-03	5.66E-02	6.20E-02	7.78E-02	5.66E-01	6.20E-01	7.78E-01			
10	7.76E-03	8.51E-03	1.07E-02	7.76E-02	8.51E-02	1.07E-01	7.76E-01	8.51E-01	1.07E+00			
11	1.03E-02	1.13E-02	1.42E-02	1.03E-01	1.13E-01	1.42E-01	1.03E+00	1.13E+00	1.42E+00			
12	1.34E-02	1.47E-02	1.85E-02	1.34E-01	1.47E-01	1.85E-01	1.34E+00	1.47E+00	1.85E+00			
13	1.71E-02	1.87E-02	2.35E-02	1.71E-01	1.87E-01	2.35E-01	1.71E+00	1.87E+00				
14	2.13E-02	2.33E-02	2.93E-02	2.13E-01	2.33E-01	2.93E-01						
15	2.62E-02	2.87E-02	3.60E-02	2.62E-01	2.87E-01	3.60E-01						
16	3.18E-02	3.49E-02	4.37E-02	3.18E-01	3.49E-01	4.37E-01						
17	3.81E-02	4.18E-02	5.25E-02	3.81E-01	4.18E-01	5.25E-01						
18	4.53E-02	4.96E-02	6.23E-02	4.53E-01	4.96E-01	6.23E-01						
19	5.32E-02	5.84E-02	7.32E-02	5.32E-01	5.84E-01	7.32E-01						
20	6.21E-02	6.81E-02	8.54E-02	6.21E-01	6.81E-01	8.54E-01						

reduces the contact angle and thus interfacial energy between steel and oxide phases, which should reduce the amount of agglomeration and precipitate size as governed by equations 2.17, 2.18, and 2.19. TiC additions were shown to reduce agglomerate area, equivalent diameter, and the number of oxide agglomerates present in as-built specimens. Added TiC powder was incompletely dissolved during AM as suggested by DICTRA simulations in **Figure 5.9**. These partially dissolved powder particles likely acted as nucleation sites for grain formation, which led to the reduction in agglomeration as well as reduction in defect density. SiC additions did not appreciably influence either agglomerate area, equivalent diameter, or the number of agglomerates compared to the unblended specimens. This work showed little change in precipitate size and number densities because of TiC or SiC additions, however, significant changes in precipitate complexity did occur. Instead of Y-rich intermetallic phases surrounding oxide precipitates, additions of TiC and SiC led to co-precipitation of various carbides around available oxides. Increased amounts of grain boundary segregation were also noticed. is likely due to a couple of reasons. By virtue of incomplete dissolution of TiC particles in the melt pool, the concentration of Ti available to reduce interfacial energy between oxide and BCC Fe is overestimated from compositional data. Additionally, TiC is sufficiently stable that it precipitates out of solution third as demonstrated for Specimen B4 in the Scheil simulation in **Figure 6.2**. This would further decrease the elemental Ti available to reduce oxide-Fe interfacial energy. There is also conflicting data regarding how much Ti should be added to reduce interfacial energy and achieve wetting. Humenik noted that only a 0.04 wt% addition of Ti was needed to significantly reduce the contact angle formed by electrolytic Fe on Al_2O_3 [149]. However, work by Madzivhandila discovered that a Ti

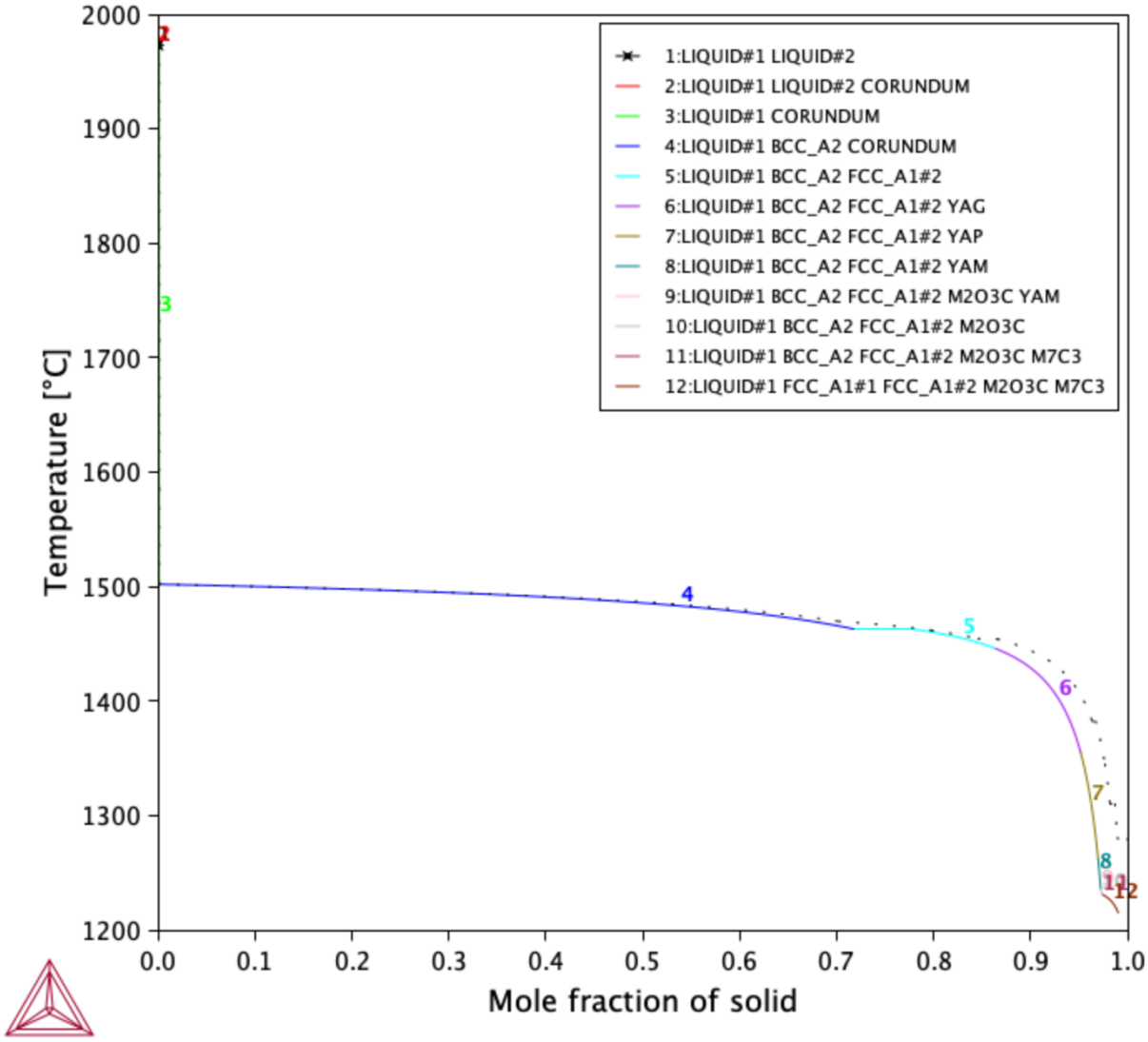

Figure 6.2: Scheil simulation of Specimen B4. TCFE9 was used for this simulation.

addition of 1.5 wt% was needed to achieve complete wetting of a Fe-25Cr-2C-1Mn alloy on Al_2O_3 [60].

The ineffectiveness of a SiC addition was likely also plagued by insufficient amounts of Si available to reduce oxide-Fe interfacial energy. As demonstrated in **Figure 5.1b**, approximately half of the intended Si addition to was lost between blending and manufacturing. This is most likely a result of stratification of dissimilar powders between the conclusion of blending and initiation of manufacturing. SiC added specimens were produced last; therefore, more time passed between blending and AM. Si is also has a high vapor pressure, which makes it prone to volatilizing during AM [149]. These losses combined with results from Verhiest et al. (Fe-9Cr on Y_2O_3), and Kingery (Fe on Al_2O_3) that suggest Si concentrations above 0.7 wt% and 9 wt%, respectively, are needed make it unlikely that the achieved 0.17 wt% concentration of Si was sufficient to make a difference [61, 148].

Aside from concerns of too small of additions of TiC and SiC, there are two other possible factors at play. First is a temperature effect on interfacial energy or contact angle. Looking at **Figure 3.3**, contact angle and temperature are directly correlated with one another across all concentration of Ti added. Increases in temperature cause increases in contact angle and interfacial energy. Further, the sessile drop method literature studying oxide-Fe interfacial energies performs their experiments at or below 1600 °C. With melt pool temperatures in these experiments exceeding the boiling point of Fe (2861 °C), there is a significant potential for the literature data to have underestimated how much added Ti or Si would be required for AM related conditions [60, 61, 148, 149]. Second, Madzivhandila et al., noticed a time dependency on contact angle during their sessile drop

method experiments. They started taking images at 1440 °C and continued taking images every 10 minutes until their specimen reached 1340 °C. They noticed a change in contact angle between their first and second images of the contact angle [60]. A change in measured interfacial energy over such a significant period of time when compared to AM melt pool lifetimes (~ 0.5 s to 1 s) in this work could suggest that there is insufficient time in a melt pool for the influence of added Ti or Si to appreciably affect oxide-Fe interfacial energies.

6.2. Future Work

As suggested earlier in this chapter, for AM of ODS alloys to approach number densities achieved by traditional powder metallurgy methods (10^{23} to 10^{24} m^{-3}), significant additional process development is needed to prevent deleterious agglomeration from wasting valuable oxide forming components. As demonstrated by Wassermann in 2024, agglomerates formed during AM tend to end up near or on melt pool's surface [145]. Convection currents in a melt pool carry oxides to a melt pool surface (**Figure 2.19**) where oxides stay and collide because of their lower density compared to liquid Fe encouraging agglomeration (**Table 3.2**) [50, 60-62, 81, 82, 143, 146]. This problem is made increasingly difficult because agglomeration happens quickly. As shown by Babu et al. in 1996, small increases in weld time lead to significant, rapid growth in precipitate size of oxide inclusion in low alloy steel welds [147]. This can partially be mitigated by the increased solidification rates in AM; however, during subsequent layers in AM, some portion of previous layers are remelted. This carries oxides from previous layers to the surface of the new melt pool as demonstrated in optical mosaics presented in **Figure 5.6** where agglomerates are present at regular intervals greater than a single

layer height across the z-direction. Additional studies examining how increases in oxide density could look to counteract some of these effects. As shown in **Table 3.2**, an addition of Hf would allow for formation of a complex Y-Hf-O phase with a density comparable to liquid Fe. Alternatively, Ce could also be considered as a heavier complex oxide former as has been shown in the literature on ODS FeCrAl [221, 222].

Another means of reducing agglomeration could be to maximize solidification velocity to minimize time allowed for agglomeration. Utilizing some application of a pulsed laser raster would help achieve this [202]. As shown in Chapter 4, use of a pulsed laser raster proved beneficial to O dissolution and retention while proving detrimental to as-built part quality. Modifying pulsed laser amplitude could provide a solution to capture O retention improvements while minimizing defect formation that plagued samples in this work utilizing a pulsed laser raster vs. a continuous laser raster. For example, instead of pulsing a laser from 400 W to 0 W, a laser could be pulsed from 400 W to 200 W. This dramatic change in laser power would cause a surge in melt pool solidification front due to reducing the effective power delivered to the sample while reducing extreme thermal gradients potentially leading to lack of fusion or other defects.

TiC additions performed in this work showed promise at improving build quality and reducing agglomeration through inoculation. High stability of TiC, however, reduced the potential for Ti to form complex Y-Ti-O phases via stifled dissolution and thermodynamically favored reprecipitation as predicted by ThermoCalc. Choosing an alternative inoculating material like TiO_2 powder could potentially provide similar benefits while reducing the presence of partially dissolved powder particles and complex co-precipitation and grain boundary segregation encouraged by the presence of C.

Lastly, a thorough spatial examination of precipitate distributions across a specimen could provide some valuable insights. Specimens produced in these experiments were simplistic and small. Their simple shape combined with intentional sampling near the center of the top 10 mm of material attempts to avoid any potential geometric effects. Examining other regions of these specimens (i.e. the periphery) could provide valuable information on how different thermal histories and gradients influence O dissolution and oxide precipitation in ODS alloy systems. It is also possible that these specimens were too small to reach steady-state conditions during manufacturing. Examining precipitate characteristics at different z-heights could give valuable insight as to how oxide precipitates evolve in an additive environment during subsequent layers as well as check that the chosen build height of 20 to 30 mm was sufficient to reach steady-state thermal conditions representative of what would be expected for an actual part.

LIST OF REFERENCES

[1] A. Putnis, Introduction to mineral sciences, Cambridge University Press, Cambridge [England] ;, 1992.

[2] L.L. Hsiung, M.J. Fluss, A. Kimura, Structure of oxide nanoparticles in Fe–16Cr MA/ODS ferritic steel, Materials Letters 64(16) (2010) 1782-1785.

[3] G.E. Dieter, Mechanical metallurgy, 3rd ed. ed., McGraw-Hill, New York, 1986.

[4] S.J. Zinkle, K.A. Terrani, J.C. Gehin, L.J. Ott, L.L. Snead, Accident tolerant fuels for LWRs: A perspective, Journal of Nuclear Materials 448(1) (2014) 374-379.

[5] K.A. Terrani, Accident tolerant fuel cladding development: Promise, status, and challenges, Journal of Nuclear Materials 501 (2018) 13-30.

[6] S.J. Zinkle, J.T. Busby, Structural materials for fission & fusion energy, Materials Today 12(11) (2009) 12-19.

[7] S.J. Zinkle, G.S. Was, Materials challenges in nuclear energy, Acta Materialia 61(3) (2013) 735-758.

[8] B. Raj, T. Jayakumar, S. Saibaba, K. Bhanu Sankara Rao, P.V. Sivaprasad, P. Shankar, Advances in stainless steels, Hyderabad (India), India, 2010.

[9] S. Dryepondt, K.A. Unocic, D.T. Hoelzer, C.P. Massey, B.A. Pint, Development of low-Cr ODS FeCrAl alloys for accident-tolerant fuel cladding, Journal of Nuclear Materials 501 (2018) 59-71.

[10] K.G. Field, M.A. Snead, Y. Yamamoto, K.A. Terrani, Handbook on the Material Properties of FeCrAl Alloys for Nuclear Power Production Applications (FY18 Version: Revision 1), United States, 2018.

[11] M.N. Gussev, K.G. Field, Y. Yamamoto, Design, properties, and weldability of advanced oxidation-resistant FeCrAl alloys, Materials & Design 129 (2017) 227-238.

[12] B.A. Pint, S. Dryepondt, K.A. Unocic, D.T. Hoelzer, Development of ODS FeCrAl for Compatibility in Fusion and Fission Energy Applications, JOM 66(12) (2014) 2458-2466.

[13] B.A. Pint, K.A. Terrani, Y. Yamamoto, L.L. Snead, Material Selection for Accident Tolerant Fuel Cladding, Metallurgical and Materials Transactions E 2(3) (2015) 190-196.

[14] R.B. Rebak, Chapter 5 - FeCrAl—iron–chromium–aluminum monolithic alloys, in: R.B. Rebak (Ed.), Accident Tolerant Materials for Light Water Reactor Fuels, Elsevier2020, pp. 83-141.

[15] H. Shibata, S. Ukai, N.H. Oono, S. Hayashi, K. Sakamoto, M. Hirai, Development of Accident-Tolerant FeCrAl Steels Containing Al2O3 Particles by Means of Internal Al Oxidation, Metallurgical and Materials Transactions A 50(4) (2019) 1816-1824.

[16] G.R. Odette, M.J. Alinger, B.D. Wirth, Recent Developments in Irradiation-Resistant Steels, Annual Review of Materials Research 38(1) (2008) 471-503.

[17] S. Ukai, 4.08 - Oxide Dispersion Strengthened Steels, in: R.J.M. Konings (Ed.), Comprehensive Nuclear Materials, Elsevier, Oxford, 2012, pp. 241-271.

[18] S. Ukai, M. Harada, H. Okada, M. Inoue, S. Nomura, S. Shikakura, K. Asabe, T. Nishida, M. Fujiwara, Alloying design of oxide dispersion strengthened ferritic steel for long life FBRs core materials, Journal of Nuclear Materials 204 (1993) 65-73.

[19] S.J. Zinkle, Fusion materials science: Overview of challenges and recent progress, Physics of Plasmas 12(5) (2005) 058101.

[20] E.E. Bloom, S.J. Zinkle, F.W. Wiffen, Materials to deliver the promise of fusion power – progress and challenges, Journal of Nuclear Materials 329-333 (2004) 12-19.

[21] U.S.E.I. Administration, Electric Power Annual 2021, in: D.o. Energy (Ed.) www.eia.gov, 2021, p. 31.

[22] S. Goldberg, R. Rosner, Nuclear reactors: Generation to generation, American academy of arts and sciences Cambridge, 2011.

[23] G.R. Odette, R.K. Nanstad, Predictive reactor pressure vessel steel irradiation embrittlement models: Issues and opportunities, JOM 61(7) (2009) 17-23.

[24] G.S. Was, Materials degradation in fission reactors: Lessons learned of relevance to fusion reactor systems, Journal of Nuclear Materials 367-370 (2007) 11-20.

[25] S. Ukai, M. Fujiwara, Perspective of ODS alloys application in nuclear environments, Journal of Nuclear Materials 307-311 (2002) 749-757.

[26] S.J. Zinkle, L.L. Snead, Designing Radiation Resistance in Materials for Fusion Energy, Annual Review of Materials Research 44(1) (2014) 241-267.

[27] M.J. Alinger, G.R. Odette, D.T. Hoelzer, The development and stability of Y–Ti–O nanoclusters in mechanically alloyed Fe–Cr based ferritic alloys, Journal of Nuclear Materials 329-333 (2004) 382-386.

[28] D.T. Hoelzer, J. Bentley, M.A. Sokolov, M.K. Miller, G.R. Odette, M.J. Alinger, Influence of particle dispersions on the high-temperature strength of ferritic alloys, Journal of Nuclear Materials 367-370 (2007) 166-172.

[29] Y. Xu, Z. Zhou, M. Li, P. He, Fabrication and characterization of ODS austenitic steels, Journal of Nuclear Materials 417(1) (2011) 283-285.

[30] S.J. Zinkle, J.L. Boutard, D.T. Hoelzer, A. Kimura, R. Lindau, G.R. Odette, M. Rieth, L. Tan, H. Tanigawa, Development of next generation tempered and ODS reduced

activation ferritic/martensitic steels for fusion energy applications, Nuclear Fusion 57(9) (2017) 092005.

[31] S.J. Zinkle, H. Tanigawa, B.D. Wirth, Chapter 5 - Radiation and Thermomechanical Degradation Effects in Reactor Structural Alloys, in: G.R. Odette, S.J. Zinkle (Eds.), Structural Alloys for Nuclear Energy Applications, Elsevier, Boston, 2019, pp. 163-210.

[32] F. Ning, X. Wang, Y. Yang, J. Tan, Z. Zhang, D. Jia, X. Wu, E.-H. Han, Uniform corrosion behavior of FeCrAl alloys in borated and lithiated high temperature water, Journal of Materials Science & Technology 70 (2021) 136-144.

[33] K.A. Terrani, B.A. Pint, Y.J. Kim, K.A. Unocic, Y. Yang, C.M. Silva, H.M. Meyer, R.B. Rebak, Uniform corrosion of FeCrAl alloys in LWR coolant environments, Journal of Nuclear Materials 479 (2016) 36-47.

[34] D.J. Park, H.G. Kim, J.Y. Park, Y.I. Jung, J.H. Park, Y.H. Koo, A study of the oxidation of FeCrAl alloy in pressurized water and high-temperature steam environment, Corrosion Science 94 (2015) 459-465.

[35] K.A. Terrani, S.J. Zinkle, L.L. Snead, Advanced oxidation-resistant iron-based alloys for LWR fuel cladding, Journal of Nuclear Materials 448(1) (2014) 420-435.

[36] R.L. Klueh, J.P. Shingledecker, R.W. Swindeman, D.T. Hoelzer, Oxide dispersion-strengthened steels: A comparison of some commercial and experimental alloys, Journal of Nuclear Materials 341(2) (2005) 103-114.

[37] C.P. Massey, S.N. Dryepondt, P.D. Edmondson, M.G. Frith, K.C. Littrell, A. Kini, B. Gault, K.A. Terrani, S.J. Zinkle, Multiscale investigations of nanoprecipitate nucleation, growth, and coarsening in annealed low-Cr oxide dispersion strengthened FeCrAl powder, Acta Materialia 166 (2019) 1-17.

[38] C.P. Massey, S.N. Dryepondt, P.D. Edmondson, K.A. Terrani, S.J. Zinkle, Influence of mechanical alloying and extrusion conditions on the microstructure and tensile properties of Low-Cr ODS FeCrAl alloys, Journal of Nuclear Materials 512 (2018) 227-238.

[39] G.R. Odette, S.J. Zinkle, Overview of Reactor Systems and Operational Environments for Structural Materials in Fusion Reactors, Structural Alloys for Nuclear Energy Applications, Elsevier2019, pp. 51-102.

[40] J. Wang, S. Liu, B. Xu, J. Zhang, M. Sun, D. Li, Research progress on preparation technology of oxide dispersion strengthened steel for nuclear energy, International Journal of Extreme Manufacturing 3(3) (2021) 032001.

[41] M.J. Alinger, G.R. Odette, D.T. Hoelzer, On the role of alloy composition and processing parameters in nanocluster formation and dispersion strengthening in nanostuctured ferritic alloys, Acta Materialia 57(2) (2009) 392-406.

[42] K. Dawson, S.J. Haigh, G.J. Tatlock, A.R. Jones, Nano-particle precipitation in mechanically alloyed and annealed precursor powders of legacy PM2000 ODS alloy, Journal of Nuclear Materials 464 (2015) 200-209.

[43] J. Fu, T.P. Davis, A. Kumar, I.M. Richardson, M.J.M. Hermans, Characterisation of the influence of vanadium and tantalum on yttrium-based nano-oxides in ODS Eurofer steel, Materials Characterization 175 (2021) 111072.

[44] M.K. Miller, D.T. Hoelzer, E.A. Kenik, K.F. Russell, Nanometer scale precipitation in ferritic MA/ODS alloy MA957, Journal of Nuclear Materials 329-333 (2004) 338-341.

[45] M.K. Miller, K.F. Russell, D.T. Hoelzer, Characterization of precipitates in MA/ODS ferritic alloys, Journal of Nuclear Materials 351(1) (2006) 261-268.

[46] J.R. Rieken, Gas atomized precursor alloy powder for oxide dispersion strengthened ferritic stainless steel, Materials Science and Engineering, Iowa State University, 2011, p. 362.

[47] J.R. Rieken, I.E. Anderson, M.J. Kramer, G.R. Odette, E. Stergar, E. Haney, Reactive gas atomization processing for Fe-based ODS alloys, Journal of Nuclear Materials 428(1) (2012) 65-75.

[48] X. Wang, J.T. Darsell, X. Ma, J. Liu, T. Liu, R. Prabhakaran, I.E. Anderson, D. Zhang, Manufacturing ODS Steels from GARS Powders by Friction Consolidation and Extrusion, JOM 76(6) (2024) 2899-2913.

[49] D. Zhang, J.T. Darsell, J. Wang, X. Ma, G.J. Grant, I.E. Anderson, J.R. Rieken, D.J. Edwards, W. Setyawan, T.J. Horn, G.R. Odette, No ball milling needed: Alternative ODS steel manufacturing with gas atomization reaction synthesis (GARS) and friction-based processing, Journal of Nuclear Materials 566 (2022) 153768.

[50] F. Bergner, I. Hilger, J. Virta, J. Lagerbom, G. Gerbeth, S. Connolly, Z. Hong, P.S. Grant, T. Weissgärber, Alternative Fabrication Routes toward Oxide-Dispersion-Strengthened Steels and Model Alloys, Metallurgical and Materials Transactions A 47(11) (2016) 5313-5324.

[51] E. Gil, N. Ordás, C. García-Rosales, I. Iturriza, Microstructural characterization of ODS ferritic steels at different processing stages, Fusion Engineering and Design 98-99 (2015) 1973-1977.

[52] Z. Hong, X. Zhang, Q. Yan, Y. Chen, A new method for preparing 9Cr-ODS steel using elemental yttrium and Fe2O3 oxygen carrier, Journal of Alloys and Compounds 770 (2019) 831-839.

[53] M.A. Moghadasi, M. Nili-Ahmadabadi, F. Forghani, H.S. Kim, Development of an oxide-dispersion-strengthened steel by introducing oxygen carrier compound into the melt aided by a general thermodynamic model, Scientific Reports 6(1) (2016) 38621.

[54] G. Qiu, D. Zhan, C. Li, M. Qi, Z. Jiang, H. Zhang, Development of a micro-scale Y–Zr–O oxide-dispersion-strengthened steel fabricated via vacuum induction melting and electro-slag remelting, Nuclear Engineering and Technology 51(6) (2019) 1589-1595.

[55] G.-x. Qiu, X.-l. Wei, C. Bai, D.-j. Miao, L. Cao, X.-m. Li, Inclusion and mechanical properties of ODS-RAFM steels with Y, Ti, and Zr fabricated by melting, Nuclear Engineering and Technology 54(7) (2022) 2376-2385.

[56] Z. Shi, F. Han, The microstructure and mechanical properties of micro-scale Y2O3 strengthened 9Cr steel fabricated by vacuum casting, Materials & Design (1980-2015) 66 (2015) 304-308.

[57] Z. Shi, F. Han, Microstructures and properties of cast T91-ODS alloys, Materials Research Innovations 19(sup5) (2015) S5-832-S5-835.

[58] D. Zhan, G. Qiu, Z. Jiang, H. Zhang, Effect of Yttrium and Titanium on Inclusions and the Mechanical Properties of 9Cr RAFM Steel Fabricated by Vacuum Melting, steel research international 88(12) (2017) 1700159.

[59] H. Tang, X. Chen, M. Chen, L. Zuo, B. Hou, Z. Wang, Microstructure and mechanical property of in-situ nano-particle strengthened ferritic steel by novel internal oxidation, Materials Science and Engineering: A 609 (2014) 293-299.

[60] T. Madzivhandila, S. Bhero, F. Varachia, The influence of titanium addition on wettability of high-chromium white cast iron-matrix composites, Journal of Composite Materials 53(11) (2019) 1567-1576.

[61] K. Verhiest, S. Mullens, J. Paul, I. De Graeve, N. De Wispelaere, S. Claessens, A. DeBremaecker, K. Verbeken, Experimental study on the contact angle formation of solidified iron–chromium droplets onto yttria ceramic substrates for the yttria/ferrous alloy system with variable chromium content, Ceramics International 40(1, Part B) (2014) 2187-2200.

[62] T. Boegelein, E. Louvis, K. Dawson, G. Tatlock, A.R. Jones, Characterisation of a complex thin walled structure fabricated by selective laser melting using a ferritic oxide dispersion strengthened steel, Materials Characterization 112 (2015).

[63] J. Fu, J. van Slingerland, H. Brouwer, V. Bliznuk, I. Richardson, M. Hermans, Applicability Study of Pulsed Laser Beam Welding on Ferritic–Martensitic ODS Eurofer Steel, Metals 10(6) (2020) 736.

[64] M. Seki, K. Hirako, S. Kono, Y. Kihara, T. Kaito, S. Ukai, Pressurized resistance welding technology development in 9Cr-ODS martensitic steels, Journal of Nuclear Materials 329-333 (2004) 1534-1538.

[65] J. Fu, I. Richardson, M. Hermans, Microstructure Study of Pulsed Laser Beam Welded Oxide Dispersion-Strengthened (ODS) Eurofer Steel, Micromachines 12(6) (2021) 629.

[66] S. Liang, Y. Lei, Q. Zhu, The filler powders laser welding of ODS ferritic steels, Journal of Nuclear Materials 456 (2015) 206-210.

[67] E. Getto, B. Baker, B. Tobie, S. Briggs, K. Hattar, K. Knipling, Effect of friction stir welding and self-ion irradiation on dispersoid evolution in oxide dispersion strengthened steel MA956 up to 25 dpa, Journal of Nuclear Materials 515 (2019) 407-419.

[68] H. Dawson, M. Serrano, S. Cater, E. Jimenez-Melero, Characterization of ODS steel friction stir welds and their abnormal grain growth behaviour, Fusion Engineering and Design 135 (2018) 174-182.

[69] B.S. Taysom, T.W. Nelson, C.D. Sorensen, R. DiDomizio, S. Huang, I.R. Potts, Weld strength and heat-affected zone size in friction welded NFA and CostE, Science and technology of welding and joining 26(8) (2021) 581-589.

[70] C.R. Lear, J.G. Gigax, M.M. Schneider, T.E. Steckley, T.J. Lienert, S.A. Maloy, B.P. Eftink, Solid-State Welding of the Nanostructured Ferritic Alloy 14YWT Using a Capacitive Discharge Resistance Welding Technique, Metals 12(1) (2022) 23.

[71] T.J. Lienert, C.R. Lear, T.E. Steckley, L.R. Lindamood, J.E. Gould, S.A. Maloy, B.P. Eftink, Projection-capacitor discharge resistance welding of 430 stainless steel and 14YWT, Journal of Manufacturing Processes 75 (2022) 1189-1201.

[72] L. Zhou, S. Feng, M. Sun, B. Xu, D. Li, Interfacial microstructure evolution and bonding mechanisms of 14YWT alloys produced by hot compression bonding, Journal of Materials Science & Technology 35(8) (2019) 1671-1680.

[73] S. Noh, B. Kim, R. Kasada, A. Kimura, Diffusion bonding between ODS ferritic steel and F82H steel for fusion applications, Journal of Nuclear Materials 426(1) (2012) 208-213.

[74] S. Noh, A. Kimura, T.K. Kim, Diffusion bonding of 9Cr ODS ferritic/martensitic steel with a phase transformation, Fusion Engineering and Design 89(7) (2014) 1746-1750.

[75] T. DebRoy, H.L. Wei, J.S. Zuback, T. Mukherjee, J.W. Elmer, J.O. Milewski, A.M. Beese, A. Wilson-Heid, A. De, W. Zhang, Additive manufacturing of metallic components – Process, structure and properties, Progress in Materials Science 92 (2018) 112-224.

[76] R.R. Dehoff, M.M. Kirka, W.J. Sames, H. Bilheux, A.S. Tremsin, L.E. Lowe, S.S. Babu, Site specific control of crystallographic grain orientation through electron beam additive manufacturing, Materials Science and Technology 31(8) (2015) 931-938.

[77] W.J. Sames, F.A. List, S. Pannala, R.R. Dehoff, S.S. Babu, The metallurgy and processing science of metal additive manufacturing, International Materials Reviews 61(5) (2016) 315-360.

[78] D. Dubey, A.S. Mirhakimi, M.A. Elbestawi, Negative Thermal Expansion Metamaterials: A Review of Design, Fabrication, and Applications, Journal of Manufacturing and Materials Processing, 2024.

[79] F. Mas, C. Tassin, F. Roch, M. Yescas, P. Todeschini, Y. Bréchet, Growth Morphologies and Primary Solidification Modes in a Dissimilar Weld between a Low-Alloy Steel and an Austenitic Stainless Steel, Metals, 2018.

[80] M. Ghayoor, S. Mirzababaei, A. Sittiho, I. Charit, B.K. Paul, S. Pasebani, Thermal stability of additively manufactured austenitic 304L ODS alloy, Journal of Materials Science & Technology 83 (2021) 208-218.

[81] R.M. Hunt, K.J. Kramer, B. El-Dasher, Selective laser sintering of MA956 oxide dispersion strengthened steel, Journal of Nuclear Materials 464 (2015) 80-85.

[82] T. Boegelein, S.N. Dryepondt, A. Pandey, K. Dawson, G.J. Tatlock, Mechanical response and deformation mechanisms of ferritic oxide dispersion strengthened steel structures produced by selective laser melting, Acta Materialia 87 (2015) 201-215.

[83] M.J. Aziz, Model for solute redistribution during rapid solidification, Journal of Applied Physics 53(2) (1982) 1158-1168.

[84] P.K. Galenko, E.V. Abramova, D. Jou, D.A. Danilov, V.G. Lebedev, D.M. Herlach, Solute trapping in rapid solidification of a binary dilute system: a phase-field study, Phys Rev E Stat Nonlin Soft Matter Phys 84(4 Pt 1) (2011) 041143.

[85] K. Saeidi, Stainless steels fabricated by laser melting : Scaled-down structural hierarchies and microstructural heterogeneities, Department of Materials and Environmental Chemistry (MMK), Stockholm University, Stockholm, 2016, p. 115.

[86] K. Saeidi, L. Kvetková, F. Lofaj, Z. Shen, Austenitic stainless steel strengthened by the in situ formation of oxide nanoinclusions, RSC Advances 5(27) (2015) 20747-20750.

[87] H. Springer, C. Baron, A. Szczepaniak, E.A. Jägle, M.B. Wilms, A. Weisheit, D. Raabe, Efficient additive manufacturing production of oxide- and nitride-dispersion-strengthened materials through atmospheric reactions in liquid metal deposition, Materials & Design 111 (2016) 60-69.

[88] N. Sridharan, S.N. Dryepondt, K.G. Field, Investigation of laser direct energy deposition for production of ODS alloys, United States, 2018.

[89] X. Zhou, Z. An, Z. Shen, W. Liu, C. Yao, Particles control in selective laser melting in-situ oxide dispersion strengthened method, IOP Conference Series: Materials Science and Engineering 167 (2017) 012048.

[90] D.R. Olander, A.T. Motta, Light Water Reactor Materials, Volume I - Fundamentals, American Nuclear Society (ANS), pp. 590-630.

[91] S.Y. Zhong, V. Klosek, Y.d. Carlan, M.H. Mathon, Modeling of structural hardening in oxide dispersion-strengthened (ODS) ferritic alloys, Journal of Materials Science 51(5) (2016) 2540-2549.

[92] Z. Shen, R.H. Wagoner, W.A.T. Clark, Dislocation pile-up and grain boundary interactions in 304 stainless steel, Scripta Metallurgica 20(6) (1986) 921-926.

[93] P. Dou, A. Kimura, T. Okuda, M. Inoue, S. Ukai, S. Ohnuki, T. Fujisawa, F. Abe, Polymorphic and coherency transition of Y–Al complex oxide particles with extrusion temperature in an Al-alloyed high-Cr oxide dispersion strengthened ferritic steel, Acta Materialia 59(3) (2011) 992-1002.

[94] S.Y. Zhong, J. Ribis, N. Lochet, Y. de Carlan, V. Klosek, M.H. Mathon, Influence of nano-particle coherency degree on the coarsening resistivity of the nano-oxide particles of Fe–14Cr–1W ODS alloys, Journal of Nuclear Materials 455(1) (2014) 618-623.

[95] C.P. Massey, Multiscale Investigations of Nanoprecipitate Nucleation, Growth, and Coarsening in ODS FeCrAl Alloys: Optimizing Sink Strength for Nuclear Applications, Nuclear Engineering, University of Tennessee, 2018, p. 231.

[96] L. Tan, J.T. Busby, Formulating the strength factor α for improved predictability of radiation hardening, Journal of Nuclear Materials 465 (2015) 724-730.

[97] U.F. Kocks, The theory of an obstacle-controlled yield strength—Report after an international workshop, Materials Science and Engineering 27(3) (1977) 291-298.

[98] A. Seeger, Proc. 2nd UN Int. Conf. On Peaceful Uses of Atomic Energy, Geneva, 1958, p. 250.

[99] J. Friedel, Dislocations, Pergamon Press; [U.S.A. ed. distributed by Addison-Wesley Pub. Co., Reading, Mass.], Oxford; New York, 1964.

[100] P. Zhu, Y. Zhao, S. Agarwal, J. Henry, S.J. Zinkle, Toward accurate evaluation of bulk hardness from nanoindentation testing at low indent depths, Materials & Design 213 (2022) 110317.

[101] G.R. Odette, Recent Progress in Developing and Qualifying Nanostructured Ferritic Alloys for Advanced Fission and Fusion Applications, JOM 66(12) (2014) 2427-2441.

[102] A. Agnoli, M. Bernacki, R. Logé, J.-M. Franchet, J. Laigo, N. Bozzolo, Understanding and Modeling of Grain Boundary Pinning in Inconel 718, Superalloys 20122012, pp. 73-82.

[103] G.S. Was, Radiation-Enhanced Diffusion and Defect Reaction Rate Theory, in: G.S. Was (Ed.), Fundamentals of Radiation Materials Science: Metals and Alloys, Springer New York, New York, NY, 2017, pp. 207-252.

[104] L. Yang, Y. Jiang, G. Robert Odette, T. Yamamoto, Z. Liu, Y. Liu, Trapping helium in Y2Ti2O7 compared to in matrix iron: A first principles study, Journal of Applied Physics 115(14) (2014) 143508.

[105] M.L. Lescoat, J. Ribis, A. Gentils, O. Kaïtasov, Y. de Carlan, A. Legris, In situ TEM study of the stability of nano-oxides in ODS steels under ion-irradiation, Journal of Nuclear Materials 428(1) (2012) 176-182.

[106] S. Rogozhkin, A. Bogachev, O. Korchuganova, A. Nikitin, N. Orlov, A. Aleev, A. Zaluzhnyi, M. Kozodaev, T. Kulevoy, B. Chalykh, R. Lindau, J. Hoffmann, A. Möslang, P. Vladimirov, M. Klimenkov, M. Heilmaier, J. Wagner, S. Seils, Nanostructure evolution in ODS steels under ion irradiation, Nuclear Materials and Energy 9 (2016) 66-74.

[107] J. Ribis, I. Mouton, C. Baumier, A. Gentils, M. Loyer-Prost, L. Lunéville, D. Siméone, Nano-Structured Materials under Irradiation: Oxide Dispersion-Strengthened Steels, Nanomaterials (Basel) 11(10) (2021).

[108] X. Wang, M. Posselt, J. Faßbender, Influence of substitutional atoms on the diffusion of oxygen in dilute iron alloys, Physical Review B 98(6) (2018) 064103.

[109] K.A. Unocic, B.A. Pint, D.T. Hoelzer, Advanced TEM characterization of oxide nanoparticles in ODS Fe–12Cr–5Al alloys, Journal of Materials Science 51(20) (2016) 9190-9206.

[110] S. Ukai, S. Ohtsuka, T. Kaito, Y. de Carlan, J. Ribis, J. Malaplate, 10 - Oxide dispersion-strengthened/ferrite-martensite steels as core materials for Generation IV nuclear reactors, in: P. Yvon (Ed.), Structural Materials for Generation IV Nuclear Reactors, Woodhead Publishing2017, pp. 357-414.

[111] P. Dou, S. Jiang, L. Qiu, A. Kimura, Effects of contents of Al, Zr and Ti on oxide particles in Fe–15Cr–2W–0.35Y2O3 ODS steels, Journal of Nuclear Materials 531 (2020) 152025.

[112] C. Lu, Z. Lu, R. Xie, Z. Li, C. Liu, L. Wang, Effect of Y/Ti atomic ratio on microstructure of oxide dispersion strengthened alloys, Materials Characterization 134 (2017) 35-40.

[113] N. Cunningham, Y. Wu, D. Klingensmith, G.R. Odette, On the remarkable thermal stability of nanostructured ferritic alloys, Materials Science and Engineering: A 613 (2014) 296-305.

[114] N.J. Cunningham, Study of Structure, Composition, and Stability of Y-Ti-O Nm-scale Features in Nano-structured Ferritic Alloys, University of California, Santa Barbara2012.

[115] N.J. Cunningham, M.J. Alinger, D. Klingensmith, Y. Wu, G.R. Odette, On nano-oxide coarsening kinetics in the nanostructured ferritic alloy MA957: A mechanism based predictive model, Materials Science and Engineering: A 655 (2016) 355-362.

[116] D.T. Hoelzer, K.A. Unocic, M.A. Sokolov, T.S. Byun, Influence of processing on the microstructure and mechanical properties of 14YWT, Journal of Nuclear Materials 471 (2016) 251-265.

[117] C. Suryanarayana, Mechanical alloying and milling, Progress in Materials Science 46(1) (2001) 1-184.

[118] E. Aydogan, S.A. Maloy, O. Anderoglu, C. Sun, J.G. Gigax, L. Shao, F.A. Garner, I.E. Anderson, J.J. Lewandowski, Effect of tube processing methods on microstructure, mechanical properties and irradiation response of 14YWT nanostructured ferritic alloys, Acta Materialia 134 (2017) 116-127.

[119] C. Capdevila, H.K.D.H. Bhadeshia, Manufacturing and Microstructural Evolution of Mechanuically Alloyed Oxide Dispersion Strengthened Superalloys, Advanced Engineering Materials 3(9) (2001) 647-656.

[120] H. Jia, R. Zhang, D. Long, Y. Sun, Z. Zhou, Effect of zirconium content on mechanical properties of ODS FeCrAl alloy, Materials Science and Engineering: A 839 (2022) 142824.

[121] T.K. Kim, S. Noh, S.H. Kang, J.J. Park, H.J. Jin, M.K. Lee, J. Jang, C.K. Rhee, Current Status and Future Prospective of Advanced Radiation Resistant Oxide Dispersion Strengthened Steel (ARROS) Development for Nuclear Reactor System Applications, Nuclear Engineering and Technology 48(2) (2016) 572-594.

[122] S. Ohtsuka, S. Ukai, M. Fujiwara, T. Kaito, T. Narita, Improvement of 9Cr-ODS martensitic steel properties by controlling excess oxygen and titanium contents, Journal of Nuclear Materials 329-333 (2004) 372-376.

[123] B. Hary, R. Logé, J. Ribis, M.H. Mathon, M. Van Der Meer, T. Baudin, Y. de Carlan, Strain-induced dissolution of Y–Ti–O nano-oxides in a consolidated ferritic oxide dispersion strengthened (ODS) steel, Materialia 4 (2018) 444-448.

[124] T. Okuda, M. Fujiwara, Dispersion behaviour of oxide particles in mechanically alloyed ODS steel, Journal of Materials Science Letters 14(22) (1995) 1600-1603.

[125] M.J. Alinger, On the formation and stability of nanometer scale precipitates in ferritic alloys during processing and high temperature service, 2004.

[126] M. Herrmann, J. Räthel, Hot Pressing and Hot Isostatic Pressing, in: M. Pomeroy (Ed.), Encyclopedia of Materials: Technical Ceramics and Glasses, Elsevier, Oxford, 2021, pp. 270-277.

[127] H.V. Atkinson, S. Davies, Fundamental aspects of hot isostatic pressing: An overview, Metallurgical and Materials Transactions A 31(12) (2000) 2981-3000.

[128] A. Upadhyaya, G.S. Upadhyaya, Powder Metallurgy: Science, Technology and Materials, 2011.

[129] E. Aydogan, S. Pal, O. Anderoglu, S.A. Maloy, S.C. Vogel, G.R. Odette, J.J. Lewandowski, D.T. Hoelzer, I.E. Anderson, J.R. Rieken, Effect of tube processing methods on the texture and grain boundary characteristics of 14YWT nanostructured ferritic alloys, Materials Science and Engineering: A 661 (2016) 222-232.

[130] S. Pal, M.E. Alam, S.A. Maloy, D.T. Hoelzer, G.R. Odette, Texture evolution and microcracking mechanisms in as-extruded and cross-rolled conditions of a 14YWT nanostructured ferritic alloy, Acta Materialia 152 (2018) 338-357.

[131] A. Das, H.W. Viehrig, F. Bergner, C. Heintze, E. Altstadt, J. Hoffmann, Effect of microstructural anisotropy on fracture toughness of hot rolled 13Cr ODS steel – The role of primary and secondary cracking, Journal of Nuclear Materials 491 (2017) 83-93.

[132] G.R. Odette, On the status and prospects for nanostructured ferritic alloys for nuclear fission and fusion application with emphasis on the underlying science, Scripta Materialia 143 (2018) 142-148.

[133] X. Gao, H. Ren, H. Wang, S. Chen, Activity coefficient and solubility of yttrium in Fe-Y dilute solid solution, Journal of Rare Earths 34(11) (2016) 1168-1172.

[134] M. Ghayoor, K. Lee, Y. He, C.-h. Chang, B.K. Paul, S. Pasebani, Selective laser melting of austenitic oxide dispersion strengthened steel: Processing, microstructural evolution and strengthening mechanisms, Materials Science and Engineering: A 788 (2020) 139532.

[135] L.L. Yuan Zhong, Ji Zou, Xiaodong Li, Daqing Cui, Zhijian Shen, Oxide dispersion strengthened stainless steel 316L with superior strength and ductility by selective laser melting, J. Mater. Sci. Technol. 42(0) (2020) 97-105.

[136] S. Saptarshi, M. deJong, C. Rock, I. Anderson, R. Napolitano, J. Forrester, S. Lapidus, D. Kaoumi, T. Horn, Laser Powder Bed Fusion of ODS 14YWT from Gas Atomization Reaction Synthesis Precursor Powders, JOM 74(9) (2022) 3303-3315.

[137] X. Zhou, Z. An, Z. Shen, W. Liu, C. Yao, Particles control in selective laser melting in-situ oxide dispersion strengthened method, IOP Conference Series: Materials Science and Engineering 167(1) (2017) 012048.

[138] S. Zhong, J. Ribis, V. Klosek, Y. De Carlan, N. Lochet, V. Ji, M. Mathon, Study of the thermal stability of nanoparticle distributions in an oxide dispersion strengthened (ODS) ferritic alloys, Journal of nuclear materials 428(1-3) (2012) 154-159.

[139] D. Zhang, J.T. Darsell, J. Wang, X. Ma, G.J. Grant, I.E. Anderson, J.R. Rieken, D.J. Edwards, W. Setyawan, T.J. Horn, G.R. Odette, No ball milling needed: Alternative ODS steel manufacturing with gas atomization reaction synthesis (GARS) and friction-based processing, Journal of Nuclear Materials (2022) 153768.

[140] S. Kuo, Chemical Reactions in Welding, Welding Metallurgy, John Wiley & Sons, Inc.2003, pp. 65-96.

[141] T. DebRoy, S.A. David, Physical processes in fusion welding, Reviews of Modern Physics 67(1) (1995) 85-112.

[142] X. Guo, H.-L. Huang, M. Zhu, K. Hariharan, S.-C. Chien, N. Huynh, J. Hwang, W. Windl, C.D. Taylor, E.J. Schindelholz, G.S. Frankel, Interstitial elements created via metal 3D printing, Materials Today 66 (2023) 92-104.

[143] D.-R. Eo, S.-G. Chung, J. Yang, I.-H. Jung, J.-W. Cho, Numerical modeling of oxide particle evolution during additive manufacturing, Additive Manufacturing 51 (2022) 102631.

[144] K.J. Malmberg, H. Shibata, S.-y. Kitamura, P.G. Jönsson, S. Nabeshima, Y. Kishimoto, Observed behavior of various oxide inclusions in front of a solidifying low-carbon steel shell, Journal of Materials Science 45(8) (2010) 2157-2164.

[145] N.A. Wassermann, Y. Li, A.J. Myers, C.A. Kantzos, T.M. Smith, J.L. Beuth, J.A. Malen, L. Shao, A.J.H. McGaughey, S.P. Narra, Limits of dispersoid size and number

density in oxide dispersion strengthened alloys fabricated with powder bed fusion-laser beam, Additive Manufacturing 81 (2024) 104022.

[146] O. Grong, Ø. Grong, I.o. Materials, Metallurgical Modelling of Welding, Institute of Materials1997.

[147] S.S. Babu, S.A. David, T. DebRoy, Coarsening of oxide inclusions in low alloy steel welds, Science and Technology of Welding and Joining 1 (1996) 17-27.

[148] W.D. Kingery, Metal-Ceramic Interactions:IV, Absolute Measurement of Metal-Ceramic Interfacial Energy and the Interfacial Adsorption of Silicon from Iron-Silicon Alloys, Journal of the American Ceramic Society 37(2) (1954) 42-45.

[149] M. Humenik Jr, W.D. Kingery, Metal-Ceramic Interactions: III, Surface Tension and Wettability of Metal-Ceramic Systems, Journal of the American Ceramic Society 37(1) (1954) 18-23.

[150] C. Douvris, T. Vaughan, D. Bussan, G. Bartzas, R. Thomas, How ICP-OES changed the face of trace element analysis: Review of the global application landscape, Science of The Total Environment 905 (2023) 167242.

[151] H.-M. Hong, Y.-B. Kang, Simultaneous Analysis of Soluble and Insoluble Oxygen Contents in Steel Specimens Using Inert Gas Fusion Infrared Absorptiometry, ISIJ International 61(9) (2021) 2464-2473.

[152] E. Hallberg, Investigation of hot cracking in additive manufactured nickel-base superalloys, Department of Industrial and Material Science, Chalmers University of Technology, Gothenburg, Sweded, 2018, p. 54.

[153] J. Schindelin, I. Arganda-Carreras, E. Frise, V. Kaynig, M. Longair, T. Pietzsch, S. Preibisch, C. Rueden, S. Saalfeld, B. Schmid, J.-Y. Tinevez, D.J. White, V. Hartenstein, K.

Eliceiri, P. Tomancak, A. Cardona, Fiji: an open-source platform for biological-image analysis, Nature Methods 9(7) (2012) 676-682.

[154] P. Wang, Y. Qiao, W. Qi, S. Du, Z. Liu, F. Meng, X. Zhang, K. Wang, Q. Li, Z. Yao, C. Bai, X. Wang, Preparation and Properties Study of Cr on FeCrAl Cladding Materials, Frontiers in Materials 8(621086) (2021) 1-11.

[155] R.F. Egerton, Physical Principles of Electron Microscopy: An Introduction to TEM, SEM, and AEM, Physical Principles of Electron Microscopy (2005).

[156] A.J. Schwartz, M. Kumar, B.L. Adams, Electron Backscatter Diffraction in Materials Science, 2000.

[157] M.K. Miller, K.F. Russell, Atom probe specimen preparation with a dual beam SEM/FIB miller, Ultramicroscopy 107(9) (2007) 761-6.

[158] T. Malis, S.C. Cheng, R.F. Egerton, EELS log-ratio technique for specimen-thickness measurement in the TEM, Journal of Electron Microscopy Technique 8(2) (1988) 193-200.

[159] B. Gault, A. Chiaramonti, O. Cojocaru-Mirédin, P. Stender, R. Dubosq, C. Freysoldt, S.K. Makineni, T. Li, M. Moody, J.M. Cairney, Atom probe tomography, Nat Rev Methods Primers 1(51) (2021).

[160] K. Nogi, K. Ogino, Role of Interfacial Phenomena in Deoxidation Process of Molten Iron, Canadian Metallurgical Quarterly 22(1) (1983) 19-28.

[161] N. Takiuchi, T. Taniguchi, Y. Tanaka, N. Shinozaki, K. Mukai, Effects of Oxygen and Temperature on the Surface Tension of Liquid Iron and Its Wettability of Alumina, Journal of the Japan Institute of Metals 55(2) (1991) 180-185.

[162] K. Nakashima, K. Mori, Interfacial Properties of Liquid Iron Alloys and Liquid Slags Relating to Iron- and Steel-making Processes, ISIJ International 32(1) (1992) 11-18.

[163] T. Horn, C. Rock, D. Kaoumi, I. Anderson, E. White, T. Prost, J. Rieken, S. Saptarshi, R. Schoell, M. DeJong, S. Timmins, J. Forrester, S. Lapidus, R. Napolitano, D. Zhang, J. Darsell, Laser powder bed fusion additive manufacturing of oxide dispersion strengthened steel using gas atomized reaction synthesis powder, Materials & Design 216 (2022) 110574.

[164] M. Yesim Yalcin, D. Bora, E. Aydogan, Development and additive manufacturing of oxide dispersion strengthened inconel 718: Thermochemical and experimental studies, Journal of Alloys and Compounds 914 (2022) 165193.

[165] X. He, T. DebRoy, P.W. Fuerschbach, Alloying element vaporization during laser spot welding of stainless steel, Journal of Physics D: Applied Physics 36(23) (2003) 3079.

[166] J. Dupont, J. Regina, K. Adams, Improving the weldability of fecral weld overlay coatings, Annual Conference on Fossil Energy Materials, Citeseer, 2007, p. 132.

[167] J. Regina, J. Dupont, A. Marder, The effect of chromium on the weldability and microstructure of Fe-Cr-Al weld cladding, WELDING JOURNAL-NEW YORK- 86(6) (2007) 170.

[168] K.G. Field, M.N. Gussev, Y. Yamamoto, L.L. Snead, Deformation behavior of laser welds in high temperature oxidation resistant Fe–Cr–Al alloys for fuel cladding applications, Journal of Nuclear Materials 454(1) (2014) 352-358.

[169] M. Rappaz, J.M. Drezet, M. Gremaud, A new hot-tearing criterion, Metallurgical and Materials Transactions A 30(2) (1999) 449-455.

[170] J.H. Martin, B.D. Yahata, J.M. Hundley, J.A. Mayer, T.A. Schaedler, T.M. Pollock, 3D printing of high-strength aluminium alloys, Nature 549(7672) (2017) 365-369.

[171] S. Kou, A criterion for cracking during solidification, Acta Materialia 88 (2015) 366-374.

[172] P. Ewels, T. Sikora, V. Serin, C.P. Ewels, L. Lajaunie, A Complete Overhaul of the Electron Energy-Loss Spectroscopy and X-Ray Absorption Spectroscopy Database: eelsdb.eu, Microsc Microanal 22(3) (2016) 717-24.

[173] V.K. B.R, A. Dasgupta, C. Ghosh, S.K. Sinha, Analysis of structural transformation in nanocrystalline Y2O3 during high energy ball milling, Journal of Alloys and Compounds 900 (2022) 163550.

[174] F. Pailloux, D. Imhoff, M. Jublot, F. Paumier, R.J. Gaboriaud, M. Jaouen, HRTEM and EELS study of Y2O3/MgO thin films, Micron 37(5) (2006) 420-425.

[175] A.A.B. Sugden, H.K.D.H. Bhadeshia, The nonunjform distribution of inclusions in low-alloy steel weld deposits, Metallurgical Transactions A 19(3) (1988) 669-674.

[176] S. Babu, S. David, J.M. Vitek, K. Mundra, Model for inclusion formation in low alloy steel welds, Science and Technology of Welding & Joining 4 (1999) 276-284.

[177] S. Babu, S. David, J. Vitek, K. Mundra, T. Debroy, Development of macro and microstructures of carbon-manganese low alloy steel welds: Inclusion formation, Materials Science and Technology 11 (1995) 186-199.

[178] F. Christien, R. Le Gall, G. Saindrenan, Phosphorus grain boundary segregation in steel 17-4 PH, Scripta materialia 48(3) (2003) 301-306.

[179] J.A. Hudson, S.G. Druce, G. Gage, M. Wall, Thermal ageing effects in structural steels, Theoretical and Applied Fracture Mechanics 10 (1988) 123-133.

[180] M. Militzer, J. Wieting, Comments on the grain boundary segregation and diffusion of phosphorus in a 12%CrMoV-steel, Scripta Metallurgica et Materialia 28(9) (1993) 1043-1046.

[181] A.V. Nikolaeva, Y.A. Nikolaev, Y.R. Kevorkyan, Grain-Boundary Segregation of Phosphorus in Low-Alloy Steel, Atomic Energy 91(1) (2001) 534-542.

[182] S.H. Song, Z.X. Yuan, D.D. Shen, J. Liu, L.Q. Weng, Grain boundary segregation of phosphorus and molybdenum in a Cr - Mo low alloy steel, Materials science and technology 20(1) (2004) 117-120.

[183] Z. Wang, S. Yang, S.B. Lawson, V.V.K. Doddapaneni, M. Albert, B. Sutton, C.H. Chang, S. Pasebani, D. Xu, Atomic Diffusivities of Yttrium, Titanium and Oxygen Calculated by Ab Initio Molecular Dynamics in Molten 316L Oxide-Dispersion-Strengthened Steel Fabricated via Additive Manufacturing, Materials (Basel) 17(7) (2024).

[184] K.S. Mao, C.P. Massey, M.N. Gussev, Y. Yamamoto, A.T. Nelson, K.G. Field, P.D. Edmondson, Irradiation-induced amorphization of Fe-Y-based second phase particles in accident-tolerant FeCrAl alloys, Materialia 15 (2021) 101016.

[185] S.L. Shang, H.Z. Fang, J. Wang, C.P. Guo, Y. Wang, P.D. Jablonski, Y. Du, Z.K. Liu, Vacancy mechanism of oxygen diffusivity in bcc Fe: A first-principles study, Corrosion Science 83 (2014) 94-102.

[186] J. Takada, S. Yamamoto, S. Kikuchi, M. Adachi, Internal oxidation of Fe-Al alloys in the α-phase region, Oxidation of Metals 25(1) (1986) 93-105.

[187] J.T. Busby, M.C. Hash, G.S. Was, The relationship between hardness and yield stress in irradiated austenitic and ferritic steels, Journal of Nuclear Materials 336(2) (2005) 267-278.

[188] Z. Sun, H. Bei, Y. Yamamoto, Microstructural control of FeCrAl alloys using Mo and Nb additions, Materials Characterization 132 (2017) 126-131.

[189] A. Spierings, K. Wegener, G. Levy, Designing material properties locally with additive manufacturing technology SLM, 23rd Annual International Solid Freeform Fabrication Symposium - An Additive Manufacturing Conference, SFF 2012 (2012) 447-455.

[190] D.R. Clymer, J. Cagan, J. Beuth, Power–Velocity Process Design Charts for Powder Bed Additive Manufacturing, Journal of Mechanical Design 139(10) (2017).

[191] D. Svetlizky, M. Das, B. Zheng, A.L. Vyatskikh, S. Bose, A. Bandyopadhyay, J.M. Schoenung, E.J. Lavernia, N. Eliaz, Directed energy deposition (DED) additive manufacturing: Physical characteristics, defects, challenges and applications, Materials Today 49 (2021) 271-295.

[192] S.M. Yusuf, N. Gao, Influence of energy density on metallurgy and properties in metal additive manufacturing, Materials Science and Technology 33(11) (2017) 1269-1289.

[193] N. Diaz Vallejo, C. Lucas, N. Ayers, K. Graydon, H. Hyer, Y. Sohn, Process Optimization and Microstructure Analysis to Understand Laser Powder Bed Fusion of 316L Stainless Steel, Metals 11(5) (2021) 832.

[194] B. Fotovvati, S.F. Wayne, G. Lewis, E. Asadi, A Review on Melt-Pool Characteristics in Laser Welding of Metals, Advances in Materials Science and Engineering 2018 (2018) 4920718.

[195] S. Lu, H. Fujii, H. Sugiyama, M. Tanaka, K. Nogi, Effects of Oxygen Additions to Argon Shielding Gas on GTA Weld Shape, ISIJ International 43(10) (2003) 1590-1595.

[196] Y.Z. Zhao, H.Y. Zhao, Y.P. Lei, Y.W. Shi, Theoretical study of Marangoni convection and weld penetration under influence of high oxygen content in base metal, Science and Technology of Welding and Joining 12(5) (2007) 410-417.

[197] Y.M. Wang, T. Voisin, J.T. McKeown, J. Ye, N.P. Calta, Z. Li, Z. Zeng, Y. Zhang, W. Chen, T.T. Roehling, R.T. Ott, M.K. Santala, Philip J. Depond, M.J. Matthews, A.V. Hamza, T. Zhu, Additively manufactured hierarchical stainless steels with high strength and ductility, Nature Materials 17(1) (2018) 63-71.

[198] C.K. Gupta, Thermodynamics and Kinetics, Chemical Metallurgy2003, pp. 225-342.

[199] S. Otsuka, Z. Kozuka, The Diffusivities of Oxygen in Liquid Nickel and Liquid Iron Determined by Electrochemical Measurements, Transactions of the Japan Institute of Metals 18(10) (1977) 690-696.

[200] K.A. Gamble, T. Barani, D. Pizzocri, J.D. Hales, K.A. Terrani, G. Pastore, An investigation of FeCrAl cladding behavior under normal operating and loss of coolant conditions, Journal of Nuclear Materials 491 (2017) 55-66.

[201] W.D. Callister, Materials Science and Engineering: An Introduction, 7th Edition, 2006.

[202] A. Plotkowski, M.M. Kirka, S.S. Babu, Verification and validation of a rapid heat transfer calculation methodology for transient melt pool solidification conditions in powder bed metal additive manufacturing, Additive Manufacturing 18 (2017) 256-268.

[203] S.A. David, S.S. Babu, J.M. Vitek, Welding: Solidification and microstructure, JOM 55(6) (2003) 14-20.

[204] P. Singha, Insights Thermodynamic in Basic Oxygen Steel Making Process, ISIJ International 63(8) (2023) 1343-1350.

[205] N. Ordás, E. Gil, A. Cintins, V. de Castro, T. Leguey, I. Iturriza, J. Purans, A. Anspoks, A. Kuzmin, A. Kalinko, The role of yttrium and titanium during the development of ODS ferritic steels obtained through the STARS route: TEM and XAS study, Journal of Nuclear Materials 504 (2018) 8-22.

[206] A. Almomani, A.-H. I. Mourad, I. Barsoum, Effect of sulfur, phosphorus, silicon, and delta ferrite on weld solidification cracking of AISI 310S austenitic stainless steel, Engineering Failure Analysis 139 (2022) 106488.

[207] K. Kadoi, S. Ueno, H. Inoue, Effects of ferrite content and concentrations of carbon and silicon on weld solidification cracking susceptibility of stainless steels, Journal of Materials Research and Technology 25 (2023) 1314-1321.

[208] J. Yoo, K. Han, Y. Park, C. Lee, Effect of silicon on the solidification cracking behavior and metastable carbide formation in austenitic high Mn steel welds, Materials Chemistry and Physics 148(3) (2014) 499-502.

[209] L. Boatemaa, J.C. Brouwer, S. van der Zwaag, W.G. Sloof, The effect of the TiC particle size on the preferred oxidation temperature for self-healing of oxide ceramic matrix materials, Journal of Materials Science 53(8) (2018) 5973-5986.

[210] V.A. Lavrenko, L.A. Glebov, A.P. Pomitkin, V.G. Chuprina, T.G. Protsenko, High-temperature oxidation of titanium carbide in oxygen, Oxidation of Metals 9(2) (1975) 171-179.

[211] W. Nakao, S. Abe, Enhancement of the self-healing ability in oxidation induced self-healing ceramic by modifying the healing agent, Smart Materials and Structures 21(2) (2012) 025002.

[212] K. Shinozaki, P. Wen, M. Yamamoto, K. Kadoi, Y. Kohno, T. Komori, Effect of Grain Size on Solidification Cracking Susceptibility of Type 347 Stainless Steel during Laser Welding, QUARTERLY JOURNAL OF THE JAPAN WELDING SOCIETY 29 (2011) 90s-94s.

[213] L. Reimer, H. Kohl, Transmission electron microscopy : physics of image formation, 5th ed ed., Springer, New York, NY, 2008.

[214] M. Bachhav, F. Danoix, B. Hannoyer, J.M. Bassat, R. Danoix, Investigation of O-18 enriched hematite (α-Fe2O3) by laser assisted atom probe tomography, International Journal of Mass Spectrometry 335 (2013) 57-60.

[215] I. Blum, L. Rigutti, F. Vurpillot, A. Vella, A. Gaillard, B. Deconihout, Dissociation Dynamics of Molecular Ions in High dc Electric Field, The Journal of Physical Chemistry A 120(20) (2016) 3654-3662.

[216] A. La Fontaine, B. Gault, A. Breen, L. Stephenson, A.V. Ceguerra, L. Yang, T. Dinh Nguyen, J. Zhang, D.J. Young, J.M. Cairney, Interpreting atom probe data from chromium oxide scales, Ultramicroscopy 159 (2015) 354-359.

[217] Z. Peng, F. Vurpillot, P.-P. Choi, Y. Li, D. Raabe, B. Gault, On the detection of multiple events in atom probe tomography, Ultramicroscopy 189 (2018) 54-60.

[218] W. Sha, L. Chang, G.D.W. Smith, C. Liu, E.J. Mittemeijer, Some aspects of atom-probe analysis of Fe□C and Fe□N systems, Surface Science 266(1) (1992) 416-423.

[219] G.R. Odette, N.J. Cunningham, T. Stan, M.E. Alam, Y. De Carlan, Chapter 12 - Nano-Oxide Dispersion-Strengthened Steels, in: G.R. Odette, S.J. Zinkle (Eds.), Structural Alloys for Nuclear Energy Applications, Elsevier, Boston, 2019, pp. 529-583.

[220] J. Rösler, E. Arzt, A new model-based creep equation for dispersion strengthened materials, Acta Metallurgica et Materialia 38(4) (1990) 671-683.

[221] H. Shibata, S. Ukai, N.H. Oono, K. Sakamoto, M. Hirai, Development of accident tolerant FeCrAl-ODS steels utilizing Ce-oxide particles dispersion, Journal of Nuclear Materials 502 (2018) 228-235.

[222] Z. Li, Z. Lu, R. Xie, C. Lu, Y. Shi, C. Liu, Effects of Y2O3, La2O3 and CeO2 additions on microstructure and mechanical properties of 14Cr-ODS ferrite alloys produced by spark plasma sintering, Fusion Engineering and Design 121 (2017) 159-166.

VITA

Ty Austin grew up in small-town Neosho, MO. After graduating as Valedictorian in high school, he attended the University of Arkansas where he studied chemical engineering. During a summer research experience at Texas A&M University, Ty discovered his interest in nuclear materials. After graduating summa cum laude with his bachelor's degree in chemical engineering, he decided that he wanted to change career paths and explore his newfound interest with a Doctor of Philosophy in Nuclear Engineering with a focus on nuclear materials. He chose to attend the University of Tennessee, Knoxville under Dr. Steven Zinkle, where he studied advanced fabrication techniques for producing structural materials for nuclear applications. Ty will obtain his Doctor of Philosophy in Nuclear Engineering in August of 2024.